MICROSTRUCTURAL ANALYSIS OF WELD CRACKING IN 718 PLUS SUPERALLOY

by

Krutika Vishwakarma

A Dissertation submitted to the Faculty of Graduate Studies of

The University of Manitoba

in partial fulfilment of the requirements of the degree of

DOCTOR OF PHILOSOPHY

Department of Mechanical and Manufacturing Engineering

University of Manitoba

Winnipeg

Copyright © 2007 by Krutika Vishwakarma

THE UNIVERSITY OF MANITOBA

FACULTY OF GRADUATE STUDIES

*****

COPYRIGHT PERMISSION

MICROSTRUCTURAL ANALYSIS OF WELD CRACKING IN 718 PLUS SUPERALLOY

BY

Krutika Vishwakarma

A Thesis/Practicum submitted to the Faculty of Graduate Studies of The University of Manitoba in partial fulfillment of the requirement of the degree

DOCTOR OF PHILOSPHY

Krutika Vishwakarma © 2007

Permission has been granted to the University of Manitoba Libraries to lend a copy of this thesis/practicum, to Library and Archives Canada (LAC) to lend a copy of this thesis/practicum, and to LAC's agent (UMI/ProQuest) to microfilm, sell copies and to publish an abstract of this thesis/practicum.

This reproduction or copy of this thesis has been made available by authority of the copyright owner solely for the purpose of private study and research, and may only be reproduced and copied as permitted by copyright laws or with express written authorization from the copyright owner.

Acknowledgements

My sincere thanks to my supervisor, Prof. M. C. Chaturvedi for giving me the opportunity to work with him and for guiding me, both, academically and personally throughout the years. I would also like to thank him for providing me the financial support for the project. I also thank the University of Manitoba for the graduate fellowship.

I am grateful to Prof. B. P. Kashyap (IIT Bombay) who helped me to come to Winnipeg. I would also like to thank Prof. N.L.Richards for his constant encouragement and extremely useful discussions. Thanks are also due to Dr. Ojo for his valuable suggestions. I am indebted to Dr. Sidhu for her unending support and advice. I sincerely acknowledge the support of Dr. R.G.Ding and fellow students in the lab Mr. Oluwaseun Idowu and Mr. Dotun Akinlade. I also want to thank Mr. John Van Dorp, Mr. Don Mardis, Mr. Dan McCooeye, Mr. Mike Boskwick and Dr. Rong Liu for their technical support.

I would like to express my greatest appreciation to my family for their blessings without which I couldn't have been here. Thanks to my long standing friends Phalguni, Satya and Eswar for putting up with me and getting me through my difficult times.

Abstract

Allvac 718® PLUS™ (718 Plus) is a new Ni-base superalloy developed to be used in land and aero gas turbine applications. 718 Plus was developed to have high temperature properties superior to its baseline superalloy Inconel 718, while maintaining its workability. Besides its high temperature properties superior to Inconel 718, limited information exists about its physical metallurgy or weldability. This project studied the microstructure and electron beam welding response of this new superalloy in two selected pre-weld heat treated conditions. To further understand the effect of minor alloying elements on its weldability, two versions of 718 Plus with varying concentrations of boron and phosphorus, HC 49 with higher B and P and HC 20 with normal B and P, were also studied. Finally, the weldability of 718 Plus alloys was compared to that of Inconel 718 and Waspaloy under similar welding conditions.

Hot rolled wrought plates of Inconel 718, Waspaloy and 718 Plus alloys were supplied by ALLVAC Inc. 12.7 mm × 12.7 mm × 101.6 mm sections were cut normal to the rolling direction of the plates and were subjected to their recommended respective solution heat treatments, viz., 950°C for 1 hour for 718 Plus alloys and Inconel 718 and 1020°C for 1 hour for Waspaloy. 718 Plus alloys and Inconel 718 were also examined after another solution heat treatment at 1050°C for 1 hour. All the heat treatments were followed by water quenching. Thorough microstructural characterization before and after welding was carried out using optical microscopy, analytical scanning electron microscopy, electron microprobe analysis and analytical transmission electron microscopy. In addition,

Secondary Ion Mass Spectrometer (SIMS) was used to study the grain boundary segregation in the two 718 Plus alloys.

Interestingly, the microstructure of 718 Plus alloy, in the heat treated conditions it was studied, was very similar to that of Inconel 718 despite of the considerable difference in their chemistries. The main discernible difference was the formation of γ' as the main strengthening precipitate in 718 Plus alloys in the as received and 950°C solution heat treated condition. The other phases present in the pre-weld microstructure were Nb rich MC type carbides, Ti rich carbonitrides and grain boundary δ phase.

Solution heat treated plates of all the three alloys were welded with a sharp focus electron beam with the welding parameters of 44 kV voltage, 79 mA current and 152 cm/min speed. The microsegregation pattern of 718 Plus during solidification of the fusion zone indicated that while Fe, Co, W and Cr segregated to the core of the gamma dendrites, Nb, Ti and Al were extensively rejected into the interdendritic liquid. Electron diffraction and x-ray microanalysis using transmission electron microscopy (TEM) of the fusion zone showed that the major secondary phases that formed from the interdendritic liquid were gamma/MC type carbide eutectic and gamma/Laves eutectic constituents.

Heat affected Zone (HAZ) microfissuring due to liquation was observed in all the alloys with resolidified products on the liquated and resolidified grain boundaries. Grain boundary liquation and segregation of minor alloying elements was considered to be the primary reason for liquation of HAZ grain boundaries which caused cracking. Evidence

of constitutional liquation of Nb rich MC type carbides in 718 Plus was found in the region adjacent to the fusion zone and also on the cracked grain boundaries. The resolidified products along the microfissures consisted of γ + Laves and γ + MC type carbide eutectics. Complete and partial healing of microfissuring by backfilling was also observed.

Segregation of B was detected by SIMS on the grain boundaries of both the 718 Plus alloys, with higher concentration of B on HC 49 grain boundaries. Also, for the first time, P was detected by SIMS on the cracked grain boundaries on both the alloys, which confirmed that grain boundary segregation of B and P was directly related to microfissuring.

Weldability evaluated by using weld cracking measurement and hot ductility measurements, using Gleeble Thermo-mechanical simulator, suggested that weldability of the lower B and P alloy was comparable to that of Inconel 718. An increase in B and P in 718 Plus alloy however, deteriorated the weld cracking resistance and the on-cooling hot ductility values. Cracking in all the alloys increased with an increase in the solution heat treatment temperature. Cracking in Waspaloy was significantly more pronounced than that observed in the other alloys. The hot ductility and welding measurements were in agreement with each other and indicated that the cracking susceptibility of the alloys increased in the following order – Inconel 718 < lower B and P 718 Plus alloy < higher B and P 718 Plus alloy.

TABLE OF CONTENTS

List of Figures

List of Tables

CHAPTER 1 - INTRODUCTION

Superalloys are used to manufacture high temperature components of gas turbine engines, and the ever increasing demands of higher output has pushed the research in the direction of developing newer alloys with higher working temperatures and better high temperature properties. Superalloys have to be manufactured into intricate shapes which require them to have good fabricability (including formability, weldability, etc.) besides high temperature strength. Further, the severe operating conditions lead to frequent wear and tear, and owing to their cost, superalloy components are often repaired rather than replaced. Superalloys are frequently repaired by welding, and fusion welding is one of the most commonly used repair welding techniques. Therefore, it is desirable that superalloys have good weldability along with good high temperature properties.

A combination of these properties is often difficult to obtain in a single alloy. For example, Waspaloy has very good high temperature creep properties, but like many other γ' strengthened superalloys, is prone to microfissuring during welding and during post-weld heat treatments. Alternately, Inconel 718, which is strengthened by γ'' has good weldability compared to other Ni-base superalloys, but it cannot be used above a temperature of 650°C, as γ'' starts transforming to δ phase. Cao et al. [1] at Allvac Inc. developed an alloy based on Inconel 718, which is γ' strengthened and has a 55°C working temperature advantage over it. Initial experiments and numerical modeling results show that 718 Plus has superior high temperature properties [1], but limited information exists about physical metallurgy and weldability of this new alloy in open

literature. Hence, this Ph.D. project was started to study the microstructure of this new alloy and understand its weldability.

Fusion zone microstructure developed during the rapid solidification of a weld influences the integrity and properties of weldments. Post weld heat treatments (PWHTs) are generally applied to homogenize the as-welded microstructure, relieve the residual welding stresses, and also to re-strengthen the welds of precipitation hardening type of alloys. Development of suitable PWHT however depends primarily upon the initial microstructure of fusion and heat affected zones, and, a proper understanding of them is essential. Hence a thorough microstructural characterization of the as-welded structure is a very important component of the weldability studies.

Gamma prime strengthened, Ni-base superalloys are prone to liquation cracking during welding and strain age cracking during post weld heat treatment (PWHT) in the HAZ region. Heat affected zone liquation cracking results from formation of liquid film at grain boundaries during the weld thermal cycle and the inability of this film to accommodate the thermally induced stresses during weld cooling [2]. The grain boundary liquation in HAZ may occur by combination of various mechanism(s). Constitutional liquation of second phase particles like MC type carbides [3] and the segregation of melting point depressant minor alloying elements like B, P and S [4, 5] are the most commonly encountered mechanisms. These mechanisms are principally governed by the pre-weld microstructure and the microstructure developed in the HAZ during the weld – thermal cycle, and would essentially determine the extent of HAZ

cracking in the alloy. The weldability was also compared with other established superalloys like Waspaloy and Inconel 718, to better comprehend the scale of welding response.

The research undertaken has yielded fundamental information about the physical metallurgy of the alloy and its physical metallurgy of welding under the most commonly used welding conditions.

CHAPTER 2 - LITERATURE REVIEW

Introduction:

Considerable amount of research has been conducted on various physical metallurgical aspects of Inconel 718 and Waspaloy, while limited information is available about a comparatively new superalloy, Allvac® 718 PLUS™ (718 Plus). As 718 Plus was developed to meet the high temperature characteristics of Waspaloy and workability of Inconel 718, knowledge about these two superalloys was considered imperative for the proper understanding of 718 Plus alloy. The literature review mainly consists of physical metallurgy of Inconel 718 and Waspaloy and the information about their weldability. The development and physical metallurgy of Allvac 718 Plus has also been reviewed briefly.

The remaining part of the chapter considers issues related to welding and weldability in general. Fusion welding processes employed in welding of superalloys, especially Electron Beam Welding (EBW) are discussed. Frequently encountered weld cracking and other welding defects are also outlined. The theories pertaining to cracking in the welds and in the HAZ are reviewed next. Finally, weldability testing techniques like Gleeble test, Varestraint test and the actual weld cracking measurements are discussed.

2.1: Physical Metallurgy of Waspaloy

2.1.1: Microstructure of Waspaloy

Waspaloy is a Ni-base wrought superalloy used as turbine disks, turbine blades and fasteners since early 1950s. The nominal composition (in wt%) of Waspaloy is 58 Ni, 19.5 Cr, 13.5 Co, 4.3 Mo, 1.3 Al, 3 Ti, 0.08 C,0.006 B. The working temperature for Waspaloy is 700°C [6]. Waspaloy has been extensively used due to its high creep resistance at elevated temperature. The long term creep rupture strength of about 300 MPa at 100,000 hours at 700°C can be achieved for Waspaloy, whereas turbine rotor material requires only 100 MPa at 700°C temperature [7]. The standard solution heat-treatment generally involves a solution anneal heat-treatment at1080°C for 4 hours followed by water quenching and then holding at 850°C for 2 hrs followed by air cooling + 760°C for 16 hours followed by air cooling. This heat treatment has been reported to produce optimum creep and stress-rupture properties. Some investigators have also utilised lower, sub-solvus solution annealing temperatures [8, 9] followed by the two step ageing process. Major phases present in Waspaloy are γ' phase, MC type and $M_{23}C_6$ type carbides.

Gamma prime phase:

The principal strengthening phase for Waspaloy is FCC ordered A_3B type γ' phase. γ' phase found in Waspaloy is spherical in shape with a volume fraction of 20 %. The volume fraction of γ' is low as compared to other γ' strengthened Ni-base superalloys. The solution annealing and ageing heat treatment introduces a bimodal distribution of γ' particles – coarse primary γ' with an average size of 194 ± 39 nm and fine secondary γ'

with an average size of 44 ± 11 nm [10]. The primary γ′ particles nucleate during the cooling after solution annealing and grow during the first step of the precipitation annealing at 850°C whereas the secondary γ′ particles nucleate at 760°C and grow simultaneously with primary particles [7]. Fayman [11] found that primary γ′ particles were rich in Cr, Al and Ti whereas the secondary γ′ were rich in Fe and Mo. The compositions of primary and secondary γ′ particles in wt% were also reported by Fayman as ($Ni_{0.75}Cr_{0.02}Co_{0.03}Mo_{0.02}Ti_{0.10}Al_{0.07}Fe_{0.004}$) and ($Ni_{0.72}Cr_{0.04}Co_{0.03}Mo_{0.05}Ti_{0.10}Al_{0.06}Fe_{0.006}$) respectively. The solvus temperature of γ′ in Waspaloy is in the range of 1020°C [12] to 1058°C [10] and is influenced by its composition, especially Co content. Gamma prime particles can contain upto 10% Co. Cobalt in ordered γ′ lattice has been observed to substitute for Ni, and when present in higher concentrations, it can also displace Cr [13]. The solvus also depends on Ti/C ratio and (Ti+Al) atomic content [14]. The lattice parameter of γ′ has been reported to be 0.353 ± 0.003 nm and its lattice mismatch with the γ matrix of Waspaloy is less than 0.3% [15]. Waspaloy is amongst those alloys that can retain most of the γ′ forming elements in solution when rapidly cooled from the solution heat treatment temperature. γ′ forms intragranularly in γ but is occasionally also found on the grain boundaries [16].

Carbides:

Both MC type and $M_{23}C_6$ type of carbides precipitate in Waspaloy [17]. Ti rich and Mo rich MC type carbides form inter and intra-granularly. Cr rich $M_{23}C_6$ carbides are found to precipitate at the grain boundaries in as forged condition and in the aged condition.

Carbide compositions are approximately $(Ti_{0.57}Mo_{0.23}Ni_{0.15}Cr_{0.03}Al_{0.02})C$ and $(Cr_{0.80}Ni_{0.09}Mo_{0.08}Co_{0.03})_{23}C_6$ for MC and $M_{23}C_6$ respectively [11].

2.1.2: Welding of Waspaloy

Like other γ′ strengthened Ni-base superalloys with superior high temperature tensile strength, Waspaloy is susceptible to post-weld heat-treatment cracking. PWHT cracking generally occurs in HAZ of the weldment due to liquation of MC type carbide particles [6], segregation of minor alloying elements like boron [18], rapid precipitation of γ′ phase [19] and also due to segregation of Al and Ti from fusion zone grain boundaries [20]. Majority of the studies have been concentrated on PWHT cracking in the HAZ, although Waspaloy has been reported to exhibit fusion zone and HAZ liquation cracking during welding [6]. Fusion zone and HAZ liquation cracking was also observed in the present work, which will be reported in the results section.

PWHT cracking was found to initiate in the grain boundaries of the HAZ which were liquated due to constitutional liquation of TiC particles or due to segregation of minor alloying elements. Grain boundary films of MC type carbides have been reported to increase the sensitivity of Waspaloy to HAZ cracking [21] . It was found that critical stress required to initiate cracking was dependent on the heating rate during the PWHT. Decreasing the heating rate decreased the critical stress, with slower heating rates allowing more time for precipitation of γ′ and eventually increasing the hardness. Temperature range of reheat cracking was found to be similar to the precipitation range of γ′ particles in Waspaloy [19].

Pipeline segregation of Al and Ti during welding was also proposed as liquation mechanism. Epitaxial nature of solidification in case of FCC metals facilitated the grain boundaries to be continuous from the HAZ to the fusion zone. Aluminum and Ti can diffuse through these grain boundaries into the HAZ and reduce the melting point. As a consequence, the grain boundaries were susceptible to melting during welding [20].

Possible methods to alleviate PWHT cracking include rapid cooling during welding and rapid heating during the subsequent PWHT through precipitation temperature range of γ' phase [22]. Also, PWHT cracking can be controlled by over-ageing pre-weld heat treatment to soften the base metal and reduced restraint conditions during welding[20].

Another approach to eliminate the PWHT cracking problem is using grain boundary engineering (GBE) to increase the fraction of special grain boundaries and twin boundaries in the alloy [23, 24]. It is established that low $\sum$ coincidence site lattice (CSL) grain boundaries are better resistant to liquation during welding. Qian et al. [18] developed a heat treatment utilising Gleeble thermo mechanical simulator that simulates the PWHT. Long-term isothermal heat treatments at 40hr and 100hr at 1079°C were used to simulate the effect of multiple PWHT cycles at 1079°C/4hrs for 10 cycles and 25 cycles respectively [25]. It was found that after the PWHT of 1079°C/40 hrs the weldability of wrought Waspaloy degraded due to increased grain size resulting from exposure to elevated temperature. The weldability was restored in 1079°C/100hrs PWHT that had comparable grain size but a greater fraction of twin boundaries and special grain boundaries which were induced during annealing [24].

2.2: Physical Metallurgy of Inconel 718

2.2.1: Microstructure of Inconel 718

Inconel 718 is a Ni-Fe base high temperature superalloy and is one of the most widely used materials in the fabrication of jet engine turbine blades and vanes. The nominal composition of Inconel 718 is (wt%) 17-21 Ni, 1 Co, 2.8 – 3.3 Mo, 4.75 – 5.5 Nb, 0.65-1.15 Ti, 0.2-0.8 Al, 0.08 C, 0.35 Mn, 0.35 Si, 0.006 B, 0.30 Cu, balance Fe. The commonly present phases in alloy 718 are the Nb rich MC type carbides, TiN, δ phase, Laves, γ'' and γ' phases. The γ'' and γ' are the main strengthening phases and their precipitation behaviour is determined primarily by the amount of Nb, the temperature and time of exposure [26]. Some other phases reportedly observed in Inconel 718 are α-Cr, sigma and M_6C [26]. Occasionally $Cr_{23}C_6$ and M_3B_2 phase are also found in Inconel 718.

Principal strengthening phases in Inconel 718:

Paulonis et al. [27] showed that the strengthening phase in Inconel 718 is the metastable body centered tetragonal Ni_3Nb (DO_{22}) γ'' phase. This phase is disc-shaped and lies on the {100} planes of the matrix. The relationship between the crystalline structures of the γ'' precipitates and the γ phase is the following [28]:

$(001)\gamma'' \parallel \{001\}\gamma$ and $<100>\gamma'' \parallel <100>\gamma$

A small amount of a coherent γ' phase $Ni_3(Al,Ti)$ fcc $L1_2$ appearing as a fine dispersion of quasi-spherical particles has also been reported. The γ' and γ'' phases precipitate

between 600 – 900°C as uniformly distributed small particles and form a basis for the precipitation hardening of the alloy.

The schematic diagram of the unit cells of γ' and γ'' phases is shown in Figure 2.1. The open circles in the figure correspond to Ni atoms, whereas the close circles corresponds to Nb atoms. The figure also shows the relative difference in the lattice parameters of the two cells.

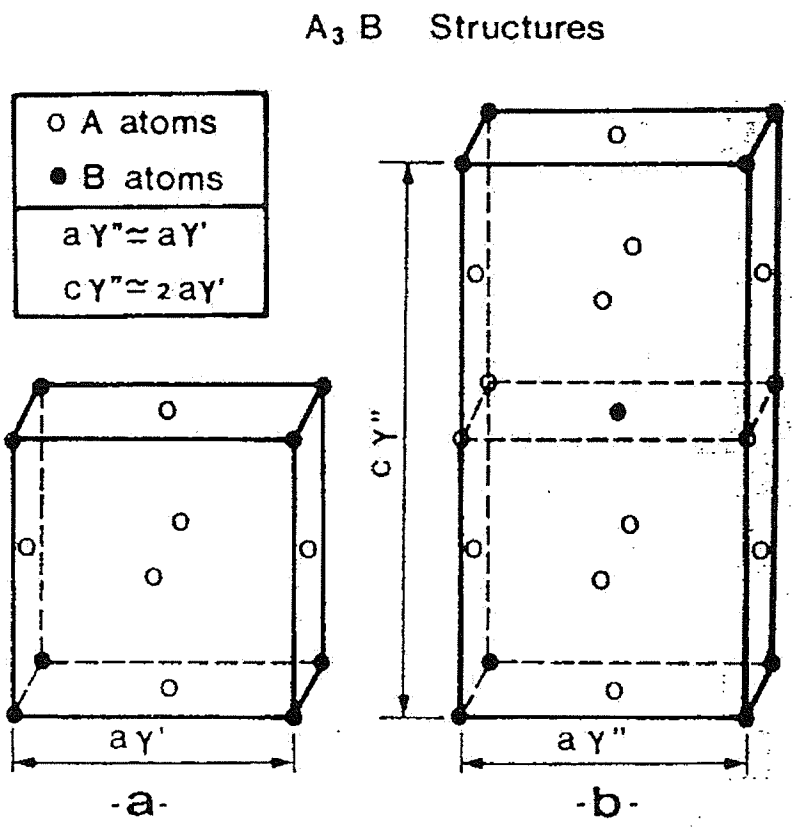

Figure 2.1: Unit cells of FCC and BCT structures of γ′ and γ″ phase respectively [28]

γ'' particles also precipitate at the grain boundaries, as was revealed by Gao and Wei [29], in solution treated and aged condition in Inconel 718. This was suggested to be the cause of segregation of niobium at grain boundaries as detected by XPS earlier by the same research group. Unlike the γ'' particles found in the matrix of Inconel 718, these grain boundary particles showed no crystallographic relationship with either of the neighbouring grains.

It is established that precipitation of γ'' and γ' phase depends on the amount of aluminum, titanium and niobium as well as on the ratio of (aluminum + titanium / niobium). Several studies have been done to adjust the amounts of these elements and to stabilize the γ'' phase beyond the highest working temperature of Inconel 718, which is 650°C. Xie et al. [30] by their detailed TEM and high resolution electron microscopy study concluded that a compact morphology of γ'' and γ' phase characterizes better high temperature stability than the separate precipitation of these phases. They also concluded that creep rupture life of Inconel 718 depends not only on Nb+Al+Ti content but also a coefficient k, which is defined as

$$k = \sqrt{\frac{(Al + Ti / Nb)^2}{(Al / Ti)^2}} \times Nb$$

Cozar and Pineau in the early 70s [28] studied a Fe-Ni-Cr-Ti-Al-Nb alloy with different Ti+Al/Nb ratios and concluded that a minimal Ti + Al / Nb ratio between 0.9 and 1 gave a compact morphology of γ' and γ'' precipitates. This compact morphology consisted of cube-shaped γ' particles coated on their six faces with a shell of γ'' particles. The microstructure proved to be very stable on prolonged aging.

γ'' phase transforms to delta and γ' with increasing time and temperatures. Eventually the γ' phase will dissolve and the delta phase becomes the terminal phase in the 718 system [26].

Delta (δ) phase:

δ phase (Ni_3Nb) is a stable intermetallic phase with an orthorhombic ($D0_a$) crystal structure. Figure 2.2 shows a schematic representation of the unit cell of delta phase.

The solvus temperature range of 1005 to 1015°C has been reported for δ phase in Inconel 718 with Nb contents of 5.06 to 5.41 wt% [31]. The rate of its precipitation is highest around 900°C. It normally precipitates by nucleation at grain boundaries followed by the growth of thin plates extending into the grains. Nucleation can also occur intragranularly in the presence of γ''.

Because of needle like morphology of δ phase, it does not contribute significantly to the hardening of the alloy but has beneficial effect on stress-rupture ductility when compared with γ' and γ'' particles [31].

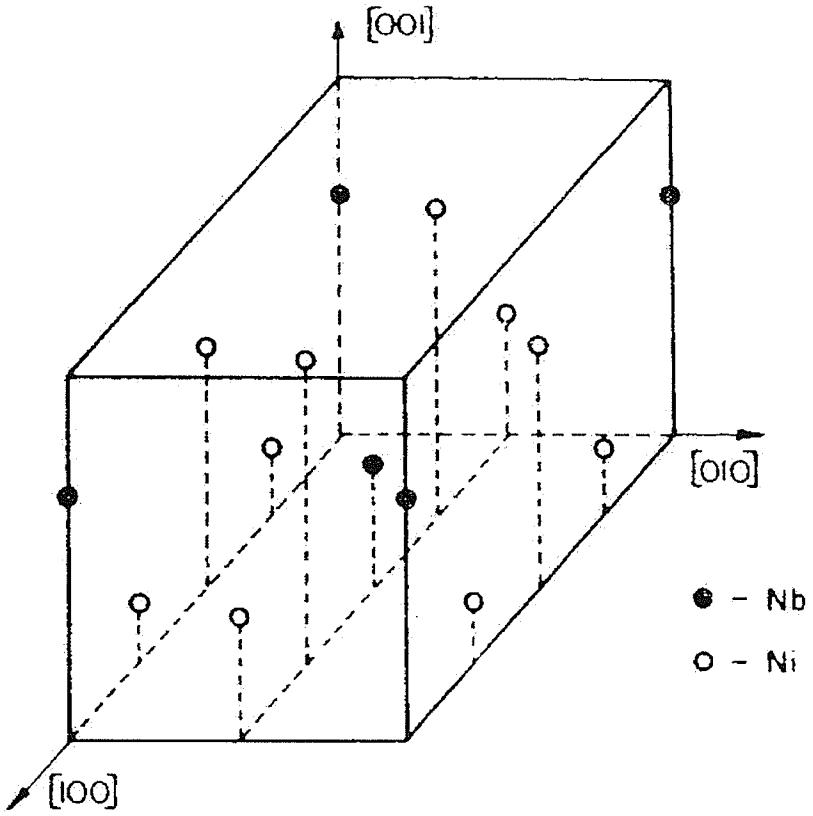

Figure 2.2: Schematic representation of unit cell of Ni_3Nb δ phase[32].

The orientation relationship for δ phase with the γ matrix is as follows:

(010) δ ||{111}γ and [100] δ || <1 $\bar{1}$0>γ

δ phase pins down the grain boundaries during the forging process and is used to control the grain size of the material. The δ phase's solvus depends on the amount of Nb present in the billet prior to working the material. The solvus temperature is decreased as the Nb content is decreased, and areas low in Nb would undergo recrystallization and grain growth early in the processing and/or during solution heat treatment [26].

Niobium Carbides:

Two types of Niobium carbides (namely, primary and secondary carbides) have been reported in the literature to form in Inconel 718. The primary NbC form during solidification and are large and stable. They contain substantial amount of Nb. They often appear in chains aligned in the rolling direction [33]. TEM investigations showed that there was no crystallographic orientation relationship between these particles and the matrix on either side of the grain boundary. The secondary niobium carbide was observed to form during aging and precipitate at the grain boundaries. These particles were found to be rich in Cr, Fe, Ni and Ti besides Nb and showed the following relationship with the surrounding γ matrix.

$(020)_{\gamma}//(220)_{particle}$ and $[001]_{\gamma}//[001]_{particle}$

This type of carbide may re-dissolve or be replaced by $Cr_{23}C_6$ ($M_{23}C_6$) at temperatures higher than 700°C. Primary NbC particles are usually found at the grain boundaries, although they do not preferentially precipitate at the grain boundaries. In contrast, secondary NbC particles generally form along the grain boundaries.

Grain boundary NbC particle along with other grain boundary precipitates containing Nb, assist in environmentally assisted crack growth under static loading at elevated temperatures. The mechanism for crack growth is controlled by the rate of oxidation and decomposition of these carbides [33].

Laves phase:

Laves phase is a brittle, intermetallic phase that forms in Inconel 718 and is usually considered deleterious to the mechanical and metallurgical properties of the alloy [34]. Laves phase has a C14 crystal structure with lattice parameters of $a_0 = 0.47$ nm and $c_0 = 0.75$ nm [35]. This phase is hexagonal closed packed and has a $MgZn_2$ type crystal lattice. The general formula for Laves phase is of the A_2B type, with Ni, Fe and Cr in the A type atoms and Nb, Mo and Si in the B type atoms [36].

Large amount of Nb is required to form Laves phase and hence, it forms in heavily segregated regions and is typically observed as large globular particles in cast Inconel 718. It is possible to eliminate Laves phase in wrought Inconel 718 by careful thermo-mechanical processing in wrought product, but it can form if the composition, primary ingot solidification and the processing route are not properly controlled. However, Laves

phase is commonly found in the weld zone and in the resolidified products during the solidification stage of the wrought welded Inconel 718.

Other minor phases in Inconel 718:

Long temperature exposures of Inconel 718 in and around the service temperature of 650°C has resulted in the formation of several minor phases like α- Cr, a high Cr-Mo Laves phase with Si and a Cr-Ni-Fe σ phase. All of these phases have a signature temperature range and have been found to nucleate either on the surface of an advancing δ phase or along a grain boundary. The temperature of 621°C was found to be favourable for the precipitation of Cr-rich α- Cr phase, while Laves phase was found to precipitate more favourably at a slightly higher temperature of 677°C. 732°C temperature was favourable for the formation of σ phase [37].

2.2.2: Welding of Inconel 718

Inconel 718 shows better weldability compared to other γ′ strengthened Ni-base superalloys due to the slow precipitation kinetics of γ″ strengthening phase [38]. Although, Inconel 718 is free from strain-age cracking during post-weld heat treatment, it suffers from microfissuring during manufacturing and repair welding. The cracking occurs predominantly in the heat affected zone (HAZ), although fusion zone cracking has also been observed in severely restrained welds [16]. Cracking is intergranular in nature and is due to liquation of the grain boundaries or the phases present on them [36].

Heat affected zone microfissuring:

Intergranular microfissuring is frequently encountered in weld heat affected zones in Inconel 718 and has been extensively studied. It has been now established that HAZ microfissuring is associated with

i. constitutional liquation of grain boundary precipitates like NbC in wrought Inconel 718 [39]; constitutional liquation of Laves and NbC in cast Inconel 718 [40, 41]
ii. δ phase assisted liquation [42]
iii. GB segregation of minor alloying elements like boron, sulphur, phosphorus and carbon [4, 43].

Constitutional Liquation of second phase particles:

Constitutional liquation occurs during the rapid heating cycle of the material during weld heating cycle to above its eutectic temperature, but below its solvus and solidus temperatures. The dissolution of any second phase particle is a diffusion controlled process. Under slow equilibrium heating, the particle would slowly dissociate and the solute rejected from the particle will diffuse in the matrix and ultimately homogenize. But due to rapid heating during welding, the particles start dissociating, but the diffusion cannot be completed and the local concentration around the particle enriches the solute content of the matrix. Eventually the matrix concentration reaches the eutectic composition causing the matrix to liquate below the solidus temperature of the alloy [44].

The slope of the concentration gradient produced due to partial dissolution of the second phase particle depends on

- The heating rate – the faster is the heating rate, the steeper would be the concentration gradient.
- The diffusivity of solute – the faster is the diffusivity of solute atoms, the shallower would be the concentration gradient.
- The relative ease with which the solute atoms are accommodated by each successive single phase region in the diffusion couple.

Constitutional liquation of NbC was reported in wrought alloy Inconel 718 by Duvall and Owczarski in their hot-ductility study of the alloy [39]. Laves phase was not observed in the wrought alloy in the pre-weld heat treatment condition. Subsequently after development of cast Inconel 718, constitutional liquation of Laves phase was recognized in it besides the constitutional liquation of carbides [45, 46]. Study of cast Inconel 718 also suggested that the eutectic reaction temperature for carbide + gamma eutectic is higher than that for Laves + gamma eutectic reaction [41]. Observation of HAZ microstructure, starting from the base metal and approaching fusion zone revealed that constitutional liquation of Laves phase particles occurred in the regions farther away from the fusion zone boundary, compared to carbide particles. It was also observed that constitutional liquation of Laves phase was the principal contributor to the liquation phenomenon.

Delta phase dissolution assisted liquation:

Unlike constitutional liquation of Laves phase and carbides, delta phase is mostly seen to dissolve in the matrix. The dissolution of δ phase during weld thermal cycle was reported

to be a factor in grain boundary liquation by promoting grain boundary segregation of niobium. Although the study was done on the material in post-weld heat treated condition with abundant amount of δ phase, the same phenomenon can occur during other pre-weld heat treatments of material that contain δ phase [42]. Grain boundary δ phase will dissolve above the solvus temperature (1000°C-1025°C) enriching the grain boundary with niobium. As niobium is a known melting point depressant, it will decrease the grain boundary material's melting point and assist in liquation.

Grain boundary segregation of minor alloying elements:

Grain boundary segregation influences the formation and stability of the intergranular liquid that may form during the welding cycle. Segregation of minor alloying elements or impurities can (i) reduce the melting point of the grain boundary material [21, 47] (ii) increase the wetting behavior of the liquid [48] (iii) form low melting compounds that dissociate during the welding thermal cycle [49]. The presence of elements like boron [46, 49, 50], sulphur [51, 52], carbon and phosphorus [43, 53] are known to adversely affect the weldability of superalloys.

Segregation at grain boundaries either occurs by equilibrium or non-equilibrium modes. Solute atoms in a solid solution have a tendency to segregate to the grain boundaries because their atomic mismatch with the matrix atoms can be more easily accommodated there as it reduces the free energy of the system. This is known as equilibrium segregation [54]. It decreases with an increase in the solutionizing temperature as the microstructure is homogenized [5]. Non-equilibrium segregation which occurs due to the

formation of vacancy- solute complexes during the cooling of the alloy from the heat treatment temperature depends on the cooling rate from that temperature. Increase in the heat treatment temperature increases the number of vacancies exponentially and during cooling from this temperature, the solute-vacancy complexes move towards the grain boundaries which act as sink for the vacancies [46].

Elemental segregation of B has been observed by SIMS analysis [46] and the deleterious effect of B on weldability has been widely reported [43, 45, 49]. Boron was also observed to affect the on-heating and on-cooling hot ductility values and eventually increased the nil ductility temperature range of the alloy where it has essentially no ductility. Sulphur was also observed to reduce the weldability of Inconel 718, but the affect was moderate as compared to the boron [51]. Phosphorus was also found to be detrimental to the weldability of Inconel 718 [48], the mechanism of which is not clearly understood.

While analyzing the effects of B, P and C individually and in combination, in Inconel 718-type alloys, Benhadad et al. [53] found that:

i. B and P when present by themselves adversely affect weldability of Inconel 718, but their effect was much more adverse when they were present together
ii. C mitigated the adverse effect very significantly.

Factors affecting HAZ microfissuring:

Some of the factors that significantly affect HAZ microfissuring are discussed next.

Characteristics of intergranular liquid: An intergranular liquid phase is a prerequisite for the type of microfissuring found in the weld HAZ of alloy 718. However, such liquid films are often unavoidable and generic in many complex alloy systems regardless of heat treatment, grain size or heat-to-heat chemistry variation. As has been pointed out by Thompson [55], the characteristics of this intergranular liquid would determine the amount of cracking in the alloy. There are three main characteristics – resistance to chemical homogenization, eutectic temperature and wetting angle. Wetting angle is further influenced by intergranular chemistry and chemistry of the bulk material adjacent to the liquid. Any bulk alloy constituent or thermal treatment which increases a liquid's wetting angle, reduces the eutectic temperature or slows the diffusive flux of solute from the liquid to the matrix will increase microfissuring. The metallurgical solutions to minimize microfissuring, in order of their magnitude of benefit, are: reduced grain size, pre-weld solution heat treatment, minimization of impurity concentrations, and reduced volume fraction of carbides and Laves phase.

Stability of the intergranular liquid: The stability of the intergranular liquid as a function of temperature is dependent on diffusion and eutectic temperature. Intergranular liquation during welding of wrought Inconel 718 occurs due to constitutional liquation of NbC particles and due to segregation induced liquation of the grain boundaries [56]. During the non-equilibrium reaction of constitutional liquation a transient diffusion

gradient is created between NbC and the local matrix. The liquated region can homogenize dissipating the composition gradient, if sufficient time is available. Homogenization will be determined by the diffusion gradient and cross-section area. A steep diffusion gradient and a large diffusion cross-section will increase the homogenization rate, and cause the liquid to solidify rapidly, thus reducing the microfissuring susceptibility. This concentration gradient is shallow in the interdendritic region of the cast alloys, which increases the stability of the interdendritic liquid, and hence its susceptibility to microfissuring compared to the wrought alloys. Smaller grain size material will have more grain boundary area and therefore more cross-sectional area for diffusion through the grain boundaries [57]. Thus a smaller grain size increases the diffusion cross-sectional area, and hence will homogenize the liquid faster, reducing the susceptibility to microfissuring.

Solidification of intergranular liquid: Solidification of intergranular liquid generally occurs via non-equilibrium mode. The solute rich liquid will solidify via a eutectic reaction. In Inconel 718, two solidification modes have been recognized - the Laves + gamma binary eutectic or Laves + gamma + MC type carbide eutectic [56, 58].

Effect of heat treatment: Weldability of Inconel 718 is affected by pre-weld heat treatment. Solution annealing is beneficial to weldability while age hardening increases the susceptibility to microfissuring. The pre-weld heat treatment involves precipitation of different phases and/or other metallurgical changes like grain growth, atomic diffusion and equilibrium atom segregation. Since microstructural changes like precipitation of

γ',γ'' and δ phases and grain size effect did not correlate with the observed changes in the weldability, it was proposed that intergranular segregation of impurities mainly influenced the alloy's susceptibility to microfissuring. The increased microfissuring in age-hardened condition was attributed to the grain boundary segregation of impurities in that temperature range [4].

Effect of grain size: Increasing grain size, independently of other variables, causes increasing microfissuring susceptibility. Microfissuring susceptibility is known to be linearly dependent on the grain size for wrought Inconel 718, with increasing grain size leading to more cracking. Earlier study by Thompson et al. [57], proved that grain size affected the liquid distribution and grain boundary sliding. A large grain size will have longer interface sliding length, larger stress concentrations and large strain at grain boundary triple points, all increasing the susceptibility to microfissuring. While investigating the effect of grain size on weldability in Microcast (MX ^{TM}) Alloy 718, Huang et al. found a reversed trend from that observed in wrought Inconel 718 [59]. It was found that the microcast material with average grain size of 82-93μm showed more HAZ cracking when compared to conventionally cast material with a grain size of 3 mm. It was proposed that more cracking in the smaller grain size resulted from a combination of effects of stress concentration, probability of microfissuring and the number of available cracking sites.

Guo et al. [47] studied the effect of grain size on weldability by maintaining the segregation constant in different grain size material. Grain sizes of 50μm, 100μm and

200μm were produced by high temperature annealing at 1200°C for different interval of times. The time for equilibrium segregation of boron for different grain size materials at 1050°C was theoretically calculated for the grain sizes and the alloys were heat treated accordingly. Gleeble on-cooling hot ductility tests were performed on these alloys to evaluate their weldability and it was found that coarser grain size material recovered its ductility at lower temperatures compared to the finer grain size material. This suggested that increasing the grain size, increased the susceptibility to microfissuring[47].

Effect of thickness of the intergranular liquid: Thickness of the intergranular liquid which forms during weld thermal cycle is a very important parameter influencing microfissuring. It is generally accepted that thicker intergranular liquid increases the susceptibility to microfissuring. The tensile force, σ, required to overcome the grain boundary cohesion due to surface tension of the liquid, γ_L, was shown to be dependent on the thickness of the intergranular liquid film, h and is given by $\sigma = 2\gamma_L/h$ [60]. Hence as the thickness of the film increases the tensile force required for decohesion will decrease. Also, thicker intergranular films are difficult to be removed by Liquid Film Migration (LFM) which is one of the fundamental mechanism by which a metastable grain boundary liquid can be removed. LFM is beneficial to HAZ liquation cracking as it facilitates the rapid elimination of liquid [61]. Removal of the liquid film by LFM depends on the thickness of the film and the total time, *t,* required for a liquid film of initial thickness h_0 to completely solidify by LFM is given by [62],

$$t = \frac{h_0}{2kv_0},$$

where k is the equilibrium solute distribution coefficient and v_0 is the initial migration velocity of the liquid film. v_0 is expressed by

$$v_0 = \frac{D_L(\Delta C)_0}{(C_{L,T} - C_{S,T})h_0},$$

Where D_L is the diffusivity of solute in the liquid, $(\Delta C)_0$ is the initial concentration difference across the liquid film, $C_{L,T}$ and $C_{S,T}$ are the equilibrium interfacial concentrations of solute in the liquid and solid phases. These equations show that the initial velocity of the liquid film decreases as the thickness of the intergranular liquid increases, eventually increasing the time for solidification by LFM.

Grain boundary character distribution: Watanabe [63] introduced the concept of "Grain Boundary Design and Control" with the primary purpose being to improve the bulk properties of polycrystalline materials through enhancement of the number of structurally (and chemically) 'special' grain boundaries in the grain boundary character distribution (GBCD) [64]. Research teams in several laboratories have demonstrated that it is possible to manipulate the distribution of character of grain boundaries, triple points and network arrangements within the microstructure of a material, thus, engineer their properties [65]. Different grain boundaries in metals can have different crystallographic structure. These structural differences could lead to different grain boundary energies with differing properties. A three dimensional lattice is created in the region of inter penetration of lattices of the two adjoining grains (i.e., crystals) with lattice points common to both. This lattice is called Coincident Site Lattice or CSL and is considered to be the smallest common sub-lattice of the adjacent grains [65]. These special grain boundaries are usually described in the CSL (coincidence site lattice) framework as being close to low Σ

interfaces. A special grain boundary (GB) is described crystallographically by the CSL model of interface structure as the one lying within $\Delta\theta$ of Σ, where $\Sigma \leq 29$, and $\Sigma \leq 15\Sigma^{-1/2}$.

Interdependence of grain boundary character and intergranular segregation of boron was revealed in Inconel 718. It was found that grain boundary liquation was heterogeneously distributed [23]. High – angle boundaries were observed to have the highest probability of being segregated with boron, and the highest tendency to liquate. Moreover, CSL boundaries were with relatively reduced segregation of B and rarely liquated and low angle boundaries did not liquate [65].

Similar results were obtained on simulated post weld heat treatment studies done on Inconel 718 [66]. Excessive precipitation of δ phase during the PWHT increased the susceptibility of the alloy to microfissuring. A "rejuvenation" heat treatment that involved heating the alloy above the δ phase solvus, improved the resistance towards HAZ liquation by increasing the fraction of special grain boundaries [42, 67].

2.3 Physical metallurgy of ALLVAC® 718PLUS™ (718 Plus)

2.3.1: Development of 718 Plus alloy

ALLVAC® 718PLUS™ (718 Plus) is a newly developed nickel base superalloy strengthened by ordered face centered cubic (FCC) intermetallic γ' phase. It was developed to increase the operating temperature range of its baseline superalloy, Inconel 718, from 650°C to 700°C , while maintaining its workability at the same level as that of of Inconel 718 [1]. The chemical composition of 718 Plus alloy was modified considerably from that of Inconel 718 to meet these requirements. Table 2.1 shows the composition of 718 Plus superalloy, while Table 2.2 illustrates the main compositional changes in 718 plus with respect to the Waspaloy and Inconel 718. As compared to the standard Inconel 718 alloy however, the iron content has been decreased, the cobalt and aluminium content has been increased. The other major difference is in the Al + Ti content, which has a value that is intermediate of Waspaloy and Inconel 718. The change in aluminium to titanium ratio is interesting to note. Both Waspaloy and Inconel 718 have the ratio of 0.47 (wt%) while in 718 Plus it is completely reversed and has a value of 2. Table 2.3 shows the high temperature properties for the three alloys. High temperature strength, stress rupture and creep properties for 718 Plus are superior to those of Inconel 718 and Waspaloy. The effects of changes in the composition on metallurgy of 718 Plus are still being evaluated and some of the results are discussed next.

Table 2.1: Chemistry of Inconel 718, 718 Plus and Waspaloy

wt %	Conventional Inconel 718	718 Plus HC 20 (normal B, P)	Waspaloy
Ni	54.44	52.18	58.55
Cr	17.94	17.92	18.36
Fe	17.62	9.33	0.61
Co	0.13	9.00	14.02
Nb	5.36	5.51	0.02
Ti	0.94	0.74	3.12
Al	0.46	1.50	1.49
B	0.004	0.003	0.005
P	0.007	0.006	<0.003
C	0.026	0.022	0.032
Mo	2.93	2.68	3.73
W	<0.01	1.04	0.02
S	<0.0003	<0.0003	<0.0003
Si	0.05	0.02	0.02
Mn	0.05	0.03	0.02
Mg	0.0014	0.0008	not detected

Table 2.2: Major differences in composition of the three alloys

Alloys	Chemistry (wt%)						
	Fe	Co	Al	Ti	Al + Ti	Al / Ti	P
Alloy 718	17.62	0.13	0.46	0.94	1.4	0.48	0.007
Waspaloy	0.61	14.02	1.49	3.12	4.61	0.47	<0.003
Allvac 718 plus HC 20	9.66	9.13	1.46	0.71	2.17	2.05	0.013

Table 2.3: High temperature properties of Inconel 718, Waspaloy and 718 Plus alloys

Alloy	ASTM Grain size	Tensile strength at 704°C				Stress rupture 704°C/552 MPa		Creep 704°C/ 483 MPa	
		UTS MPa	YS MPa	EL %	RA %	Life, hrs	EL, %	$t_{0.2}$ hrs	$t_{0.5}$ hrs
718	6	1051	936	20.3	27.5	157.9	19.5	29.0	63.5
718 P	7	1174	1005	24.1	30.7	433.1	35.4	226.4	456.1
Wasp.	6	1087	885	38.6	55.4	430.5	27.8	124.0	

2.3.2: Microstructure of 718 Plus alloy

The basic physical metallurgy of 718 Plus is similar to that of Inconel 718 in terms of the type of phases present in both the alloys, but significant difference has been reported in terms of volume fraction and precipitation kinetics. One of the major differences brought by the modification of chemistry is the change in the main strengthening phase of γ'' in base line Inconel 718 to that of γ' in 718 Plus. Systematic modelling (JMatPro 2.0) approach employed during the development of 718 Plus, showed that the volume of γ' increased while γ'' and δ decreased as the Al+Ti content and Al/ Ti ratio increased. At an Al+Ti concentration of 4 at% and a Al/Ti ratio of 4 in 718 Plus, the predominant strengthening phase was γ' [68]. Alloy 718 Plus has a much larger volume fraction of γ', about 21%, in the as heat treated condition [69] than alloy 718 and a smaller amount of δ. Solvus temperatures of γ' and γ'' are reported to be also higher when compared to alloy 718 [68, 70]. In another study [70] , it was found that if the alloy was held for prolonged time at higher temperatures, near the solvus, i.e., around 954°C, coarser γ' formed. At certain lower temperatures like 706°C, finer γ' formed and at temperatures about 872°C, intermediate size of γ' formed.

Smaller amount of γ'' is expected to form in 718 plus compared to Inconel 718, although no γ'' has been observed in the standard heat treated samples [70]. Even after long exposure at 760°C for 350 hrs, no γ'' was detected in the scanning electron microscopy for 718 Plus alloy [69].

A new HCP phase, $Ni_3Al_{0.5}Nb_{0.5}$ has been reported in 718 Plus alloy [71]. The morphology of this new phase is similar to that of δ phase and it shows all the peaks of δ phase and eta phase in the x-ray diffraction pattern. It was also found that this new phase deforms in conjuction with the matrix, thus not affecting the stress-rupture properties.

Precipitation kinetics in 718 Plus alloy:

The γ′ precipitation in 718 plus alloy is much slower than in other γ′ strengthened alloys or even in alloy 718, due to the presence of Nb in it, which has a slower diffusion rate [68]. Also the growth rate of γ′ phase in alloy 718 plus showed the lowest rate when compared to Waspaloy and Inconel 718, implying that this alloy may have the highest stability in terms of particle growth [72]. Hardness tests conducted on 718 Plus as an indication of precipitation of γ′ and γ″ indicated that the precipitation hardening process in 718 Plus was a little bit faster than that in conventional Inconel 718. In 718 Plus, the nose of the TTT curve for γ′/γ″ precipitation occurs at about 900°C in less than 0.1 hr and that of δ phase precipitation occurs at about 900-950°C in less than 0.1hr [71].

2.4: Welding and welding defects

2.4.1. Fusion welding processes and Electron beam welding

Many gas turbine components rely on welding for their fabrication and repair, and fusion welding is the most commonly used welding technique. Fusion welding is a joining process that involves melting of the components to be joined, with or without a filler alloy which fuse together on solidification. Alloys can be welded by the following fusion welding techniques: Gas tungsten arc welding (GTAW), Gas metal arc welding (GMAW), Shielded metal arc welding (SMAW), Submerged arc welding (SAW), Plasma arc welding (PAW), Electron beam welding (EBW), Laser beam welding (LBW), Resistance spot welding (RSW) and Resistance seam welding (RSEW) [73]. Superalloys can be welded by all versions of arc welding processes. In general, in an arc welding process, an arc is struck between the electrode and the workpiece which generates heat to melt the base metal, filler metal and consumable electrode if used. A molten weld pool is created and is protected either by a slag blanket or inert gas cover. The pool solidifies as the heat source retreats from the area and a solidified weld nugget is formed. A heat affected zone (HAZ) is created around the fusion zone which is metallurgically different than the base metal or the fusion zone metal.

Gas tungsten arc welding (GTAW) is most widely used technique, especially for joining thin sections. GTAW process is schematically represented in Figure 2.3a and 2.3b. It utilises a non-consumable tungsten electrode. A shielding gas cylinder is connected to the torch holding the electrode. The shielding gas such as argon or helium goes through the torch body and is directed by the nozzle toward the weld pool to protect it from air.

GTAW offers superior protection against oxidation and nitridation compared to other arc processes and is also called tungsten-inert gas welding (TIG) [74].

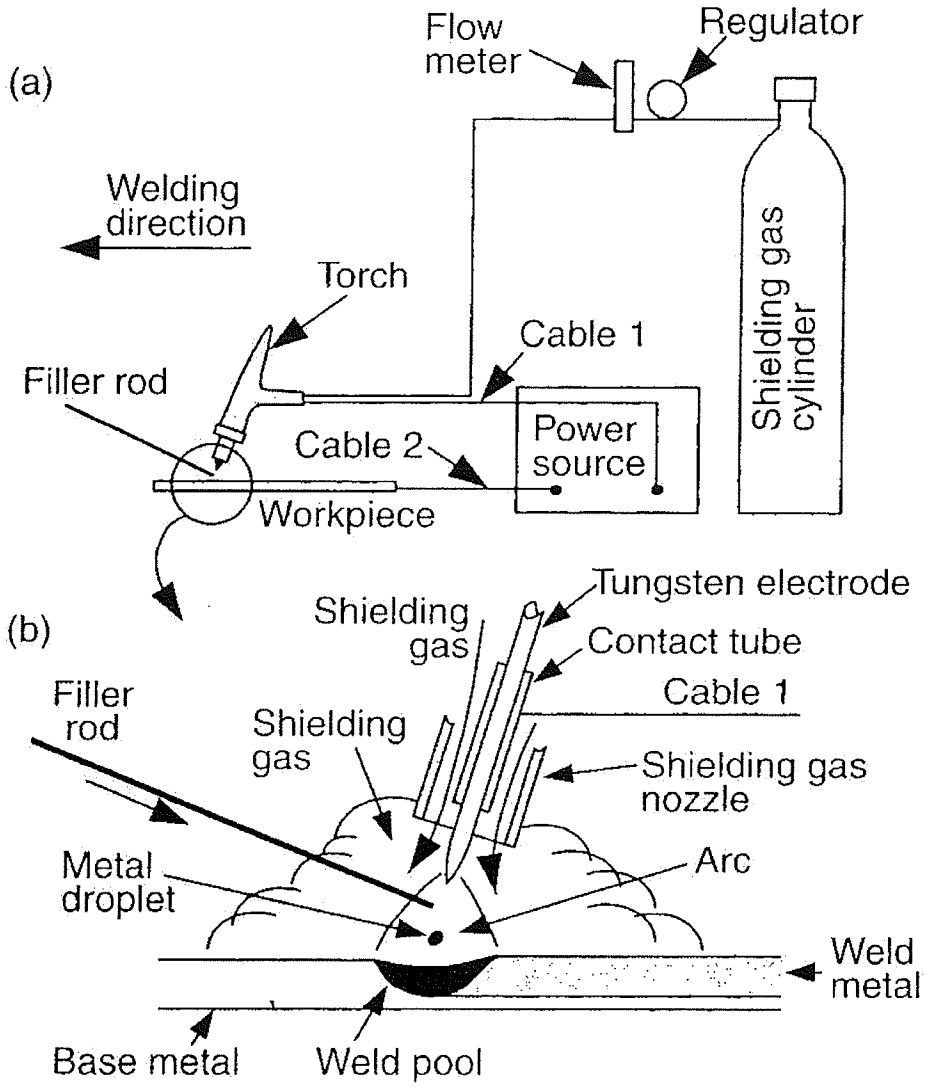

Figure 2.3: Gas Tungsten arc welding (a) overall process (b) welding area enlarged [74]

Electron Beam Welding

Electron beam welding (EBW) is a high-energy density fusion process that is accomplished by bombarding the joint to be welded with a strongly focussed beam of electrons at 25 to 200 kV voltages which travels at very high speeds. The kinetic energy of the electrons is converted to thermal energy instantaneously on impact which causes melting and vaporization of the surfaces to be welded. Power densities of 10^8 W/cm^2 can be obtained with typically high vacuum EBW beams with the spot sizes in the range of 0.25 to 1.3mm in diameter.

Principle of operation:

Figure 2.4 shows schematically the main components of EBW equipment. The electron beam is produced by an electron gun assembly consisting of a cathode, a heated source of electrons that is maintained at some high negative potential and a grid cup which is negatively biased with respect to the hot cathode filament. An anode at ground potential is placed below the gun assembly, through which the electrons flow in the form of collimated beam. The cathode is heated to the required emitting temperature and the negative bias on the grid is used to alter flow of the electrons. High voltages are applied across the cathode and anode to accelerate the electrons. The electron beam thus generated passes through a series of magnetic lens to focus, control and bend the beam as necessary. The focusing of the beam increase the energy density creating a high intensity beam spot on the work piece. Earlier, EBW was only performed with the work piece also being in vacuum, but now three different types of EBW modes have developed: High-vacuum (EBW-HV), where the work piece is kept in vacuum of 10^{-6} to 10^{-3} torr, Medium

–vacuum (EBW-MV), where the work piece is at 10^{-3} to 25 torr and a Nonvacuum (EBW-NV) where the work piece is in air or protective gas. In all the EBW applications, the electron-beam gun region is maintained at a pressure of 10^{-4} torr or lower.

The high level of beam spot intensity generates temperatures of approximately 14,000°C, sufficiently high to vapourize any material, forming a vapour hole that penetrates deep into the workpiece. This vapour hole advances along the weld joint during welding, where the material at the leading edge of the hole melts, flows around the sides of the hole to the trailing edge and solidifies.

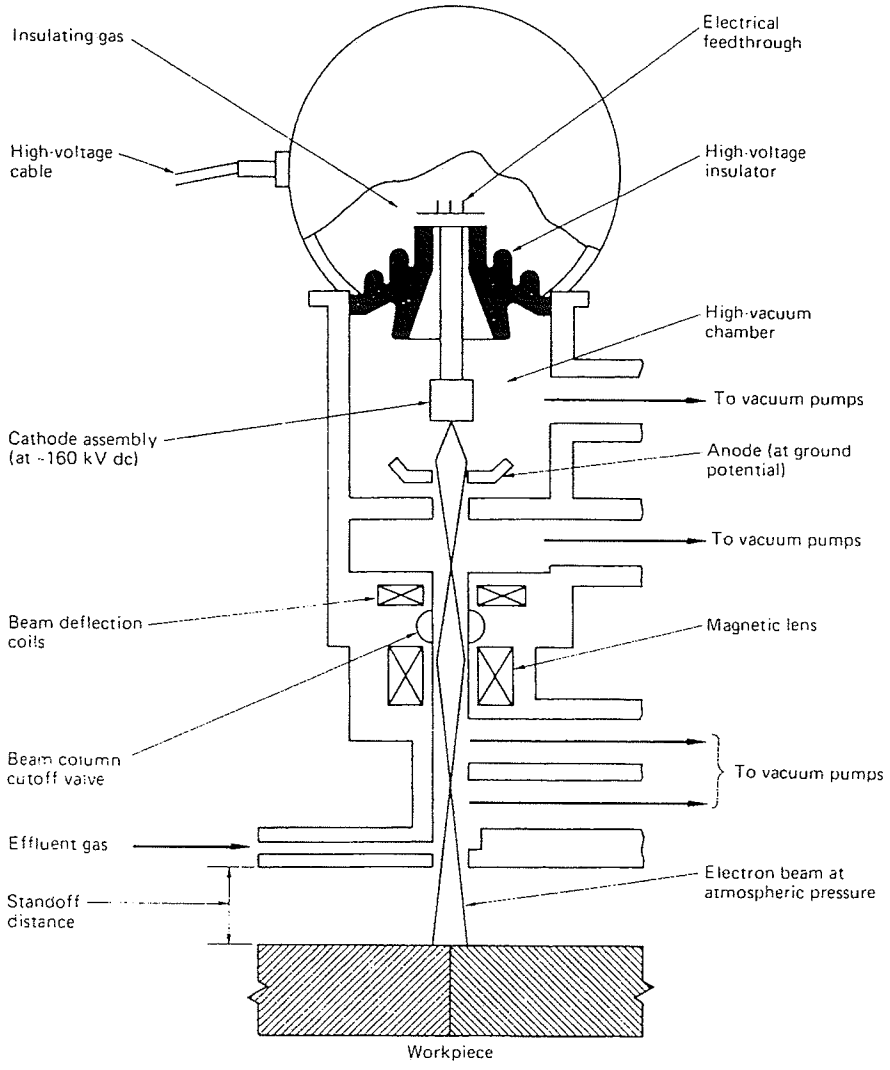

Figure 2.4: Schematic showing the primary components of an electron beam welding head

Advantages and Disadvantages of EBW:

The ability to make deeper and narrower welds with very low total heat input sets EBW apart from arc welding processes. High depth-to-width ratio and narrower heat affected zone (HAZ) are obtained in EBW. Also, EBW carried out in vacuum results in oxide and nitride free welds. Higher welding speeds can be employed due to high melting rates associated with concentrated heat sources which would eventually reduce the time required to accomplish welding. Besides these, some other advantages of EBW include: minimum distortion and shrinkage during welding; welding of most hardened or work-strengthened metals; welding in close proximity to heat sensitive components or attachments; hermetic seal welding of evacuated chambers and the ability to weld refractory metals that are not joinable by arc welding processes.

Initial equipment cost and installation is one of the biggest limitations of EBW. The cost of joint preparation and tooling is more than that encountered in arc welding processes, because relatively small electron beam spot size requires precise joint gap and position. The size of the sample is often limited to the size of the vacuum chamber employed. If welding is not carried out in vacuum, the maximum stand-off distance between the gun assembly and the workpiece is limited to 35 mm. The production rates are also affected due to evacuation needed at every production load [75].

Some of the important welding parameters that affect the penetration and beam geometry are as follows:

1. Accelerating Potential – As the accelerating potential is increased, the penetration of the weld bead will also increase. For long stand-off distances, or when narrow parallel-sided welds are desired, the acceleration potential should be increased so as to attain maximum beam density
2. Beam current – As the beam current is increased, penetration of the weld bead is also increased.
3. Welding Speed – As the welding speed is increased, the weld beam will become narrower and the penetration will also start to decrease. Welding speed is considered the most influential parameter affecting microfissuring [76].
4. Focus- Sharp focus will produce narrow parallel-sided weld bead geometry, since the effective beam density is at its maximum. Defocusing the beam either by over-focusing or by under-focusing will increase the effective beam diameter thereby causing the beam density to be reduced, which, in turn, will produce a shallow or a more V-shaped weld bead.
5. Beam oscillation: The beam energy can be manipulated by using auxiliary accessories for creating AC signals. These AC signals can deflect the beam to form discrete oscillation patterns like sinusoidal, square, triangular, ramp, circle and elliptical.

Study of electron beam welding parameters on microfissuring of Incoloy 903 showed that the most important EB welding parameters were travel speed and beam current at a fixed focus [77]. It was found that reducing welding speed and increasing current for a given heat input reduced cracking in the alloy. In another study, it was found that beam

oscillation perpendicular to the weld direction also affects microfissuring behaviour, but the effect was comparatively less than that produced by beam focus, beam current and travel speed [76].

2.4.2 Residual stresses in welds

Complete melting and resolidification of weld induces stresses in and around the weld. Tensile stresses that develop during welding induce cracking and residual stresses that remain after welding can prove harmful if not eliminated by suitable post weld heat treatment. Mostly the stresses are induced due to differential thermal expansion and contraction in the HAZ and weld [78]. The variations in stresses-strains are illustrated in an example of a butt-weld shown in Figure 2.5.

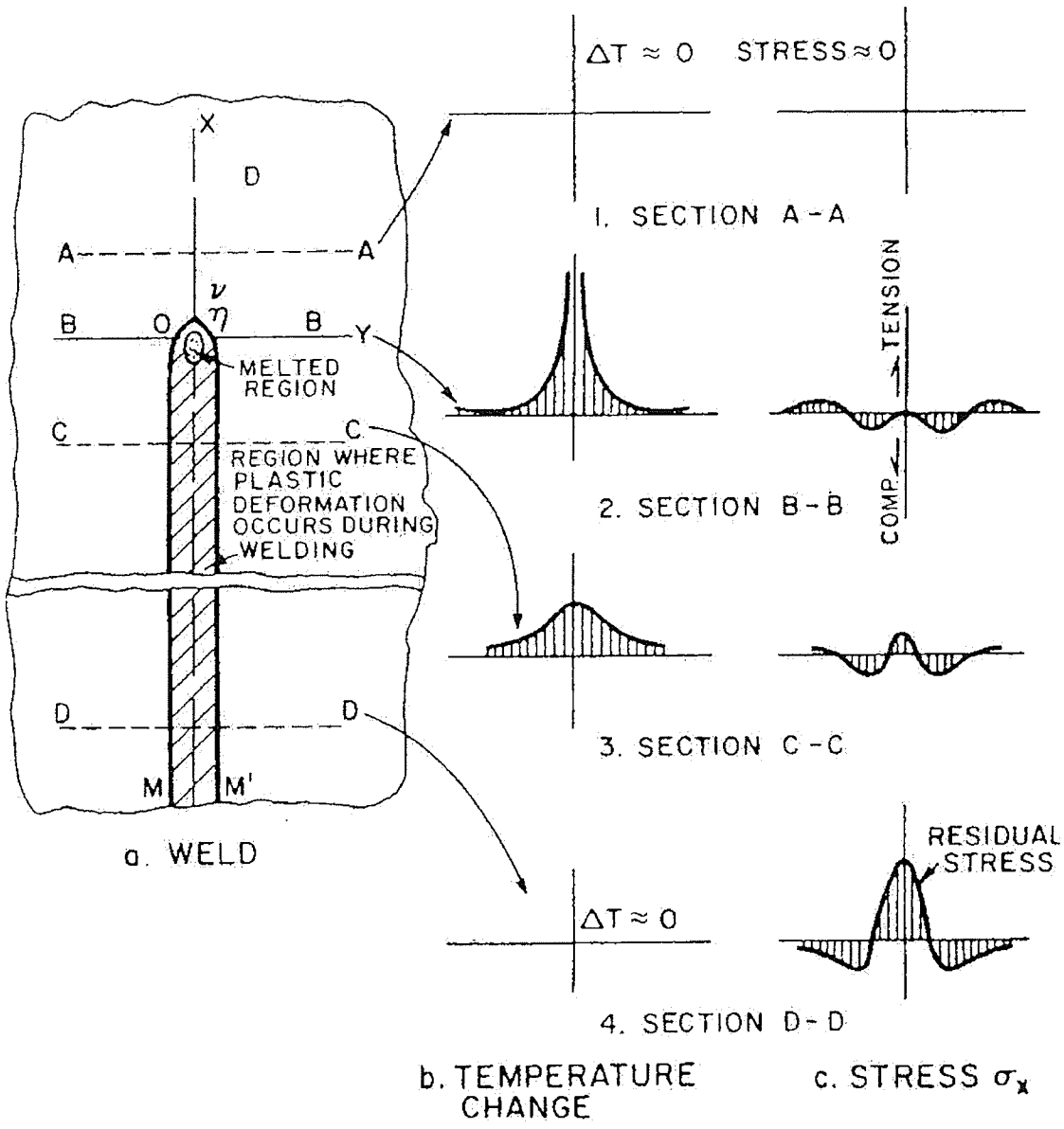

Figure 2.5: Schematic representation of changes of temperature and stresses during welding [78]

Various mechanical properties like elastic modulus E, yield strength, Poisson's ratio, etc., change as a function of temperature and have to be considered to evaluate the magnitude of stresses and strains in HAZ. Figure 2.6 shows a schematic illustration of development of stresses and strains as a function of temperature as experienced by a section of HAZ during a weld thermal cycle. As the temperature increases the initial expansion of the section is restrained by material further away from the heat source, which generates compressive stresses in the section. At some critical temperature (point 2), the flow stress of the section is exceeded, and further heating results in a decline in stress as the metal starts to flow. As the peak temperature is reached, the stress is practically zero, but considerable strain may occur. At this point, the net strain is given by the vector 1→4. On cooling, as the temperature of the section decreases, resistance by adjacent hotter material initially reverses the plastic strain pattern until a temperature is reached at which the section's flow resistance increases, which subjects the section to tensile stresses (point 5). Further decrease in temperature causes elastic stresses to form until it cools down completely (point 6). This remains as residual stress in the weld. These stresses could equal the yield stress of the metal, depending on the rigidity of the structure [78].

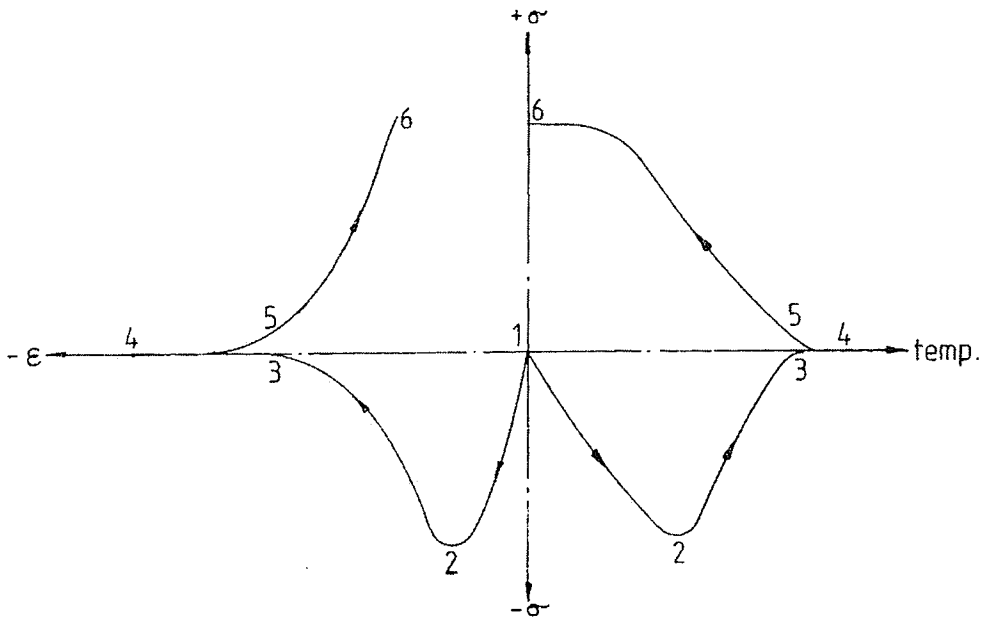

Figure 2.6: Schematic illustration of the variations in stress-strain during a weld thermal cycle [78].

2.4.3. Welding defects and weld cracking

The presence of surface or internal defects can degrade the performance of a weld. Some of the typical defects found in welds are porosity, lack of fusion, undercut, overlap, lack of penetration, shrinkage voids, crater cracking, melt –through or burn through and weld cracking [75].

Porosity is gas pores found in the weld bead. These pores vary in size and are randomly distributed. The most common causes for porosity are atmospheric contamination, excessive oxidised work piece surfaces, inadequate deoxidising alloys in the filler wire and the presence of foreign matter. Other causes of porosities may be extremely fast solidification rates, which entraps any gas which would normally escape. Severe weld turbulence caused by erratic arc characteristics also causes porosities by breaking the shielding gas cover and contaminating the solidifying molten weld pool.

Lack of fusion, also called cold lapping or cold shuts, occurs when there is no fusion between the weld metal and the surfaces of the base plate. Poor welding technique is the principal cause of lack of fusion. Arc placement at the leading edge of the weld puddle prevents formation of too large weld puddle, which can cause lack of fusion. Very wide joints also suffer from this problem. A very low weld speed or use of very low voltages for welding must also be avoided. Any oxide layers present on the surface should be removed to improve wetting, before welding.

Weld cracking is one of the most commonly encountered problems during welding of strong high temperature materials. Cracks in welds can be broadly classified into two main categories – those attributed to the welding process itself and those that occur during service. The cracking that occurs during service is mainly concerned with external factors like environment, vibration or thermal cycling [78].

The common types of cracking phenomenon associated with the welding process are of interest here and include:

1. Solidification cracking (occurs in weld deposit)
2. Liquation cracking (occurs in the HAZ)
3. Lamellar tearing (occurs in the HAZ)
4. Cold cracking (occurs in the HAZ)
5. Post weld heat treatment cracking (occurs both in HAZ and fusion zone)

Solidification cracking:

Solidification cracking is generally encountered in the fusion zone and results due to segregation that occurs during weld solidification. Segregation occurs because of partitioning of elements during the initial stages of solidification and is an inevitable process. The amount of segregation depends on the partition coefficient k, which is defined as the ratio of the concentration of the solute in solid to that in the liquid in equilibrium with it.

$$k = \frac{X_s}{X_L}$$

where, X_S and X_L are mole fractions of solute in the solid and liquid phases at a given temperature. The greatest partitioning occurs with the smallest values of 'k'. Many alloying/trace elements like S, O, B, P, C, Ti, N and H in the complex austenitic matrix of high temperature alloys have k values considerably less than unity and have a tendency to segregate into the solidifying liquid. Also most of these elements are melting point depressants and form low melting phases and eutectics with the metal to produce wetting films at grain boundaries. These films are unable to withstand the tensile stresses during cooling cycle of the weld and weaken the microstructure ultimately leading to cracking. Figure 2.7 schematically illustrates the mechanism of solidification cracking [78]. Mechanism of solidification cracking is further discussed in section on mechanisms of cracking.

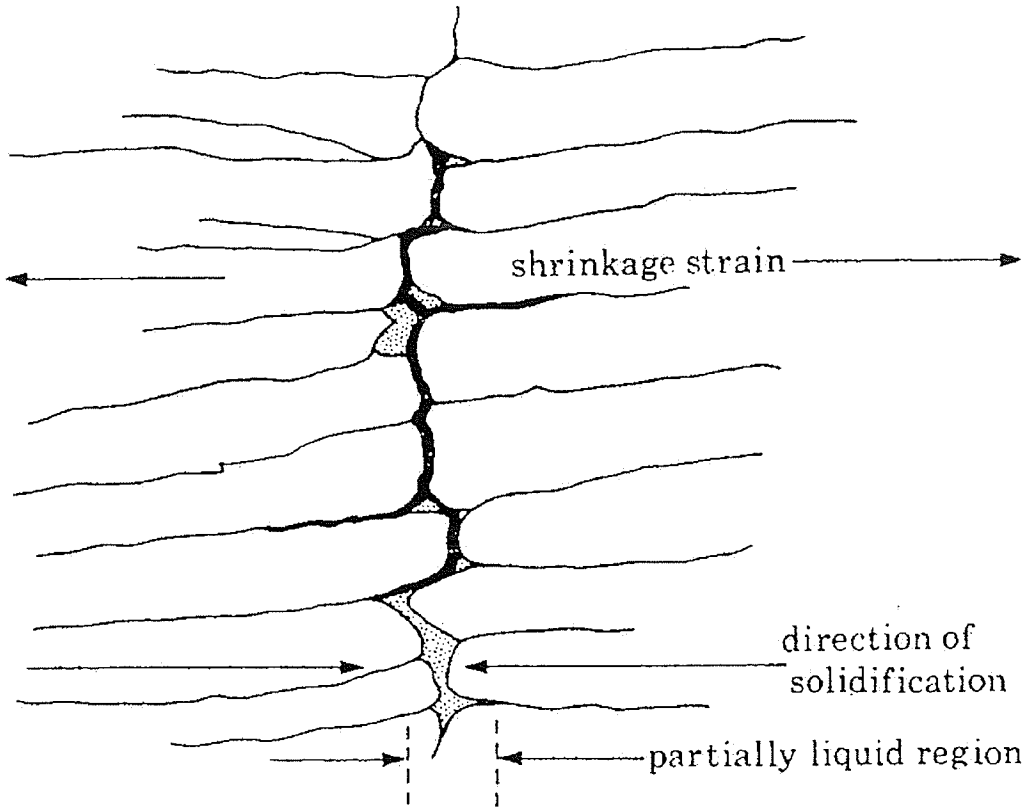

Figure 2.7: Schematic representation of the mechanism of solidification cracking [78]

Liquation cracking:

Liquation cracking is generally found in the HAZ and is due to formation and persistence of intergranular liquid. Intergranular liquid can form due to segregation of melting point depressing impurities on the grain boundary and/or due to the constitutional liquation of second phase particles present on the grain boundaries. Second phase particles present intragranularly can also contribute to liquation if sufficient grain boundary movement occurs during the weld heating cycle. The moving grain boundary thus intersects the liquating particles and the liquid wets and pins the grain boundary. Another important requirement of liquation cracking is the presence of liquid long enough for the tensile stresses to develop during the cooling cycle [79]. Complete elimination of liquation is not possible as some intergranular liquid will always be present in the HAZ adjacent to the fusion zone, where the temperature is between the solidus and liquidus temperatures of the alloy. Liquation cracking is dependent on the amount and type of impurities in the base metal, the volume fraction and density of low melting precipitates, and the degree of restraint [78]. Mechanisms of liquation cracking are also discussed in the section on cracking theories.

Lamellar tearing:

Lamellar tearing is encountered in HAZ, often close to the edge of fusion zone. Lamellar tearing can occur as a result of a very low through-thickness or short transverse ductility owing to the presence of segregation of elongated inclusions. This problem is generally encountered with those steels that have (MnFe)S inclusions that form during steel processing stage and are present as stringers after hot rolling. Under the action of weld residual stresses, particularly in high restraint geometries, the inclusion-matrix interface ruptures in a number of places; the last stage of fracture causes vertical tearing between the planes. The main factors likely to cause lamellar tearing are:

1. low, short transverse ductility of the present plate material
2. a high surface area of planar shaped defects, in the form of flattened out inclusions or stringers
3. a weld joint configuration which gives rise to high residual tensile stresses in the short transverse direction
4. the use of thick plates [78]

Cold cracking:

Cold cracking is also called hydrogen induced cracking. Hydrogen can be introduced into the weld during the welding process, from the atmosphere, from hydro-carbons on the plate being welded, or from the damp electrode flux. There is an incubation period, prior to initiation of cracking and crack propagation is slow with further incubation times between the steps in the crack growth. The cold cracking can be inter or intra granular. Initiation of cold cracking is particularly associated with notches, such as the toe of the

weld, or microstructural inhomogeneities which exhibit sudden changes in hardness, such as slag inclusion, martensite-ferrite interfaces or even grain boundaries [78].

Post-weld heat treatment (PWHT) cracking:

This type of cracking happens during the post-weld heat treatment which is generally employed to restore the properties of the weld. Post weld heat treatment cracking (PWHT) cracking is also encountered during repair welding where the weld is given a complete heat treatment involving solution heat treatment followed by aging. It is also known as strain-age cracking or delayed cracking. This type of cracking is generally found in HAZ but can extend into the fusion zone and into the parent base metal. Superalloys hardened by γ' phase are particularly susceptible to PWHT cracking due to the rapid precipitation rate of γ' phase. The precipitation temperature range of γ' coincides with the temperature of PWHT which substantially strengthens the material while stress relieving. The strengthening is usually accompanied by a reduction in overall ductility which makes the microstructure susceptible to cracking [16].

The cracking tendency is often related to the total amount of precipitate hardening elements, that is Al and Ti content of the alloy. Figure 2.8 shows a very widely used diagram to rank the PWHT cracking of various superalloys strengthened by Al and Ti. As the arrow shows, those alloys with higher total Al+Ti content are more subject to PWHT cracking than those which are lower in hardener content. This correlation has been observed many times and appears to be related to the fact that the higher the

hardener content the more rapid the age hardening response during PWHT and the lower the ductility of the alloy, all of which increase the tendency to cracking.

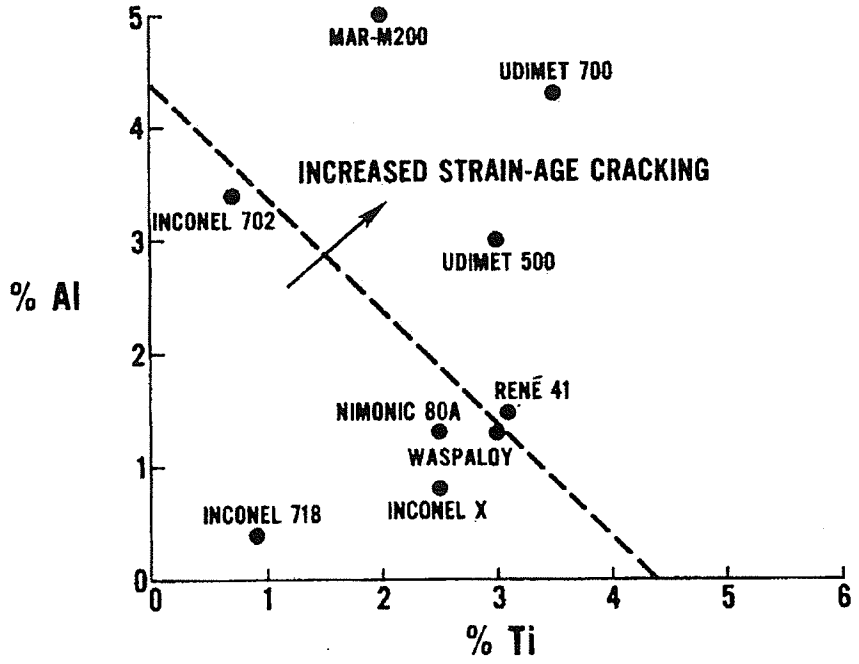

Figure 2.8: Effect of aluminum and titanium content on PWHT cracking tendency in several superalloys [80]

2.4.4: Theories of weld cracking

Weld cracking theories have mostly been derived from the earlier work done on hot tearing in castings. There are two main theories for solidification cracking – Strain theory of Hot Tearing and Shrinkage-Brittleness theory [81]. A modified theory was proposed by Borland [82] which incorporated and modified these two theories, which is known as Generalised Theory. Solidification cracking theories are generally applied to cracking found in the fusion zone but can also be used to understand cracking in the HAZ involving liquation. Cracking in the HAZ during welding or post weld heat treatment also involves melting of the grain boundaries and the two major sources of intergranular liquid in HAZ are: (i) constitutional liquation of second phase particles (ii) liquation due to segregation of melting point depressant elements like boron. This section reviews the solidification cracking theories and liquation cracking mechanisms in HAZ.

Solidification cracking theories:

Strain Theory of Hot Tearing

The study of hot-tearing in castings led to the development of Strain theory. It was recognized since early 1950s that hot tearing actually represents fracture through liquid films which exist at near-solidus temperatures. It was also realised that hot tearing is synonymous to hot cracking and the problem is related to the solidification behaviour of the alloy. Based on the existence of various stages of solidification of an alloy, the following concept was proposed by Pellini [83].

During heating or cooling, when the alloy passes through the solidification temperature, it invariably develops an essentially continuous liquid film, where the strength and ductility of a mass of solid grains separated by liquid films is of extremely low order. This stage was recognized as the "Film Stage" [83]. In the presence of appreciable stress at near solidus temperatures, this thin continuous liquid film can cause immediate intercrystalline rupture of the specimen. Segregation of minor alloying elements on the grain boundaries can depress the melting point locally. If the grain boundaries contain a uniform segregation of minor alloying elements or impurity elements then the liquid films can form below the bulk solidus of the alloy at the melting point of the segregated material. If the segregation is not uniform the failure would occur at some intermediate temperature between the melting point of the segregated material and the bulk solidus of the material.

The development of a crack (hot tear) involves separation of grains, or dendrites during the liquid film stage. The mechanism of hot tearing is illustrated in Figure 2.9 by a simple schematic diagram. Experiments done on aluminum and steel castings established the correlation between metallurgical factors (solidification behaviour and composition) and the mechanical factors (stress and strain) by x-ray radiography and thermal analysis of the samples [83]. It was found in aluminum, and steel castings with different carbon concentrations that hot tears were principally observed near the solidus temperatures in all the cases. Hot tearing was dependent on the amount, distribution and thickness of the liquid layer at the grain boundary, which would be higher at higher temperatures. It was also found that reducing the mechanical restraints resulted in appreciable decrease in the

hot tearing, but it did not affect the temperature of hot tearing. Temperature of hot tearing was appreciably reduced by addition of P and S. The effect of P and S was to delay the time at which steel acquires complete coherence as observed by the tensile rupture tests conducted on steel samples.

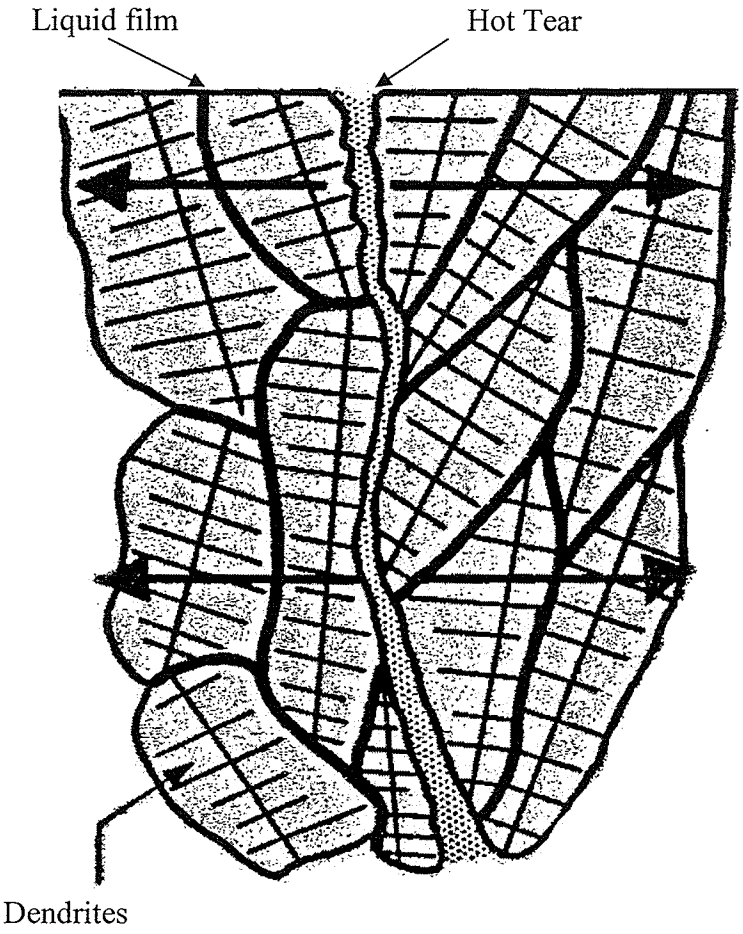

Figure 2.9: Schematic illustration of hot tearing in castings by fracture through interdendritic liquid films existing near solidus temperatures [83]

The analogous process of hot-tearing in welding is called **hot-cracking**. Such cracks have been found to occur in the fusion zone and/or in the heat affected zone (HAZ). It has also been accepted that hot cracking in HAZ occurs as a result of grain boundary liquation, and fusion zone cracking is governed by the same factors as those that affect hot tearing in casting. Figure 2.10 presents a schematic representation of combined hot cracking of the HAZ and the fusion zone. It shows the cross-sectional view perpendicular to the travelling weld arc. Figure 2.10(a) illustrates that grain boundary melting occurs up to the distance in the HAZ where the temperature essentially rises above the solidus temperature of the alloy. If there is appreciable segregation of melting point depressing alloying element on the grain boundary, the grain boundary melting would occur below the bulk solidus.

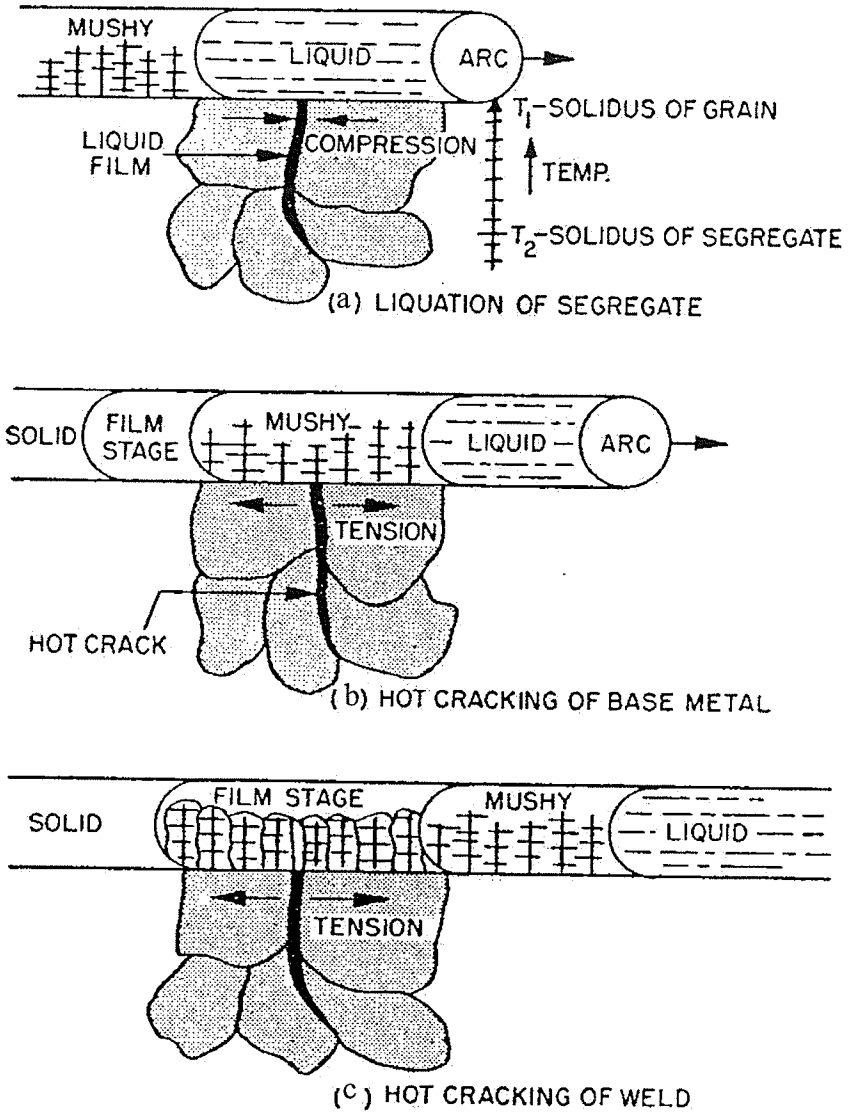

Figure 2.10: Schematic illustration of the process of hot cracking in the fusion zone and the HAZ [83]

Although liquated, the grain boundaries do not crack as they are under compression at this point in time. When the arc advances further, the fusion zone behind the arc starts solidifying and a mushy zone is created, which is illustrated in Figure 2.10 (b). The HAZ is now in tension due to the contraction of the solidifying fusion zone. This is when hot cracking occurs in the HAZ. No cracking occurs at this point of time in the fusion zone as the mushy zone is capable of holding itself together. The mushy zone stage is followed by the film stage in the fusion zone (Figure 2.10 (c)). The HAZ cracks serve as the notches and points of strain concentration for the development of crack in the weld zone. Although, fusion zone cracking can be considered an extension of the HAZ cracking, fusion zone contraction stresses alone can be high enough to cause cracking in absence of HAZ cracking.

During solidification, due to the inherent composition, the alloy will pass through the liquidus-solidus temperature region. Therefore, all the alloys are susceptible to the liquid film stage. The cracking although, not only depends upon the formation of the liquid film, but on other mechanical factors such as the strain developed at that instant. The presence of low melting point segregates often results in extension of the liquidus-solidus temperature range thus increasing the time over which the liquid film is stable, as well as the time for the build up of considerable stresses due to thermal strain. Thus, if the critical strain is exceeded and the alloy is in the thin liquid film stage near the solidus temperature, cracking is expected to occur [83].

Shrinkage-Brittleness Theory:

The other theory that was proposed to explain the hot tearing/cracking was Shrinkage-brittleness theory [82]. In this theory, it was believed that the cracking occurs due to the inability of the new formed dendrites to accommodate the thermal contraction strains. The cracks could still be healed if liquid was still present around the cracks. The temperature range for cracking was thought to be between the solidus and the coherence temperature, where the growing dendrites come in contact for the first time. Hence a brittle temperature range was proposed which essentially is the temperature range between the coherence temperature and the bulk solidus of the alloy where in the alloy is susceptible to cracking if the shrinkage strains exceed the critical rupture stress. Pellini's strain theory was different from this theory principally in the claim that the stresses are distributed uniformly in the mushy zone or the zone where a semi solid mass of dendrites is formed suggesting that cracking cannot occur during this stage.

Generalised Theory:

A generalised theory was proposed by Borland in the 1960's incorporating and also modifying some aspects of the earlier theories [82]. The solidification sequence during welding was divided into four stages:

a) Stage I - Primary dendrite formation: The solid phase is dispersed and liquid is continuous; both liquid and solid phases are capable of relative movement

b) Stage II - Dendrite interlocking (Coherence temperature): Both liquid and solid phases are continuous, but only the liquid is capable of relative movement and is able to circulate freely between the interlocking dendrites

c) Stage III - Grain boundary development: The temperature at which this stage commences is called the critical temperature. The solid crystals are in an advanced stage of development and the semi-continuous network restricts the free passage of liquid.

d) Stage IV - Solidification: The remaining liquid solidifies.

Borland also suggested that the material is susceptible to cracking once the temperature drops below the coherence temperature, although healing of the cracks is possible during this stage as the movement of liquid is not restricted.

The concept of Critical Solidification Range (C.S.R.) was proposed which is the stage past the interlocking of dendrites (Stage III) where the dendrites are in advanced stage of solidification and the relative movement of liquid and solid is impossible. Increase in C.S.R. would increase the likelihood of cracking.

The emphasis of Generalised theory lies on the distribution and spread of the liquid between the interlocking dendrites besides a wider C.S.R. A liquid phase covering almost all the grain faces during freezing will allow the development of high stresses on the narrow bridges joining the adjacent grains, but liquid confined to the grain edges will prevent these high stresses from being built up.

Distribution of liquid depends on the interfacial energies - grain boundary energy Υ_{SS}, solid-liquid interface energy Υ_{SL} which is related to the dihedral angle as by the following expression:

$$\frac{\gamma_{SL}}{\gamma_{SS}} = \frac{1}{2\cos\left(\frac{\theta}{2}\right)} \Rightarrow \tau = \frac{1}{2\cos\left(\frac{\theta}{2}\right)}$$

At $\theta = 0$ ($\tau = 0.5$), there will be complete wetting. If this condition exists in the weld pool over a temperature range while freezing, then there is a possibility of cracking under adverse stress conditions. But as θ increases or τ increases beyond 0.5, the liquid progressively occupies less of the grain faces. At $\theta = 60$ ($\tau = 0.57$) it can only exists as a continuous network along the grain edges. For values $\tau \geq 0.57$, the liquid phase will collect at the grain corners.

For $\tau \leq 0.5$ ($\theta = 0$), wetting would be complete but in such cases there will be small stresses, and moreover the bridging between the grains would not occur and the C.S.R. cannot be established. Therefore, ideally fissures cannot form. Also this condition can only be satisfied by pure metals. However, under non-equilibrium conditions and rapid rate of cooling, τ to just above 0.5 in case of solid-solutions, making them inherently susceptible to cracking. Hence the increase in τ competes with the increasing thermal strains in the alloy during freezing, and the fissuring can only be avoided if the stresses are below the critical level.

The information of dihedral angle-temperature relationship is important for application of this generalised theory. According to the theory, an alloy is highly susceptible to cracking when the composition of the liquid in contact with the growing crystals is similar to that of the solid and changes very little over a relatively wide temperature interval.

Liquation cracking:

Liquation cracking in the heat affected zone has been observed in various austenitic alloy welds. The concept of Partially Melted Zone (PMZ) has been proposed to understand the liquation in the HAZ. The PMZ is the area immediately outside the fusion zone where liquation can occur during welding. Liquation mechanisms can be broadly divided into two categories – one involving a second phase particle, as for an example, an intermetallic compound like A_xB_y or the one involving segregation of melting point depressant minor alloying elements or other impurities. A hypothetical eutectic phase diagram can be used to explain the mechanisms of liquation occurring in the PMZ of a weld involving the A_xB_y as shown in the Figure 2.11. Two main compositions have been considered for the explanation viz., C_1, which is within the solubility limit C_{SM} of α phase, and C_2 is beyond it. A $L \rightarrow A_xB_y + \alpha$ type eutectic reaction occurs at temperature T_E and composition C_E. These mechanisms can be further divided into five different types which are listed in Table 2.4 and are explained next.

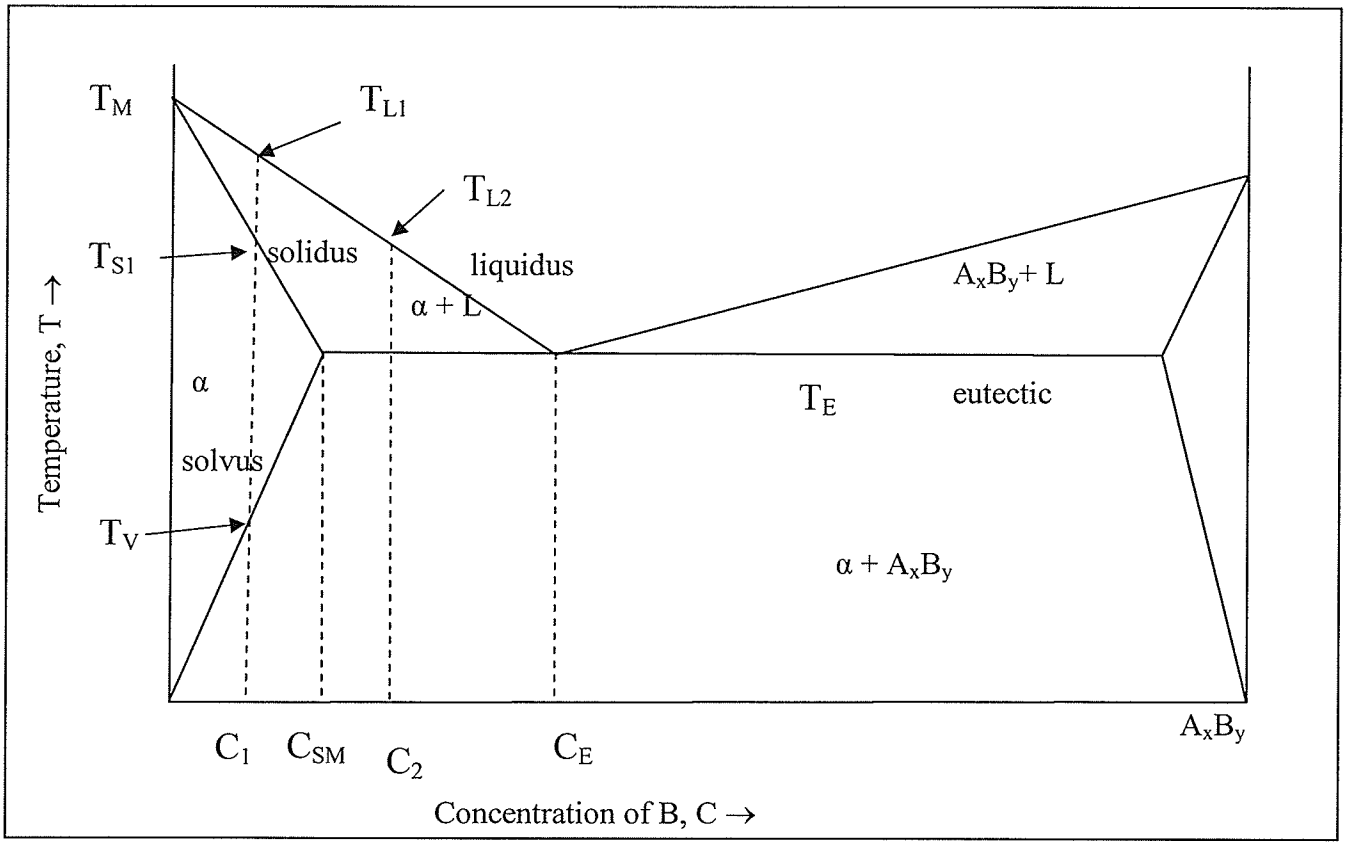

Figure 2.11: Hypothetical binary phase diagram(modified from ref.[74])

Table 2.4: Five mechanisms for liquation in the partially melted zone [74]

#	Reaction/ Mechanism	
	Two mechanisms for an alloy beyond the solubility limit (C_{SM})	
1	<u>A_xB_y reacting with the matrix:</u> $A_xB_y + \alpha \rightarrow L$ at T_E	A_xB_y is always present at T_E regardless of heating rate
2	<u>Melting of eutectic:</u> Eutectic (solid) $\rightarrow$ eutectic (liquid) at T_E	Eutectic is always present at T_E regardless of heating rate
	Three mechanisms for an alloy within the solid solubility limit	
3	<u>Residual A_xB_y reacting with the matrix:</u> **Constitutional liquation** $A_xB_y + \alpha \rightarrow L$ at T_E	If A_xB_y is still present at T_E
4	<u>Melting of residual eutectic:</u> Eutectic (solid) $\rightarrow$ eutectic (liquid) at T_E	If eutectic is still present at T_E
5	<u>Melting of matrix:</u> $\alpha \rightarrow L$ at T_{SI}	If no A_xB_y or eutectic is present at T_E

Mechanism 1: A_xB_y reacting with the matrix

The reaction involved in this mechanism is listed in Table 2.4. Here alloy C_2, consists of an α matrix and A_xB_y particles at any temperature upto the eutectic temperature T_E, regardless of the heating rate to T_E during welding. At T_E liquation is initiated by the eutectic reaction $A_xB_y + \alpha \rightarrow L$. This type of liquation is found to occur in aluminum alloy 2219 which contains Al_2Cu (θ) particles both within grain and along the grain boundaries. Irrespective of the cooling rate, θ particles are always present when T_E is reached which leads to the formation of eutectic liquid.

Mechanism 2: Melting of eutectic

Here alloy C_2 consists of α matrix and the eutectic $A_xB_y + \alpha$. Generally such a eutectic would be present on the grain boundaries and in the interdendritic areas of a cast structure. The eutectic will begin to melt as the T_E temperature is reached and initiates liquation.

Mechanism 3: Constitutional liquation of A_xB_y

This mechanism is the well-known constitutional liquation phenomenon first proposed by Pepe and Savage in 1960 [44]. Consider the alloy with a composition C_1 which when heated at a very slow rate to above the solvus temperature T_v, will be in a single phase region. A_xB_y phase will be completely dissolved by solid-state diffusion to give a homogenous α solid-solution. However, when alloy C_1 is heated rapidly above T_V, as often is the case in welding, coarser size A_xB_y would not have enough time to dissolve

completely in the α matrix because solid-state dissolution is slow. Consequently, upon heating to the eutectic temperature T_E, the residual A_xB_y reacts with the surrounding α matrix and forms the liquid eutectic C_E at the interface. Further heating to above T_E would allow additional time for further dissolution of A_xB_y, and further formation of the liquid phase. Hence localized melting should be possible with rapid heating rates at temperatures significantly below the equilibrium solidus temperature T_S.

Constitutional liquation of second phase particles has been observed in several nickel base alloys such as M_6C in Hastealloy X, MC carbide in Udimet 700, Waspaloy and Inconel 718, and Ni_2Nb Laves phase in Inconel 718 have been commonly reported. A recent study by Ojo et al. [84] on welding of cast Inconel 738 reported for the very first time, liquation of the principal strengthening phase γ' besides liquation of other secondary solidification constitutents like MC carbides, M_2SC sulphocarbides, M_3B_2 borides and γ - γ' euctectic.

However, it has been recognized that constitutional liquation alone is not enough to cause the liquid to penetrate most grain boundaries in the PMZ. Intragranularly located second phase particles undergoing constitutional liquation can only penetrate grain boundaries, if the latter migrate at the same time. Significant coarsening of grains can occur during welding above the effective grain coarsening temperature. Meanwhile some of the moving grain boundaries intersect with the solute rich liquid pools formed by the

liquating second phase. The grain boundaries are pinned due to the wetting action of the liquid and no further grain growth is possible until the solute rich liquid is dissipated by homogenization or the local temperature decreases to below the effective solidus of the solute-rich liquid.

Mechanism 4: Melting of residual eutectic

In this mechanism the alloy with composition C_1 still contains a residual $A_xB_y + \alpha$ eutectic, along the grain boundaries or in between the interdendritic arms. The mechanism is similar to the constitutional liquation of A_xB_y particles, where instead of A_xB_y the residual $A_xB_y + \alpha$ liquates due to the faster non-equilibrium heating involved during welding.

Mechanism 5: Melting of the matrix

Here alloy C_1 contains neither A_xB_y particles nor $A_xB_y + \alpha$ eutectic when the eutectic temperature T_E is reached. For a homogenised solid solution α, the melting would occur within the solidus temperature (T_{S1}) to the liquidus (T_{L1}) temperature range. This would result in partial melting in the PMZ when the material in this temperature range. This liquation is mainly restricted to the grain boundaries.

Mechanism 6: Segregation induced liquation

In this mechanism, melting point depressant alloying and/or impurity elements segregate to the grain boundaries causing them to liquate during the weld thermal cycle[53]. Segregation of boron[45, 46], phosphorus, carbon[53] and sulphur[51] in wrought and cast Inconel 718 have been extensively investigated. It was found that boron can

segregate to the grain boundaries by equilibrium and non-equilibrium modes and can also affect the on-heating and on-cooling hot ductility values. In another study, it was found that elemental segregation of boron, and hence grain boundary liquation associated with it, is not only dependent on the grain size but also the character of the grain boundary[23, 47]. High angle grain boundaries had more segregation and were more susceptible to liquation. Sulphur, like boron, also increased the solidification temperature range by increasing the nil ductility temperature range on cooling [51]. Effects of other alloying elements on weldability of superalloys are presented in the review article by Richards and Chaturvedi [43]. Grain boundary segregation can also occur by grain boundary sweeping of atoms during grain boundary migration and by "pipeline" diffusion of such atoms along grain boundaries that are continuous from the fusion zone to the PMZ [74].

2.5: Weldability and weldability testing:

Lin et al. [85] in their analysis of weldability testing techniques classified the test into three categories, namely, representative (self-restraint) test, simulative (augmented restraint) tests and high temperature mechanical tests. Figure 2.12 shows these general categories and several commonly used test techniques. The widely used weldability testing techniques are the Gleeble hot ductility test, the longitudinal and spot type Varestraint tests.

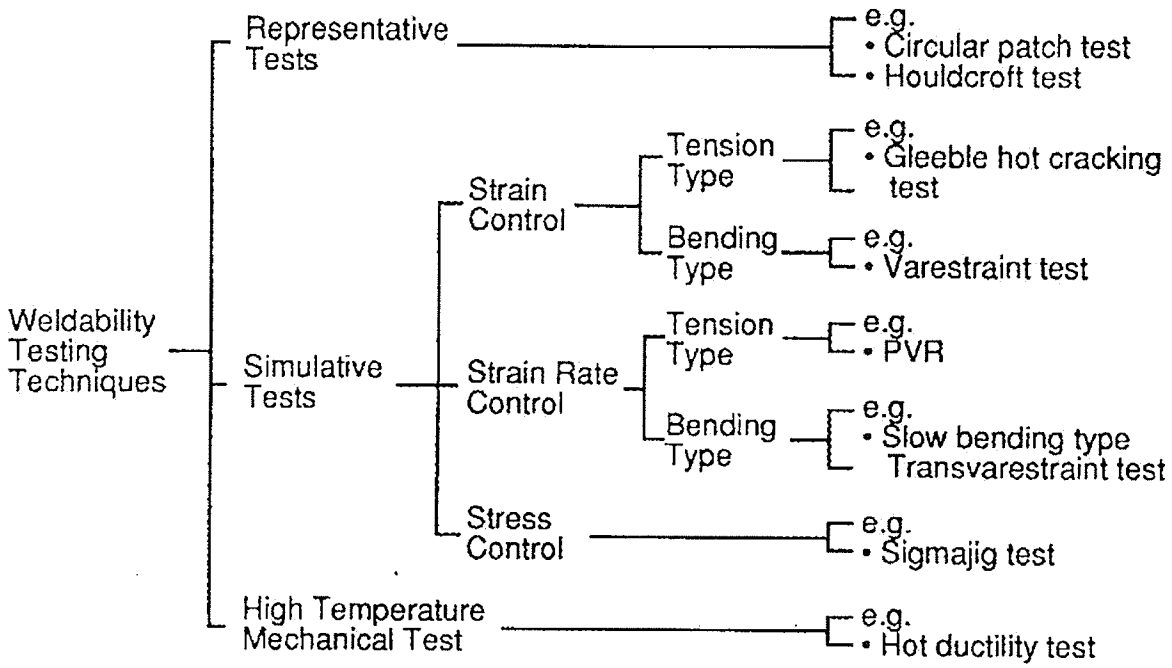

Figure 2.12: Classification of various weldability testing techniques [85]

2.5.1. Gleeble Hot Ductility Test

The microstructure within the narrow region of HAZ varies considerably, from the fusion zone boundary to the unaffected base metal, due to the steep temperature gradient created during the welding thermal cycle. In order to characterize the metallurgical and mechanical changes a sufficient volume of HAZ area is required which can be synthesized by Gleeble thermo-mechanical simulator. It can perform high speed hot tensile tests and is instrumented so that the heating and cooling of test specimens can be accurately programmed to reproduce the rapid temperature changes that occur during welding. The test employs a cylindrical specimen which is clamped between two water cooled copper or stainless steel jaws/grips separated by a given distance (called the free span). The grips also provide a means for introducing current into the specimen and ensure rapid heat extraction (on cooling) when the current flow is interrupted. The heating current is controlled electronically through out the thermal excursion by mean of a signal obtained from a fine wire thermocouple welded to the center of the specimen gauge length. The instantaneous temperature of the specimen is compared with a reference temperature and the current level is increased, decreased, or interrupted as required to maintain the temperature [86].

The alloy's ductility as a function of temperature varies on heating and cooling which is measured by pulling the specimen to failure and measuring the elongation or reduction in area. On heating, at a particular temperature, the ductility of the alloy drops to zero. This temperature is known as the Nil Ductility Temperature (NDT). On further heating, the alloy loses all its strength along with the ductility which is the recognised as the Nil

Strength Temperature (NST). On cooling, the ductility of the alloy is recovered at a specific temperature called the Ductility Recovery Temperature (DRT). Hot ductility test essentially involves the detection of these three main temperatures, the reduction in area measurements and the ultimate tensile stress measurements for any particular alloy under study. Figure 2.13 shows a typical on-heating and on-cooling ductility behaviour for any alloy with the important temperatures marked.

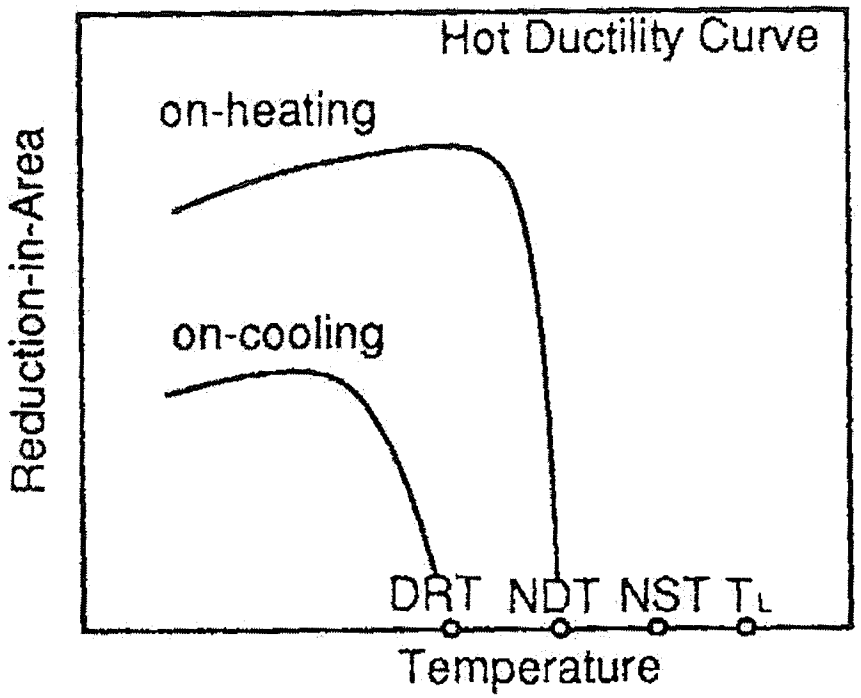

Figure 2.13: Typical hot-ductility curve showing on-heating and on-cooling curves with important temperatures

Hot-ductility test data has been interpreted in several ways to correlate with the HAZ liquation cracking since the development of hot ductility measurement technique by Gleeble thermo-mechanical simulator. Ductility recovery temperature and the rate of recovery on cooling from elevated temperatures were proposed as a measure of HAZ liquation cracking susceptibility by Nippes et al. [86]. Figure 2.14 shows the Nippes criteria schematically. According to the figure, a material can have two main types of on-heating behaviour, H1 and H2. If a material has H2 on- heating behaviour it should be rejected because of its high HAZ cracking susceptibility and when a material has a H1 on-heating ductility behaviour, further on-cooling tests should be done to evaluate the cracking potential. On cooling, the material can have C1, C2 and C3 type ductility behaviour, which are most commonly encountered in a material that exhibits a H1 type of heating ductility curve. A material with behaviour described by C1 is considered to be readily weldable without any tendency toward HAZ cracking, while C2 and C3 type of behaviour indicate a less desirable HAZ hot cracking resistance with C3 type indicative of the highest susceptibility to HAZ cracking.

TYPICAL TESTED ON – HEATING BEHAVIOR

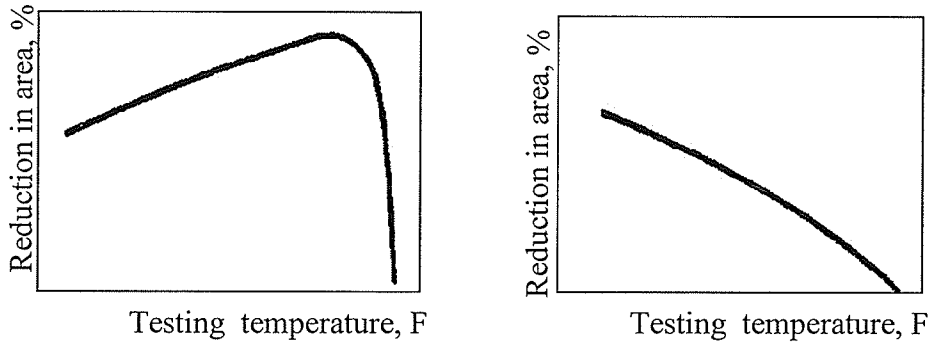

(a) Class H1 (b) Class H2

TYPICAL TESTED ON- COOLING BEHAVIOR

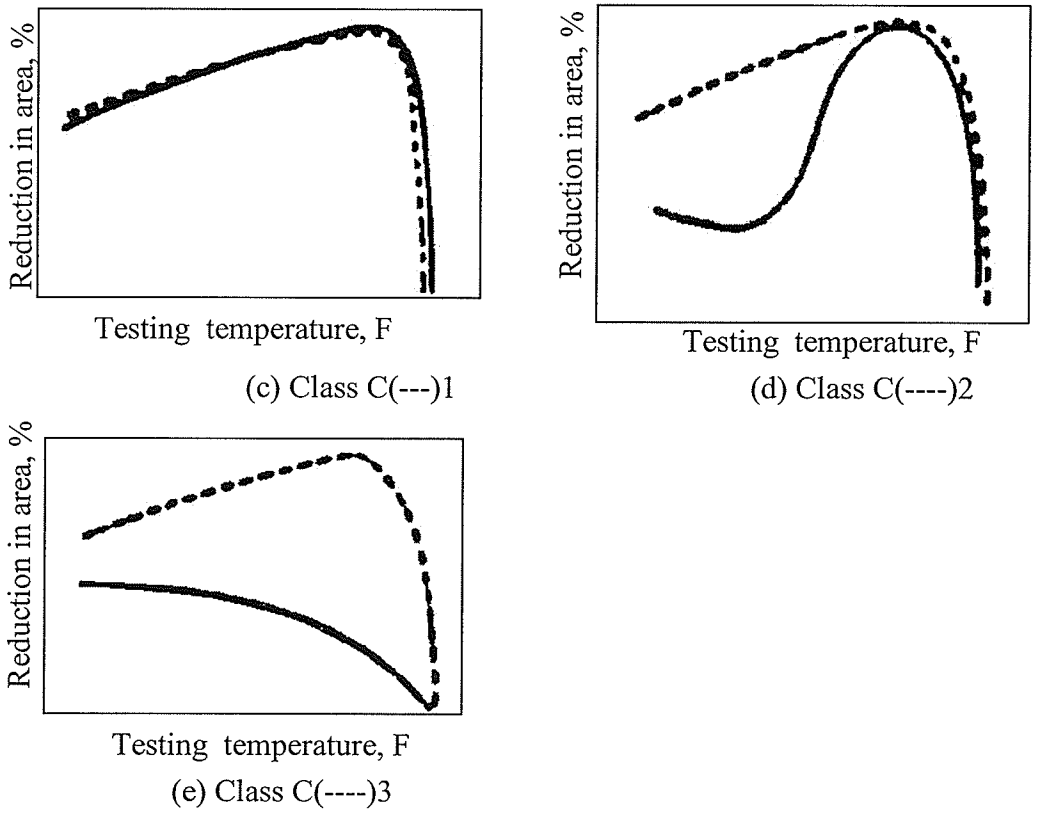

(c) Class C(---)1 (d) Class C(----)2

(e) Class C(----)3

Figure 2.14: Nippes criteria for classification of on-heating and on-cooling hot ductility behaviour (modified from ref. [86])

Kreischer [87] later proposed that strength along with ductility is an important parameter in determining the alloy's resistance to HAZ cracking. Owczarski et al. [39] suggested that on-cooling tests from NST or above provided with more appropriate data than the tests conducted with NDT as the peak temperature. In their examination of HAZ microfissuring in four superalloys, they concluded that the two most important factors that affect the HAZ microfissuring were the extent and duration of the zero ductility range and the amount and rate of recovery of ductility. A wider nil ductility region or slower recovery was related to higher susceptibility to cracking. They also suggested that the hot-ductility results normalized relative to the NST provided a direct comparison of cracking susceptibility. Owczarski et al.'s [21] criterion has been widely utilized in the interpretation of the hot-ductility data. Muesch proposed a cracking factor, (NST-DRT)/NST which was also utilitized by Donati et al. [88] to predict cracking tendency. Besides the different criteria used for evaluation of hot-ductility data, the testing parameters used affects the assessment of hot-ductility. Lundin et al. [89] recognised that the critically important testing parameters to be considered were thermal cycle, peak temperature, crosshead speed or stroke rate, holding time at the testing temperature, holding time at the peak temperature and the thermocouple attachment technique. They also suggested a recommended set of parameters in order to standardize the hot-ductility measurements [89]. These parameters are listed in Table 2.5.

Table 2.5: Recommended Gleeble hot ductility testing conditions and procedures [89]

Parameter	Conditions
Sample	Diameter: 6.35 ± 0.025mm; cylindrical; length 102 ± 3 mm; thread ¼-20 on both ends
Thermocouple	Diameter: 0.254 mm; Chromel-alumel: < 1371°C Noble Metal/Alloy: > 1371°C Attachment methods: Percussion/Spot Welding, Separate Wire Technique
Thermal cycle	Characteristics of a SMAW weld in 38 mm thick stainless steel with an energy input of 2.8 KJ/mm at 22°C preheat
On cooling peak temperature	Nil ductility or nil strength temperature
Hold time	Test temperature : 1-2 seconds permitted Peak temperature: Not permitted
Cross head speed	63.5 ± 13 mm/sec
Jaw separation	20 ± 5 mm
Testing	Minimum of 2 tests at each temperature. A difference of greater than 30% in reduction in area, will necessitate one more test. Testing Temperature Intervals : 56-111°C intervals below NDT-56°C or NST-56°C; 14°C intervals between NDT and NST

Fracture surfaces of hot-ductility samples have also been examined for information about the mechanisms involved in ductility/strength loss and liquation cracking. Qian et al. [18] observed that a complete intergranular fracture occurred in Waspaloy bar and disk samples at temperature above DRT and NST indicating a high-temperature grain boundary weakening phenomenon being the major contributor to failure. Another study [90] revealed that mixture of liquid film and ductile features exist at fracture temperatures slightly below the DRT indicating the solidification range is extended to even below the DRT temperature. Fracture surfaces have also revealed the presence of liquation of carbides and grain boundary liquation due to segregation of boron in some nickel base superalloys [18].

2.5.2: The Varestraint Test

Varestraint test was originally developed by Savage and Lundin [91] in mid 1960's for weldability testing and has been widely utilized as weldability testing technique for quantifying susceptibility of a material to solidification and HAZ liquation cracking. Three modifications of the original version have been developed, namely mini-varestraint test, spot-varestraint and Transvarestraint test.

Mini-varestraint test uses a smaller test sample compared to the original Varestraint test and is also called longitudinal varestraint test as the welding is performed longitudinally to the direction of bending. A schematic of the longitudinal-varestraint test is shown in Figure 2.15. A specimen is supported as a cantilever beam and a gas tungsten arc weld (GTAW) is produced along the center section of the specimen. The cantilever beam is

also attached to a removable die block with a known radius of curvature. When the arc approaches the center of the die block (marked A), a pneumatically operated ram is triggered forcing the specimen to conform to the surface of the die block. The applied augmented strain (ε) of the top surface of the specimen can be varied by adjusting the radius of the die block (R) following the equation,

$$\varepsilon = \frac{t}{(2R + t)},$$

where, t is the specimen thickness. This induces solidification and liquation cracking in the test sample.

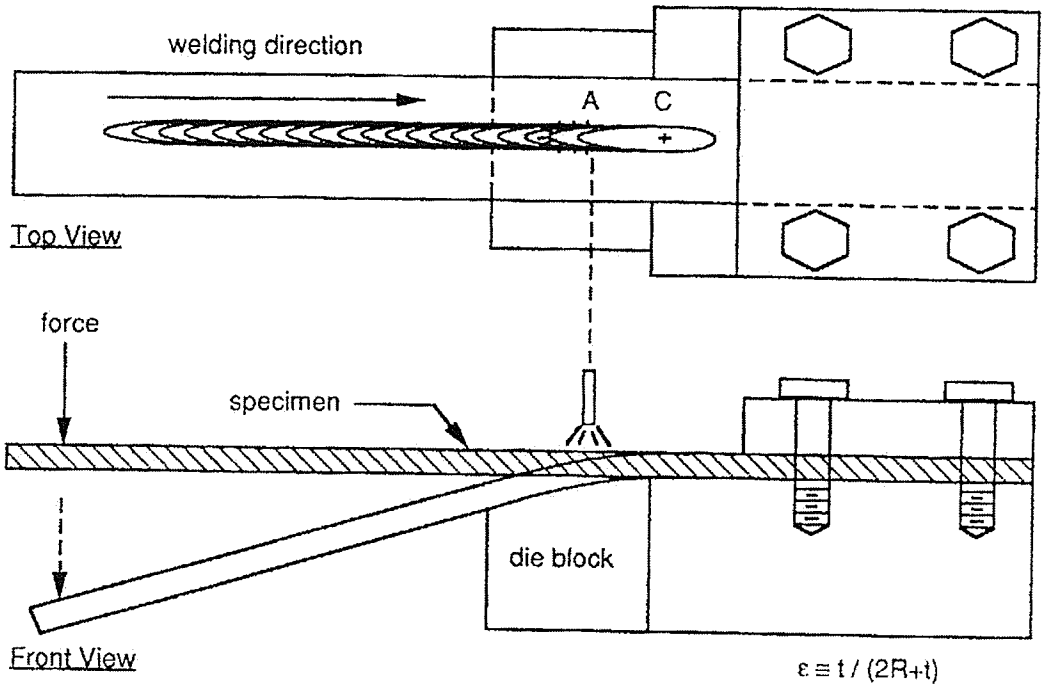

Figure 2.15: Schematic representation for the longitudinal varestraint test [91]

Spot-Varestraint Test:

In this modified version of varestraint test, instead of a continuous longitudinal weld, a Gas Tungsten Arc spot weld is generated in the center of a test sample. The specimen dimensions are nominally 140 × 25 × 6.4 mm (5.5 × 1 × 0.25 in). A schematic of the test apparatus is shown in Figure 2.16. After a predetermined weld time, the arc is extinguished and the specimen is forced to confirm a die block with known radius. In this manner, HAZ liquation cracks can be generated in the specimen adjacent to the GTA spot weld.

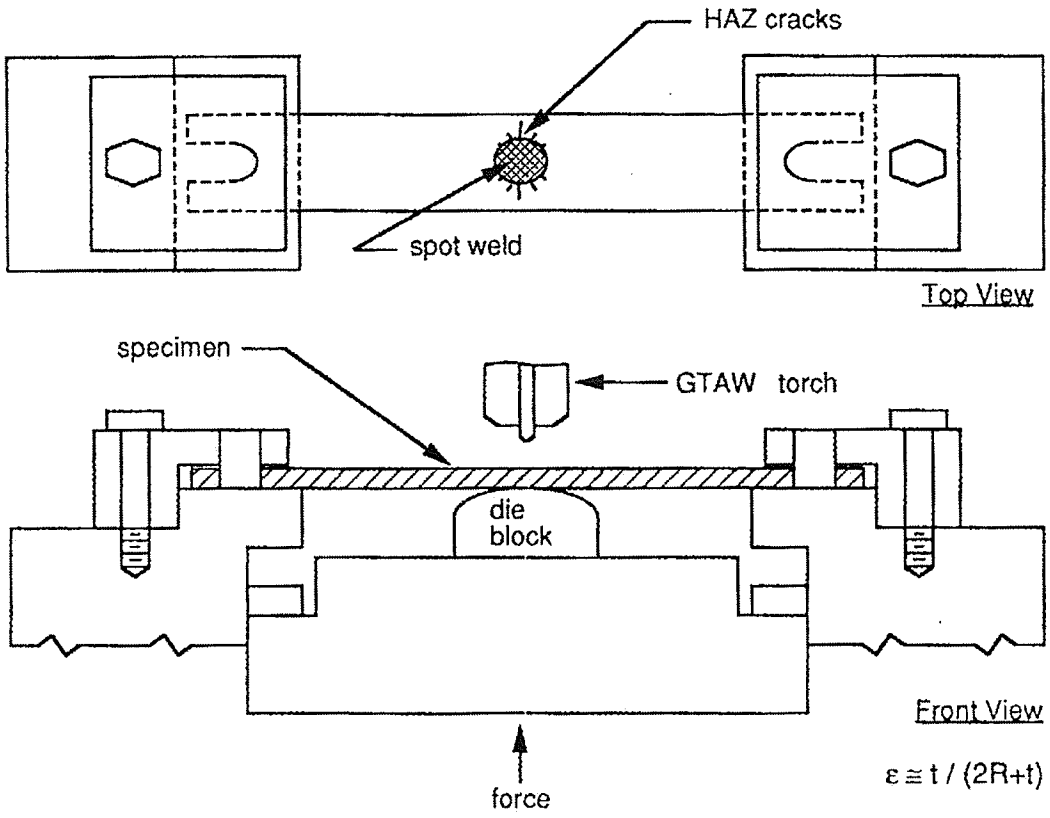

Figure 2.16: Schematic representation of the spot-varestraint test

2.5.3: Total crack length measurements

The microfissuring tendency can also be evaluated by measuring the crack lengths in welds, especially made for experimental purpose. The actual pre- and post- weld heat treatment can be given to the material that is to be evaluated. The material is welded with the welding technique and parameters that are to be used to make actual welds. The welded specimens are then cut into sections perpendicular to the welding direction. The microfissuring tendency can be evaluated by using a cracking index [92]. The cracking index is defined as

$$C.I. = \frac{l_1 + l_2 + l_3 + ...}{A_{HAZ}},$$

where *C.I.* is the cracking index, l_1, l_2 and l_3 are individual crack length measurements from one section and A_{HAZ} is the area of the HAZ. For similar alloys under identical welding parameters A_{HAZ} can be considered to be constant. Also total crack length TCL′ can be determined by

$$TCL' = \sum l_1 + l_2 + l_3 + ...$$

To increase the statistical reliability of the TCL′ value, measurements are made on 10 or more sections of one weldment, and the sum of these values, TCL, is used for analysis, i.e.,

$$TCL = \sum_{n=1}^{10} [TCL'_1 + TCL'_2 + TCL'_3 + TCL'_4 + ... + TCL'_{10}]$$

The average of TCL and its standard deviation are calculated and are directly used as a measure of cracking index. Some other parameters generally measured are number of cracks, average total crack length and maximum crack length.

Scope and nature of study

As discussed earlier, 718 Plus is a newly developed alloy based on the conventional Inconel 718 and no detail study exists on the weldability of this alloy in open literature. Furthermore physical metallurgy data for 718 Plus is scarce and limited experimental evidence is available the microstructure of this alloy. For a successful commercial application of this alloy the fundamental knowledge of physical metallurgy of 718 Plus and its weldability is essential. Superalloys in general are susceptible to HAZ liquation cracking, and γ' strengthened Ni-base superalloys are prone to PWHT cracking. Moreover, minor alloying elements like boron and phosphorus, which are known to affect weldability adversely, were intentionally added to 718 Plus to improve its high temperature performance. Hence, it is very important to know the welding characteristics of this new superalloy and understand the mechanism of cracking, if any cracking is found. The present study of weldability of this alloy, being one of the first for it, will not only provide the necessary database and guidelines for future research, but add valuable information to the existing knowledge about weld cracking. It was also imperative to compare the weldability of 718 Plus with other superalloys, that have been thoroughly studied in the past, to comprehend the scale of response.

Therefore, this project aims to understand the physical metallurgy of the 718 Plus alloy and thereby understand its response to welding. There were two main objectives of this research:

1. To study and assess the weld cracking susceptibility of 718 Plus and compare it with the base line superalloy Inconel 718 and Waspaloy under similar welding conditions.
2. To study the mechanism(s) responsible for weld cracking in 718 Plus alloy and the influence of the following metallurgical parameters on it :
    a. Effect of minor alloying elements.
    b. Effect of solutionizing pre-weld heat treatments.

Investigations were performed to:

i. Determine microconstituents present in the as received, solution pre-weld heat treated at 950°C/1hr and 1050°C/1hr condition
ii. Characterize microstructures that develop in fusion zone and the HAZ of 718 Plus during electron beam welding
iii. Analysis of HAZ and fusion zone in Electron beam welded material for weld cracking and compare its weld cracking behaviour with those of Waspaloy and Inconel 718 under same welding conditions.
iv. Determine the effect of minor alloying elements like boron and phosphorus on weld cracking, by studying and comparing the cracking in a higher boron and phosphorus version of 718 Plus
v. Determine hot ductility data of 718 Plus alloy in the commercial solution treated condition and compare with Inconel 718
vi. Correlate the HAZ liquation cracking and the hot ductility data to obtain an understanding of mechanisms of HAZ cracking mechanism in this alloy

CHAPTER 3 - EXPERIMENTAL PROCEDURES

Introduction:

The alloys used in this investigation were Waspaloy, Inconel 718 and two versions of Allvac®718 PlUS™ (718 Plus). Hot rolled plates of all the alloys of dimensions 15.9 mm × 304.8 mm × 127 mm were supplied by ATI ALLVAC Ltd. The normal composition of the alloys is listed in Table 3.1.

3.1: Materials and Processing

Heat treatments:

The hot worked oxidised surface layer of the plates was removed by grinding all the four sides, and 12.7 mm × 12.7 mm × 101.6 mm sections were cut normal to the rolling direction of the plates. These sections were subsequently heat treated in a Marshal tube furnace in controlled argon atmosphere. Pre-weld heat treatment of the three alloys consisted of their commercial solution heat treatments. The commercial solution heat treatment for 718 Plus alloys and Inconel 718 is 954°C for 1hr followed by air cooling. For Waspaloy, two solution heat treatments can be used, a sub-solvus heat treatment of 1020°C for 1 hr and a super-solvus heat treatment of 1080°C for 4 hrs followed by air cooling. Here, the sub-solvus heat treatment was used to keep the grain size comparable with the 718 type alloys. Generally, commercial heat treatments use air cooling, but water quenching was used in this investigation to suppress any precipitation or segregation during cooling in the alloys. Further, the 718 type of alloys, i.e. Inconel 718 and the two 718 Plus alloys were also subjected to a higher solution heat treatment of 1050°C for 1hr followed by water quenching. This heat treatment was used essentially to

dissolve the grain boundary δ phase present in the 950°C heat treated condition and to essentially induce a single phase microstructure, which is desirable for welding. These heat treatments are listed in Table 3.2.

Electron beam welding:

Bead on plate autogenous welds were made on heat treated blocks with sharp focussed electron beam using 44 kV voltage, 79 mA current and 152 cm/min speed at Bristol Aerospace Ltd., Winnipeg. Welded samples were sectioned transversely to the welding direction using electro – discharge machining (EDM). These sections were mounted and polished using standard metallographic techniques. Metallographic specimens were mostly etched by Kalling's modified reagent - 40 ml distilled water + 480 ml HCl + 48 gm of $CuCl_2$. Samples were also occasionally electrolytically etched in 10% oxalic acid and a mixture of 12ml H_3PO_4 + 40ml HNO_3 + 48ml H_2SO_4 for 6V at 5-6 seconds. The latter was used to reveal γ′ phase in the microstructure.

Table 3.1: Chemical compositions of the alloys

wt %	Inconel 718 **(GM 78)**	Allvac 718 Plus **(HC 49)**	Allvac 718 Plus **(HC 20)**	Waspaloy **(WM 06)**
Ni	54.44	52.21	52.18	58.55
Cr	17.94	17.42	17.92	18.36
Fe	17.62	9.66	9.33	0.61
Co	0.13	9.13	9.00	14.02
Nb	5.36	5.48	5.51	0.02
Ti	0.94	0.71	0.74	3.12
Al	0.46	1.46	1.50	1.49
B	0.004	0.005	0.003	0.005
P	0.007	0.013	0.006	<0.003
C	0.026	0.028	0.022	0.032
Mo	2.93	2.72	2.68	3.73
W	<0.01	1.04	1.04	0.02
S	<0.0003	<0.0003	<0.0003	<0.0003
Si	0.05	0.05	0.02	0.02
Mn	0.05	0.05	0.03	0.02
Mg	0.0014	0.0012	0.0008	not detected

Table 3.2: Heat treatments used in this study

Alloys	Heat treatments
Waspaloy	1020°C for 1hr followed by water quenching – Sub solvus commercial heat treatment
Inconel 718	950°C for 1hr followed by water quenching – Standard commercial solution heat treatment 1050°C for 1hr followed by water quenching
718 plus alloys	950°C for 1hr followed by water quenching - Standard commercial solution heat treatment 1050°C for 1hr followed by water quenching

3.2: Optical Microscopy, Scanning Electron Microscopy (SEM) and Electron Microprobe Micro-analysis (EPMA):

Samples prepared by standard metallographic practice were used for optical microscopy, SEM and EPMA. Microstructural examination of pre-weld and post-weld samples was done on an inverted reflected light microscope equipped with quantitative image analyzer. The grain size of the specimens was measured before and after welding using Clemex Vision 3.0 software. Further examinations were carried out on JEOL 5900 Scanning electron microscope (SEM) equipped with an ultra thin window Oxford energy dispersive spectrometer (EDS). The SEM was used in the secondary electron (SE) mode and back scattered electron (BSE) mode. Occasionally, X-ray line scan and area mapping were also done on the samples using Inca software. A Cameca MBX electron-microprobe (EPMA) equipped with ϕ (p,z) correction algorithm was used to analyze the chemical composition of dendrite core in the fusion zone of the welded specimens. EPMA was operated at 15keV voltage and 10 nA current.

3.3: Transmission electron microscopy:

JEOL 2100 FX field emission high resolution TEM and JEOL 2000 FX TEM equipped with EDAX ultra thin window detector were used for detailed microstructural analysis of HC 20 718 Plus alloy. X-ray microanalysis in TEM, using theoretical Cliff-Lorimer k factors, and selected area diffraction analysis were performed on constituents extracted on carbon extraction replicas and on those present in thin foils prepared from weld fusion zone, using Genesis thin-film analytical software. Camera length calibration was carried out using a pure aluminum sample deposited on Cu grid. Careful measurements were

taken on the ring patterns obtained from the standard at an accelerating voltage of 160 keV.

For extraction replicas, the polished specimens were lightly etched to reveal the microstructure. This first etching was either done by Kalling's etchant, 10% oxalic acid or the γ' etchant, depending on the phase to be studied. After etching, the area of interest was observed under a low magnification microscope and the remaining area was carefully covered by a masking tape. A thin carbon film was deposited on the specimen by using Edwards Auto 36 Vacuum coater. Carbon coating was carried out in a vacuum of about 1×10^{-5} torr. After the coating, the masked tape was removed and the remaining coating was scored into approximately 3 mm^2 area. This would facilitate the electrolyte to penetrate beneath the coating and help in removing it during the final stage. After scoring, the specimen were electrolytically re-etched, either in the same solution used for initial etching or with a solution of 10 ml HCl and 1 g tartaric acid in 90 ml methanol at 4 V. Once etched, the specimens were then carefully lowered, at a shallow angle into a beaker filled with distilled water to detach the carbon replica. These replicas were then collected on to 200 mesh copper grids and dried before examination.

For thin foils, 3 mm diameter rods were machined by EDM from the areas of interest. Disks of 150-200 μm thickness were machined from these 3mm diameter rods and mechanically polished to almost 70 μm thickness. Thickness was further reduced by twin-jet polishing with 10% perchloric acid in 90% methyl alcohol at -20 to -30°C temperature, 1.5 A current and 2 V voltage. Electro-polishing rendered a very thin film

with perforation suitable for viewing under TEM. Occasionally, thin foils were ion-milled to reduce the thickness in the center portion or near the perforation after electropolishing. Ion-milling was carried out for 15 minutes to 2 hrs in Gatan Duomill equipped with liquid N_2 cooled stage. The voltage used was 4.5 keV at vacuum of less than 1×10^{-5} torr and the angle of incidence of the ion gun was kept between 5°-15°.

3.4: Secondary Ion Mass Spectroscopy:

Grain boundary segregation was examined by a Cameca IMS-7f magnetic sector Secondary Ion Mass Spectrometer. Heat treated samples, before and after welding were sectioned and prepared by standard metallographic technique. Samples were etched by modified Kallings etchant to reveal the grain boundaries. Usually, polished surfaces were preferred for observations under SIMS, and hence the areas to be analyzed were marked by hardness indentations. Vickers micro hardness diamond indenter with a load of 200 gm was used to make indentations near the areas of interest. Finally the etched layer was removed by polishing, leaving the indentations on the polished surface to help determine the areas to be observed. Lightly etched samples were also used for analysis in certain cases.

In the microprobe mode of operation of SIMS, images were constructed line-by-line by a rastering beam. O_2^+ and Cs^+ primary ion sources were used which yield spatial resolutions of the order of less than 1μm. Most ion images were acquired in microprobe mode which minimizes the ion beam damage of the sample. Positive secondary ion images of $^{11}B^+$ and negative secondary ion images of $^{31}P^-$ were acquired in microscopy

mode by means of 1nA or 300 pA O_2^+ primary ion beam and a 2nA or 600 pA Cs^+ primary ion beam rastering an area of 150 × 150 μm^2 respectively. Another mode of SIMS operation is ion-microscope, in which a large area of the sample surface is illuminated by a stationary primary beam, and chemical data is extracted from central circular areas. In this mode, information of all points in the field of view is collected simultaneously. Few $^{11}B^+$ images were acquired in microscopy mode by using 550nA O_2^+ primary ion beam. Most of the early research utilised the microscopy mode because of better sensitivity, but for new IMS-7f SIMS, microprobe mode provides equivalent sensitivity for detection of elements like B and P due to high primary beam density.

3.5: Gleeble hot-ductility tests:

The hot ductility tests were conducted with a Gleeble 1500-D thermo-mechanical simulation device using two sets of cylindrical specimens – (1) diameter 10 mm and length 158 mm and (2) diameter 6mm and average length 120 mm. The alloys were subjected to their respective standard solution heat treatments in a tube furnace with controlled argon atmosphere before the tests. The "on-heating" and "on-cooling" hot ductility tests were performed in air to simulate the welding thermal cycle. A typical Gleeble thermal cycle is depicted in Figure 3.1. During on-heating tests, the samples were heated to the test temperature at the heating rate of 150°C/s, were held there for 0.5s for stabilization, and then tensile stress to fracture was applied. During on-cooling ductility tests, the samples were heated to a peak temperature (T_p) and then controlled cooled at 45°C/s to the test temperatures. After holding for 0.5s, tensile stress was applied to fracture the sample. The hot ductility of the alloys at different test temperatures was

determined from the reduction in area of the specimens, which was obtained by measuring the initial diameter and the final diameter of the fractured specimen. The material parameters measured were on-heating – nil ductility temperature (NDT), on-cooling ductility recovery temperature (DRT) and the brittle temperature range (BTR), which is the temperature range between T_p and DRT.

NDT which is defined as the temperature at which the material loses all its ductility, was determined by on-heating tests. The samples were heated to various test temperatures at a fixed heating rate and pulled to failure by applying tensile stress. The temperature at which the material had zero ductility was determined to be the NDT temperature for the alloy. DRT was determined by on-cooling tests, and is defined as the temperature at which the material recovers 5% of its ductility, after being cooled from its melting temperature T_m. It is difficult to use T_m as the peak temperature as the material loses its integrity at this temperature, therefore, a lower temperature is generally chosen as the peak temperature for the on cooling tests. This temperature is recommended to be higher than NDT temperature [89] , as use of NDT as T_p has previously resulted in erroneous results [39]. Temperature T_p is selected after experimentation to ensure that a reasonable amount of grain boundary liquation occurs when a specimen is heated to this temperature. In the present study, peak temperature of 1250°C and 1200°C was selected for Waspaloy and 718 type alloys, respectively, which was about 50°C higher than the NDT of the alloys. A third hot ductility parameter, brittle temperature range (BTR), was derived from the peak temperature and DRT. BTR represents the temperature range over which material in the HAZ remains liquid during cooling after the welding. Larger the value of

BTR, greater is the material's susceptibility to HAZ cracking. The Gleeble parameters are summarized in Table 3.3. The parameters used in the present study had to be modified from those suggested by Lundin et al.[89] in their study of standardization of Gleeble hot-ductility test parameters due to the different sample sizes.

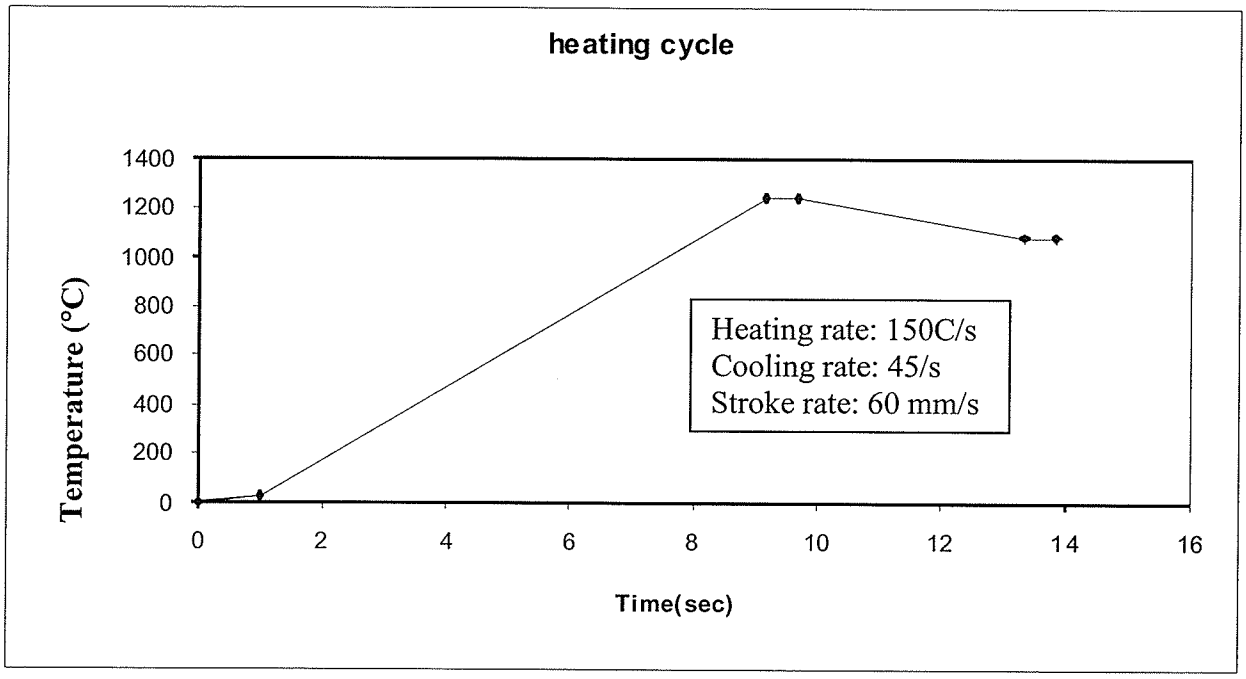

Figure 3.1: Typical Gleeble thermal cycle

Table 3.3: Gleeble parameters used in this study

Sample dimensions	6.33 mm dia., 120 mm length	10 mm dia, 158 mm length
Free Span	30 ± 2 mm	50 ± 2 mm
Heating rate	150 °C/s	150 °C/s
Hold time at test temperature	0.05 s	0.05 s
Hold time at peak temperature	0.05 s	0.05 s
Stroke rate	60 mm/s	60 mm/s
Cooling rate	45°C/s	45°C/s
Peak Temperature	1200°C for Inconel 718 and 718 Plus alloys	

CHAPTER 4 – RESULTS AND DISCUSSION

4.1: Microstructure of Waspaloy, Inconel 718 and HC 49 718 Plus

4.1.1 Introduction:

The cracking susceptibility of an alloy is known to depend upon its chemical composition, pre-weld microstructure and its modifications during welding and development of microstructure of welds. Therefore, to understand the causes of microfissuring, it was imperative to understand the pre-weld microstructure and development of microstructures in the base metal, fusion zone and HAZ of the alloys. Also to estimate the welding response of the newly developed 718 Plus alloy, its welding response was compared with other superalloys viz., Waspaloy, Inconel 718 and higher B and P containing 718 Plus under similar welding conditions. Weldability of Inconel 718 and Waspaloy have been studied earlier by various research groups and hence, in the present work, most of the attention was devoted to microstructural characterization of 718 Plus alloys, particularly the normal B and P version HC 20 718 Plus.

4.1.2 Microstructure of Waspaloy:

Pre-weld microstructure - 1020 °C/1hr followed by water quenching:

As mentioned in the experimental section, Waspaloy plates were heat treated at 1020°C for 1 hour followed by water quenching, which is almost a sub-solvus temperature of principal strengthening γ′phase in Waspaloy, and has been reported to be in the range of 1020°C [12] to 1050°C [10]. Super solvus solution heat treatment at 1080°C for 1 hour was done but it increased the grain size of the alloy considerably (126 ± 9μm), which was out of the grain size range of other alloys used in this study. Hence a sub-solvus heat

treatment was chosen. The grain size after this heat treatment was 67 ± 6 μm and the hardness was 276 ± 2 VPN/10 kg. Figure 4.1 shows a micrograph of solution heat treated Waspaloy. The microstructure consisted of uniform distribution of γ′ particles with few MC type carbides. The grain boundaries were marked with γ′ particles as shown in a higher magnification secondary electron micrograph in Figure 4.2. SEM EDS analysis indicated the MC type carbides to be rich in Ti and Mo (Figure 4.2). Similar phases were observed by other investigators [11, 93] in their characterization of Waspaloy microstructure. The average chemical composition (wt%) of metallic elements in MC type carbide as determined by SEM EDS analysis was, 57.16 Ti, 19.99 Mo, 12.77 Ni, 6.89 Cr, 2.98 Co, 0.20 Al and 0.11 W (Table 4.1).

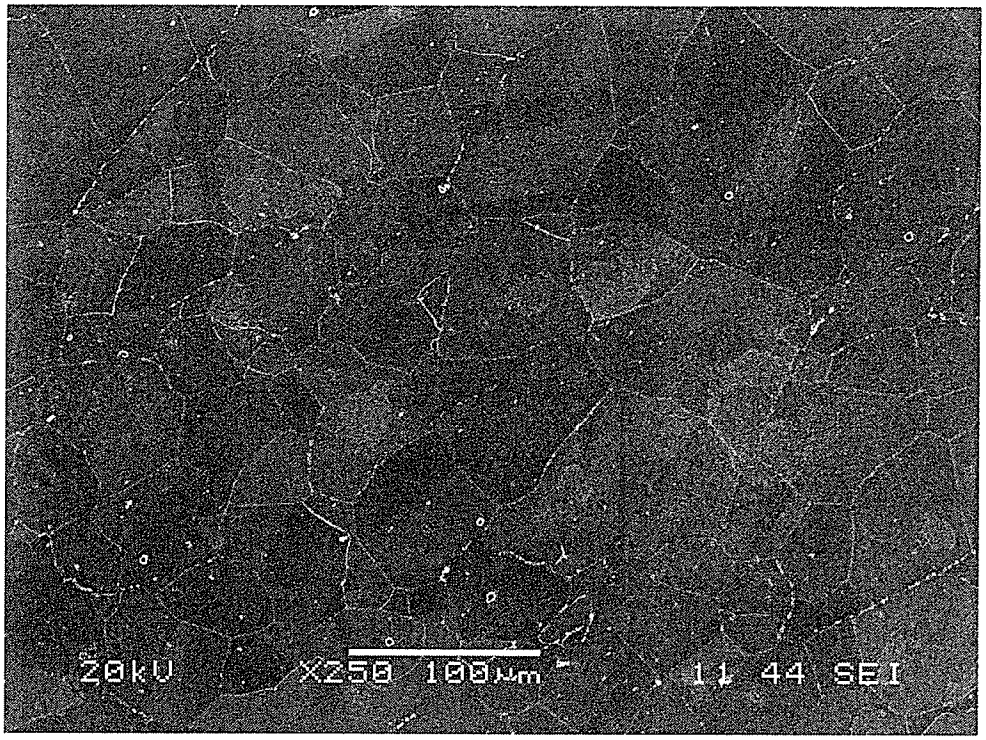

Figure 4.1: Microstructure of solution heat treated Waspaloy after 1020°C/1hr

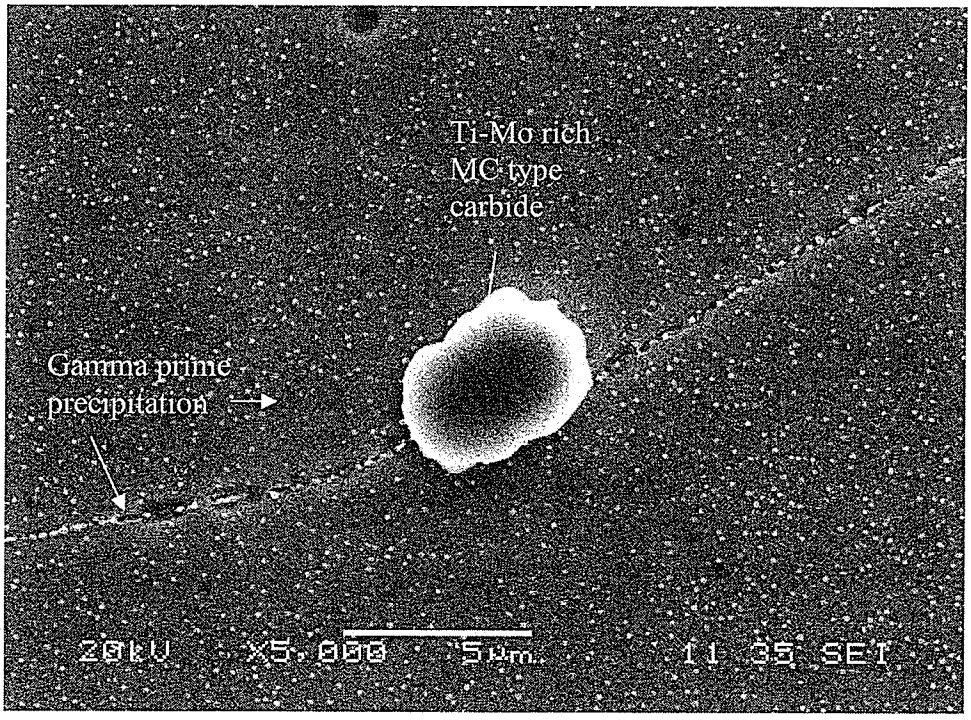

Figure 4.2: Ti-Mo rich MC type carbide at the grain boundary and γ′ precipitation after solution heat treatment in Waspaloy

Microstructure of the welds and microfissuring in the fusion zone and HAZ

The solution heat treated material was EB welded using the parameters described in Chapter 3. Figure 4.3 shows a typical nail head weld profile obtained after welding. Extensive cracking was observed in the fusion zone and the HAZ of the alloy.

Fusion zone microstructure consisted of fine cellular dendritic structure as shown in an optical micrograph in Figure 4.4. The hardness value of fusion zone was 234 ± 8 VPN, approximately 40 VPN less than the base metal. The SEM BSE image (Figure 4.5a) shows very little contrast indicating minor composition variation. The interdendritic regions as well as the phases present were found to be richer in Ti content compared to the matrix composition. An x-ray line scan shown in Figure 4.5b, which was taken from the fusion zone area marked in Figure 4.5a, shows the variation in the amount of Ti between the dendrite cores and the interdendritic regions. No significant deviation was found in the other alloying elements like Co, Cr, Ni, Al and Mo. Similar results were obtained by Sekhar et al.[94] in their study of laser and electron beam welded Waspaloy. Some Ti rich MC type carbides were identified in the fusion zone. MC type carbides and fine γ' particles were reported to be present in the fusion zone of Waspaloy in an earlier study [20]. A number of small porosities were also distributed throughout the fusion zone, especially in the interdendritic regions, as shown in the Figure 4.6. Porosities have been found in the fusion zone of Waspaloy welded by laser welding [94], however they have not been reported in electron beam welds of Waspaloy. Also, such porosities were not found in this study in other alloys welded using the same welding parameters.

Fusion zone microfissuring was found to be intergranular and interdendritic in nature. Although most of the cracking was observed to be in the HAZ (Figure 4.7a), some cracks were also found to be confined to the fusion zone only (Figure 4.7b). Also, unlike HAZ microfissures, which were predominantly found in the shoulder region of the weld; fusion zone microfissures were also found to be located further down towards the bottom of the weld. Fusion zone cracks were also visibly wider than the cracks in the HAZ.

Fusion zone cracking was identified as solidification cracking on the basis of the morphology and intergranular nature of the cracks. Solidification cracking occurs due to the presence of thin liquid film at the grain boundaries during final stages of solidification when tensile stresses begin to develop. Such a thin film can exist during the last stages of solidification because of enrichment or depletion of certain alloying elements from the liquid, increasing its solidification range and/or by presence of low melting point eutectics [78, 95]. According to the Pellini's strain theory of hot cracking [83], presence of intergranular continuous thin film during the last stages of solidification can cause tearing of the grains/dendrites. A thin film would essentially be incapable of accommodating the thermal contraction strain during solidification.

Figure 4.8 shows a secondary electron micrograph of HAZ microfissure in as-welded Waspaloy. The observed microfissuring was always intergranular in nature and associated with resolidified products. An example of a HAZ crack is shown in Figure 4.9 with liquated and resolidified products observed in and around it. Figures 4.9 b and c shows SEM EDS spectra of the resolidified liquid and the precipitates at the crack edges

respectively. Their average chemical composition was determined by semi-quantitative SEM EDS analysis, and is given in Table 4.1. The precipitate at the crack edge was identified as Ti rich MC type carbide particle. Due to the small size of the precipitates and large interaction volume, the contribution from the matrix could not be completely eliminated in the determination of the chemical composition. The resolidified liquid on the liquated grain boundary was enriched in Ti when compared to the composition of the matrix in the adjacent grain (Figure 4.9b, Table 4.1). The resolidified liquid on the HAZ grain boundary had composition similar to that of interdendritic region in the fusion zone. Constitutionally liquated Ti and Mo rich MC type carbides were also found in the HAZ microstructure near the fusion zone boundary, an example of which is shown in Figure 4.10. Constitutional liquation of TiC in Waspaloy was first recognized by Owczarski et al.[21], and has been observed since then in many other investigations [18, 22] on weldability in Waspaloy. Constitutional liquation and segregation of low melting point minor alloying elements on the grain boundaries are considered to be the primary reasons for liquation in this alloy [22].

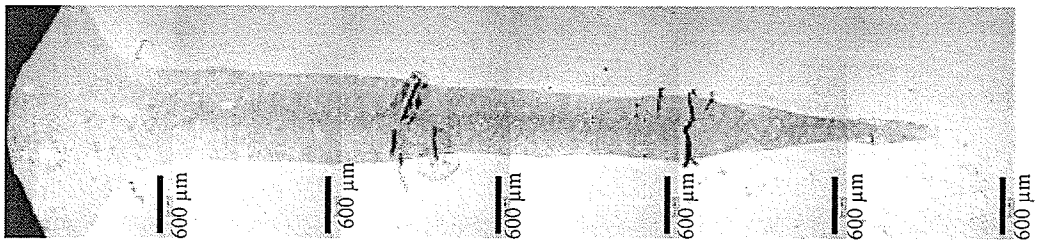

Figure 4.3: Weld cross-section of Waspaloy showing a typical nail head EB weld profile

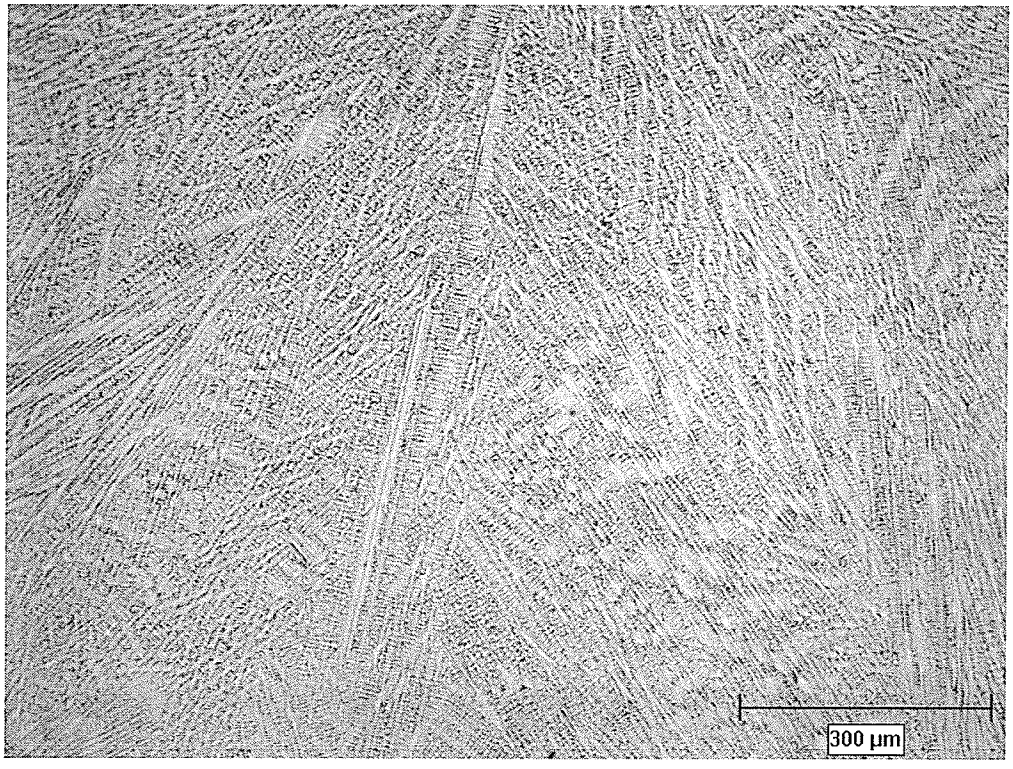

Figure 4.4: Cellular dendritic microstructure of the fusion zone of Waspaloy

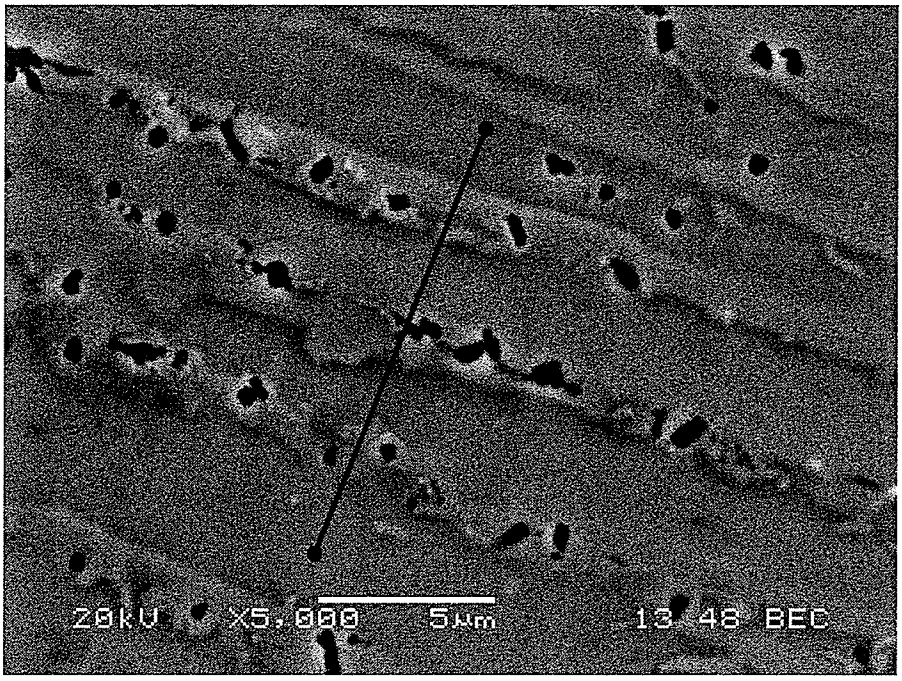

(a)

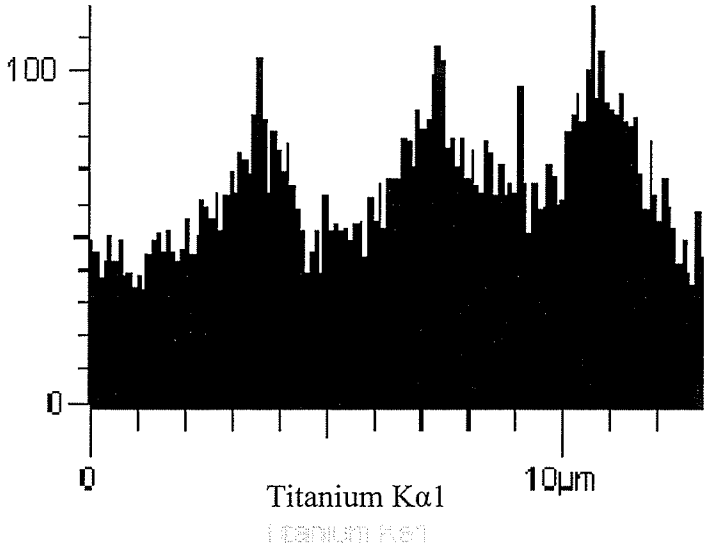

(b)

Figure 4.5: (a) Back scattered image of the fusion zone microstructure showing compositional contrast between the dendritic core and interdendritic regions (b) X-ray line scan showing variation of Titanium in the fusion zone

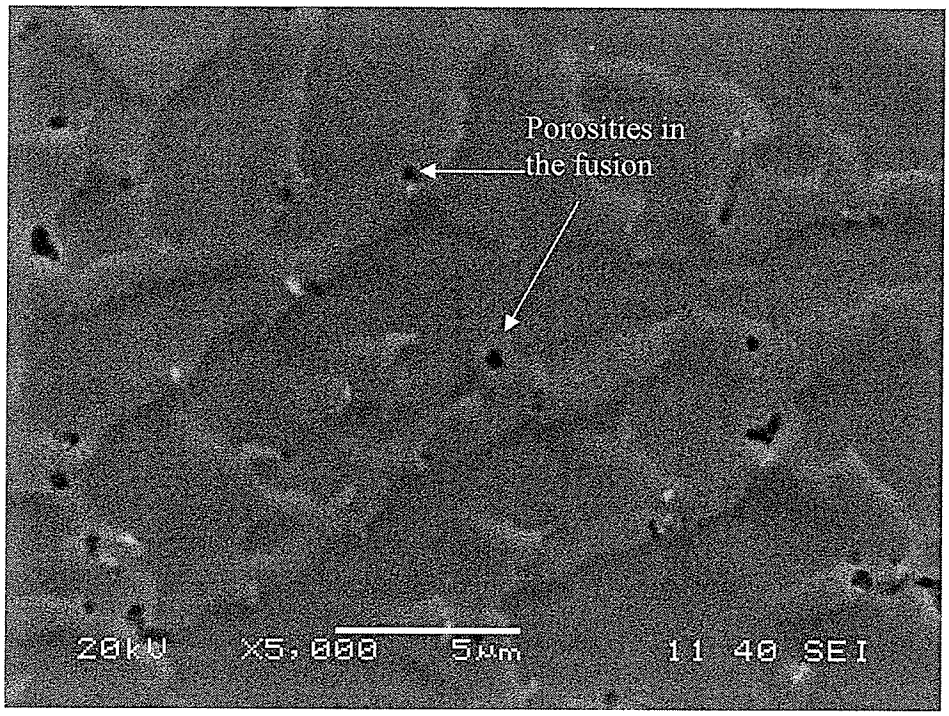

Figure 4.6: Fusion zone microstructure of Waspaloy showing porosities in the interdendritic region

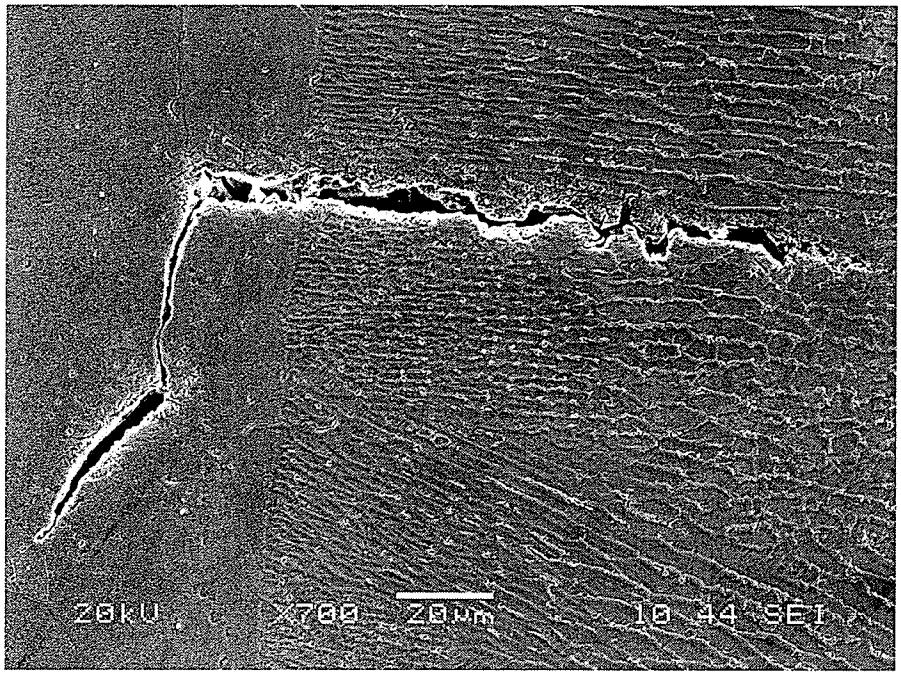

(a)

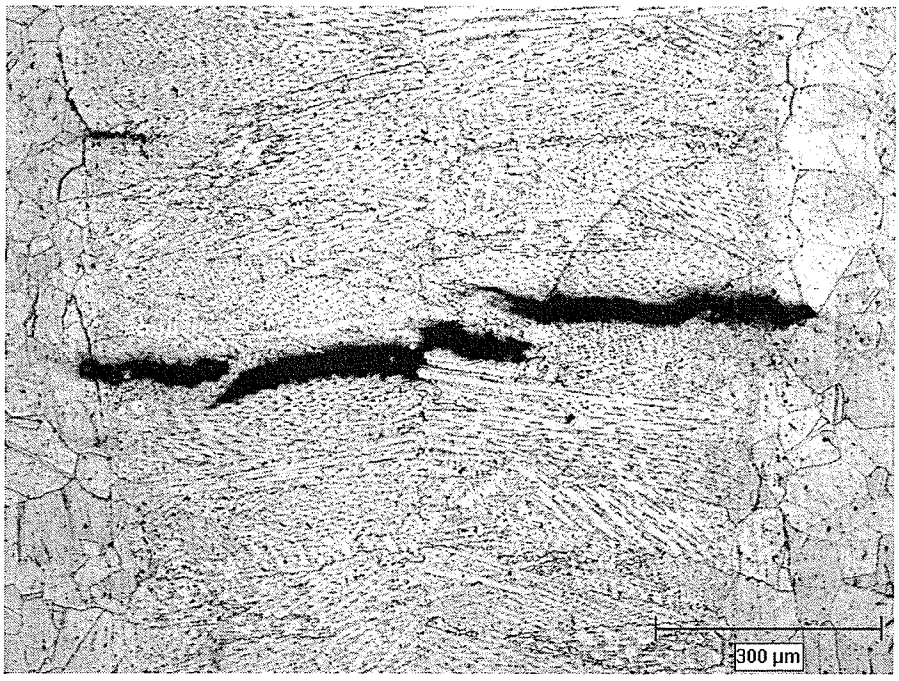

(b)

Figure 4.7: Fusion zone microfissuring (a) extending into the HAZ (b) restricted to the fusion zone

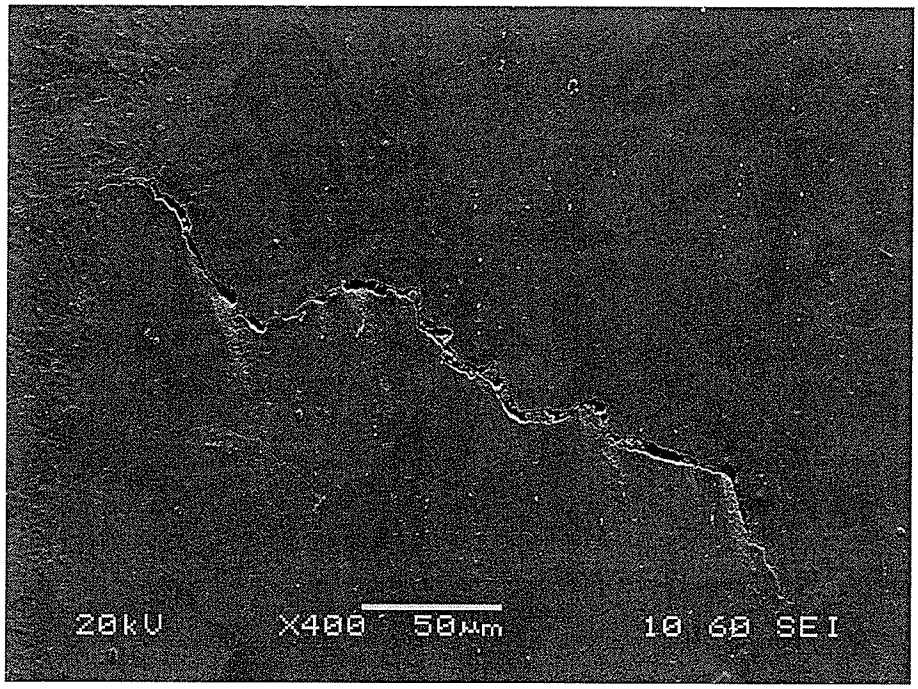

Figure 4.8: Liquation cracking in the HAZ of Waspaloy

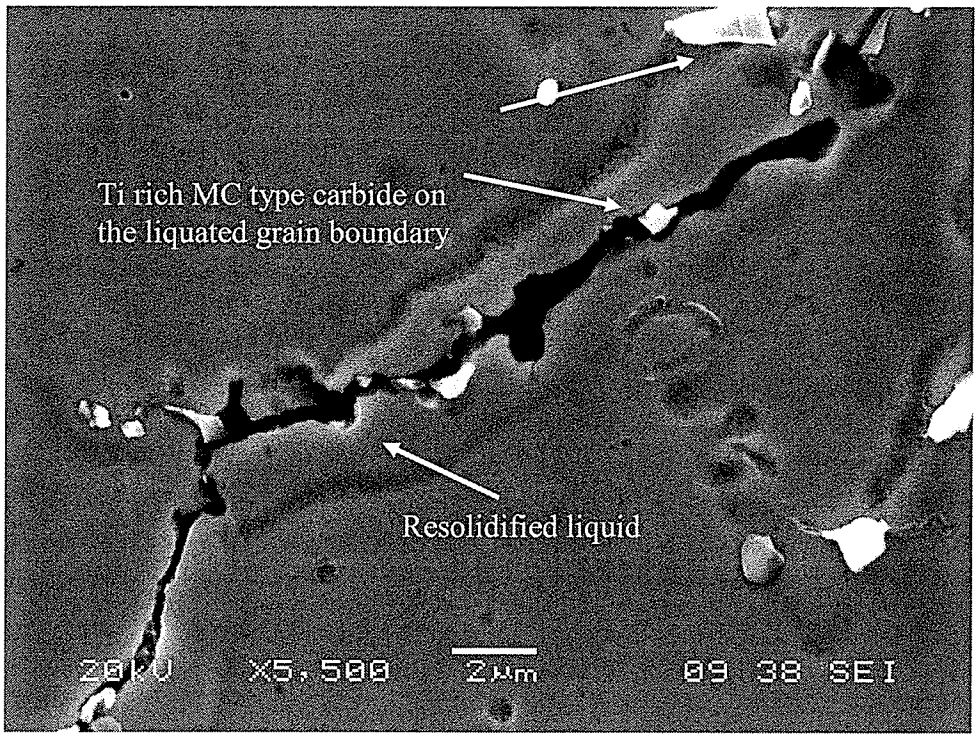

(a)

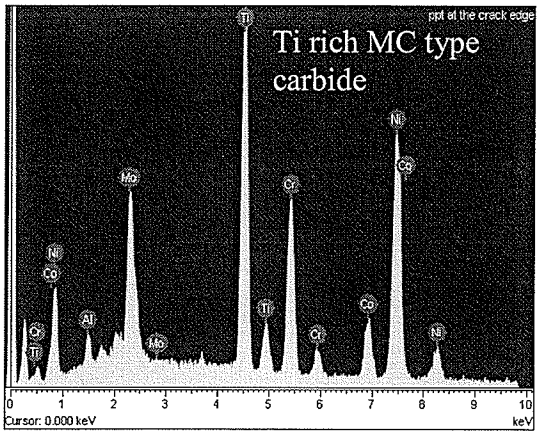

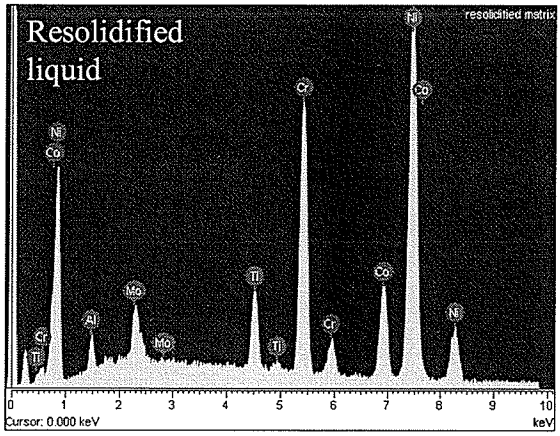

(b) (c)

Figure 4.9: (a) HAZ microfissure with liquated and resolidified products (b) EDS spectrum from Ti rich MC type carbide (c) EDS spectrum from resolidified liquid

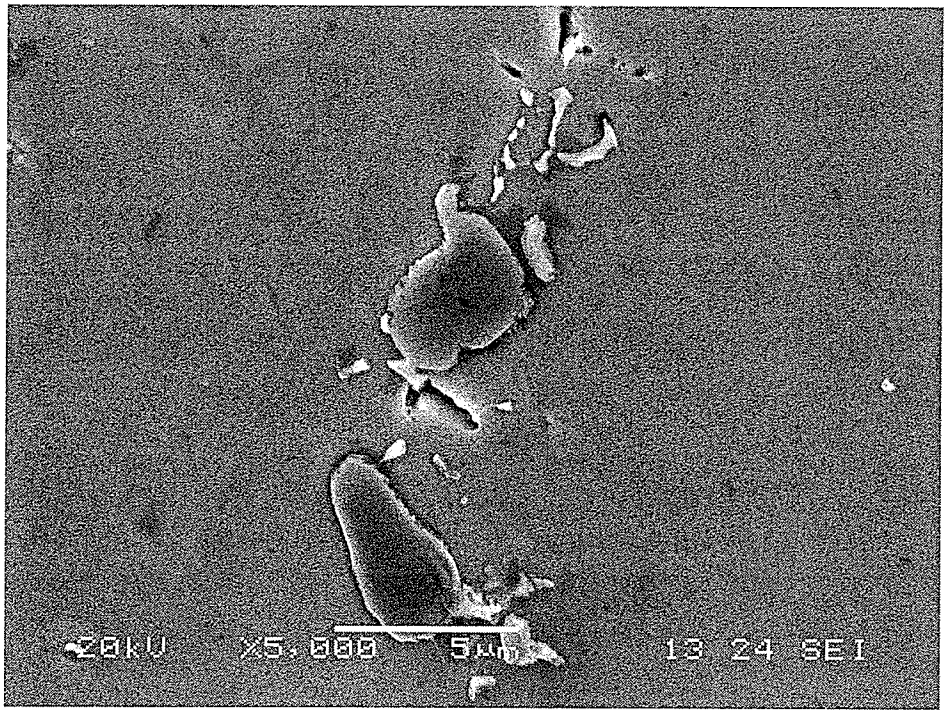

Figure 4.10: Constitutional liquation of Ti-Mo rich MC type carbides in the HAZ of Waspaloy

Table 4.1: Average composition as determined by SEM semi-quantitative EDS analysis of various phases observed in Waspaloy

Composition (wt%)	Al	Ti	Cr	Co	Ni	Mo	W
Ti – Mo rich MC type carbide	0.20 ± 0.36	57.16 ± 15.61	6.89 ± 4.74	2.98 ± 2.26	12.77 ± 8.04	19.99 ± 5.42	0.11 ± 0.37
Ti rich MC type carbide on the liquated grain boundary in the fusion zone	1.45 ± 0.06	21.52 ± 0.18	14.56 ± 0.17	8.42 ± 0.21	40.89 ± 0.31	13.16 ± 0.22	-
Resolidified liquid on the grain boundary	1.58 ± 0.07	4.14 ± 0.10	20.06 ± 0.22	13.09 ± 0.27	57.06 ± 0.35	4.07 ± 0.19	-
Matrix composition	1.28 ± 0.03	2.83 ± 0.04	19.39 ± 0.11	13.48 ± 0.13	58.75 ± 0.17	4.28 ± 0.09	-

Solidification of the liquid in the fusion zone and that of the intergranular liquid in the HAZ can be explained by the solidification sequence in Waspaloy proposed by Murata et al. [96]. Accordingly, the first solid to form from liquid is in the form of γ dendrites. The elements with partition coefficient less than unity in the Ni austenitic γ matrix get preferentially partitioned into the solidifying liquid. In the present study, it was found that interdendritic regions were enriched in Ti. The terminal reaction is in the form of γ + MC type carbide eutectic reaction which was reported to occur at 1240°C [96]. Ti rich MC type carbides and resolidified Ti enriched supersaturated γ were observed in the fusion zone as well as in HAZ of Waspaloy.

4.1.3 Microstructure of Inconel 718

Pre-weld microstructures - 950 °C/1hr and 1050 °C/1hr followed by water quenching:

Inconel 718 plates were pre-weld heat treated at 950°C and 1050°C for 1 hour and water quenched. Figures 4.11 and 4.12 show the microstructures after the solution heat treatments at 950°C and 1050°C, respectively. The alloy in the 950°C/1hr heat treated condition had a grain size of 48 ± 7 μm and hardness value of 223 ± 4 VPN. 950°C/1hr is the standard commercial solution heat treatment for Inconel 718 and it dissolves the principal strengthening phases, γ'' and γ', but the temperature is below the solvus temperature of orthorhombic δ phase. Needle like δ phase was distributed throughout the microstructure, especially along the grain boundaries. Delta phase was also present intragranularly on the twin boundaries. The microstructure also consisted of randomly distributed Nb rich MC type carbide and Ti rich carbides (or carbonitrides). The grain size increased to 100 ± 14 μm and the hardness reduced to 165 ± 3 VPN after heat treatment at 1050°C for 1 hour. The most noticeable change in the microstructure was the complete dissolution of δ phase after this heat treatment. The amount and distribution of carbide particles was not significantly different. The grain size and hardness in both the conditions are listed in Table 4.2.

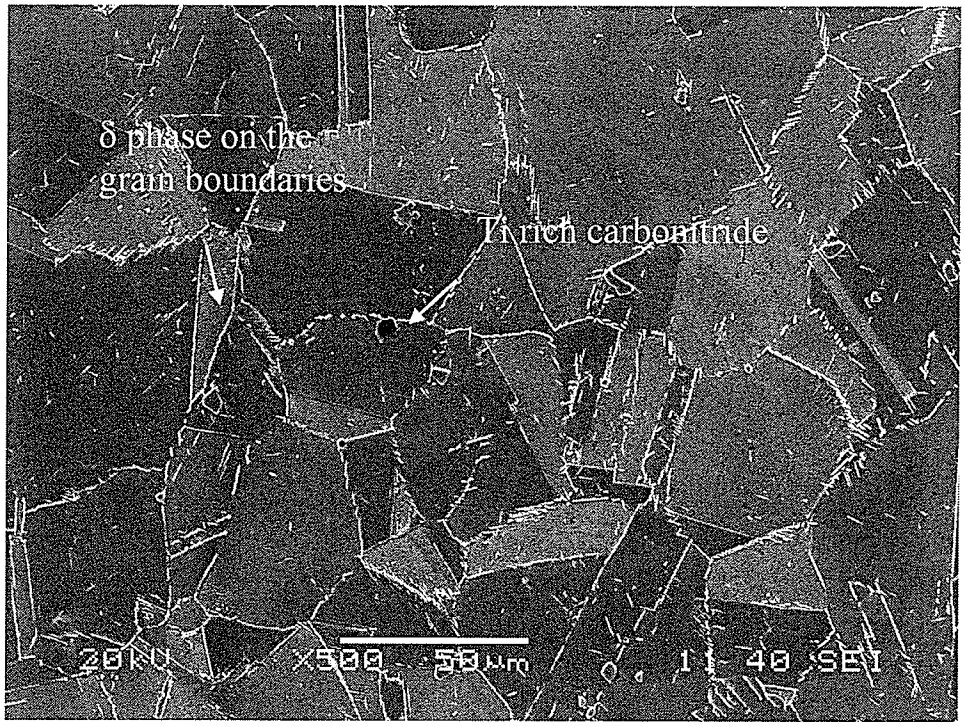

Figure 4.11: Microstructure of Inconel 718 after 950°C/1hr heat treatment

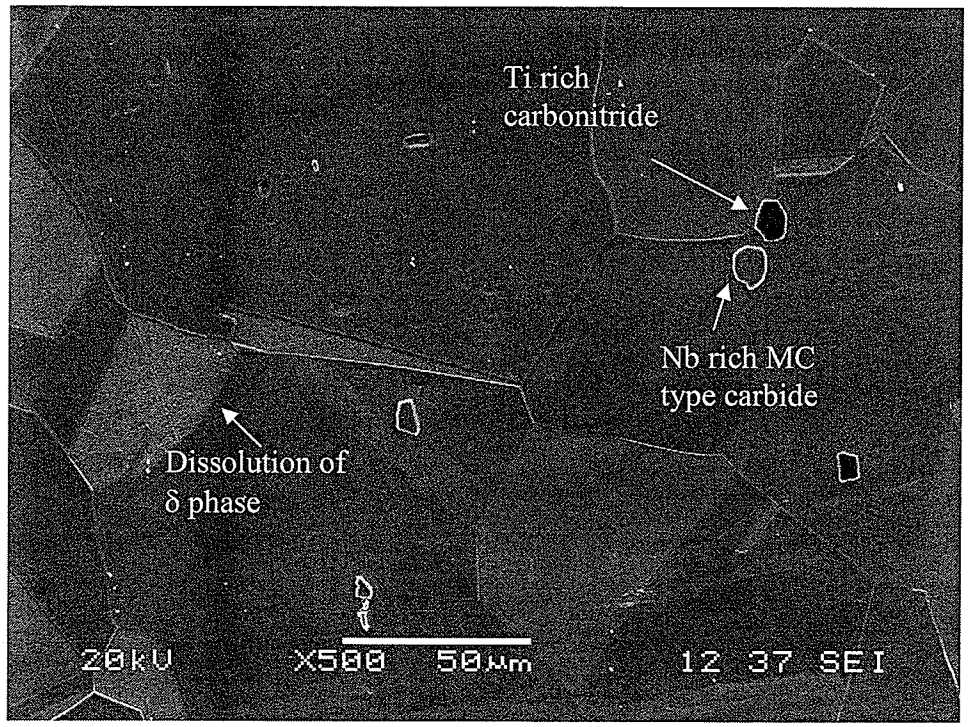

Figure 4.12: Microstructure of Inconel 718 after 1050°C/1hr heat treatment

Microstructure of welds and microfissuring in HAZ:

Electron beam autogenous welds were made on the solution treated Inconel 718 with sharp focus using the parameters described in Chapter 3. A typical weld profile is shown in Figure 4.13. Fusion zone cracking was not observed in either of the heat treated conditions.

Figure 4.14 shows an optical micrograph of the fusion zone of Inconel 718. The microstructure consisted of fine cellular dendritic structure. The atomic number contrast between the dendritic core and the interdendritic regions can be seen in the BSE image in Figure 4.15. The x-ray line scans (Figure 4.16) confirmed that there was significant enrichment in Nb and Mo in the interdendritic regions whereas, other elements did not show any considerable variation. Few Nb rich MC type carbides and Ti rich carbonitride particles were also seen to be randomly distributed in the fusion zone microstructure. The interdendritic phases present in the fusion zone were Laves phases. The presence of Laves phase in the fusion zone of Inconel 718 has been found in earlier studies also [97, 98].

Table 4.2: Grain size and hardness values for Inconel 718 before and after welding

Heat Treatment	Grain size (μm)	Pre-weld heat treated/Base metal hardness (VPN)	Fusion zone hardness (VPN)
950°C/1hr + WQ	48 ± 7	223 ± 4	245 ± 4
1050°C/1hr + WQ	100 ± 14	165 ± 3	241 ± 5

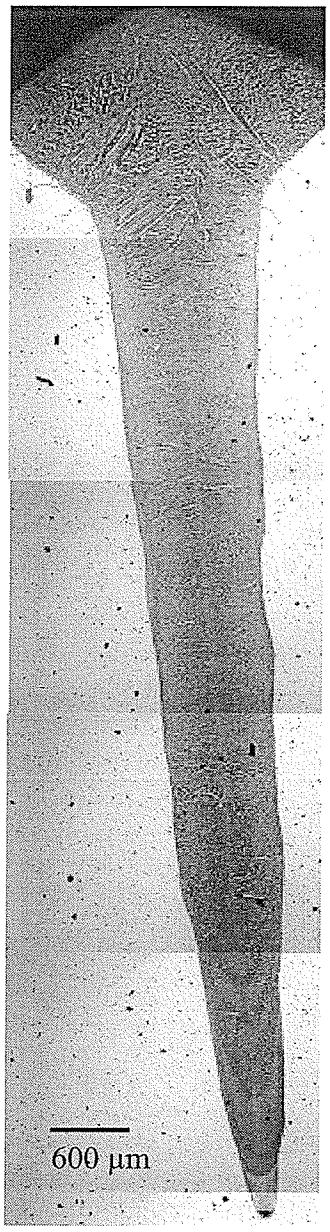

Figure 4.13: Nail head shape weld profile obtained after EB welding of Inconel 718

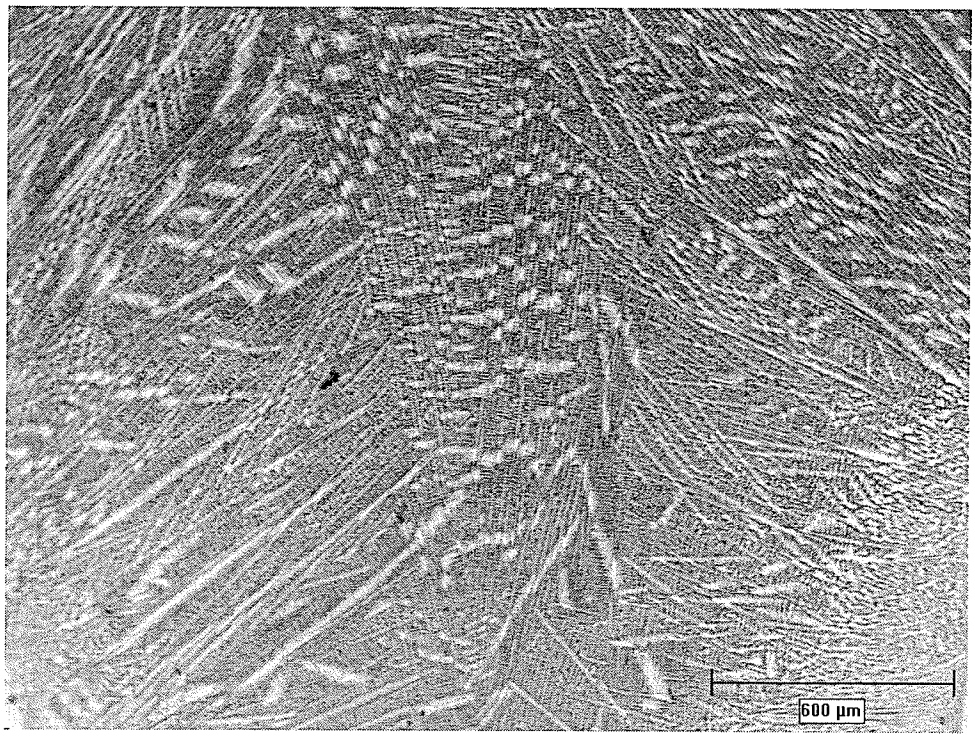

Figure 4.14: Fusion zone microstructure of Inconel 718

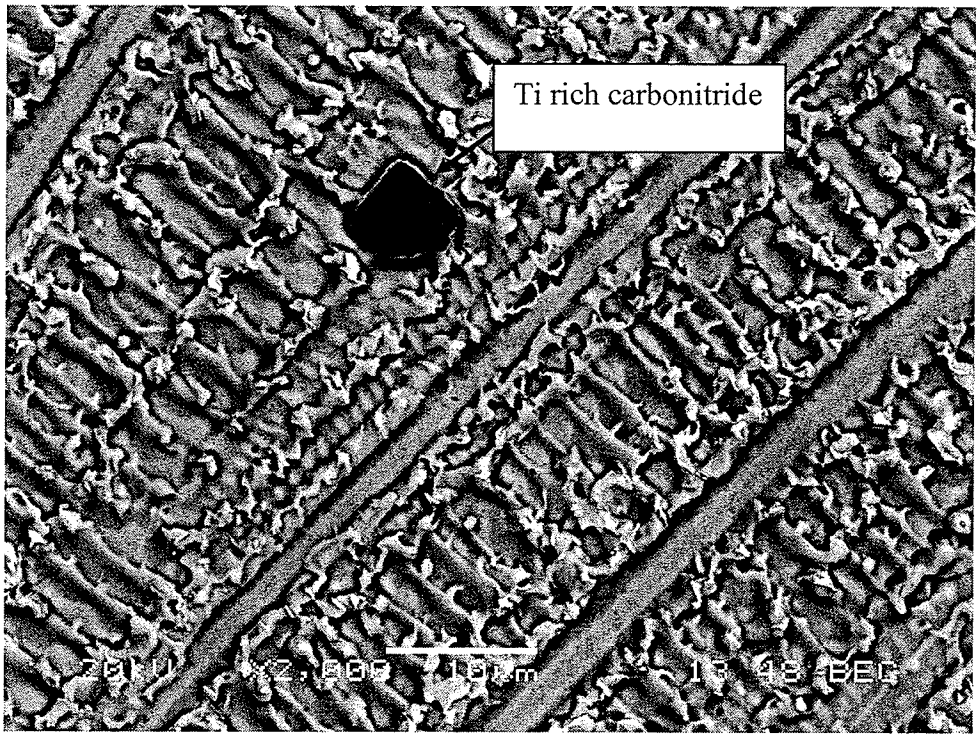

Figure 4.15: Back scattered electron image of the fusion zone microstructure of Inconel 718 showing compositional contrast

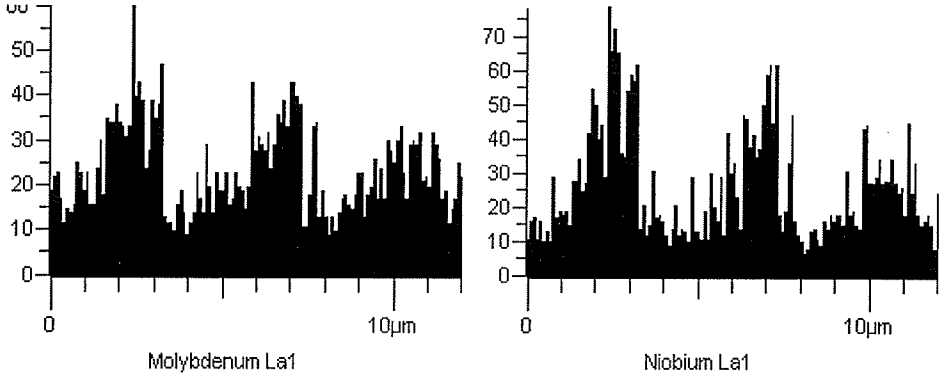

Figure 4.16: (a) X-ray line scan corresponding to Mo (b) x-ray line scan corresponding to Nb in the fusion zone of Inconel 718

Liquation cracking was observed in the HAZ of Inconel 718 welds in both the heat treated conditions. Although metallurgically and morphologically the cracking after both the heat treatments appeared similar, cracking in the 950°C treated material was significantly less than that observed in the 1050°C heat treated condition. The results of crack measurements are further discussed in section 4.3 while comparing weldability of different alloys. Cracking was always intergranular and resolidified products were associated with cracks. Most of the cracking was confined to the shoulder region of the weld with considerable backfilling. Figure 4.17a shows a BSE image of a HAZ crack observed in the 1050°C heat treated condition with resolidified products on the edges. This figure also shows constitutionally liquating Nb carbide particles near the fusion zone boundary and in the backfilled region of the crack. SEM EDS analysis of the particles (Figure 4.17b) showed an x-ray peak corresponding to boron, however the amount of boron or carbon could not be quantified with the available software. The EDS spectrum corresponding to the constitutionally liquated NbC particle at the fusion zone boundary is shown in Figure 4.17b. Semi-quantitative analysis was also carried out on the cracked grain boundary. The resolidified regions were mostly rich in Nb and Fe (Figure 4.18), suggesting them to be resolidified Laves phase. Laves + γ eutectic has been previously reported to form near the cracked boundaries by a study on characterization of welded microstructure by Vincent [36]. Similar observations were made by Huang et al. in their study on cast Inconel 718 [45, 92] .

Presence of Laves phase in the interdendritic region and on the resolidified HAZ boundary can be explained by understanding the solidification sequence of Inconel 718.

Two different solidification sequences have been reported in the literature. Knorvosky et al. [99] proposed that solidification of the liquid begins by formation of pro-eutectic gamma dendrites followed by the non-invariant eutectic reaction $L \rightarrow \gamma$ + MC carbide at 1257°C. It was reported that this reaction would deplete the liquid of its carbon and niobium and that would cause the liquid composition to re-enter the L + γ region. In their study they reported that the terminal eutectic reaction would be in the form of $L \rightarrow \gamma$ + Laves non-invariant reaction at around 1185°C. Radhakrishnan et al. suggested [58] that the eutectic reaction of γ + MC carbide could not be a non-invariant reaction and would rather occur over a temperature range. The final solidification reaction would then be a monovariant reaction of ternary type involving γ, MC carbides and Laves phase. Although both MC type carbides and Laves phases have been reported to form with γ [36, 100], the major phase during terminal reaction was Laves phase which might account for more than 90 % of the terminal solidification products [36].

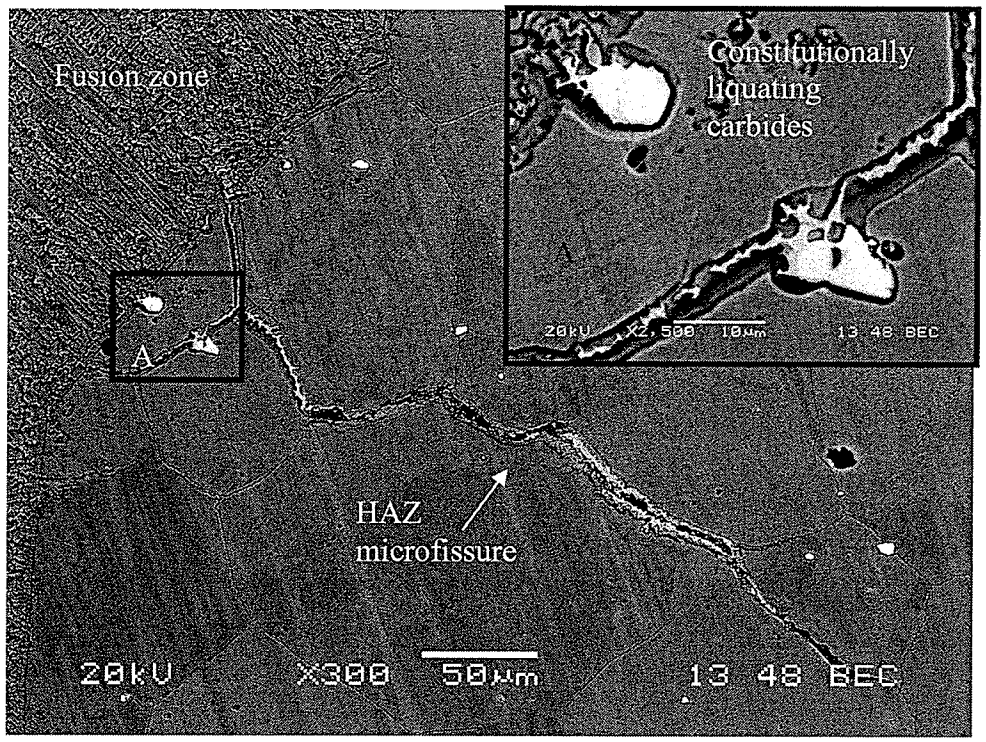

(a)

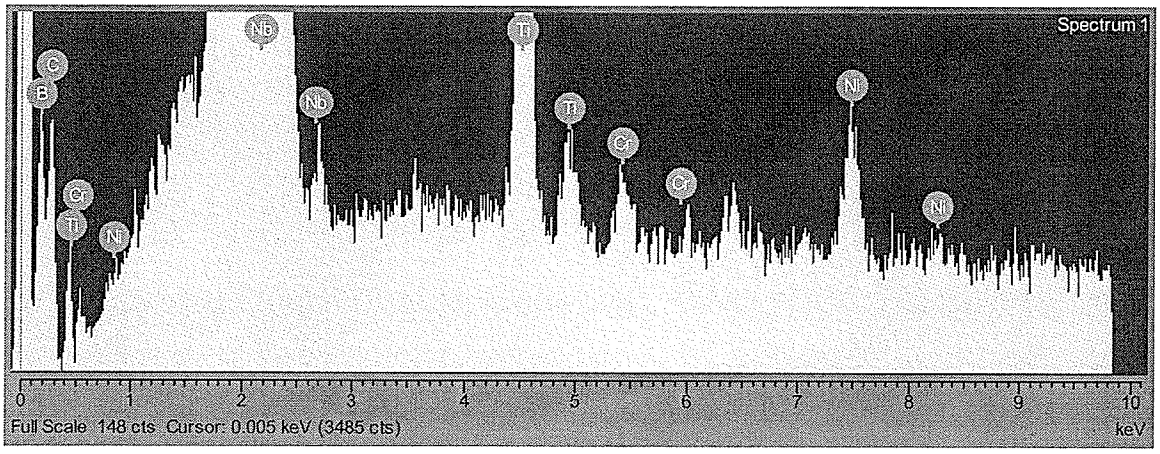

(b)

Figure 4.17: (a) HAZ microfissuring in Inconel 718, inset shows liquating MC type carbides on the grain boundaries and near the fusion zone (b) EDS spectrum corresponding to the liquating carbides showing boron peak

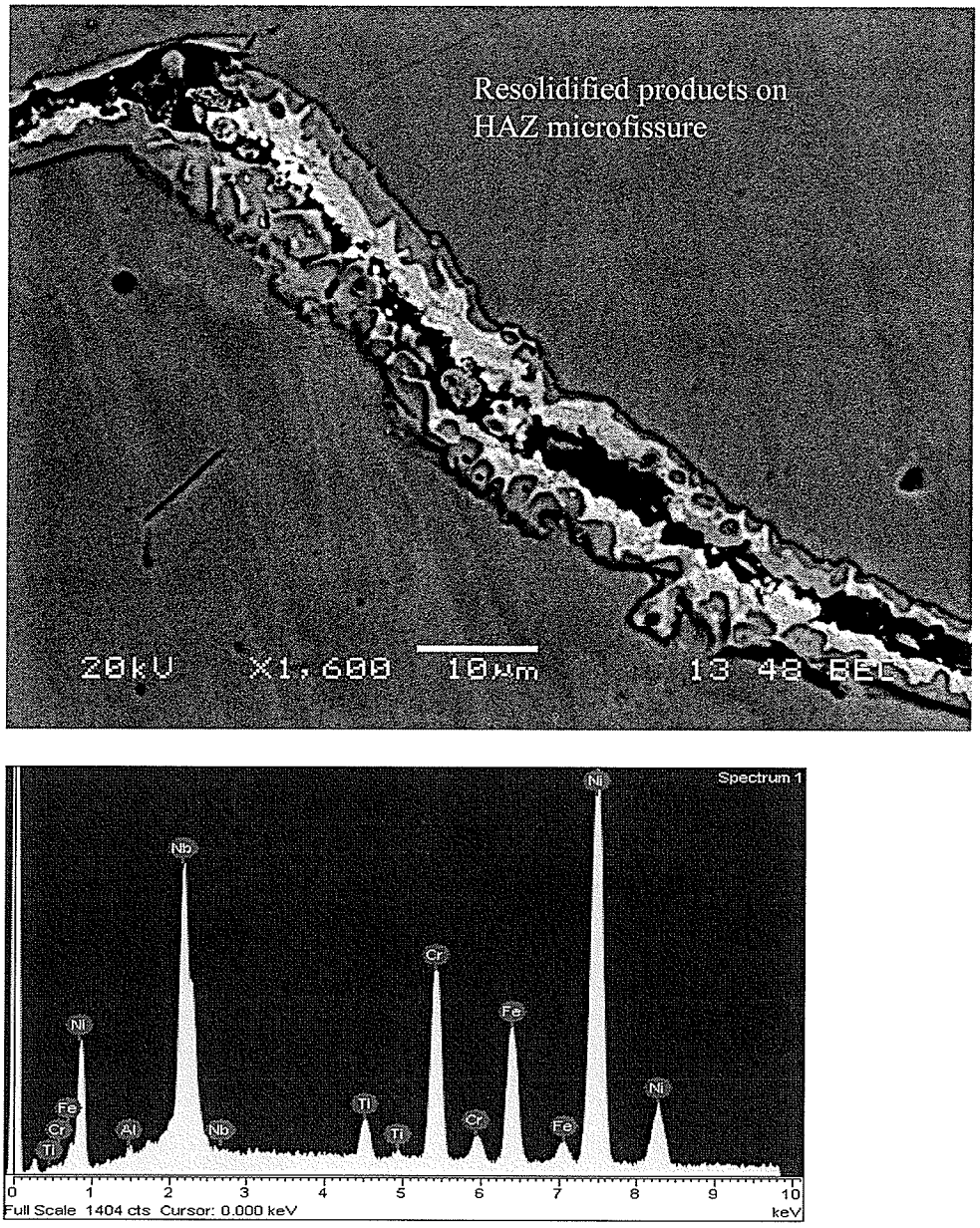

Figure 4.18: (a) Resolidified products on the cracked HAZ grain boundary (b) EDS spectrum associated with the products indicating them to be Laves + γ eutectic

4.1.4: Microstructural analysis of HC 49 718 Plus alloy

Pre-weld microstructures - 950 °C/1hr and 1050 °C/1hr followed by water quenching:

Microstructure of HC 49 718 Plus alloy was essentially similar to the microstructure of the lower B and P alloy HC 20, which will be discussed in detail in the next section of this chapter. In the 950°C heat treated material the microstructure consisted of randomly distributed Nb rich MC type carbides and Ti rich carbonitrides. Needle like δ phase was also present mostly on the grain boundaries but sometimes also as intra-granularly. The grain size after the 950°C heat treatment was 42 ± 7 μm and the hardness value was 293 ± 8 VPN. Grain size and hardness values before and after welding are also listed in Table 4.3. The microstructure after 1050°C heat treatment did not significantly change the amount and distribution of carbides and carbonitrides. The major difference, when compared to 950°C heat treatment (Figure 4.19), was the dissolution of the grain boundary δ phase and the increase in grain size as shown in Figure 4.20. The grain size was 116 ± 7 μm and the hardness was 201 ± 10 VPN after this heat treatment. Chemistry of the phases was determined by semi-quantitative SEM EDS analysis and is listed in Table 4.4. Chemical composition of δ phase could not be determined accurately by SEM/EDS analysis due to its thin needle like morphology.

Microstructure of welds and microfissuring in HAZ

Solution heat treated HC 49 plates were welded with a sharp focus electron beam and the parameters were the same as those that were used for other alloys in this study. Like Inconel 718, no cracking was seen in the fusion zone. Liquation cracking was observed in the HAZ in both the pre-weld heat treated materials.

Fusion zone microstructure with fine cellular dendritic structure was also similar to that observed in Inconel 718 and HC 20 718 Plus alloy. The fusion zone hardness was 248 ± 6 VPN. Figure 4.21 shows an optical micrograph of the fusion zone and the HAZ of HC 49. HAZ liquation crack is clearly evident under the nail head weld profile of the alloy. The presence of resolidified products is seen on the liquated grain boundaries in Figure 4.22. These products were identified as Laves + γ eutectic. Constitutional liquation of Nb rich MC type carbides was also seen in the HAZ of HC 49. HAZ microfissuring in HC 49 also increased with the increase in the pre-weld heat treatment temperature.

The microstructural evolution and the mechanisms of cracking in HC 49 718 Plus were found to be similar to that of HC 20 718 Plus alloy and are discussed in the next section.

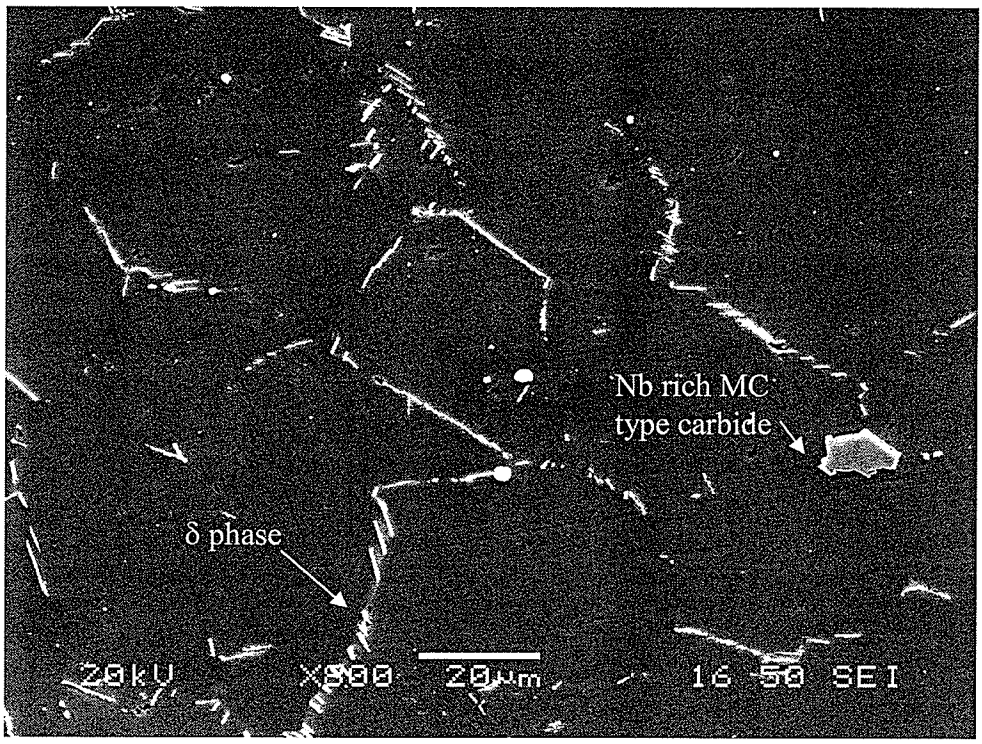

Figure 4.19: Microstructure of HC 49 after 950°C heat treatment condition

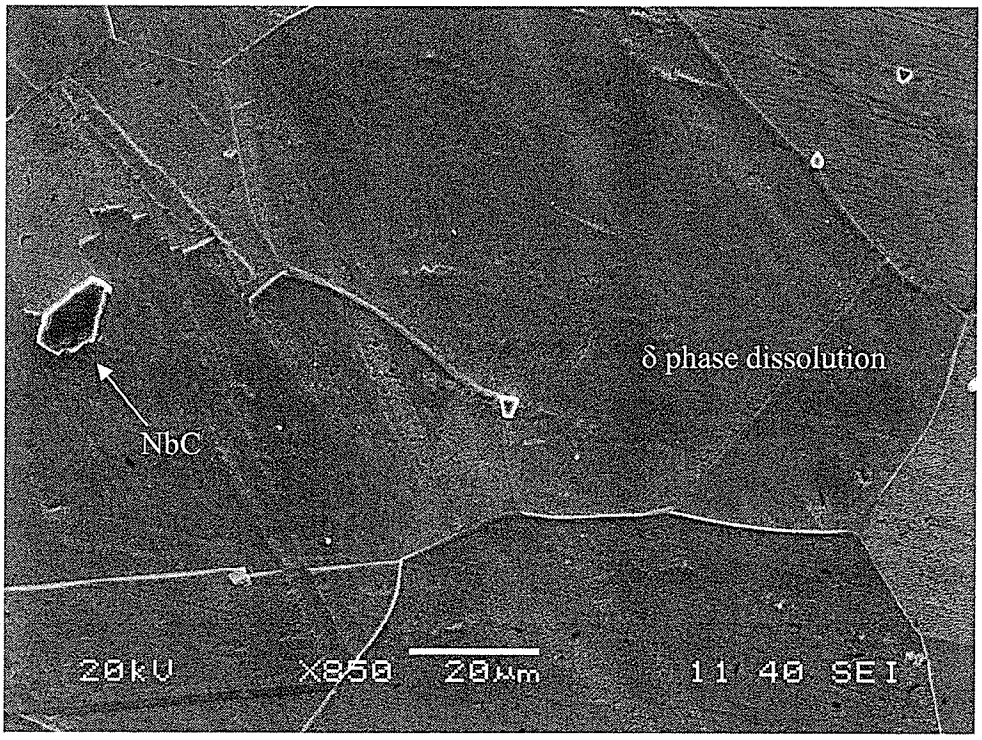

Figure 4.20: Microstructure of HC 49 after 1050°C heat treatment condition

Table 4.3: Grain size and hardness values for HC 49 before and after welding:

Heat Treatment	Grain size (μm)	Pre-weld heat treated/Base metal hardness (VPN)	Fusion zone hardness (VPN)
950°C/1hr + WQ	42 ± 7	293 ± 8	257 ± 6
1050°C/1hr + WQ	116 ± 7	201 ± 10	248 ± 6

Table 4.4: Average composition as determined by SEM semi-quantitative EDS analysis of various phases observed in HC 49 alloy

wt%	Ni	Cr	Fe	Nb	Co	W	Mo	Ti	Al
Nb rich MC type carbide	2.38 ± 0.08	0.82 ± 0.17		89.74 ± 0.39				7.05 ± 0.46	
Ti rich carbonitride	2.02 ± 0.95	1.14 ± 0.47		21.75 ± 1.91	0.63			71.91 ± 1.19	
δ phase	53.15 ± 0.26	16.83 ± 0.20	9.41 ± 0.17	4.69 ± 0.18	10.05 ± 1.13	1.05 ± 0.13	2.36 ± 0.09	0.71 ± 0.02	1.30 ± 0.03
Matrix	53.15 ±0.26	16.83 ± 0.20	9.41 ± 0.17	4.69 ± 0.18	10.05 ± 0.13	1.05 ± 0.13	2.36 ± 0.09	0.71 ± 0.02	1.27 ± 0.03

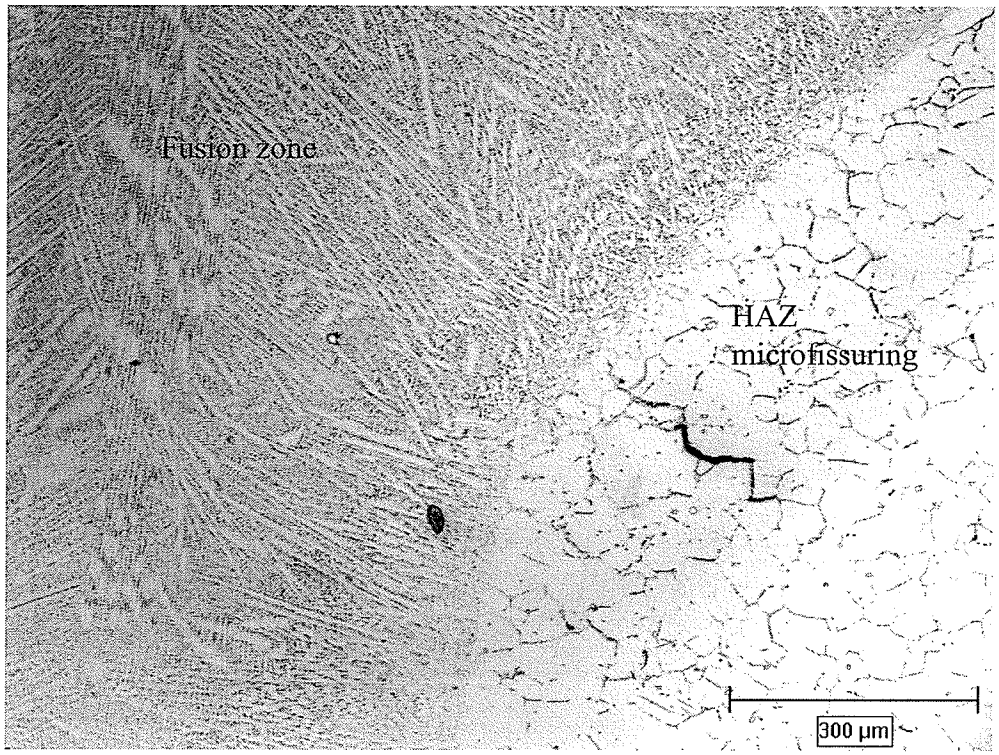

Figure 4.21: Fusion zone and HAZ of HC 49 718 Plus alloy with intergranular liquation cracking

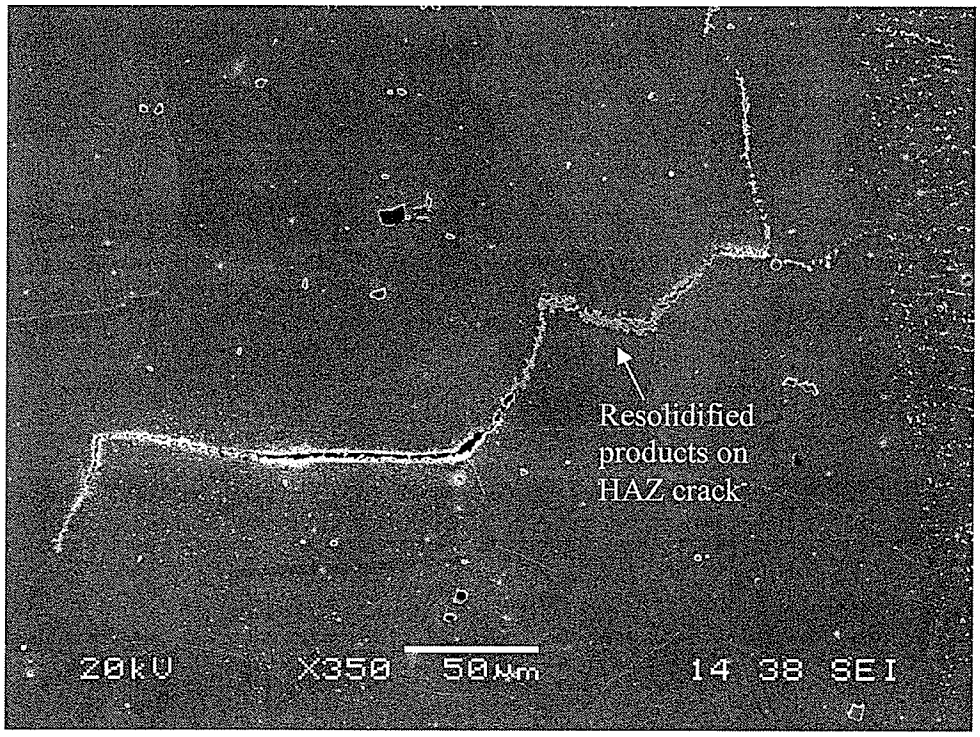

Figure 4.22: Intergranular HAZ microfissuring in HC 49 718 Plus alloy

4.2: Microstructure of HC 20 718 Plus

4.2.1 Introduction

This section discusses the microstructural characterization of 718 Plus alloy, HC 20 ALLVAC® 718 PLUS™ (HC 20 718 Plus) with normal B (30 ppm) and P(60 ppm) contents. As mentioned earlier HC 20 718 Plus is a newly developed nickel base superalloy strengthened by ordered face centered cubic (FCC) intermetallic γ′ phase, and only limited information is available about its physical metallurgy and weldability. Hence this project was initiated to understand the microstructural development and the electron beam welding response of this new alloy. The alloy was characterized in the as-received condition, pre-weld heat treated conditions and in the as-welded condition. The two pre-weld heat treatments selected were

1. 950°C for 1 hour followed by water quenching
2. 1050°C for 1 hour followed by water quenching.

Figure 4.23 shows an optical micrograph of HC 20 718 Plus in the as-received hot-rolled condition which consists of FCC austenitic γ matrix with an average grain size of 50 μm. The average composition of the matrix, as determined by the SEM EDS analysis, is given in Table 4.5. It is basically a Ni-Cr-Fe-Co solid solution with considerable amounts of Nb and Mo.

The microstructure consisted of randomly dispersed MC type carbides and carbonitrides with round-to-blocky morphology in γ matrix, as shown in Figure 4.23. MC type idiomorphic carbides and carbonitrides are found in many commercial superalloys, and

form during solidification. These carbides are generally called primary carbides to differentiate them from other carbides that may form during aging heat treatments, which are referred to as secondary carbides. Primary carbides do not change drastically during forging, heat treating or during long time service at high temperatures [101]. In alloys containing niobium, the predominant MC type carbide is NbC while in alloys containing Ti as a strengthener, the carbide is TiC [101]. SEM/EDS analysis of the MC type carbide precipitates (Table 4.5) showed them to be mainly Nb-rich with some Ti content. Carbonitride particles were found to be rich in Ti and Nb. X-ray peaks corresponding to carbon and nitrogen were identified in the spectra obtained from these precipitates, but due to software limitation it was not possible to quantify their concentrations and hence they were excluded from the quantification process. Similar compositions have been reported for carbides in other Ni-Fe base superalloys [2, 5, 102].

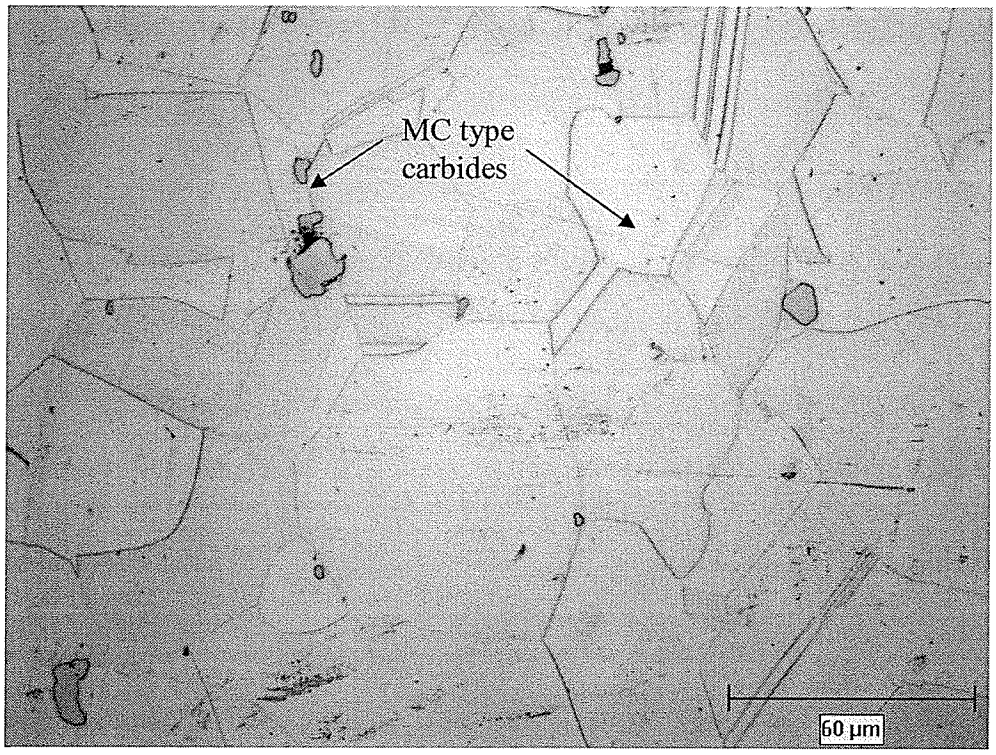

Fig. 4.23: Microstructure of the as received 718 Plus alloy

Table 4.5: Average chemical composition of the phases observed in the as received HC 20 718 Plus determined by SEM/EDS analysis:

Elements (wt%)	Al	Ti	Cr	Fe	Co	Ni	W	Nb	Mo	V	Si
Matrix comp.	1.32 ± 0.08	0.77 ± 0.09	18.98 ± 0.15	9.59 ± 0.14	9.82 ± 0.05	50.46 ± 0.16	4.97 ± 0.09	2.53 ± 0.05	1.59 ± 0.23	–	–
Nb rich carbides	–	6.89 ± 1.32	0.94 ± 0.61	0.58 ± 0.41	0.83 ± 0.45	1.96 ± 1.13	–	90.11 ± 2.89	–	–	–
Ti rich carbonitrides		70.11 ± 3.05	1.45 ± 1.13	1.08 ± 0.82	1.04 ± 0.66	1.97 ± 1.89	–	25.60 ± 2.07	–	0.45 ± 0.34	–

Other phases, such as hexagonal island shaped Laves phase and needle/plate shaped orthorhombic δ phase are commonly observed in Ni-Fe base Inconel 718, and in Incoloy 900 series [45, 102, 103]. Laves phase forms during solidification of ingot and can be eliminated by high temperature homogenization and thermo-mechanical processing of wrought Inconel 718 and 718 Plus type of alloys. It was therefore not observed in the microstructure of the as-received material. Homogenization of 718 Plus alloys is done at temperatures above the solvus of δ phase, and rapid cooling from these temperatures would have prevented the precipitation of δ phase during cooling, which would explain its absence in the as-received microstructure of 718 Plus alloy.

Optical microscopy and scanning electron microscopy did not reveal the presence of γ′ or γ″ particles, and hence thin foils were examined in a TEM. Due to high density of precipitate particles and the excessive coherency strain contrast around individual particles, the individual γ′ particles could not be easily resolved in the bright field image (Fig 4.24a). Hence selected area diffraction patterns (SADPs), obtained in [001] orientation were examined, an example of which is shown in inset of Figure 4.24a. The SADPs revealed the presence of γ′ superlattice reflections. The dark field image of fine γ′ particles using (100) reflections of γ′ particles is shown in Figure 4.24b. Diffraction patterns with [001] zone axis should also reveal the presence of γ″ by the presence of (1½0) superlattice reflections of γ″ phase [27]. The absence of these superlattice reflections due to γ″ phase suggests that γ″ phase was not present in the as–received microstructure. The hardness value of the as-received material was 383 VPN.

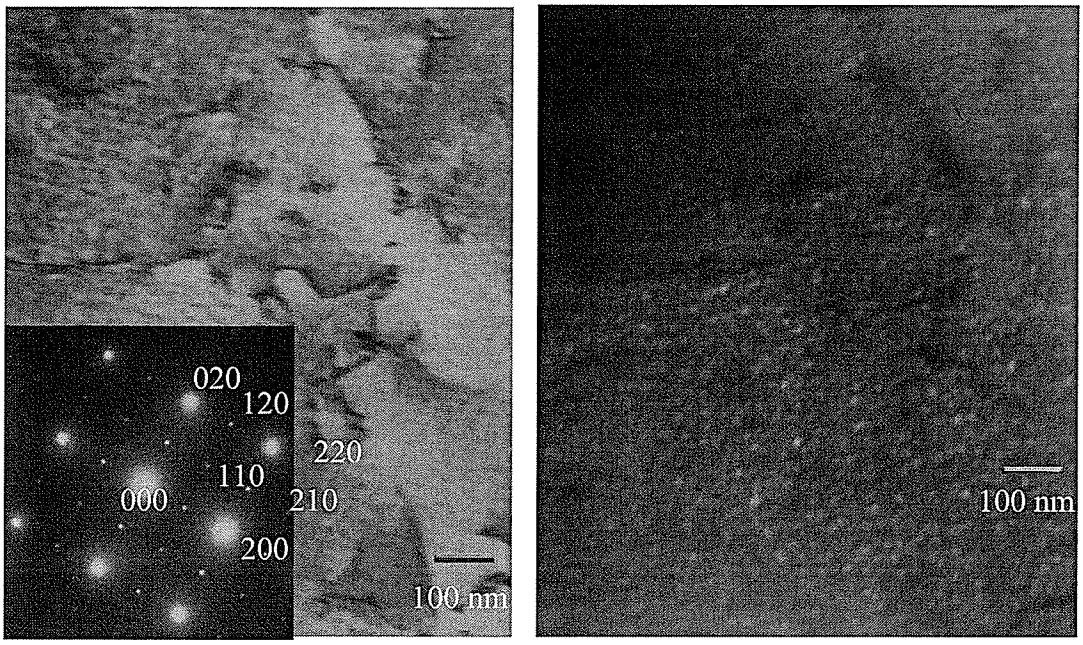

(a) (b)

Fig.4.24: As received 718 Plus alloy (a) Bright field image of the matrix and electron diffraction pattern in the direction parallel to [001] zone axis (b) Selected area diffraction pattern showing the presence of fine γ′ phase.

4.2.2 Solution treated microstructure:

The as-received material was solutionized at 950°C for 1 hour in argon atmosphere followed by water quenching. The grain size of the material did not change significantly and was 54±6 μm. Figure 4.25 shows a SEM micrograph of 950°C solution heat treated material with various phases. Besides Nb rich MC type carbides and Ti rich carbonitride particles, needle like δ phase was observed in the microstructure of the solution treated alloy. The nickel and nickel-iron base superalloys that are precipitation strengthened by γ′′ phase are susceptible to δ phase formation, which can evolve during processing or during service [32]. In Inconel 718, the metastable phase, γ′′, can transform to the δ phase at temperatures above 650°C. Essentially two modes of δ phase precipitation are observed in Inconel 718 type alloys: (i) heterogeneous precipitation on grain and twin boundaries (ii) intergranular precipitation, often in association with stacking faults located within pre-existing γ′′ precipitates [32]. The precipitation of δ phase occurs in the temperature range of 750°C to 1050°C [104]. Delta phase precipitated during the pre-weld heat treatment as it was not present in the as-received microstructure. Delta phase precipitation is fastest in the temperature range of 900-950°C, as determined by the TTT diagram derived for 718 Plus alloys[72]. Delta phase was observed on the grain boundaries and occasionally on the twin boundaries within the grains. Due to the thin needle shaped morphology of δ phase, it was difficult to accurately determine its chemical composition without eliminating the contribution from the matrix elements. The composition as determined by SEM and high resolution TEM EDS Inca software, is reported in Table 4.6.

Like in as-received alloy, it was difficult to observe γ' or γ'' using optical or scanning electron microscopy, although TEM revealed the presence of γ' particles as shown in the dark field image, Figure 4.26b. The bright field image did not clearly show the particles due to coherency strain contrast. The SADP, shown in the inset of Figure 4.26a, revealed the superlattice reflections pertaining to γ' particles only. No superlattice reflections were observed from γ'' particles. It is to be noted that the standard solution heat treatment of 950°C only results in partial dissolution of the principal strengthening phase, γ'. The hardness value decreased by almost 100 VPN from the 383 VPN of as-received material to 295 HV.

Solution heat treatment at 1050°C increased the grain size of the material to approximately by 75 μm after one hour heat treatment and dissolved the δ phase (Figure 4.27). The amount and distribution of the carbides and carbonitrides however did not change significantly. Electron diffraction patterns in [001] zone axis direction from the thin foils made from the solutionized alloy did not show any superlattice reflections corresponding to either γ' or γ'' phase (Figure 4.28) , because 1050°C is above the solvus temperature for these particles in this alloy [72]. The hardness value (196 VPN) was lower than that of the 950°C solution heat treated material by 100 VPN.

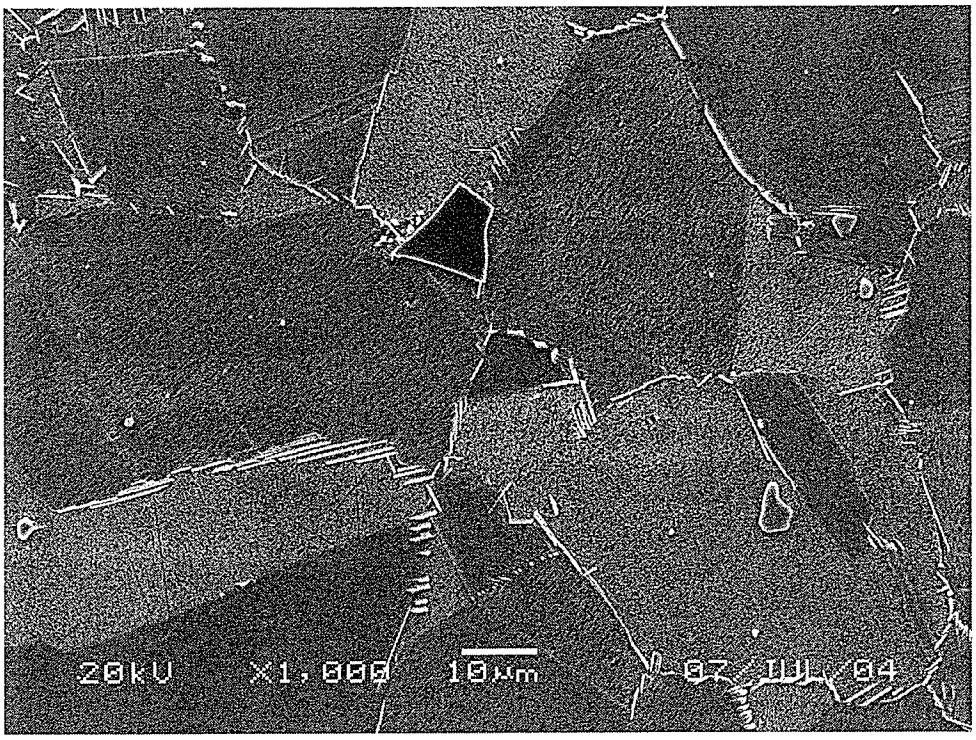

Figure 4.25: Microstructure of the 950°C/1hr solution heat treated alloy

Table 4.6: Chemical composition of δ phase as determined by SEM and TEM EDS analysis with Inca software

Wt (%)	Nb	Al	Ti	Cr	Fe	Co	Ni	W
SEM	4.62 ± 0.16	1.23 ± 0.12	0.76 ± 0.06	17.54 ± 0.32	9.20 ± 0.46	9.90 ± 0.38	54.17 ± 0.99	1.52 ± 0.22
HRTEM	20.99 ± 1.81	1.91 ± 0.02	3.03 ± 0.01	2.37 ± 0.93	2.04 ± 0.22	5.55 ± 0.46	64.13 ± 2.48	-

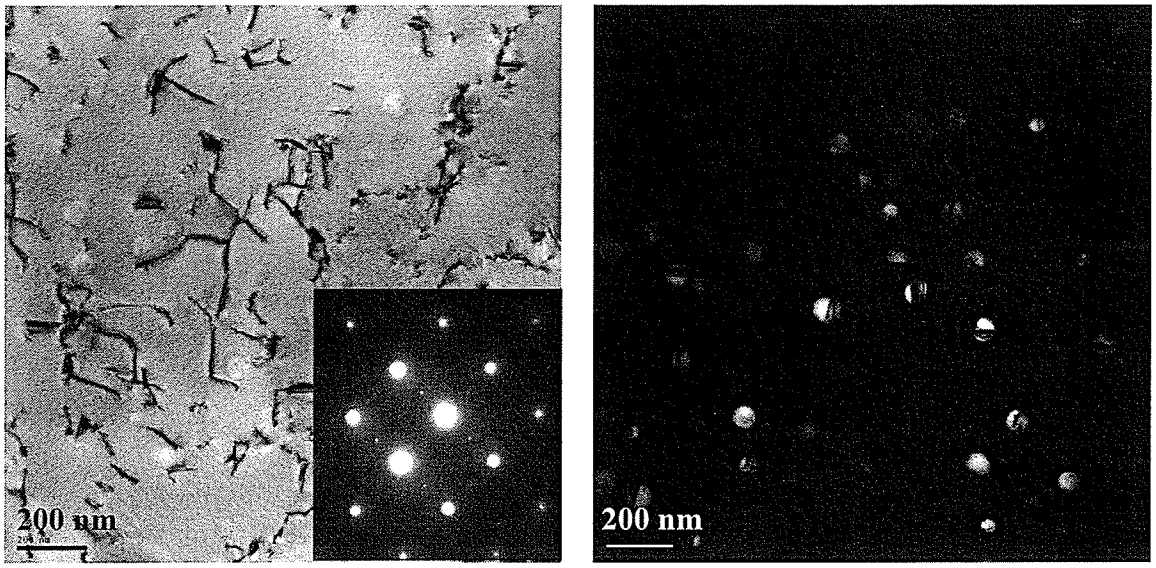

(a) (b)

Figure 4.26: 950°C solution heat treated alloy (a) bright field image of the matrix and electron diffraction pattern in the direction parallel to [001] zone axis (b) selected area dark field image showing γ′ precipitates

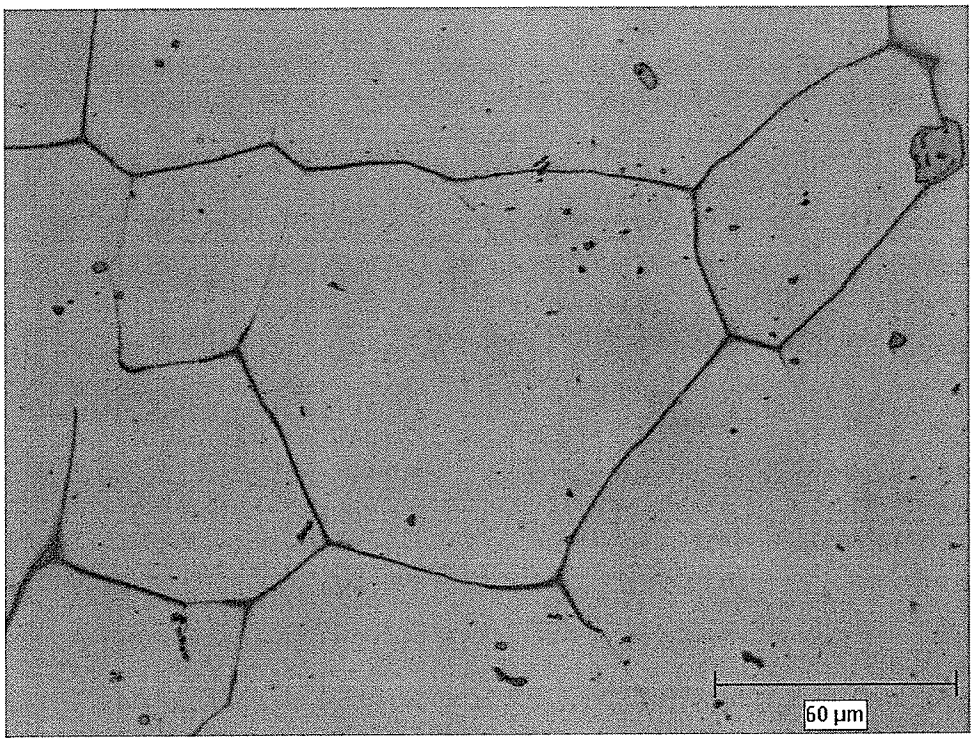

Figure 4.27: Microstructure of the 1050°C/1hr solution treated alloy

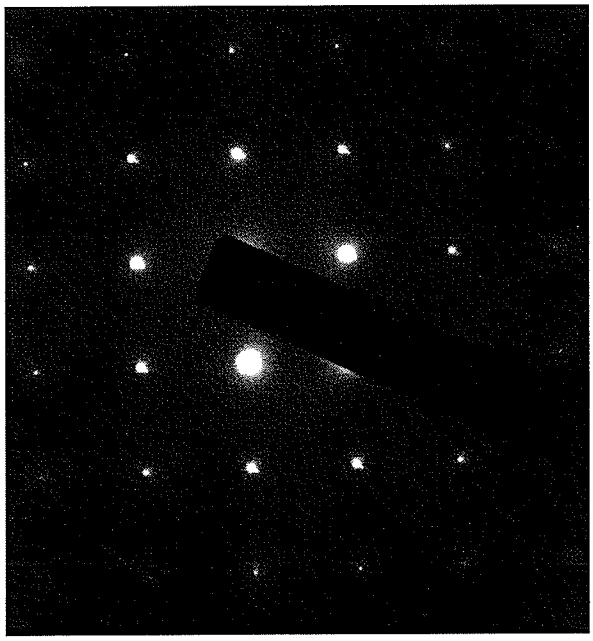

Figure 4.28: Selected area diffraction pattern in the direction parallel to the [001] zone axis, showing no superlattice reflections corresponding to γ′ phase

4.2.3 Fusion zone microstructures

Integrity and properties of weldments are generally influenced by the microstructure that develops in the fusion zone during rapid solidification of the weld. Fusion zone in superalloys typically consists of gamma dendrites and microsegregation induced secondary solidification constituents in the interdendritic regions. Microsegregation and non-equilibrium phase transformations during weld metal solidification can result in the formation of undesirable intermetallic constituents and chemical inhomogeneity in the fusion zone, which are detrimental to the mechanical properties of the welded structure [98, 105]. Presence of certain intermetallic constituents may also deplete the matrix of its useful strengthening alloying elements and adversely affect the high temperature performance of the components. Post weld heat treatments (PWHTs) are generally applied to homogenize the as-welded microstructure, to relieve the residual welding stresses, and also to re-strengthen the welds in precipitation hardening type of alloys. Development of suitable PWHT, however, depends primarily upon the initial microstructure of fusion and heat affected zones, and, a proper understanding of them is essential.

Figure 4.29a shows a low magnification optical micrograph of the nail head shaped weld profile of the electron beam weld. Porosities were frequently observed at the bottom of the welds, which are often present in partial penetration electron beam welds (inset of Fig.4.29a). No fusion zone cracking was observed in the alloy, but cracking was observed to occur in HAZ in the shoulder region under the nail head as shown in Fig.

4.29b, which will be discussed later. The hardness of the fusion zone was measured to be 248 VPN.

Figure 4.30 shows a high magnification optical micrograph of the fusion zone consisting of cellular dendritic microstructure with an average secondary dendrite arm spacing of 4 μm. Higher magnification back-scattered SEM micrograph exhibited a significant compositional contrast, as shown in Figure 4.31, suggesting segregation of elements in the fusion zone. The chemical composition of at least 15 points in the dendrite core region near the fusion zone boundary, where the solidification begins, was determined by EPMA/WDS and the average values are given in Table 4.7. It is seen that Nb and Ti undergo significant change in their concentration as compared to their concentration in the matrix, followed by Al, Fe and W. Other elements like Cr, Co, Mo undergo only a minor change in their concentration whereas Ni concentration remained close to its matrix concentration.

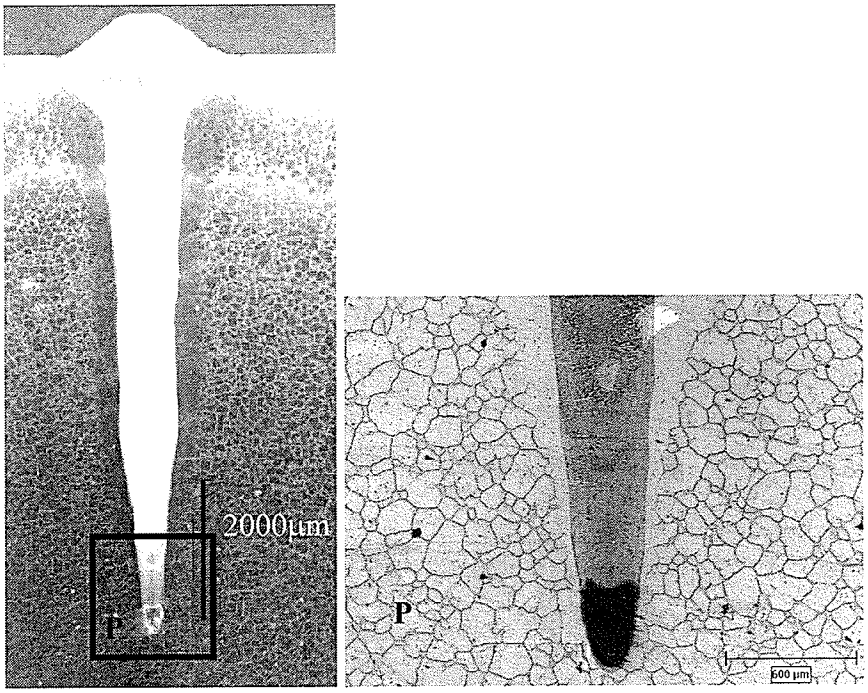

(a) (b)

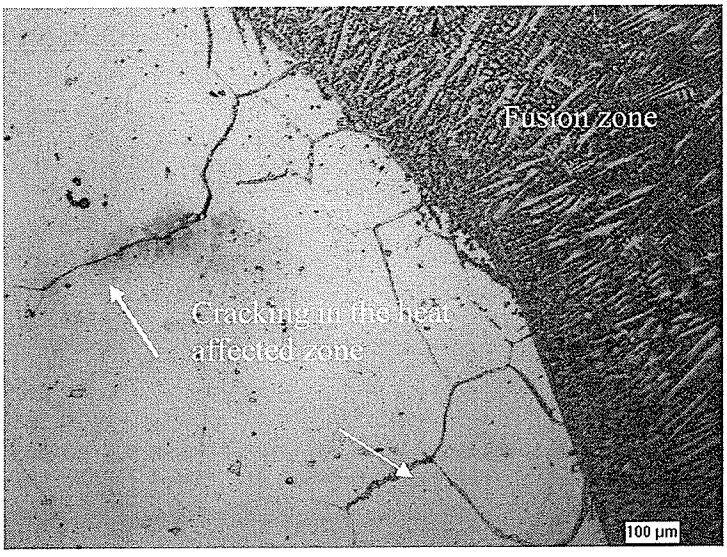

(c)

Fig. 4.29: (a) Typical nail head type of weld profile of 718 Plus welds with porosity at the bottom (b) Heat affected zone cracking as observed in the shoulder region of the nail head shaped weld profile of 718 Plus alloy; no cracking observed in the fusion zone.

Elemental distribution/partition coefficient k, which is defined as the ratio of the concentration of a solute in solid to that in the liquid in equilibrium with it was determined from this data. According to Fleming[106], under equilibrium conditions, neglecting undercooling at the dendrite tips and assuming complete mixing in the liquid and no diffusion in the solid, the solute re-distribution can be described by the following equation.

$C_s = kC_0[1-f_s]^{(k-1)}$ [Equation 1] ;

where C_s is the solid composition at the solid/liquid interface, C_0 is the nominal composition and f_s is the volume fraction of the solid. At the start of solidification $f_s = 0$, and the first solid to form from the liquid (the dendrite core), will have a composition of kC_0. Therefore, the ratio between dendrite core composition and the nominal composition will yield the partition coefficient at the beginning of solidification. Another assumption made in this approach is that the diffusion of solute elements in the solid is negligible. Solid state diffusion depends on the cooling rate and the dendrite arm spacing. The cooling rate in the fusion zone can be estimated by secondary dendrite arm spacing, which is controlled by the temperature gradient, G and the solidification velocity, R, as given by the following general relationship [107];

$d_2 = A / (GR)^n$ [Equation 2];

$d_2 = A / (V)^n$ [Equation 3];

where d_2 is the secondary dendrite arm spacing (μm), V is the cooling rate (°K/s), A is a material constant and n is a constant with a value between 0.25 and 0.5. For Inconel 718, Meharabian et al.[108] calculated the values of A and n to be 141 and 0.4, respectively. Substituting these values and the dendrite arm spacing of 4μm in equation 3, an average

cooling rate of approximately 7377 °K/s was obtained. Such a rapid cooling rate would significantly reduce the solute diffusion in the solid, thus justifying the use of equation 1 which assumes no diffusion in the solidified liquid. The k values calculated from the nominal composition and the dendrite core composition are listed in Table 4.7. It is seen that Nb and Ti have k values considerably less than unity, which implies that these elements segregated strongly into interdendritic liquid during solidification. Aluminum and Mo also segregated into interdendritic regions but to a smaller degree compared to Nb and Ti. Chromium, Co, Fe and W have k values greater than unity indicating that they selectively partitioned into the dendrite core.

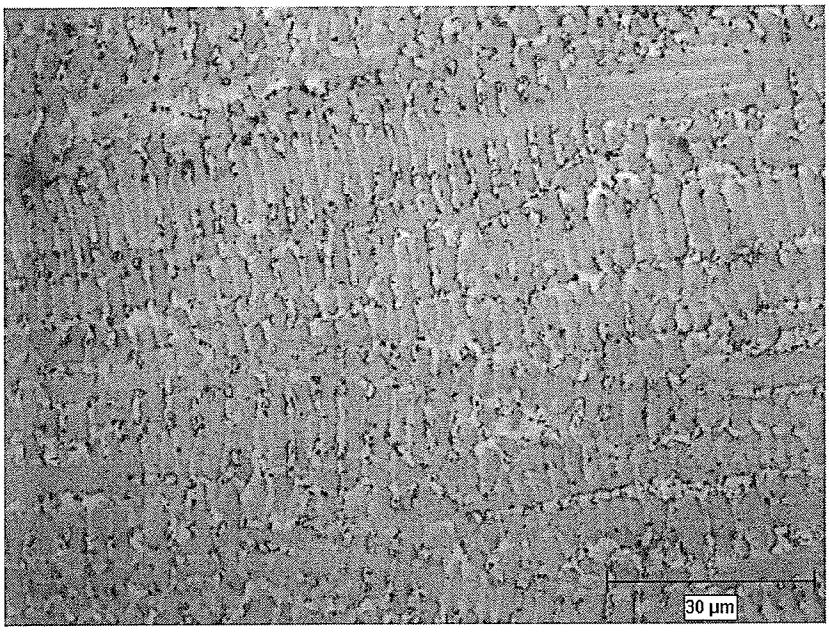

Fig. 4.30: Cellular-dendritic microstructure of the fusion zone of the 718 Plus alloy

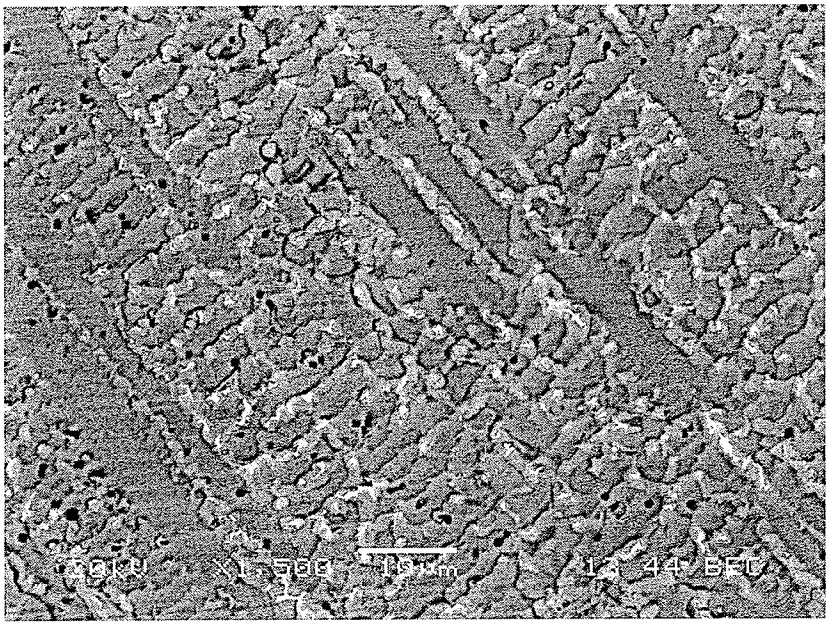

Fig. 4.31: Back scattered electron SEM image showing contrast in the interdendritic region suggesting segregation

Table 4.7: Composition of the dendritic core as determined by EPMA analysis and calculated partition coefficients

Elements	Cr	Co	Ni	Fe	Al	Ti	Nb	Mo	W	Si
Dendrite core composition (wt%)	18.37	9.55	51.92	10.39	1.42	0.59	3.97	2.66	1.15	–
k **718 Plus**	**1.02**	**1.06**	**1.00**	**1.11**	**0.94**	**0.80**	**0.72**	**0.99**	**1.11**	–
k [100] IN 718	*1.03*	–	*1.00*	*1.04*	*1.00*	*0.63*	*0.48*	*0.82*	–	*0.67*
k [109] Incoloy 909	–	*1.05*	*0.97*	*1.06*	*0.95*	*0.76*	*0.58*	–	–	–
k [110] In 738 LC	*0.98*	*1.09*	*1.03*	–	*0.92*	*0.69*	*0.58*	*0.87*	–	–

By comparing the values of k obtained in this study with those reported in previous studies on other superalloys [100, 109, 110], it is seen that the segregation behaviour of Nb, Ti, Fe and Co is similar to that observed in other alloy systems, where Nb and Ti were found to segregate in the interdendritic region and Fe and Co segregated in the dendrite core region. These values are also listed in Table 4.7 for comparison. Microsegregation in the weld zone is also strongly influenced by the type of welding process and parameters, such as the weld heat input and the subsequent cooling rates. Welding processes like gas tungsten arc welding (GTAW) with higher heat inputs and slower cooling rates showed more segregation of Nb (smaller k values) in Inconel 718 when compared to electron beam welding (EBW) with lower heat input and comparatively faster cooling rate [98].

Figure 4.32 shows a typical SEM micrograph of the fusion zone. The interdendritic regions consisted of irregular shaped second phase particles distributed in a semi-continuous fashion. SEM/EDS micro chemical analysis of these second phase particles showed them to be enriched in Nb, Ti and Mo. Few undissolved primary carbides were also observed in the fusion zone. Primary carbides, depending upon the size and the type of welding process, can survive the high temperature weld thermal cycle without dissolving completely. Similar observations were made for coarse fusion zone carbides in TIG welded cast Inconel 738 alloy [110]. These carbides were often found to be associated with eutectic type products as shown in Figure 4.33. The Nb, Ni, Mo, Fe and Cr X-ray maps of the back scatter image shown in Figure 4.34 are shown in Figs 4.34b, 4.34c, 4.34d, 4.34e and 4.34f respectively. These images corroborate the EPMA results

and suggest that the secondary solidification constituents in the interdendritic regions were rich in Nb and Mo, and depleted in Fe and Cr. Owing to the small size of these particles, it was difficult to appropriately characterize them by SEM/EDS analysis, therefore to further understand the microstructure, thin films and carbon extraction replicas were made from the fusion zone to examine by transmission electron microscopy.

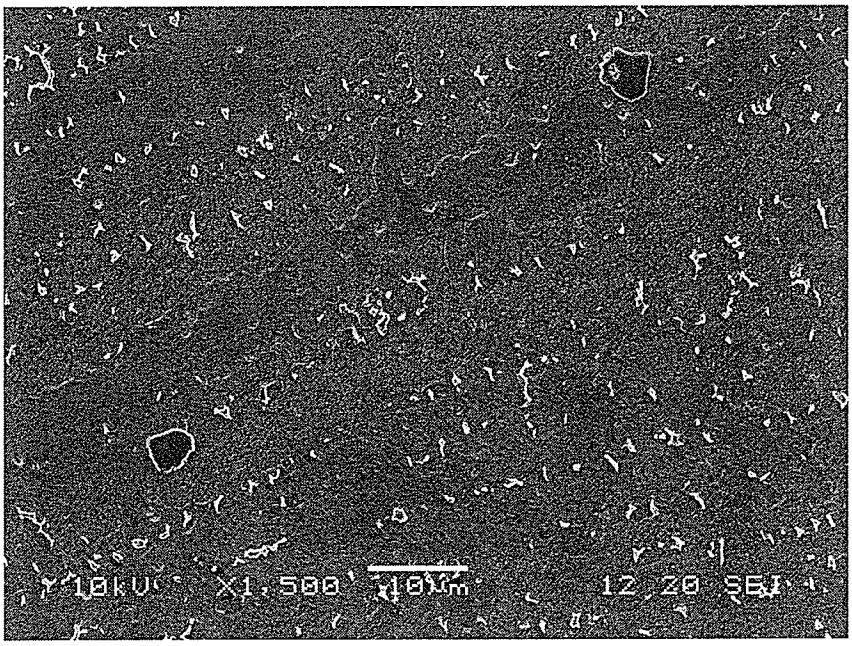

Fig. 4.32: Fusion zone microstructure of 718 Plus alloy

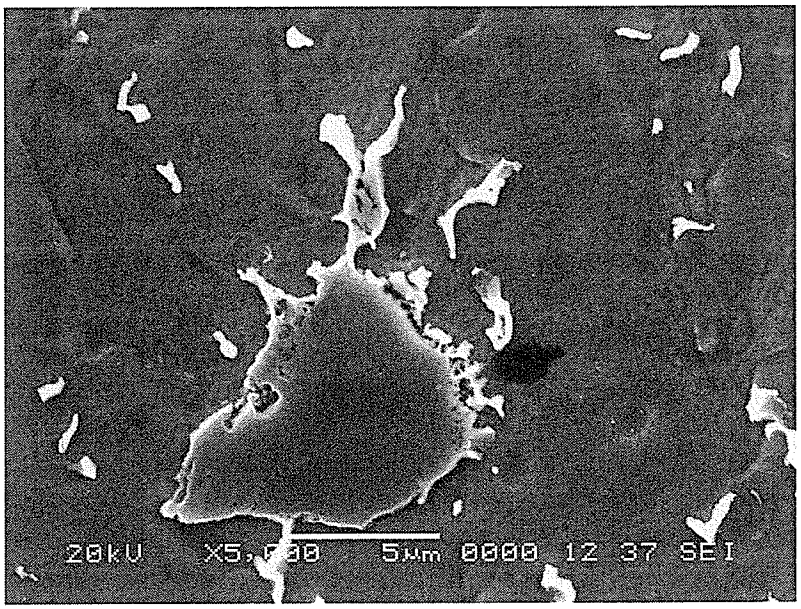

(a)

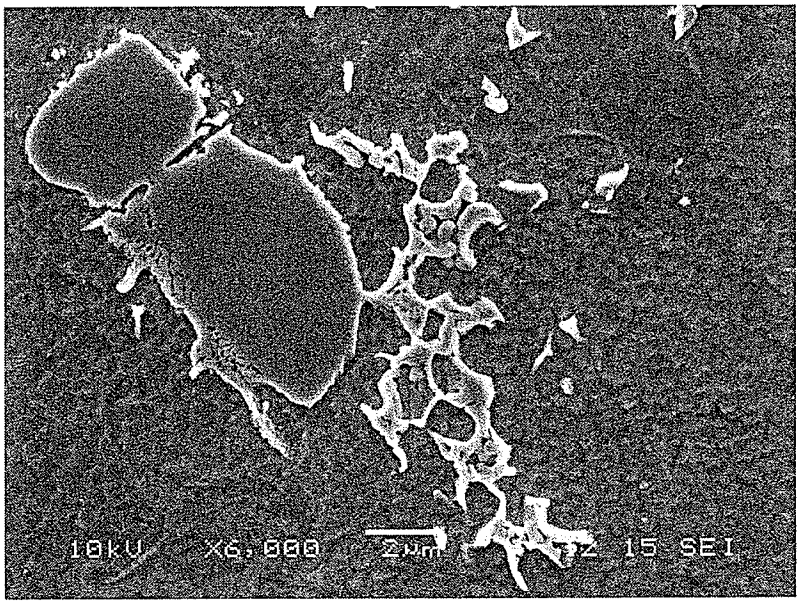

(b)

Figure 4.33 (a) and (b) : Undissolved primary carbides associated with eutectic like products in the fusion zone of HC 20

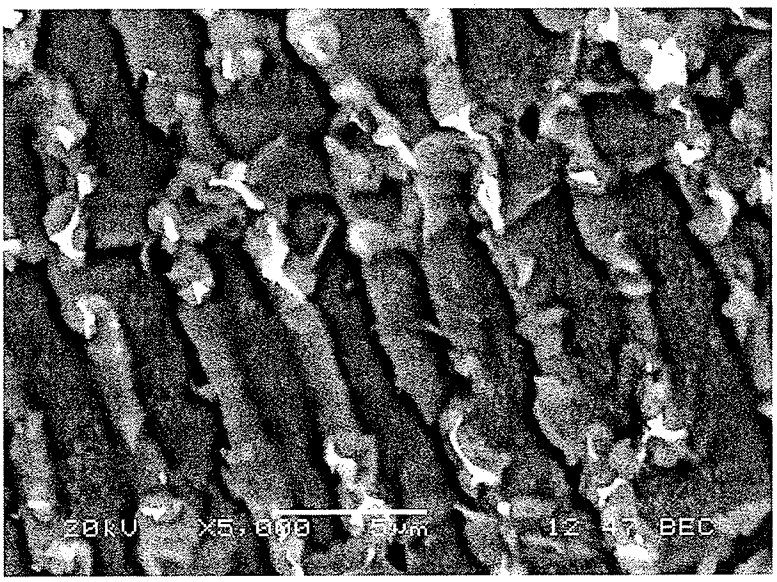

(a)

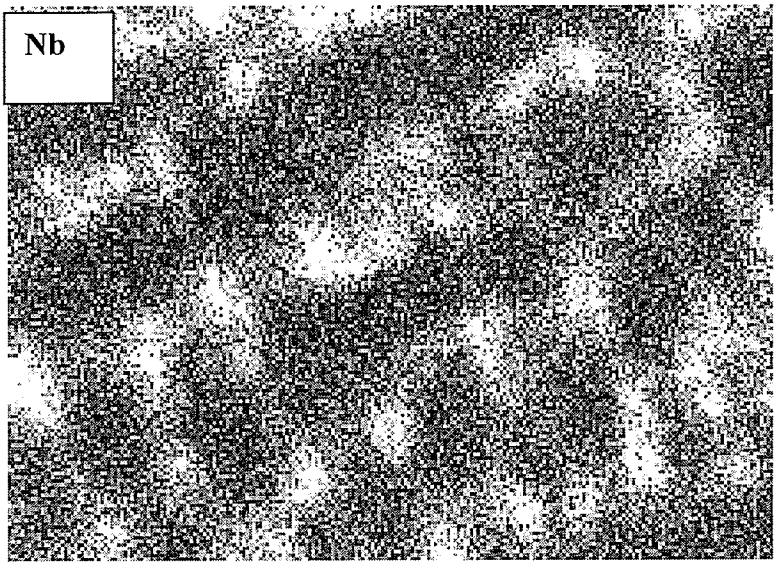

(b)

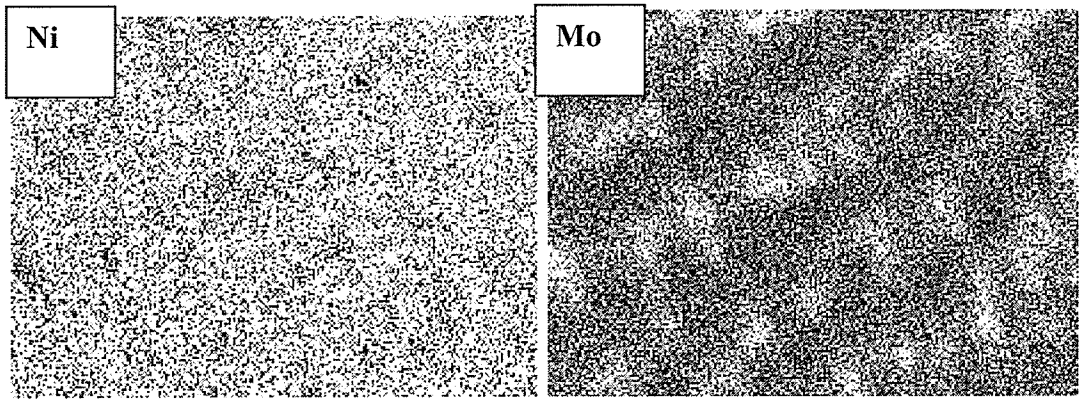

(c) (d)

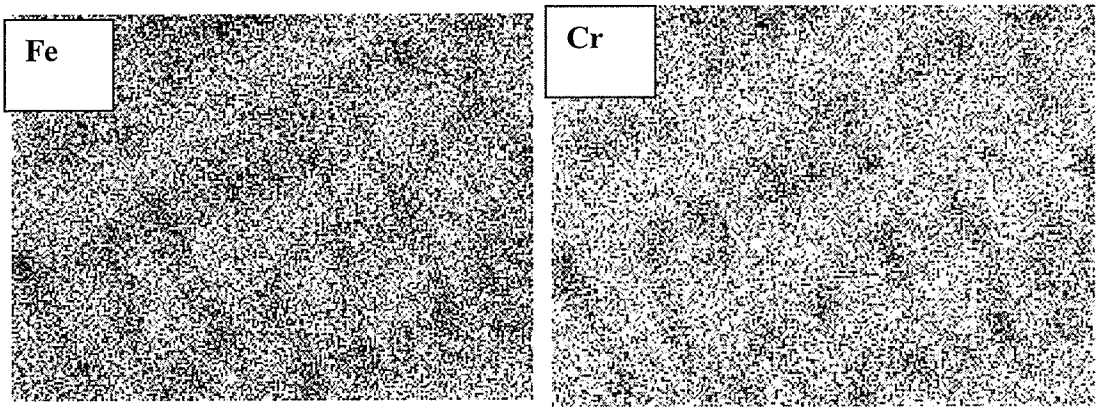

(e) (f)

Fig.4.34: (a) Back scattered electron image of the fusion zone selected for X-ray mapping (b) X-ray mapping of Nb (c) X-ray mapping of Ni (d) X-ray mapping of Mo (e) X-ray mapping of Fe (f) X-ray mapping of Cr

A typical TEM bright field image of one of the two major particles observed in the fusion zone extracted on a carbon replica, and its associated selected area diffraction pattern is shown in Figure 4.35a. The TEM/EDS spectrum suggests that the particle contains predominantly Nb and smaller amounts of other elements (Figs. 4.35b). As these particles were embedded in carbon replica, carbon could not be unambiguously identified, or quantified by available quantification software. Therefore, it was omitted from the quantification analysis. In addition, the EDS spectrum from some of these particles also showed a small amount of boron, although it could also not be quantified due to software limitation. Analysis of the electron diffraction patterns of these particles, an example of which is given in (Fig.4.35a), indicated their crystal structure to be face centered cubic with lattice parameter of a = 0.454 nm, which is similar to that of Nb rich MC type carbides Therefore, the results of the EDS and SADP analysis suggest that these particles were Nb(C, B). Average concentration of metallic components of the carbides, as determined by semi-quantitative micro-chemical analysis is given in Table 4.8.

Other particles observed in thin foils prepared from the fusion zone had irregular shape and showed faulted structure. These particles were found in the interdendritic region of the fusion zone often aligned in a semi-continuous pattern. A typical bright field image of one such particle is shown in Figure 4.36a. TEM/EDS analysis of these phases showed them to be enriched in Nb, Mo and Ni (Figure 4.36b). The crystal structure of these particles was determined to be hexagonal closed packed with lattice parameters of a =0.479 nm and c =0.779 nm. This, in addition to the chemical composition of the particles, indicates them to be Laves phase. An important modification in the chemistry

of 718 Plus alloy compared to the parent metal Inconel 718, was an increase in Co content and a reduction in Fe content. The effect of change in amount of these elements is seen in the composition of Laves phases (Table 4.8) when compared to those reported in Inconel 718 [43]. Laves phase in 718 Plus contains significantly smaller amounts of Fe than that is present in the Laves phase observed in Inconel 718, whereas it is rich in Co which is not present in the latter. It should be noted that, the total amount of Fe and Co in 718 Plus is approximately equal to the Fe content in Inconel 718. In addition, Nb concentration in the Laves phase in 718 Plus is greater than that is generally observed in Inconel 718, while the reverse is true of the Ni concentration.

Gamma prime particles were not observed during the TEM examination of thin foils made from the fusion zone of the welds. As was stated earlier, the presence of γ' can be revealed in TEM by the presence of superlattice reflections in SADP of the matrix due to the ordered FCC crystal structure of γ' even if the diffraction contrast of γ' in the image is not discernable. Superlattice reflections were not observed in SADP, an example of which is shown in Fig.4.37 which is a SADP with [001] zone axis obtained by using JEOL 2100 FX field emission high resolution TEM. If γ' particles were to be present their SADP would have (001), (100) or (010) type of superlattice reflections. Therefore, it is concluded that γ' precipitates did not form in the fusion zone of the welds. This is an important observation, considering that γ' phase is the main strengthening phase in this alloy and generally precipitates very rapidly. That is, the rate of precipitation of γ' in 718 Plus is slower than that observed in other γ' precipitation hardened superalloys, like Waspaloy.

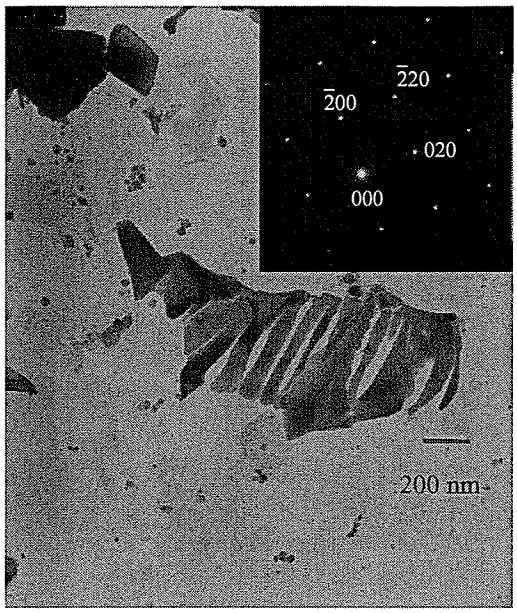

(a)

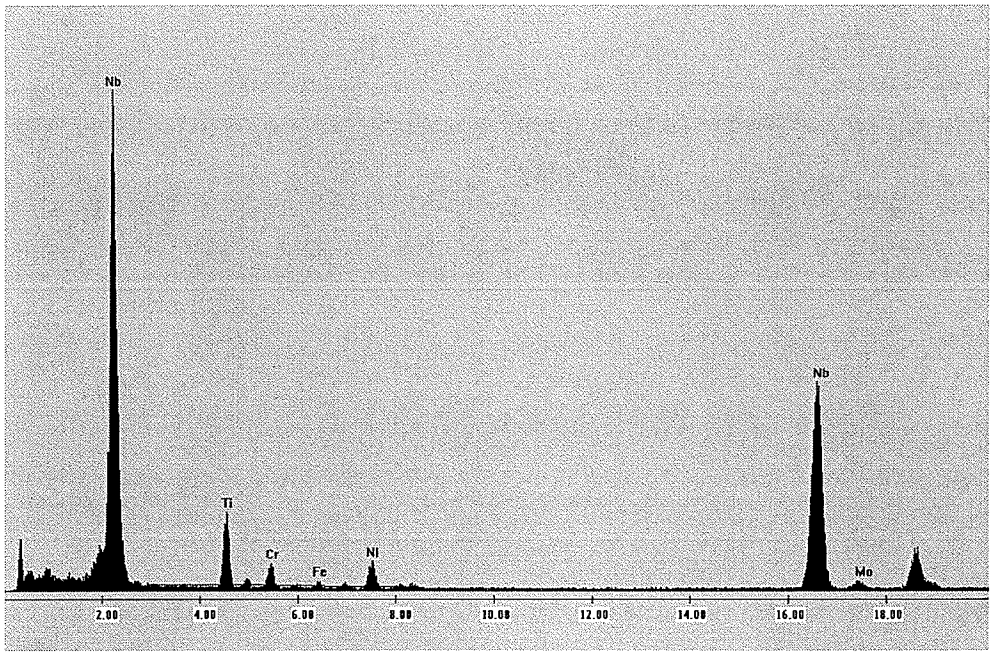

(b)

Figure 4.35: (a) Niobium carbide particle and SADP pattern corresponding to [001] zone axis (b) TEM / EDS spectrum from the carbide phase

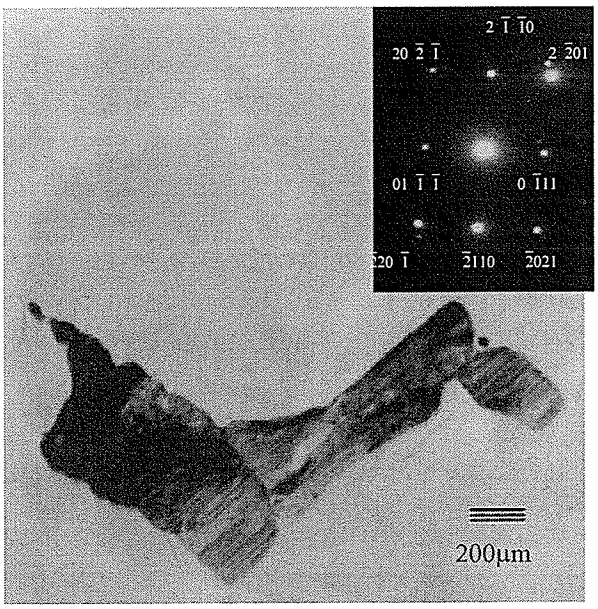

(a)

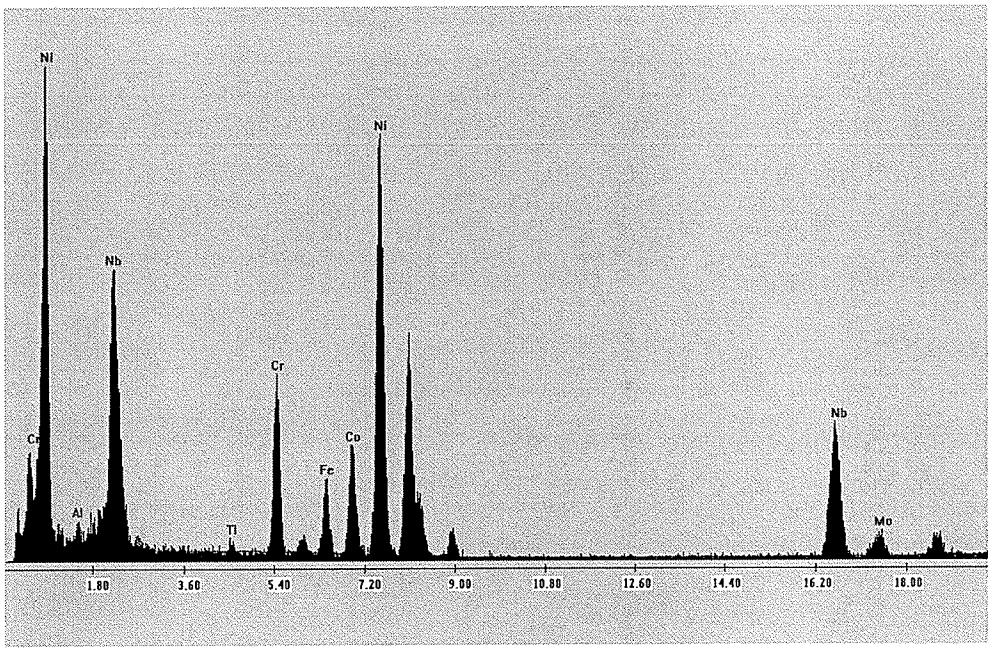

(b)

Fig. 4.36: (a) Bright field TEM micrograph of Laves phase and associated SADP pattern in [01 $\bar{1}$2] axis (b) TEM/EDS spectrum from the Laves phase particle

Table 4.8: Composition of Laves and MC type carbides as obtained by semi-quantitative TEM analysis in wt%

Elements wt%	Nb- rich carbides- fusion zone (TEM)	Laves phase – fusion zone (TEM)	Laves phase – fusion zone [57] (TEM)
Al	–	1.32 ± 0.27	0.56
Ti	5.27 ± 1.36	0.82 ± 0.13	1.9
Cr	2.84 ± 1.59	11.14 ± 0.54	12.8
Fe	1.30 ± 1.12	5.36 ± 0.13	13.6
Co	1.83 ± 1.10	7.42 ± 0.24	–
Ni	5.83 ± 5. 40	31.48 ± 3.08	46.5
W	–	2.90 ± 0.14	–
Nb	81.76 ± 7.55	34.92 ± 3.50	21.2
Mo	3.68 ± 0.96	6.38 ± 1.54	3.6
V	–	–	–
Si	–	–	0.78

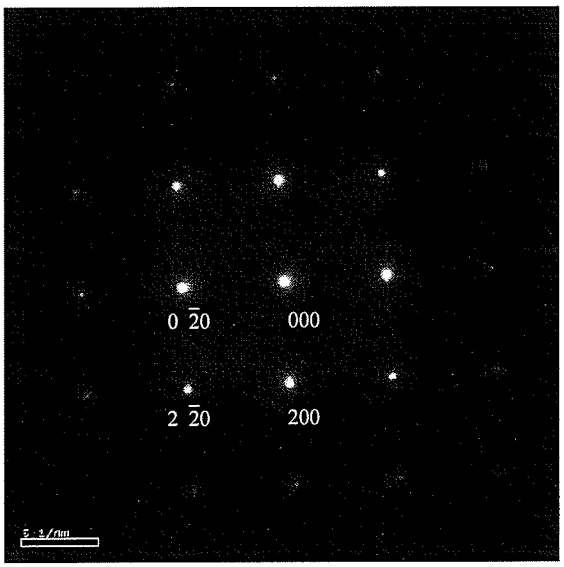

Fig. 4.37: Electron diffraction pattern of the matrix in [001] zone axis, showing absence of superlattice reflections from γ' particles

Fusion zone solidification:

The first solid to form in the weld zone of 718 Plus would be γ dendrites. During their formation and growth, solute elements with partition coefficient k<1 would be rejected in the interdendritic liquid. When solubility limit in the interdendritic liquid of solute elements is exceeded, secondary solidification constituents would begin to form. In nickel base superalloys several secondary solidification constituents are possible including carbides, borides and a number of other intermetallic constituents. In 718 Plus alloy, the interdendritic liquid was continually enriched by strong carbide forming elements Nb and Ti, which may eventually lead to formation of MC type carbides. This is most likely to occur via a non – invariant eutectic type reaction of $L \rightarrow \gamma + MC$. Based on the differential thermal analysis (DTA) of 718 plus alloy [72], the eutectic temperature for the initiation of the gamma/MC type eutectic reaction is reported to be 1292°C. The γ phase would continue to grow and MC type carbide would continue to form over a temperature range.

Formation of MC carbides would deplete the interdendritic liquid of most of the available carbon, while on further cooling; the solidifying liquid would continue to get enriched by Nb. Supersaturation of Nb would eventually result in the formation of Laves phase by a eutectic reaction $L \rightarrow \gamma + Laves$, which would necessarily occur by a non-variant reaction over a range of temperature. Solidification of Inconel 718 castings and welds is generally believed to be completed by the formation of γ/Laves eutectic product. DTA analysis of 718 Plus has shown the $L \rightarrow \gamma + Laves$ reaction to occur at 1173°C [72].

The presence of Laves phase in the fusion zone needs a careful consideration. Previous studies on Inconel 718 system have shown that Laves phase has a weak interface with the matrix and it provides preferential sites for easy crack initiation and propagation because of its inherent brittle nature [34]. Moreover, formation of Laves phase also depletes the matrix of principal alloying elements required for its strengthening. The present analysis shows that the volume fraction of the main strengthening precipitate γ', which contains considerable amount of Nb (about 14wt%), is reduced due to Laves phase formation. Hence, Laves phase needs to be eliminated by a suitable PWHT to prevent its possible detrimental effects. A high temperature solution heat treatment which dissolves Laves phase and homogenizes the fusion zone is recommended before ageing during PWHT. However, considering the low eutectic transformation temperature of Laves phase, extreme care is required to prevent incipient melting during the heating cycle of PWHT. Low melting characteristics of Laves phase also warrants attention in the application of multi-pass welding process for joining of 718 Plus alloy, as it may reduce resistance to weld-metal liquation cracking in the underlying material in such weldments in a manner similar to what happens in heat affected zone.

4.2.4 HAZ microstructures and microcracking:

HAZ microfissuring is a common problem in superalloys that occurs during welding and/or during post-weld heat treatment due to liquation of the grain boundaries. Liquation at the grain boundaries during the weld thermal cycle and the inability of this film to accommodate the thermally induced stresses during weld cooling [2] causes cracking. Majority of the research on Nb bearing superalloys has been focussed on the mechanisms of grain boundary liquation in HAZ, as it is a common occurrence during welding. The grain boundary liquation in HAZ may occur by one or more of the following mechanisms:

i. constitutional liquation of second phase particles, like NbC [3]
ii. segregation of melting point depressant minor alloying elements like B and P [4, 5]
iii. accumulation of solutes at migrated grain boundaries (grain boundary sweeping mechanism)
iv. pipeline diffusion of Nb from Nb-enriched solidification boundaries in the fusion zone
v. penetration of Nb-enriched liquid along the gamma-grain boundaries from the fusion zone in the HAZ [2].

These mechanisms are principally governed by the microstructure of the HAZ prior to, and that which develops during the weld – thermal cycle, and would essentially determine the extent of HAZ cracking in the alloy.

HAZ of 718 Plus alloy was examined in two pre-weld heat treated conditions. The HAZ microstructure immediately adjacent to the fusion zone consisted of a partially melted

region (Fig. 4.38) with many liquated and resolidified grain boundaries. The partially melted zone (PMZ) is defined as the region outside the fusion zone where liquation occurs during welding because of heating above the equilibrium solidus temperature of the alloy or the eutectic temperature of the system [111]. The PMZ has characteristics different from that of the fusion zone and the unmelted HAZ, and is often the weakest region of the weldments [21]. Most of the liquated and resolidified grain boundaries in the PMZ showed no distinct solidification sub-structure or compositional contrast with respect to the matrix when examined by SEM operating in the BSE mode, except for those associated with cracks which are discussed next (Figure 4.38). This suggests insignificant difference between the composition of the matrix and the liquid that was present on these grain boundaries during the weld heating and cooling cycle. Although considerable liquation was observed in the PMZ, most of the cracking occurred outside this region (Fig. 4.39), removed from the fusion zone. Cracking was intergranular in nature and was invariably associated with liquated and resolidified products, as is commonly observed in liquation cracking (Fig. 4.40).

Most of the cracking was found to occur in the shoulder region of the nail type weld profile, as has been observed in other electron beam welded alloys. As was previously discussed in the case of Inconel 718 and HC 49 718 Plus, morphologically the cracking in HC 20 718 Plus alloy was also similar in both the pre-weld heat treated conditions although, cracking increased considerably after the 1050°C pre-weld solution heat treatment. A typical HAZ SEM micrograph of a crack in HC 20 alloy in 950°C heat treated condition, obtained in secondary electron emission mode is shown in Figure 4.39.

It can be seen that cracking is quite removed from the fusion zone, and the grain boundaries near the fusion zone were liquated and resolidified. Cracking generally occurred on the liquated grain boundaries with resolidified products on the cracks (Fig. 4.40a), which were found to be enriched with Nb as shown in the SEM/EDS x-ray map in Fig. 4.40b.

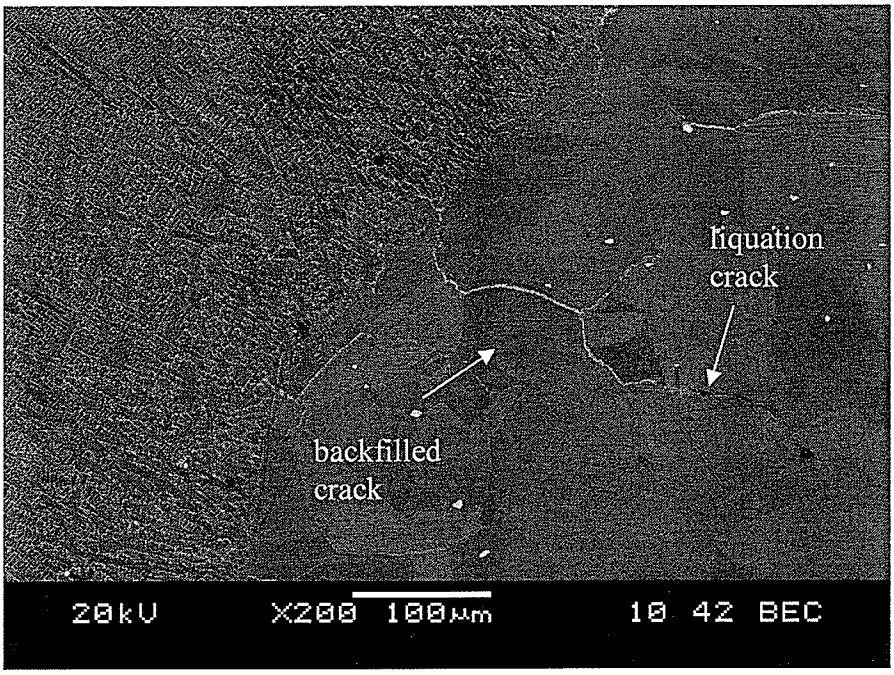

Fig. 4.38: Heat affected zone showing partially melted zone and liquation cracking

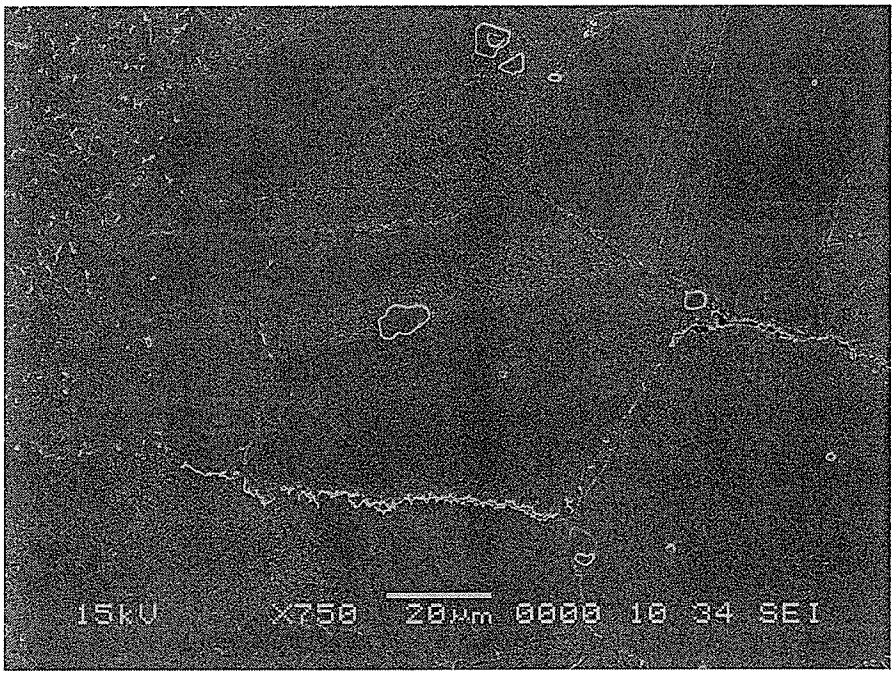

Figure 4.39: Heat affected zone cracking in HC 20 in 950°C/1hr solutionizing heat treatment

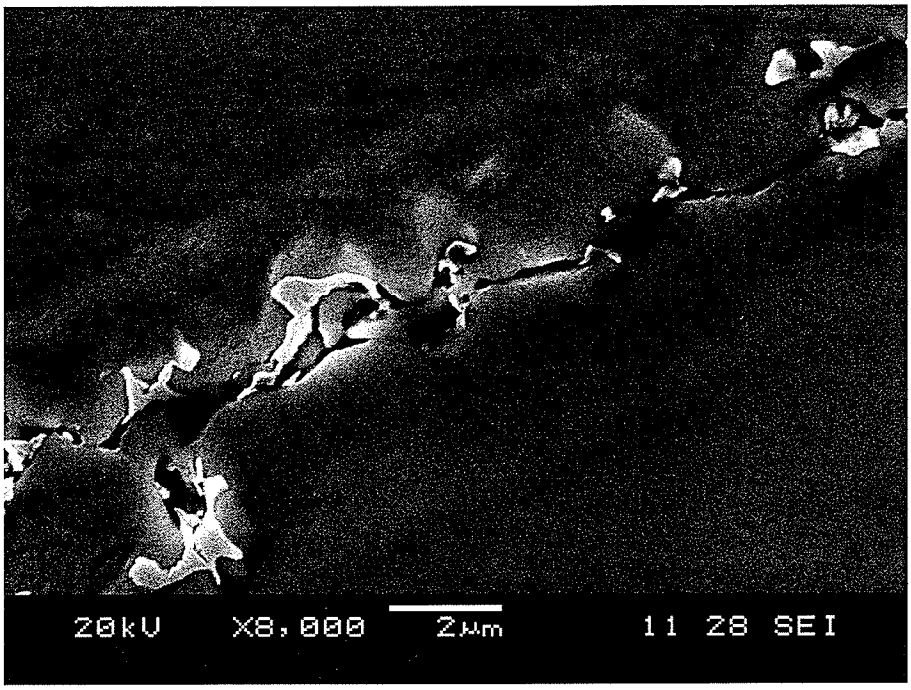

Fig. 4.40 (a) Resolidified products at the crack edges (b) SEM/EDS X-ray mapping of Nb around the crack showing enrichment in the resolidified products

Backfilling of the HAZ microfissures:

While all the grain boundaries intersecting the fusion zone in the PMZ were liquated; those which were associated with microfissuring showed enhanced compositional contrast in the SEM/BSE image. The continuity of these grain boundaries into the fusion zone on one end and their association with the cracks on the other end indicates back filling. Considerable backfilling was observed in the present investigation, with almost all the cracks being partially or completely healed. This created a sub-zone adjacent to the fusion zone that was free of cracking. The measured crack length excludes the back filled region in front of the crack. Fig. 4.41 a shows a typical example of a backfilled grain boundary near the crack with resolidified products. The resolidified products on the grain boundaries showed eutectic type of morphology, which is better evident in a higher magnification SEM/BSE image in Fig. 4.41b. The resolidified products were found to be enriched in Nb, Ti and Mo with an average composition (wt%) of 18.43Nb, 1.18Ti, 3.21Mo, 13.78Cr, 6.57Fe, 45.62Ni, 9.49Co. These products were identified as Laves/γ eutectic based on their morphology and composition. Laves/γ eutectic with similar composition and morphology have been observed in the liquated and resolidified HAZ grain boundaries in other Nb bearing austenitic alloys [2, 102].

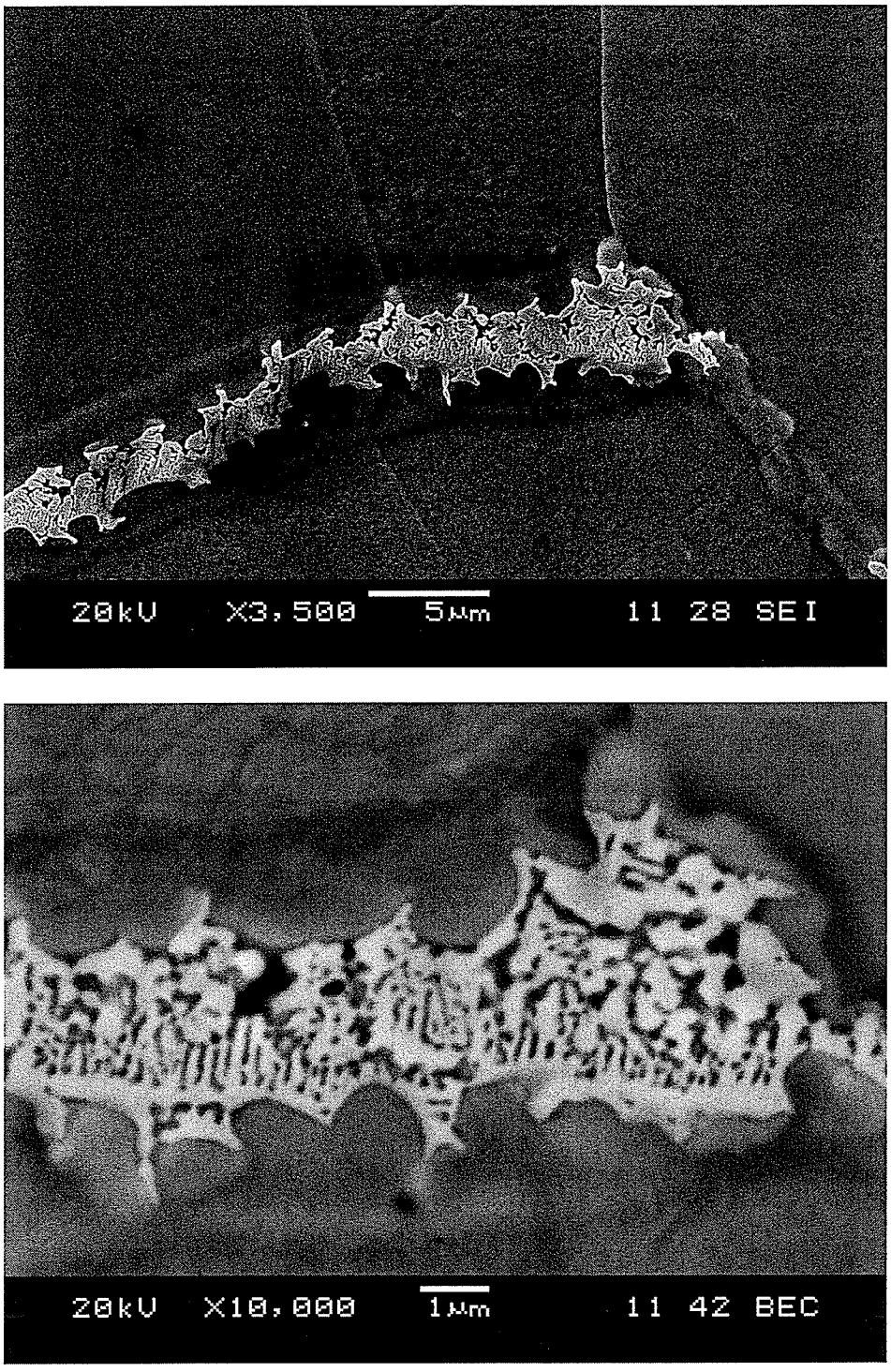

Figure 4.41: (a) Backfilled crack showing eutectic type resolidified constituents (b) inset A of (a) identifying the resolidified constituents as Laves/gamma eutectic

Heat affected zone microfissuring can be partially or completely healed by "backfilling". Backfilling occurs when a crack opens up in the solidifying fusion zone and the liquid from the fusion zone starts penetrating the crack by capillarity effect. Some other factors that govern backfilling are quantity, viscosity, surface tension and the solidification temperature range of the liquid [112]. Backfilling also requires the crack to maintain an interface with the molten weld pool, which is easier if the crack originates at the fusion boundary, but even if the crack originates in the heavily liquated region away from the fusion zone it can propagate towards the weld zone and separate the still solidifying weld liquid causing a crack to form. The backfilled liquid would penetrate the crack to the point where the instantaneous temperature of the crack walls drops sufficiently to freeze the segregated liquid [113]. Backfilling observed in the present investigation created a zone adjacent to the fusion zone which was essentially crack-free. The total crack length only takes into account the open cracks, excluding the backfilled crack length, which might influence the assessment of the alloy's actual weldability. Although a HAZ crack is healed with the liquid from the weld pool, the solidified back filled material might not have the same properties as rest of the material and induce weakness in the weldment. The backfilled grain boundaries were found to solidify into γ/Laves eutectic, which has a lower liquidus temperature and is known to be brittle in nature, and hence needs careful consideration.

Constitutional liquation of Nb rich MC type carbides:

Intergranular and intragranular constitutional liquation of NbC particles was observed in the HAZ. Constitutional liquation occurs due to an incomplete solid state dissolution of second phase particles under non-equilibrium conditions of rapid heating, as experienced during welding. Slower diffusion controlled solid-state dissolution creates a composition gradient at the particle-matrix interface. When the temperature during the heating cycle of welding reaches the eutectic temperature of the system, the interface begins to melt [44]. Hence liquid is present below the bulk solidus of the alloy due to constitutional liquation of second phase particle. Fig. 4.42a shows a BSE/SEM liquating carbide particle near the fusion boundary with resolidified eutectic like products at the matrix-carbide interface. Liquated carbide particles were also observed along the microfissured grain boundaries, as shown in Fig. 4.42b. These liquating carbides were found to be closely associated with resolidification product consisting of the Laves/γ type eutectic constituents. Constitutional liquation of NbC particles have also been observed in other Ni-Fe base superalloys such as Inconel 718 [36, 92], Incoloy 903 [102, 114], 905 and 907 [102].

TEM/EDS analysis was performed on carbon extraction replicas made from the HAZ zone by carefully masking the fusion zone and base metal regions. Fig. 4.43 shows a TEM bright field micrograph of a phase extracted on one such carbon replica. Many particles with similar characteristic arrow-head morphology were observed on the carbon replicas. The SAD pattern associated with the phase, in a direction parallel to the [011] zone axis, is shown in the inset of Figure 4.43. Lattice parameter of the phase was

calculated to be 0.455 nm, which is similar to the lattice parameter of MC type carbides. TEM/EDS spectra obtained from these carbides were also similar to those obtained from other carbides in the alloy. Hence this phase was identified to be Nb rich MC type carbide. Since the MC type carbides that precipitate in solid state have been observed to have a regular cuboidal morphology, as is seen in the base metal microstructure, the arrow-head type morphology of the carbides suggests them to have formed from the liquid state.

Some intergranular Ti carbonitride particles also liquated in the HAZ, an example of which is shown in Figure 4.44a. The corresponding SEM/EDS spectrum is shown in Figure 4.44b. It should be noted that eutectic like resolidified products (Laves + γ in the case of constitutional liquation of Nb C particles) were not observed around these particles. Romig et al. [115] made a similar observation in their study of constitutional liquation of Ti(C,N) in austenitic stainless steel Alloy 800.

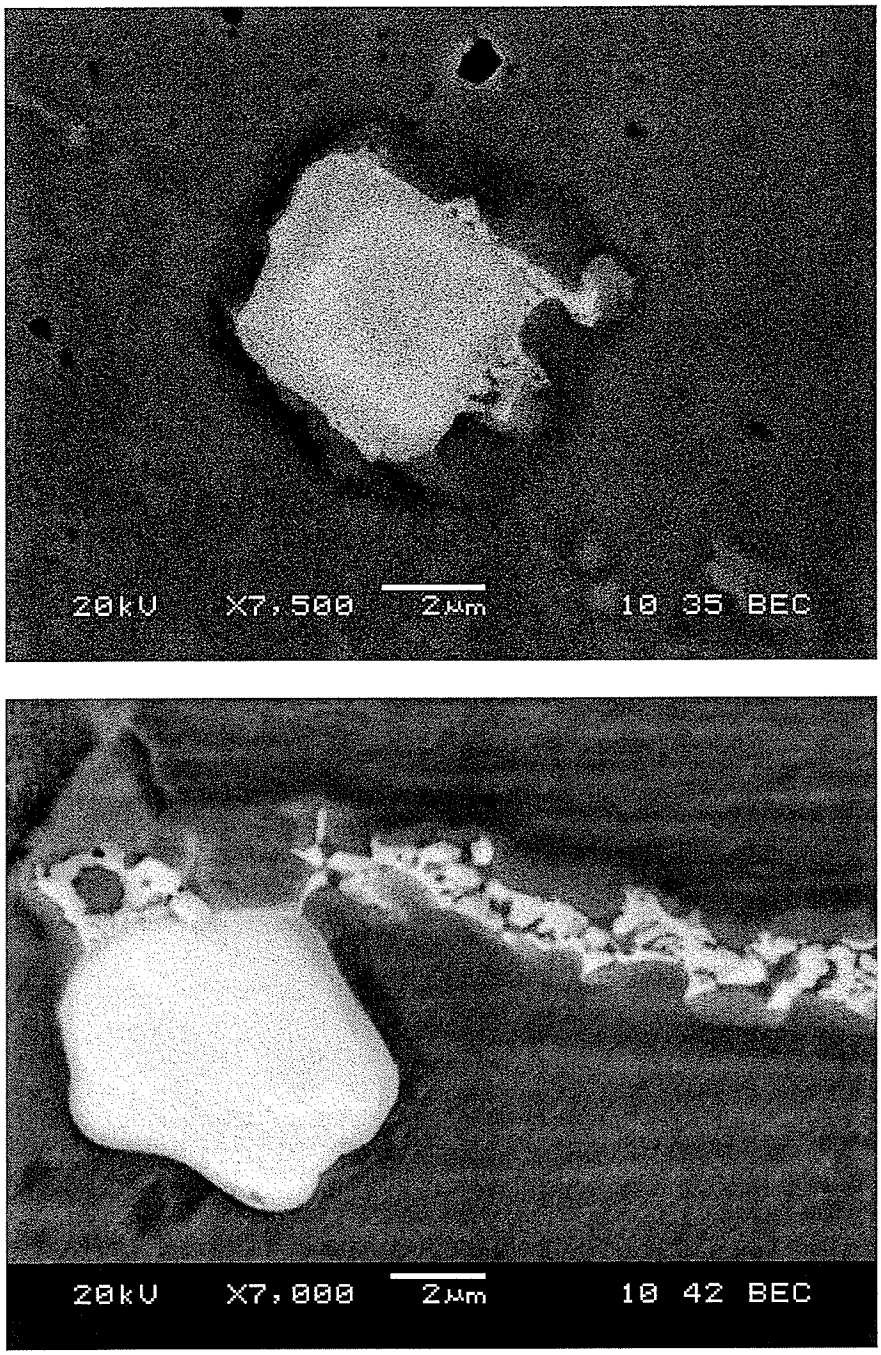

Figure 4.42 (a) Intragranular constitutional liquation of Nb rich MC type carbides; (b) Intergranular constitutional liquation of Nb rich MC type carbide and its association with Laves/gamma eutectic constituents

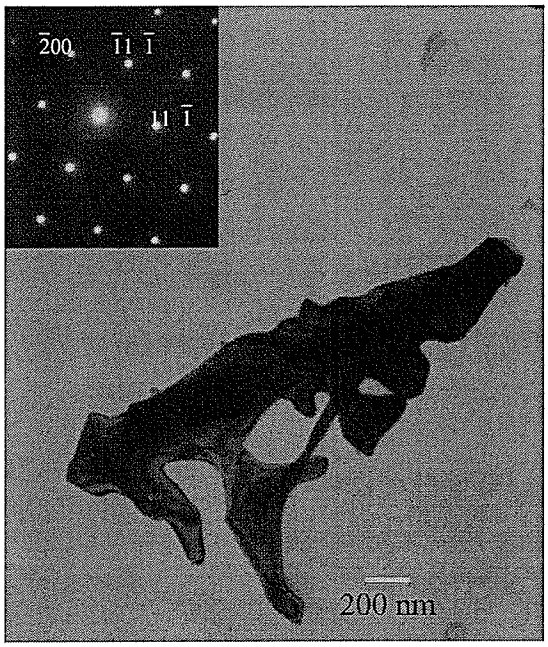

Fig. 4.43: Resolidified MC type carbide particle extracted on carbon replica and the SADP pattern in the zone axis parallel to [011] direction associated with it

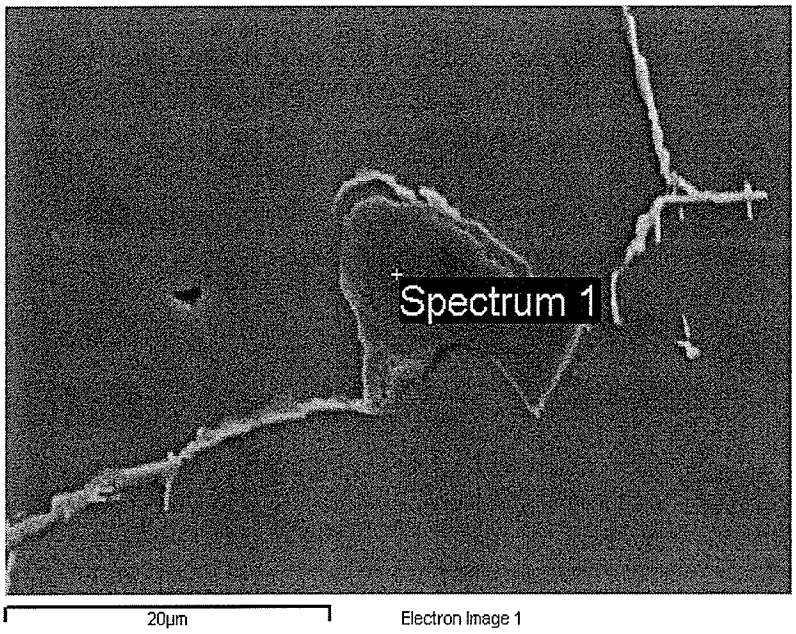

(a)

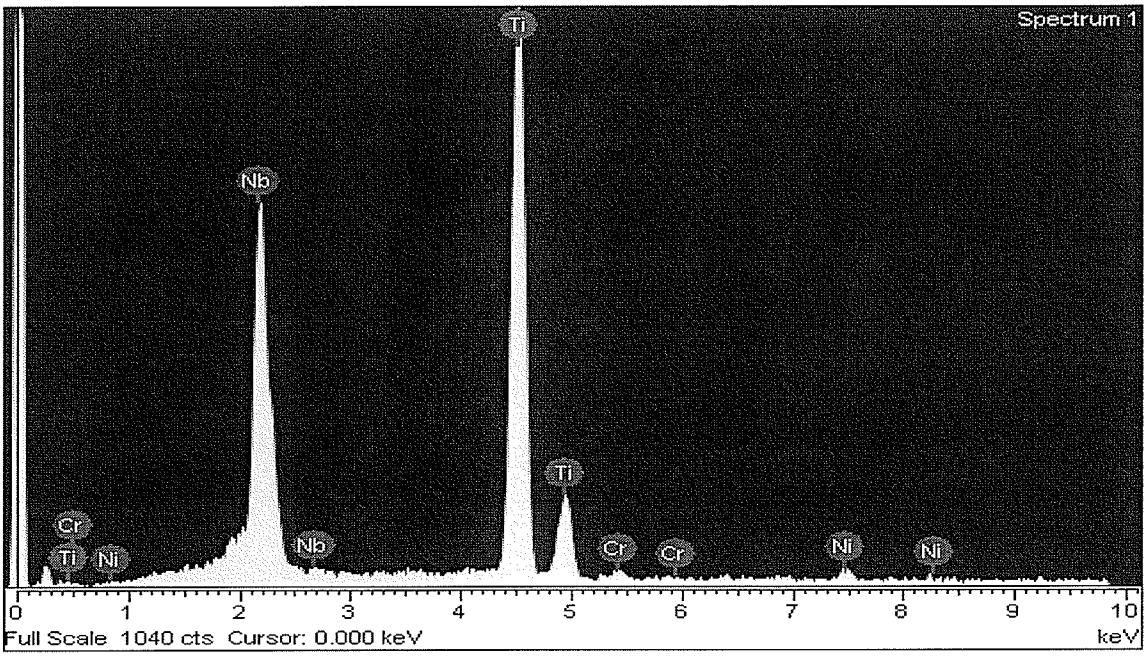

(b)

Figure 4.44: (a) Liquation of Ti rich carbonitride particle (b) SEM/EDS spectrum associated with (a)

Solidification in the HAZ liquated regions:

Liquated grain boundaries solidified either as γ solid solution or as Laves + γ eutectic and carbides + γ eutectic, depending on the source and volume of the liquid. The composition of PMZ grain boundaries that liquated due to supersolidus melting was not much different from that of the matrix, and had a smaller volume of liquated area. Hence it is suggested that under higher temperature gradients and cooling rates, these grain boundaries would solidify rapidly to γ phase without any change in composition. In contrast, the back filled grain boundaries were wider and had a solidified eutectic on them. One source of the solidified product is the back filling of grain boundaries by the liquid from the interdendritic regions of the weld zone and by analogy, the solidification pattern of the liquid on the HAZ grain boundaries is likely to be similar to the one observed in the fusion zone. The first solid to form from the liquid would be gamma solid solution followed by gamma + carbide eutectic and gamma+ Laves eutectic reactions, as was observed in the microstructure of HAZ.

Gamma prime precipitation in 718 Plus alloy:

The gamma prime phase is the principal strengthening phase in 718 Plus alloy, and was observed in the present study in the as-received and in the 950°C solution heat treated condition. This suggests that unlike Inconel 718, the solvus of γ′ phase is above 950°C, and it is expected to be present in the microstructure even after the commercial solution heat treatment of 950°C/1hr followed by air cooling. The size of primary γ′ particles was approximately 50 nm. Fine secondary γ′ particles were also observed in this heat treated material, which were distributed uniformly in the microstructure. The welding response of 718 Plus with γ′ and that of Inconel 718 without γ′ and γ″ in this heat treatment was very similar. Although, the presence of γ′ did not affect weldability of 718 Plus in this particular condition, precipitation of γ′ in the pre-weld heat treatment should be examined more closely because of their susceptibility to liquate. Ojo et al.[116, 117] in their study of cast Inconel 738, for the very first time observed the strengthening γ′ phase to undergo liquation and adversely influence weldability of the alloy. The size, composition and volume fraction of γ′ would be different in different γ′ strengthened alloys; which would affect their liquation tendency, nevertheless, the observation warrants consideration, especially when γ′ is the principal strengthening phase.

Gamma prime particles were observed in the aged condition of 718 Plus alloy by scanning electron microscopy (Figure 4.45 a and b) while as stated earlier, fine γ′ particles in the pre-weld heat treated condition could only be resolved by transmission electron microscopy. The full commercial standard heat treatment of 718 Plus consists of solution heat treatment at 950°C followed by double aging heat treatments - 950°C/1hr

air cooled + 788°C/2hrs furnace cooled to 650°C/8hrs followed by air cooling. Overaging at 650°C to upto 40 hrs, after the standard heat treatment did not greatly change the hardness of the alloy, as shown in Figure 4.46. The hardness changed from 453 ± 8 VPN after no overaging to 469 ± 9 VPN after 40 hrs at 650°C.

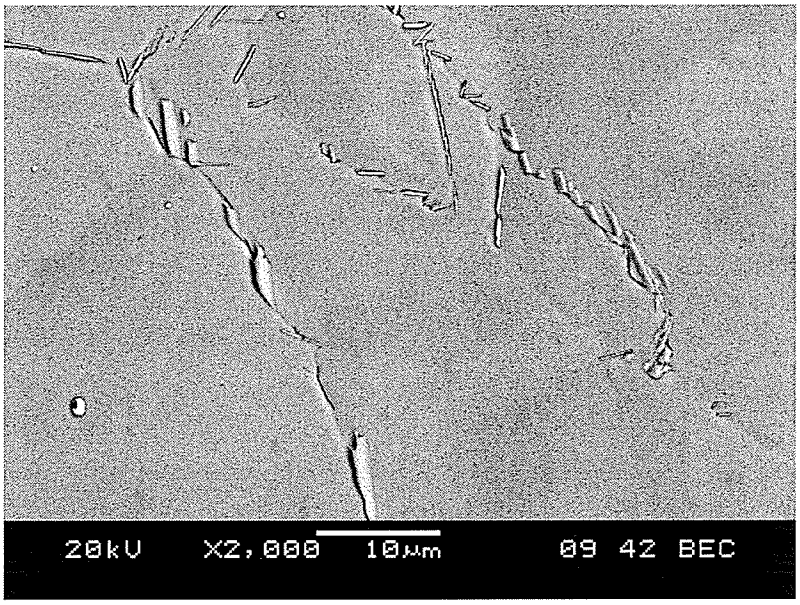

(a)

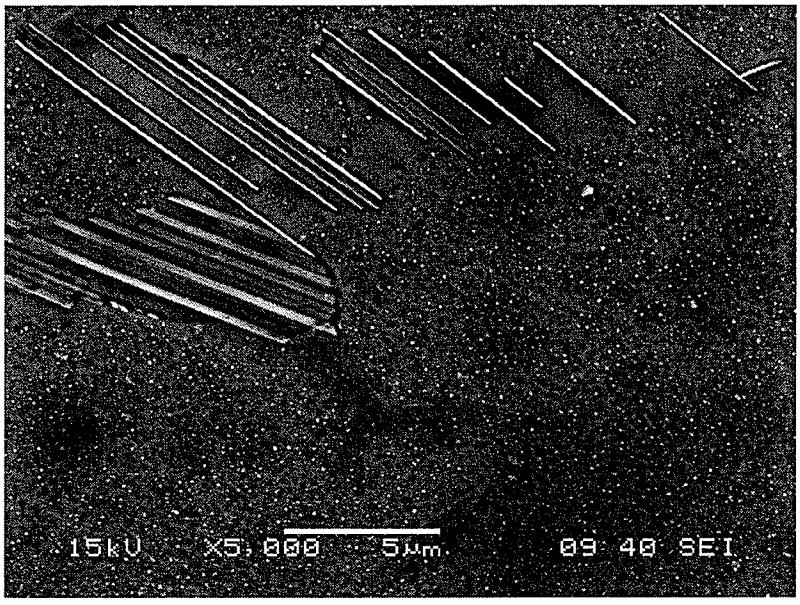

(b)

Figure 4.45: Standard solution heat treated microstructure of 718 Plus superalloy : (a) optical micrograph showing γ′ precipitates (b) back scattered image of 718 Plus microstructure

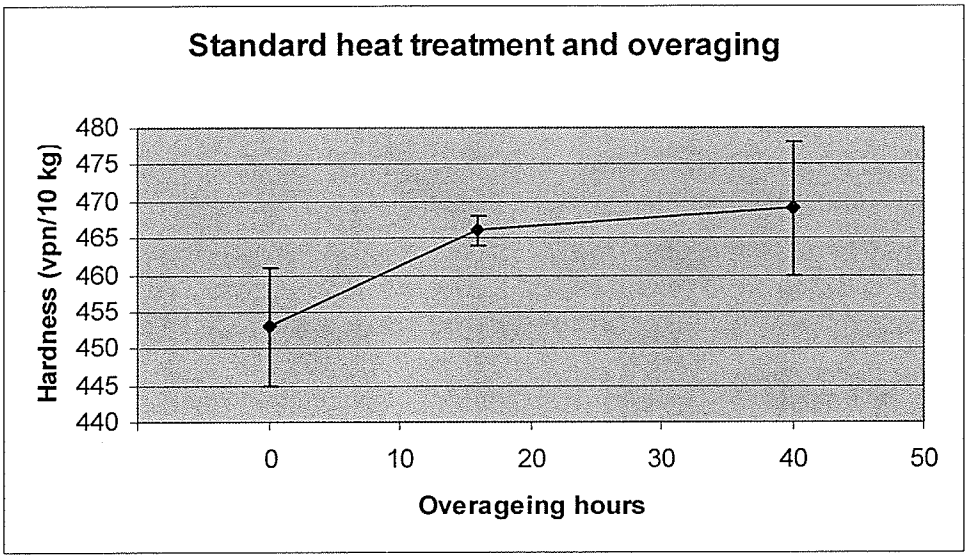

Figure 4.46: Variation of hardness with the over-ageing time after standard solution heat treatment

4.3: Weldability

4.3.1 Introduction

Superalloys were developed to have high strength and creep resistance at elevated temperatures, but these alloys are difficult to fabricate. With the ever increasing demands of the gas turbine land/aero engines, superalloys are needed to be fabricated in intricate shapes and designs either by casting, forging or by joining. Also owing to their high cost, it is economically more viable to repair these components than to replace them with new parts. Fusion welding process is extensively used both at manufacturing as well as repairing stage and hence for successful commercial application of an alloy, weldability of a material needs to be thoroughly understood. Weldability of a material is defined as the capacity of the material to be joined under imposed fabrication conditions into specific suitably designed structure and perform satisfactorily in the intended service.

Over the years many techniques to evaluate weldability have been devised and the most commonly used techniques were discussed in Chapter 2 under the weldability section. In this particular study, two techniques were used to evaluate weldability of the newly developed 718 Plus alloy.

(i) Weld cracking measurements on actual bead-on-plates welds

(ii) Gleeble hot ductility measurements

Inconel 718, the baseline superalloy, was evaluated along with 718 Plus alloys by both the techniques. Waspaloy plates were also welded and weld cracking was compared to that of Inconel 718 and 718 Plus alloys but hot ductility tests on Waspaloy rods could not be used due to the defective as-received material.

4.3.2 Weld cracking measurements

HAZ cracking in Inconel 718 and 718 Plus alloys (HC 20 and HC 49) was observed by examining the metallographically prepared cross-sections of the welds by optical microscope, although some very fine cracks could only be revealed by SEM. Crack length measurements were done by SEM using the JEOL software. Intergranular nature of the cracks and the liquated and resolidified products associated with them were discussed in Sections 4.1 and in 4.2 for those observed in Waspaloy, Inconel 718 and 718 Plus alloys. This section compares the weld cracking measurements of these alloys.

The crack lengths were measured in 10 metallographic sections in the transverse direction perpendicular to the weld. Total crack length (TCL) and maximum crack length were determined and an average total crack length per section was calculated. These values along with the standard deviation associated with the average total crack length values are listed in Table 4.9. A histogram illustrating the values of average total crack length per section, for the two pre-weld heat treatments is shown in Figure 4.47. It is evident that Inconel 718 is less susceptible to cracking than 718 Plus alloys in both the heat treated conditions. For the standard solution heat treatment at 950°C, cracking was least in Inconel 718, followed by the lower B and P 718 Plus HC 20, and the highest in high B and P alloy HC 49. Similar trend was observed after the solution heat treatment at 1050°C. Cracking in all the alloys increased considerably, more than by a factor of 4, with an increase in the solution heat treatment temperature. In 718 Plus alloys, cracking in the higher B and P version, HC 49, was almost twice the amount observed in the lower B and P alloy, in both the pre-weld heat treated conditions.

Waspaloy was solution heat treated at 1020°C in accordance with its sub-solvus standard commercial heat treatment. In all the alloys studied, Waspaloy was the only alloy that showed cracking in the fusion zone. As can be seen from Table 4.9 and Figure 4.47, the fusion zone cracking was far more severe than the total cracking observed in the HAZ. The total cracking in the fusion zone and the heat affected zone in Waspaloy was more than that observed in any of the other alloys studied.

HAZ and FZ microfissuring depend on numerous material parameters like composition, heat treatment, grain size, hardness, processing route, etc. For a comparison of weldability between the alloys, it is desirable to keep as many parameters constant as possible, although it is very difficult to precisely control them. Two widely known parameters that considerably influence weldability are grain size and hardness, and are considered in more detail next.

Table 4.9: Crack length in Inconel 718, 718 Plus alloys and Waspaloy

Alloys	Standard commercial solution heat treatment – 950°C/1hr + WQ*			1050°C/1hr + WQ		
	Total crack length (μm)	Total Average crack length (μm)	Maximum crack length (μm)	Total crack length (μm)	Total Average crack length (μm)	Maximum crack length (μm)
Inconel 718	590	59 ± 119	72	3950	395 ± 214	373
HC 20 718 Plus	1490	149 ± 201	327	7500	750 ± 330	468
HC 49 718 Plus	3990	399 ± 307	253	14390	1439 ± 557	419

Alloy	Heat treatment	Total crack length (μm)	Total average crack length in the HAZ(μm)	Total average crack length in the fusion zone (μm)	Total average crack length (μm)
Waspaloy	1020°C / 1hr + wq	36006	1152 ± 222 **[Max 424]**	2446 ± 689 **[Max 1453]**	3601 ± 612

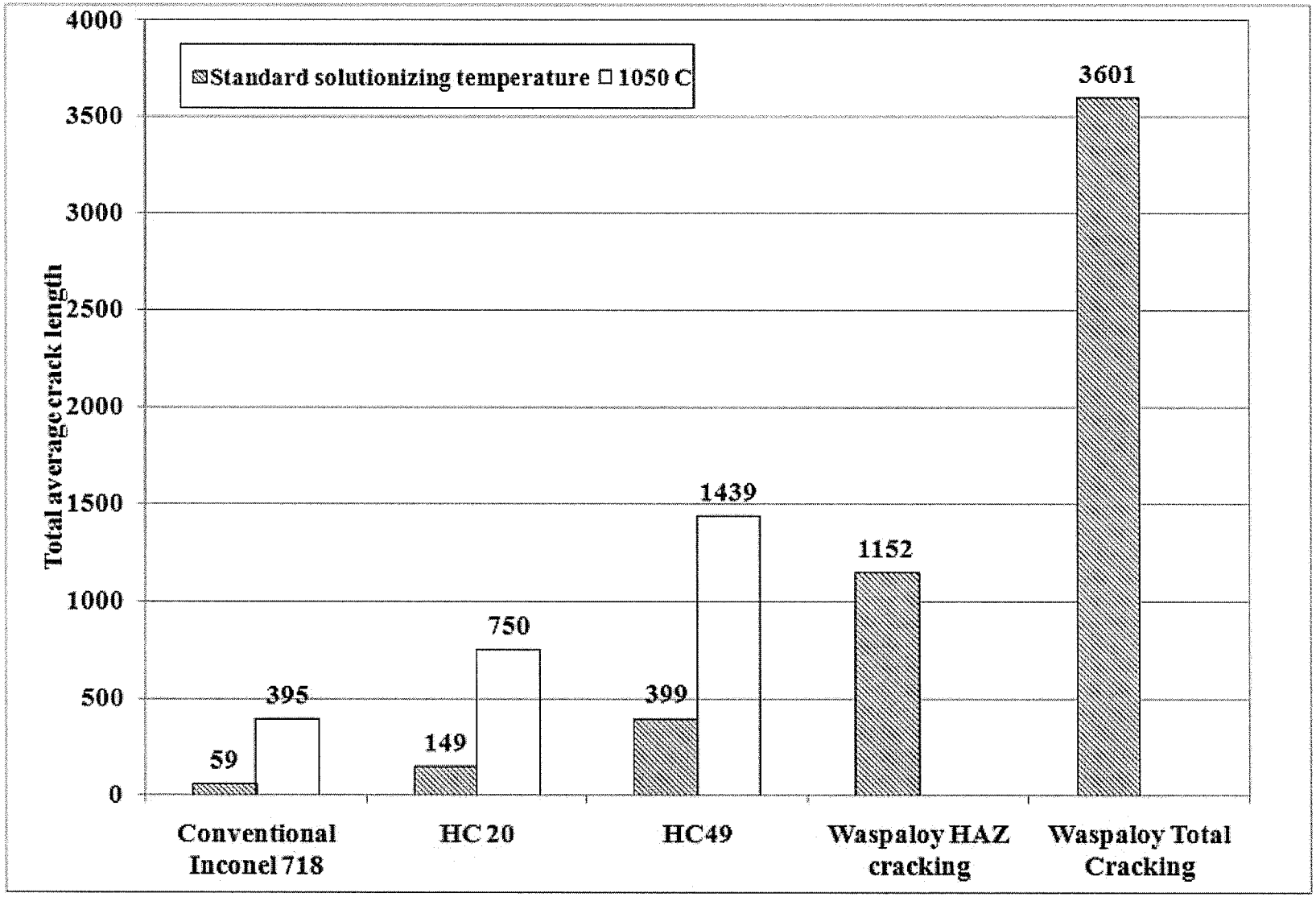

Figure 4.47 : Average total crack length in Inconel 718, Waspaloy and 718 Plus alloys in the two pre-weld heat treatment conditions

In earlier studies on IN 738 LC superalloy welded with different filler alloys, the HAZ and fusion zone microfissuring was related to the base metal hardness of the alloy [118, 119]. IN 738 LC was welded with three different filler alloys with increasing Al content, IN 625, IN 617 and HY 214; in two different pre-weld heat treated conditions. The UMT treatment, a pre-weld heat treatment developed by Thakur et al.[120] at the University of Manitoba, induced a lower base metal hardness than the standard solution pre-weld heat treatment. UMT treated welds, irrespective of the filler material, suffered less cracking compared to the SHT treated welds. The fusion zone hardness increased with the aluminum concentration in the fillers in both the pre-weld heat treatments, mainly due to the precipitation of γ' phase in the fusion zone. In a particular pre-weld condition, cracking increased with increase in Al concentration in the filler alloys. Similar results were obtained after PWHT of these alloys where the UMT treated condition with lower base metal hardness showed significantly less cracking in the fusion zone and the HAZ than in the SHT treated condition [121]. Sekhar et al.[122] in their investigation of electron and laser beam welded Waspaloy and Udimet 720 found that softer fusion zone in Waspaloy led to less distortion of the weldment, although no correlation was made between the cracking and the hardness of the materials.

The effect of difference between hardness of the fusion zone and the base metal on microfissuring is not very clear, nevertheless, it seems that a lower base –metal hardness does improve alloy's resistance to microfissuring during welding. Softer base metal and better ductility of the alloy would allow the stresses developed during welding to be relieved in the softer base metal rather than the sensitive HAZ.

Table 4.10 lists the hardness values of all the alloys along with their grain sizes. As can be seen from the hardness values, Inconel 718 had lower base-metal hardness in both the pre-weld heat treated conditions compared to that of the 718 Plus alloys. As has been discussed earlier, the microstructures of these alloys were very similar except for the presence of γ' phase in the 950°C solution heat treated 718 Plus alloys. The hardness of 718 Plus alloys was about 75 VPN higher than that of Inconel 718 in the 950°C heat treated condition. Gamma prime phase was not observed in the 1050°C solution treated condition, nevertheless, the hardness of the 718 Plus alloys was higher than that of Inconel 718 by almost 50 VPN. Hence, Inconel 718 with softer base metal suffered a significantly reduced cracking compared to 718 Plus alloys, in spite of the apparent similarities in the microstructure.

The fusion zone hardness values, on the other hand, of 718 Plus alloys and Inconel 718 were similar, with an average value of 250 VPN. This also corroborates the fact that the development of fusion zone microstructure in both the alloys was very similar. The base metal hardness value of Inconel 718 was less than that of the fusion zone in both the pre-weld heat treated conditions, although the undermatching was less in the case of 950°C condition (about 22 VPN) than in the case of 1050°C condition (about 76 VPN). The base metal hardness values of 718 Plus alloys were higher than the fusion zone hardness values of the 950°C treated material (about 45 VPN), whereas the base metal hardness values were about 52 VPN lower than the fusion zone hardness values of the 1050°C heat treated alloy. The different trends followed by the two alloys can not explain the increase in cracking in both the alloys with an increase in the solution heat treatment temperature.

Figure 4.48 shows plots of total average crack length and hardness of each of the four alloys. It can be seen that a reduction in the hardness with an increase in the solution heat treatment temperature caused a reduction in cracking in all the alloys.

Base-metal hardness of Waspaloy was higher than that of Inconel 718 in both the heat treated conditions. When compared to 718 Plus alloys, the values were in between i.e., higher than in the 1050°C condition, but lower than that of the 950°C treated material. Interestingly, the fusion zone hardness of Waspaloy was lower than the fusion zone hardness of 718 Plus alloys as well as that of Inconel 718. However, these differences in the hardness values cannot explain the enormous difference in cracking in Waspaloy as compared to the other alloys. Also, Waspaloy welds cracked in the fusion zone as well as in the HAZ, which was not observed in any of the other alloys. The microstructure of Waspaloy was considerably different than that of Inconel 718 and 718 Plus alloys, as discussed in section 4.1.2, with fine γ' particles distributed through out the microstructure. It is to be noted here, that γ' particles in the 1020°C heat treated Waspaloy could be resolved by scanning electron microscope whereas γ' particles in 718 Plus alloys in 950°C condition could only be resolved by transmission electron microscopy. Also, the volume fraction of γ' in Waspaloy was visibly higher than the volume fraction of γ' in 718 Plus alloys. It is believed that the higher volume fraction of γ' and its intergranular distribution in Waspaloy, reduced its cracking resistance compared to the other alloys.

Table 4.10: Grain size (μm) and hardness (VPN) of the alloys studied before and after welding

Heat Treatment		Inconel 718	718 Plus HC 49	718 Plus HC 20	Waspaloy
950 °C / 1 hr + water quenching	***Grain size (μm)***	***48 ± 7***	***42 ± 7***	***54 ± 6***	
	Base metal hardness	223± 4	293 ± 8	295 ± 7	
	Fusion zone hardness	245 ± 4	257 ± 6	250 ± 8	
1050°C / 1 hr + water quenching	***Grain size (μm)***	***100 ± 14***	***116 ± 7***	***73 ± 8***	
	Base metal hardness	165 ± 3	201± 10	196 ± 5	
	Fusion zone hardness	241 ± 5	248 ± 6	248 ± 6	
1020°C/1hr +water quenching	***Grain size (μm)***				***67 ± 6***
	Base metal hardness				264 ± 10
	Fusion zone hardness				234 ± 8

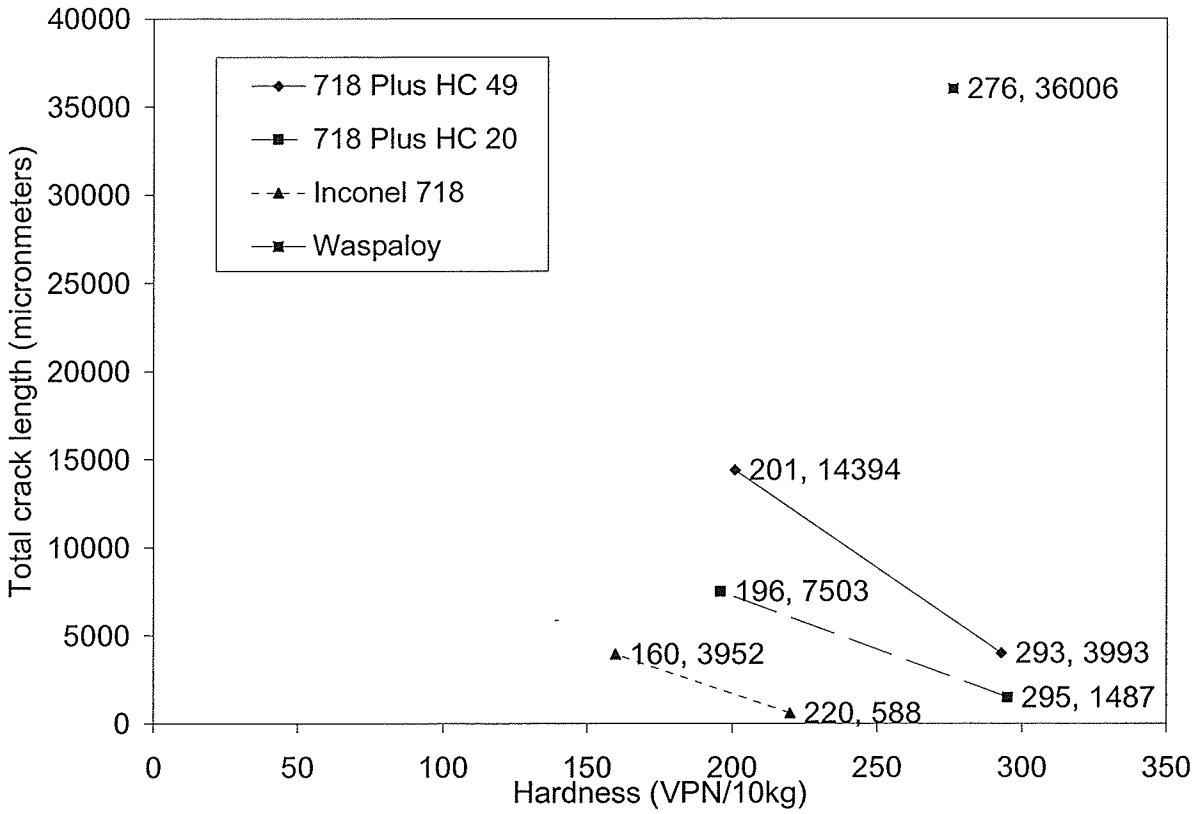

Figure 4.48: Variation of TCL with respect to base-metal hardness of the alloys studied

The effect of grain size on microfissuring in HAZ seems to be better understood than that of hardness. It has been reported that increasing grain size, independent of other variables, increased microfissuring susceptibility. A large grain size would have longer interface sliding length, larger stress concentrations and large strain at grain boundary triple points, all increasing the susceptibility to microfissuring [57]. In earlier studies, the effect of grain boundary segregation was not considered, although it was known that minor alloying elements could potentially decrease the melting point of the grain boundary material. A more precise study on the effect of grain size of Inconel 718, keeping the segregation at the grain boundaries constant by Guo et al. [23] also showed that coarse grain size material had poor hot ductility properties compared to a finer grain size material, which would negatively effect the microfissuring susceptibility. Although a reverse trend from that observed in wrought Inconel 718, was observed in Microcast (MX ^{TM}) Alloy 718 by Huang et al. [59]. It was proposed that more cracking in the smaller grain size resulted from a combination of effects of stress concentration, probability of microfissuring and the number of available cracking sites. Sidhu et al. [123] in their study on directionally solidified Inconel 738, suggested that as the number of grain boundaries in the HAZ that intersect the fusion zone decrease the probability of their microfissuring would decrease. With fewer intersecting grain boundaries, as was the case in directionally solidified Inconel 738 welded in the transverse direction, the number of sites for crack initiation and propagation decreased, leading to reduced cracking compared to the conventionally cast Inconel 738. A review of the literature, hence, suggests that increasing the grain size does increase the cracking, but in a very coarse grain size

material with few grain boundaries intersecting with the fusion zone might actually help reducing the intergranular microfissuring in the HAZ.

In the present study, solution heat treatments were selected so that the variation in grain sizes between the alloys studied was minimum. Inconel 718 and 718 type alloys had very similar grain sizes after the two solution heat treatments. In the 950°C solution heat treated material the grain sizes were in the range of ASTM 5-6 (40μm – 65um) and after the 1050°C solution heat treatment they were in the range of ASTM 3-4 (90μm – 125μm), except for HC 20 718 Plus which had a grain size of ASTM 4.7 (73μm). The 1020°C solution heat treated Waspaloy had a grain size of ASTM 5 (67μm), which is in the same range as observed in other alloys after 950°C heat treatment.

HAZ microfissuring in all the alloys increased with an increase in grain size after solution treatment at higher temperature. Figure 4.49 shows the variation in total crack length with grain size after the two heat treatments. The largest difference in grain size was seen in 718 Plus HC 49 alloy where the grain size increased by a factor of 2.7 from 950°C to 1050°C heat treatment. This was followed by Inconel 718 and 718 Plus HC 20 by a factor of 2 and 1.3 respectively. The increase in HAZ microfissuring, however, did not follow the same trend. The maximum increase in microfissuring was observed in Inconel 718 where the total crack length increased by a factor of 8 from 588μm in 950°C to 4716 um in 1050°C heat treated material. HC 20 718 Plus also showed a similar increase by a factor of 7.3 from 1655μm to 12007μm. After both the heat treatments, maximum total crack lengths were observed in HC 49 718 Plus, however, the increase in cracking was

the least, by a factor of 3.4 from 4073μm in the 950°C material to 13853μm in 1050°C heat treated material.

The grain size of Waspaloy in its standard solution heat treated condition was marginally coarser than in the other alloys in their solution heat treated condition, but the cracking was extensively more than that was observed in any of the three alloys. The single data point in Figure 4.49 corresponding to Waspaloy indicates the significantly more cracking observed in the alloy. The enormous amount of cracking in Waspaloy compared to the other alloys cannot be explained only on the basis of grain size difference. Interestingly, the grain size of 1050°C solution treated HC 20 718 Plus alloy was 75μm, which is very close to that of Waspaloy (65μm) but cracking in Waspaloy was three times more.

The grain size effect cannot completely account for the increase in cracking in all the alloys, and as will be explained later in the section 4.3.4, grain boundary segregation played a significant role in determining the extent of cracking in the alloys. Like grain size, grain boundary segregation varies with the heat treatment, and in the present case it can explain the observed increase in cracking in 718 Plus alloys adequately.

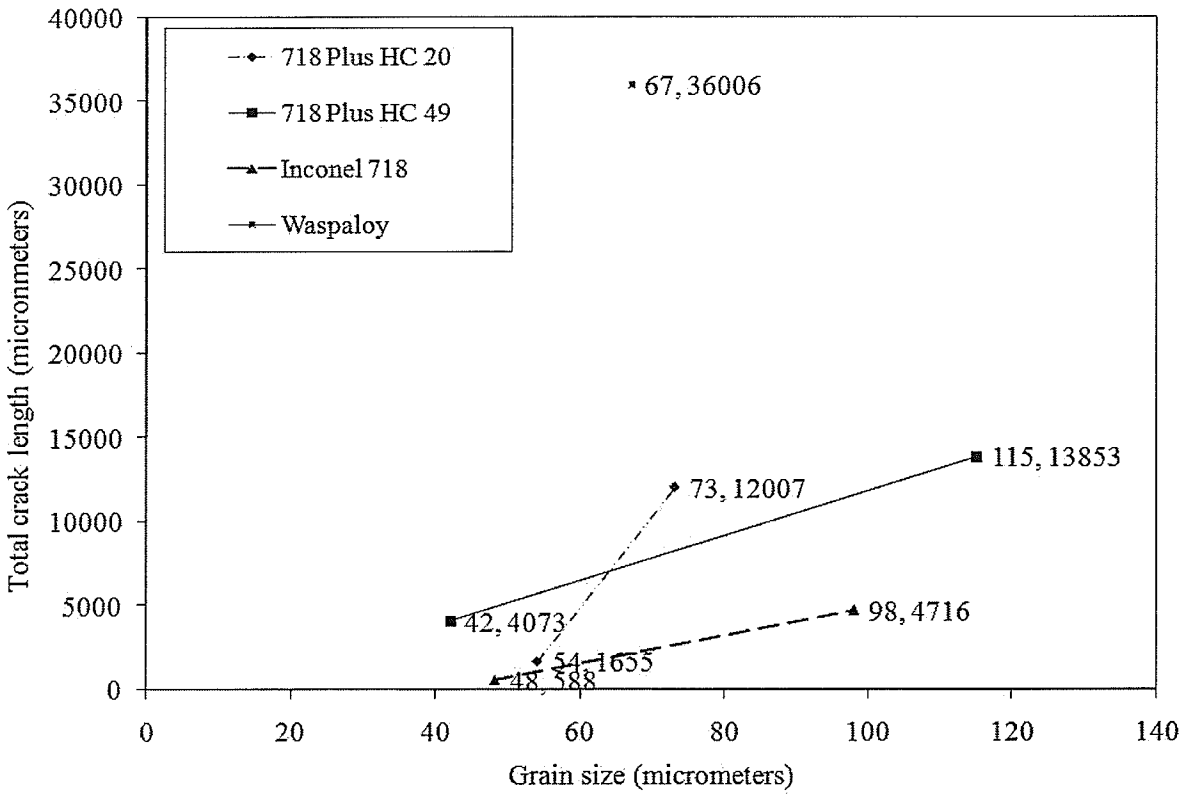

Figure 4.49: Variation in total crack length with grain size in all the alloys

4.3.3 Gleeble hot ductility measurements

Hot ductility is often used to evaluate a material's susceptibility to HAZ microfissuring. Intergranular microfissuring in HAZ occurs due to liquation of grain boundaries by constitutional liquation of grain boundary precipitates or due to segregation of melting point depressant elements on them. The liquated grain boundaries reduce the ductility of the material to almost zero and it is unable to withstand the welding stresses, resulting in the formation of intergranular microfissures. Therefore, the weldability of a material can be related to its ductility at higher temperatures, which can be measured by Gleeble thermo mechanical simulator.

Hot ductility measurements were made on Inconel 718 and, HC 20 and HC 49 718 Plus alloys but similar experiments performed on Waspaloy were not successful due to the defective as-received material, and are not included in the discussion. Weldability comparisons were made for two different sets of materials with different specimen dimensions:

a) ***10 mm diameter specimens***

   Threaded test samples of Inconel 718, 718 Plus HC 20 and 718 Plus HC 49 were supplied by ATI-ALLVAC Inc.. These were prepared from the same heat as the hot rolled plates used for weld cracking measurements.

b) ***6 mm diameter specimens***

   6mm diameter rods of Inconel 718 were acquired from a commercial source and high B and P HC 49 718 Plus alloy was supplied by ALLVAC. Since these rods were obtained from different sources it was difficult to correlate their hot ductility

results with the weld cracking results obtained earlier. Hence, weld assemblies were made from these rods and electron beam welding was performed using the same welding parameter as used earlier for the hot rolled plates. The weld cracking measurements are reported and discussed here.

The dimensions of the sample and the various testing parameters used for evaluation of hot ductility parameters were discussed in the experimental section and are listed in Table 3.3. All the samples were given the standard commercial solution heat treatment of 950°C for 1 hour followed by water quenching.

(a) 10 mm diameter specimens

Inconel 718 and the two 718 Plus alloys were heated at a rate of 150°C/s to different test temperatures and then pulled to fracture. The reduction in cross-sectional area of the samples was measured and plotted against the test temperature, as shown in Figure 4.50. Generally, beyond a certain temperature, ductility of an alloy starts to decrease with further increase in temperature. As can be seen from the curve, hot ductility of all the samples was already on the decreasing side of the curve at the lowest test temperatures used. The on-heating ductility curves of all the three alloys were very similar, and the nil ductility values (NDT) of the three alloys were within 10°C of each other (Table 4.11). Inconel 718 had the lowest NDT of 1160°C, followed by HC 20 718 Plus of 1165°C, while the high B and P alloy HC 49 718 Plus had the highest NDT of 1170°C. Although, the observed minor difference in NDT values is likely to be within the statistical scatter, and may not be significant.

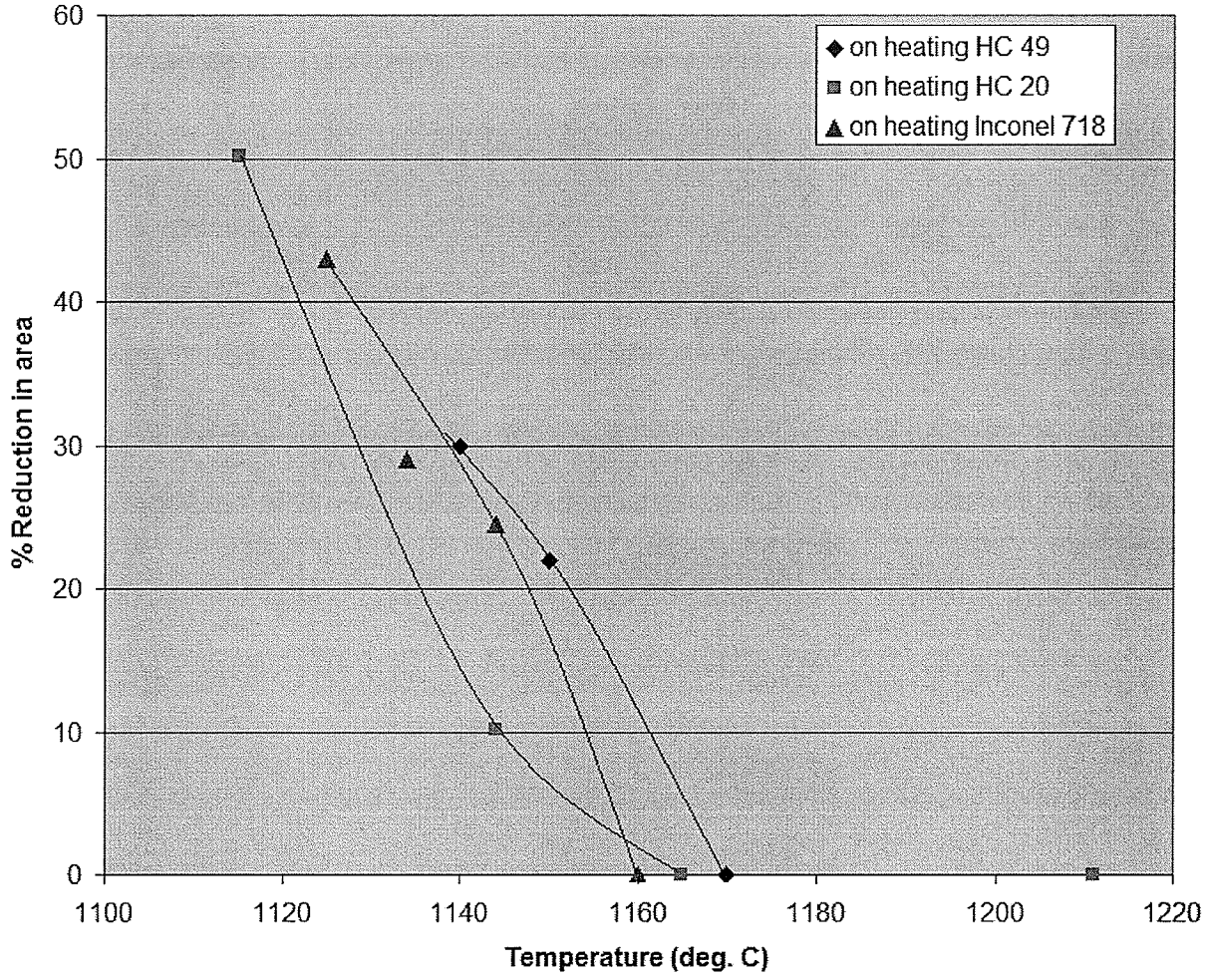

Figure 4.50: On-heating hot ductility values of Inconel 718, HC 20 718 Plus and HC 49 718 Plus alloy

Table 4.11: Hot ductility testing parameters for Inconel 718, HC 20 718 Plus and HC 49 718 Plus

Material	NDT	DRT	BTR = 1200°C – DRT
Inconel 718	1160	1065	135
Low B+P HC 20	1165	1055	145
High B+P HC 49	1170	1010	190

The on-cooling tests were performed after heating the specimens of the three alloys to a peak temperature of 1200°C. A specimen heated to a peak temperature (T_P) essentially represents that portion of the HAZ material that experiences this temperature during the heating cycle of actual welding. For a better understanding of the HAZ microfissuring, temperatures higher than the temperature where grain boundary liquation starts are selected as T_p. Although some researchers report that grain boundary liquation is encountered at NDT, temperatures above NDT are generally selected as T_p. In the present case, the peak temperature was more than 25°C higher than the NDT values of all the three alloys. As the NDT values were very similar, the same T_p was used for all the alloys, which yielded a better comparison of their hot ductility behavior. The values of on-cooling ductility are plotted in Fig. 4.51. Unlike on-heating values, on-cooling ductility curves of each alloy were found to be considerably different, and the results are also listed in Table 4.11. Inconel 718 recovered its ductility at 1065°C on cooling from 1200°C, which yields a brittle temperature range (BTR) of 135°C. HC 20 718 Plus had a DRT of 1055°C, with a BTR of 145°C. The biggest BTR, 190°C, was observed in HC 49 718 Plus, with a DRT at 1010°C. The results indicate that Inconel 718 has a better on-cooling hot ductility as compared to that of 718 Plus alloys. It is to be noted that hot-ductility value of HC 20 718 Plus was only marginally worse than that of Inconel 718. Of the two 718 Plus alloy, DRT value of the higher B and P alloy, HC 49, was 45°C lower than that of the lower B and P alloy. Similarly the BTR range of higher B and P alloy was larger than that of the lower B and P alloy.

The values of reduction in area by on-heating and on-cooling tests of the three alloys are listed in Tables 4.12 through 4.13 respectively.

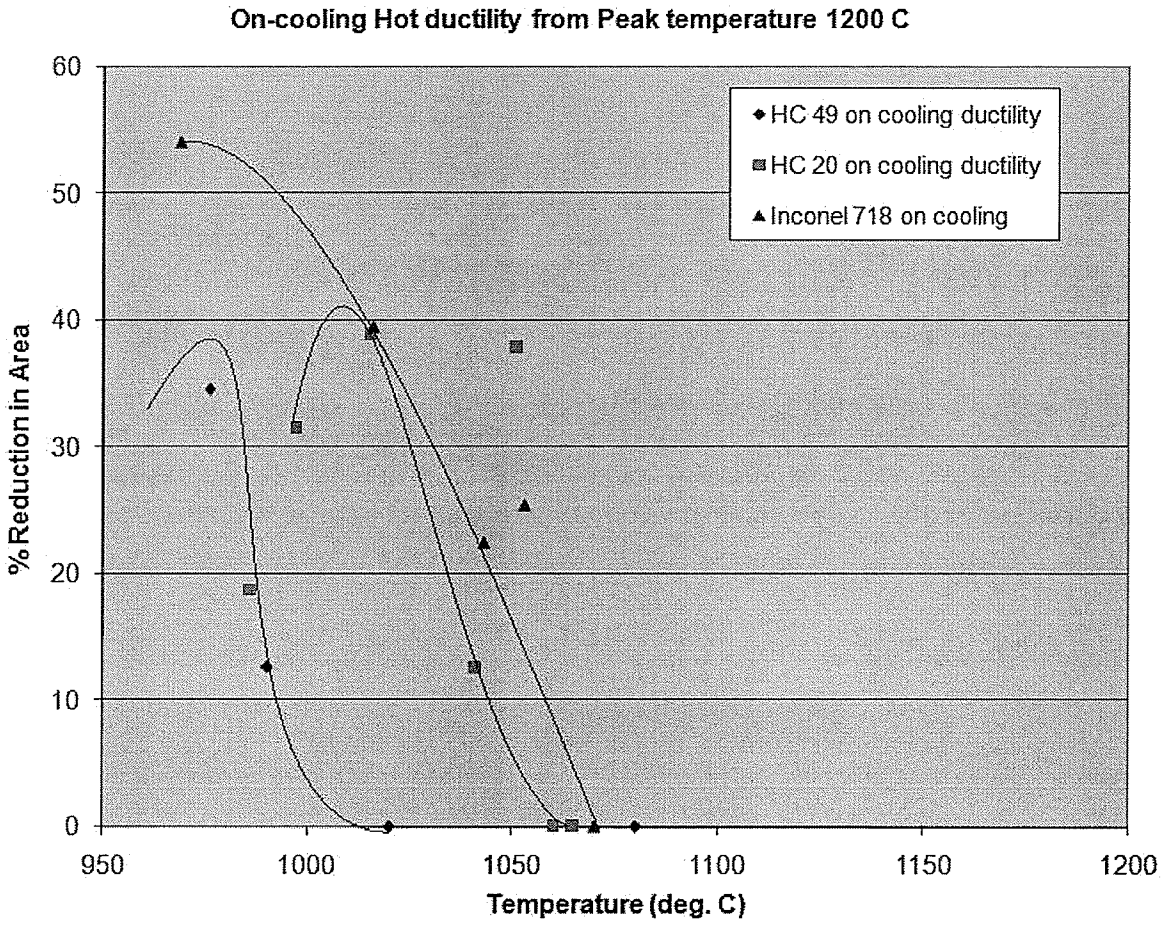

Figure 4.51: On-cooling hot ductility values of Inconel 718, HC 20 718 Plus and HC 49 718 Plus alloy

Table 4.12: On-heating reduction in area values of Inconel 718 and 718 Plus 10 mm diameter specimens

Inconel 718		718 Plus HC 20 (Low B+P)		718 Plus HC 49 (High B+P)	
Temperature	% RA	Temperature	% RA	Temperature	% RA
1125	43	1115	50.2	1140	30
1134	29	1144	10.1	1150	22
1144	24.6	1165	Nil	1170	Nil
1160	Nil	1211	Nil		

Table 4.13: On-cooling reduction in area values of Inconel 718 and 718 Plus alloys

10 mm diameter specimens

Conventional Inconel 718		Low B+P HC 20		High B+P HC 49	
Temperature	% RA	Temperature	% RA	Temperature	% RA
969	54.13	986	18.8	976	34.6
1016	39.53	997	31.5	990	12.7
1043	22.5	1041	12.6	1020	nil
1053	25.5	1051	38.9	1080	nil
1070	Nil	1051	37.9		
		1060	Nil		
		1065	Nil		

The hot-ductility behavior of Inconel 718 and HC 20 718 Plus alloy was very similar, with very small brittle temperature ranges. This indicates that their susceptibility to HAZ microfissuring should also be very similar in the 950°C solution heat treatment condition. The weld cracking behavior of the two alloys, as was discussed in section 4.3.2., indicated that HAZ of Inconel 718 was one-third of the cracking observed in HC 20 718 Plus (59μm compared to 149μm). The difference in the amount in cracking seems proportionally higher than the difference in their BTRs, although the trend remained the same, with Inconel 718 showing better resistance to microfissuring.

Comparison between the two 718 Plus alloys showed a more discernible difference. While the on-heating ductility values were not much affected, it was observed that higher amounts of B and P significantly reduced the on-cooling hot ductility values as indicated by the DRT values of both the alloys. Higher B+P alloy had a lower DRT value and a larger brittle temperature range (Table 4.11). This further suggests that intergranular liquid in the HC 49 would remain liquid to lower temperatures during cooling of the weld, which would make the alloy more susceptible to cracking. B has been known to affect the on-cooling hot ductility of Inconel 718 [23, 47], and a similar effect was seen in 718 Plus alloys. The presence of B and P increased the solidification range of 718 Plus alloys. This corroborates with the weld cracking measurements where HC 49 718 Plus had a TCL of 399μm compared to 59μm in HC 20 718 Plus alloy.

(b) 6 mm diameter specimens

120mm long samples were cut from 6mm diameter rods of Inconel 718 and HC 49 718 Plus alloy and threaded on both the ends. These samples were then solution heat treated at 950°C for 1 hour in argon protected atmosphere followed by water quenching. As these alloys were from different sources and different heats than the earlier alloys, their microstructural characterization was done prior to hot-ductility testing.

Figures 4.52 and 4.53 show optical micrographs of solution heat treated Inconel 718 and HC 49 718 Plus alloy, respectively. As can be seen, Inconel 718 had a very fine grain size with extensive inter and intra-granular precipitation of δ phase. In comparison, HC 49 718 plus had an average grain size of 42μm and very little δ phase precipitation. Hardness and grain size values of both the alloys in this heat treatment condition are listed in Table 4.14.

The on-heating ductility values of Inconel 718 and HC 49 718 Plus alloy are shown as a plot of reduction in area vs. temperature in Figure 4.54. As can be seen from the plot, at lower test temperatures, Inconel 718 had higher ductility than HC 49 718 Plus, but at higher temperatures the ductility rapidly dropped off and was reduced to zero at 1150°C. The NDT of HC 49 718 Plus was also observed to be 1150°C. Like the 10 mm diameter specimens, the on-heating ductility of the two alloys was very similar. The reduction in area values with the temperatures are also listed in Table 4.14.

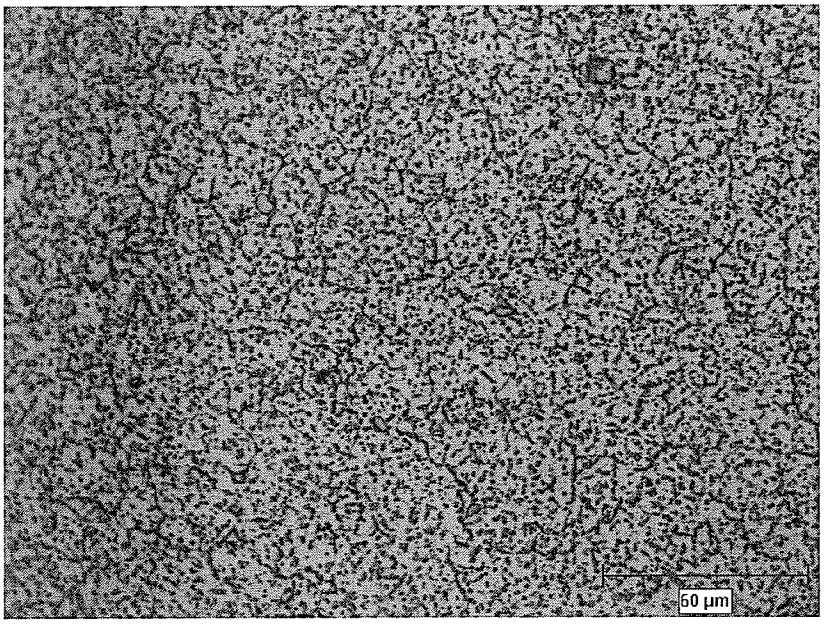

Figure 4.52: Initial microstructure of 6mm diameter Inconel 718 specimens after 950°C solution heat treatment

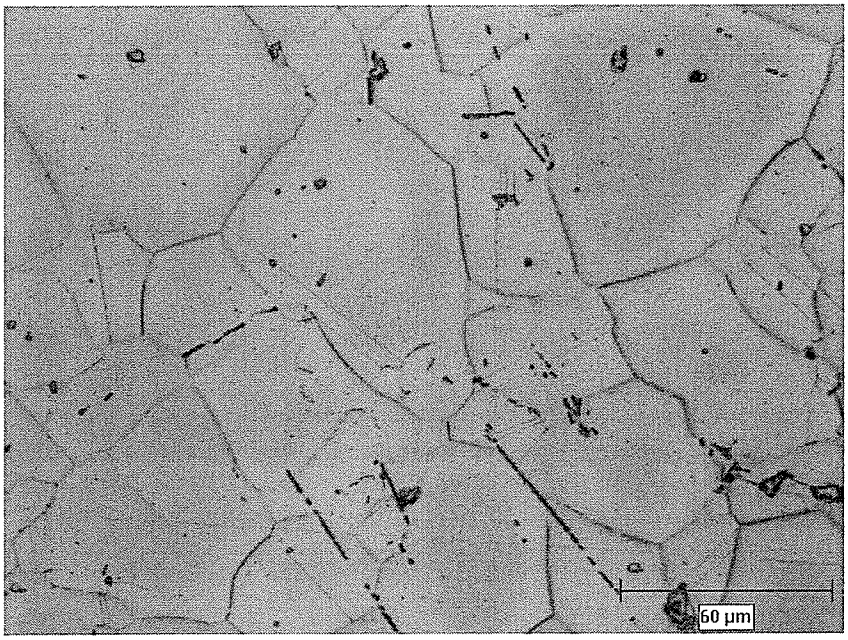

Figure 4.53: Initial microstructure of 6mm diameter 718 Plus HC 49 specimens after 950°C solution heat treatment

Table 4.14: Grain size and hardness values of 6 mm diameter Inconel 718 and 718 Plus alloys prior to hot-ductility testing

Alloy	Heat treatment	Hardness	Grain – size (μm)
Inconel 718	950°C for 1 hr followed by water quenching	277 ± 10	< 10
Allvac 718 Plus	950°C for 1 hr followed by water quenching	195 ± 6	43 ± 1

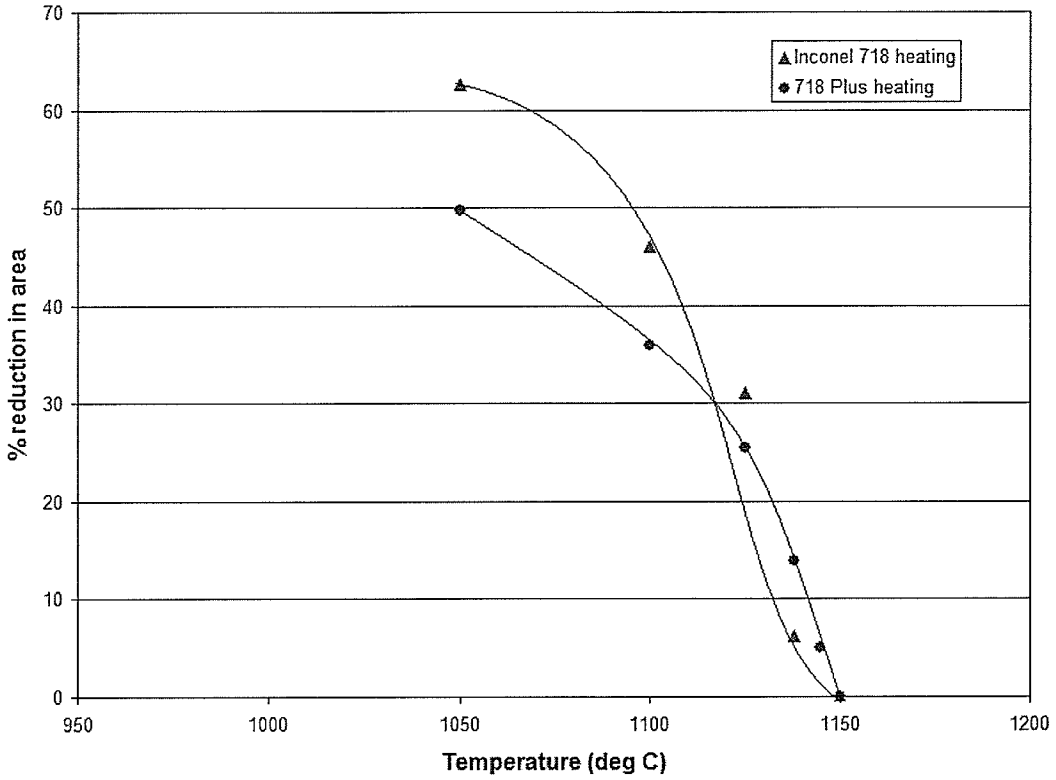

Figure 4.54: On-heating hot ductility values for HC 20 718 Plus and Inconel 718 6mm diameter samples

Table 4.15: Values of reduction in area (hot-ductility) during on-heating testing of 6mm dia. samples of Inconel 718 and high P and B 718 Plus alloy

High B+P 718 Plus		Inconel 718 HT 1	
Temperature	% RA	Temperature	% RA
1050	49.76	1050	62.54
1100	35.96	1100	46.08
1125	25.4	1125	31.14
1138	13.96	1138	6.2
1145	5.1	1150	Nil
1150	nil		

The on-cooling hot ductility tests were carried out from a peak temperature of 1200°C. The percentage reduction in area vs. temperature plot is shown in Figure 4.55. Inconel 718 recovered its ductility at 1000°C earlier whereas HC 49 718 Plus had a ductility recovery temperature of 950°C, which was 50°C lower than that of Inconel 718. As was mentioned earlier, 6 mm diameter specimens of Inconel 718 had a very fine grain size (less than 10μm). Fine grain size improved the hot-ductility of the material, as was observed in Inconel 718 by Guo et al. [47], and hence reduced the HAZ susceptibility of the alloy. To ensure that the higher DRT of Inconel 718 was not entirely due to its finer grain size, it was necessary to compare hot ductility of the alloys with specimens of similar grain sizes. Also, with a grain size of less than 10μm, Inconel 718 had very high hardness (299 VPN) compared to HC 49 718 Plus alloy. This difference in grain size and hardness was not considered desirable for weldability comparisons by hot ductility testing, although the alloys were to be compared in their solution treated condition. Hence another batch of Inconel 718 alloy was given a modified solution heat treatment so that the grain sizes and hardness were closer to that of 718 Plus alloy. After a series of tests at different solution heat treatments, it was found that 1000°C solution heat treatment resulted in a grain size of 46μm (Figure 4.56) which was similar to that of 718 Plus samples. Also the hardness of the alloys was comparable.

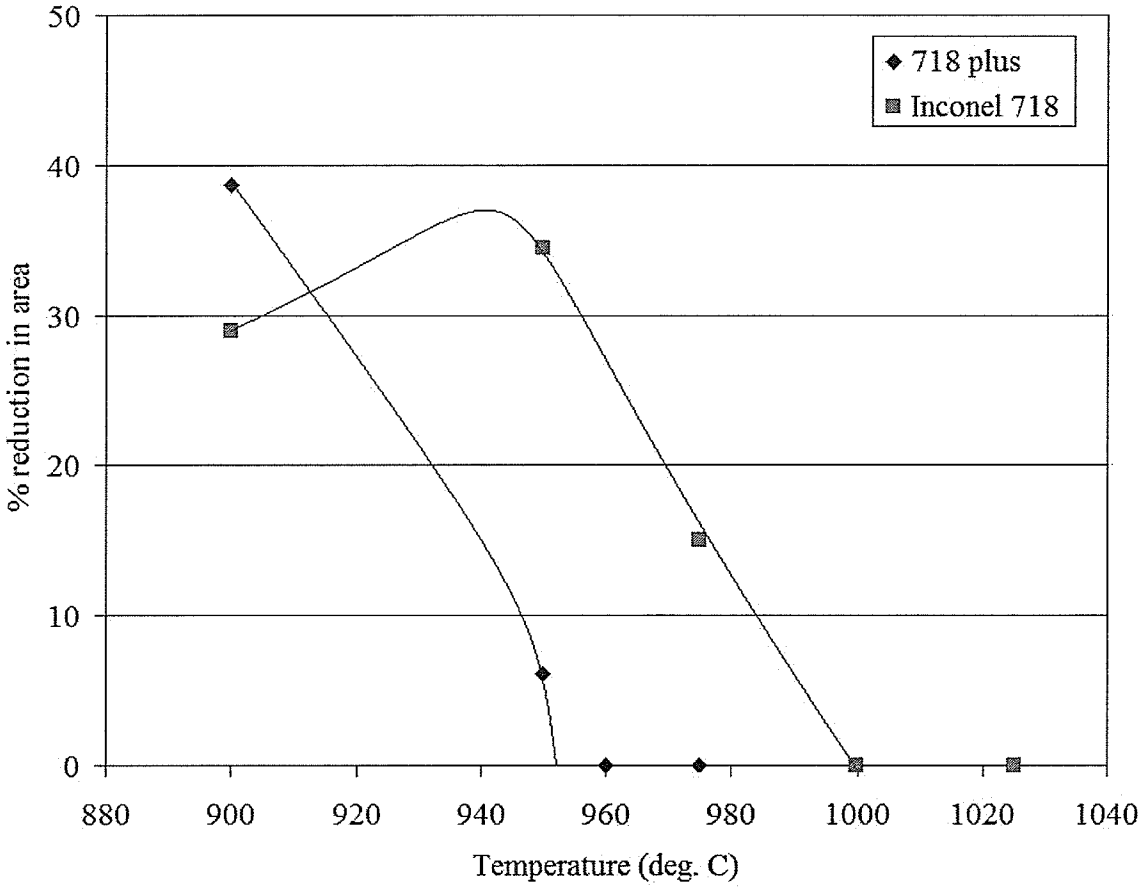

Figure 4.55: On-cooling hot ductility values of Inconel 718 and 718 Plus HC 49 6mm diameter specimens

Besides the grain size and hardness, 1000°C solution heat treatment would also change the segregation at the grain boundaries and it would be different than in the 950°C solution heat treated specimen. Intergranular segregation, especially that of boron and phosphorus, as would be addressed later, was a primary concern in this study and one of the main parameters to affect HAZ microfissuring. Although the concentration of B and P were different in both the alloys, the contribution of heat treatment and grain size effect on segregation could be maintained at the same level by subjecting the alloys to the same solution heat treatment temperatures. Therefore, the second batch, which was given a solution heat treatment at 1000°C, was again heat treated at 950°C for 1 hour followed by water-quenching. The two heat treatments for Inconel 718 are referred as HT 1 and HT 2 where,

HT 1 is 950°C/1hr followed by water quenching

HT 2 is 1050°C/1hr followed by water quenching.

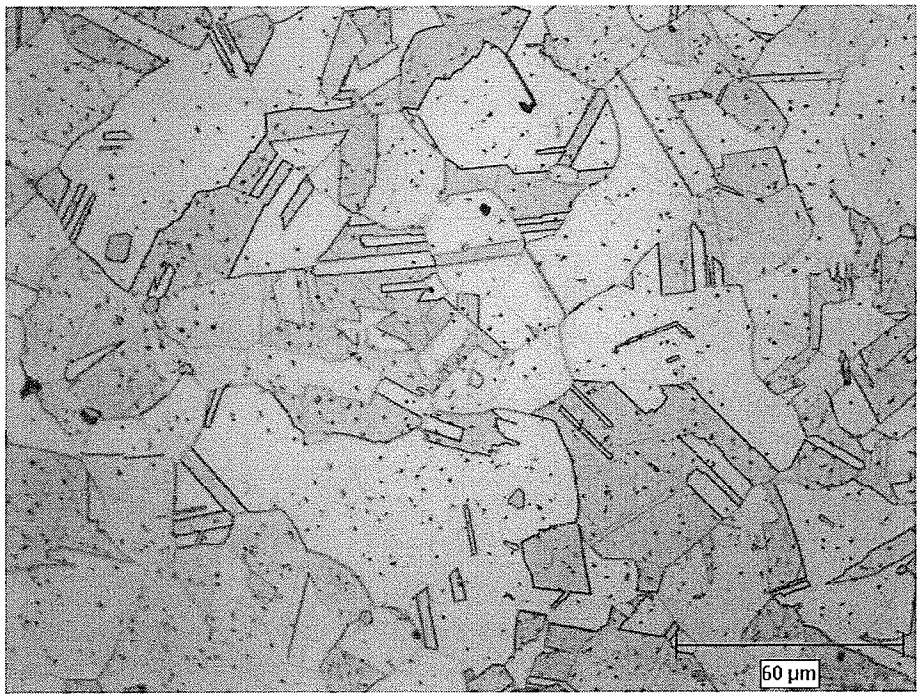

Figure 4.56: Microstructure of Inconel 718 6mm diameter samples after a modified heat treatment of 1000°C/1hr, water quenched + 950°C/1hr, water quenched (Heat Treatment 2)

Figure 4.57 shows a comparison of the on-cooling hot ductility behavior of HC 49 718 Plus and Inconel HT 1 and Inconel HT 2. The data points on the x-axis are normalized with respect to the peak temperature so that it has the co-ordinates of °C below the peak temperature. Essentially, on the x-axis the brittle temperature range for each alloy are plotted, which is the difference between the T_p and the DRT. The DRT of Inconel 718 with the modified heat treatment, HT 2, was 25° higher than that of HC 49 718 Plus and 25°C lower than that of HT 1 heat treated Inconel 718. Thus the BTR of the HT 2 Inconel 718 was in between that of HT1 Inconel 718 and HC 49 718 Plus. These results confirm that increase in grain size deteriorates the recovery of on-cooling ductility in Inconel 718, nevertheless the values were higher than that of 718 Plus alloy.

The reduction in area values of the alloys at different on-cooling test temperatures are listed in Table 4.16 and the on-cooling hot ductility parameters are summarized in Table 4.17.

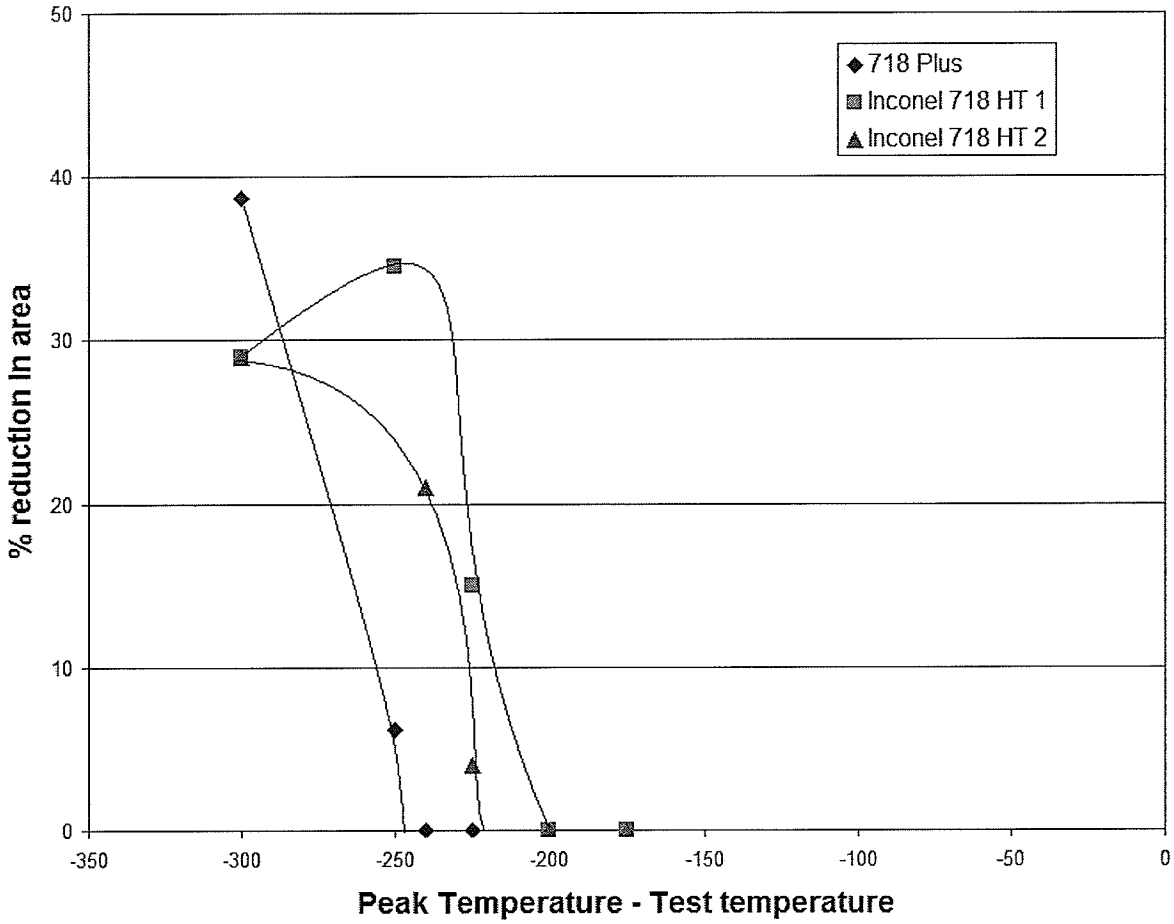

Figure 4.57: On-cooling hot ductility values of HC 20 718 Plus and Inconel 718 6mm diameter samples

Note:

Inconel 718 HT 1: Heat treated at 1000°C for 1 hr followed by water quenching + Heat treated at 950°C for 1 hr followed by water quenching

Inconel 718 HT 2: Heat treated at 950°C for 1 hr followed by water quenching

Table 4.16: Values of percentage reduction in area (hot-ductility) during on- cooling testing of 6 mm dia. samples heated to 1200°C

High B+P HC 49		Inconel 718 HT 1		Inconel 718 HT 2	
Temperature	% RA	Temperature	% RA	Temperature	% RA
900	38.6	900	29	900	29
950	6.2	950	34.5	960	21
1000	Nil	975	15	975	4
		1000	nil	1000	Nil

Table 4.17: Hot ductility parameters determined by hot-ductility testing of 718 Plus and Inconel 718

Parameters	718 Plus	Inconel 718 HT 1	Inconel 718 HT 2
On heating NDT	1150	1140	-
On heating Peak temperature T_p	1200	1200	1200
On cooling DRT	950	1000	975
BTR	250	200	225

To co-relate the hot ductility measurements of the 6 mm diameter samples with weld cracking, crack measurements were done on welded alloys. As these alloys were obtained from different sources, it was desirable to subject them to similar heat treatments and welding conditions for proper comparison. Inconel 718 and HC 49 718 Plus rods were solution heat treated at 950°C for 1 hour followed by water quenching. 6 mm diameter rods were first machined to remove the oxide layer. 12 mm long sections were cut from these rods and then tack-welded together using TIG welding technique on an Inconel 718 base plate to produce an assembly, illustrated in Figure 4.58. These samples were then electron beam welded using the same process parameters that were used for welding the hot-rolled plates, that is, 44 KV voltage, 79 mA current and 154 cm/min speed. Five transverse sections were cut from these samples and metallographically prepared for microstructural examination and crack measurements. Average total crack length was measured in both the alloys.

Figure 4.59 shows an example of intergranular microfissuring in HC 49 718 Plus alloy in the HAZ. The characteristics of microfissures were similar to those observed in the plate - samples of 718 Plus alloys. Constitutionally liquated Nb rich MC type carbides and Ti rich carbonitrides were also observed in the microstructure. The resolidified product of Laves + gamma eutectic was observed on the grain boundaries. The total average crack length in 5 sections was 1084μm ± 549 with a maximum crack length of 315μm.

Interestingly, no microfissuring was observed in Inconel 718 samples, although excessive intergranular and intragranular liquation was observed in the microstructure, as shown in Figure 4.60.

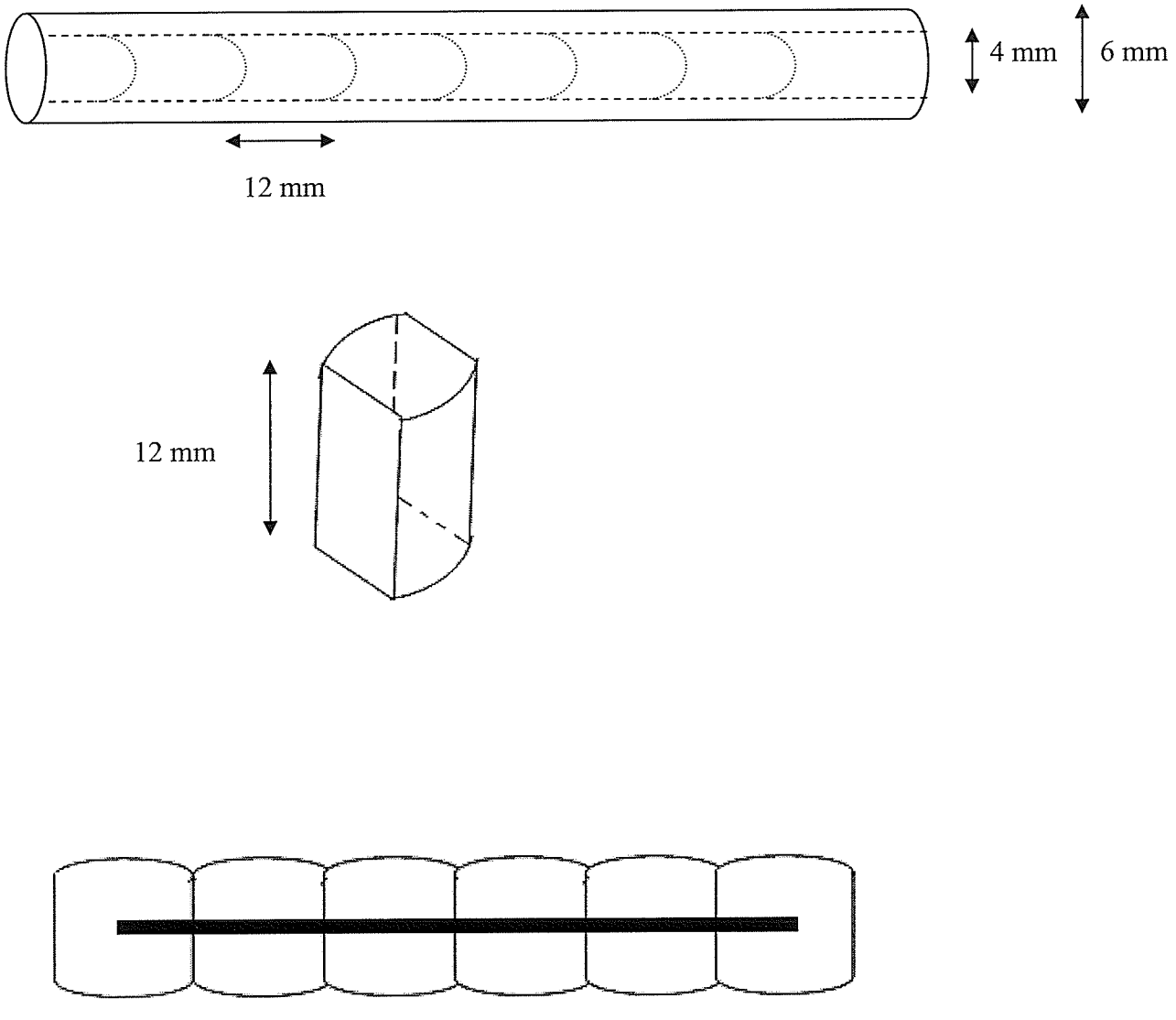

Figure 4.58: Schematic diagram of electron beam welding specimens (Tack-welded assembly of 6 mm diameter specimens)

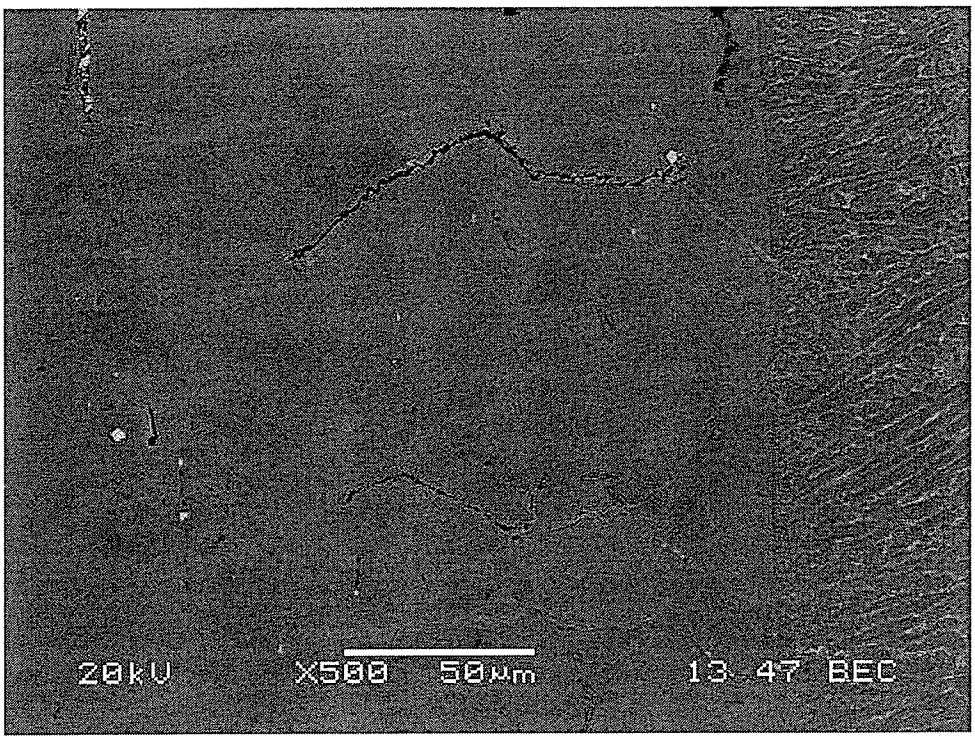

Figure 4.59: Intergranular microfissuring in HC 49 electron beam welded samples made out of 6 mm diameter rods

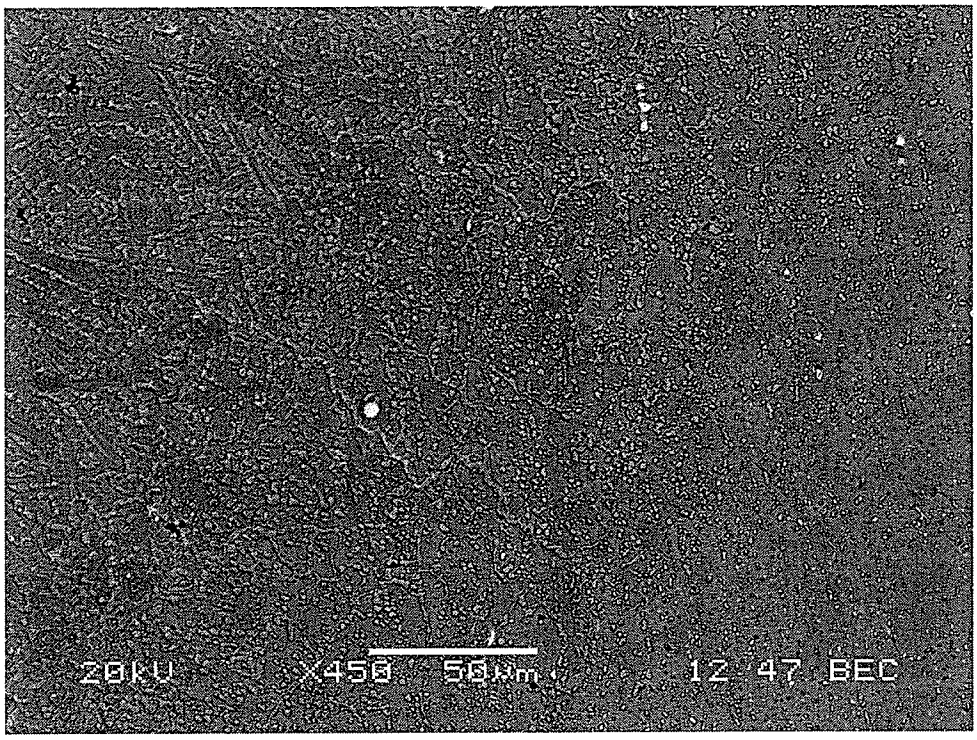

Figure 4.60: Fusion zone and HAZ of Inconel 718 showing intergranular and intragranular liquation

Figure 4.61 shows a constitutionally liquated Ti rich carbonitrides phase in the HAZ of Inconel 718 weld. Partially melted δ phase is also seen in the region around the liquating particle. The pre-weld microstructure of Inconel 718 had excessive precipitation of δ phase in it, as shown in the higher magnification SEM micrograph in Figure 4.62. Partially melted δ phase contributed to most of the liquation observed in the microstructure, besides constitutional liquation of NbC particles. Very fine grain size could be the primary reason for absence of any cracking in the material.

The crack measurements and the hot ductility measurements show that HAZ cracking resistance of Inconel 718 was better than that of 718 Plus HC 49 alloy. These results also corroborate the earlier analysis done on the hot rolled plates and 10 mm diameter specimens of 718 Plus alloys and Inconel 718.

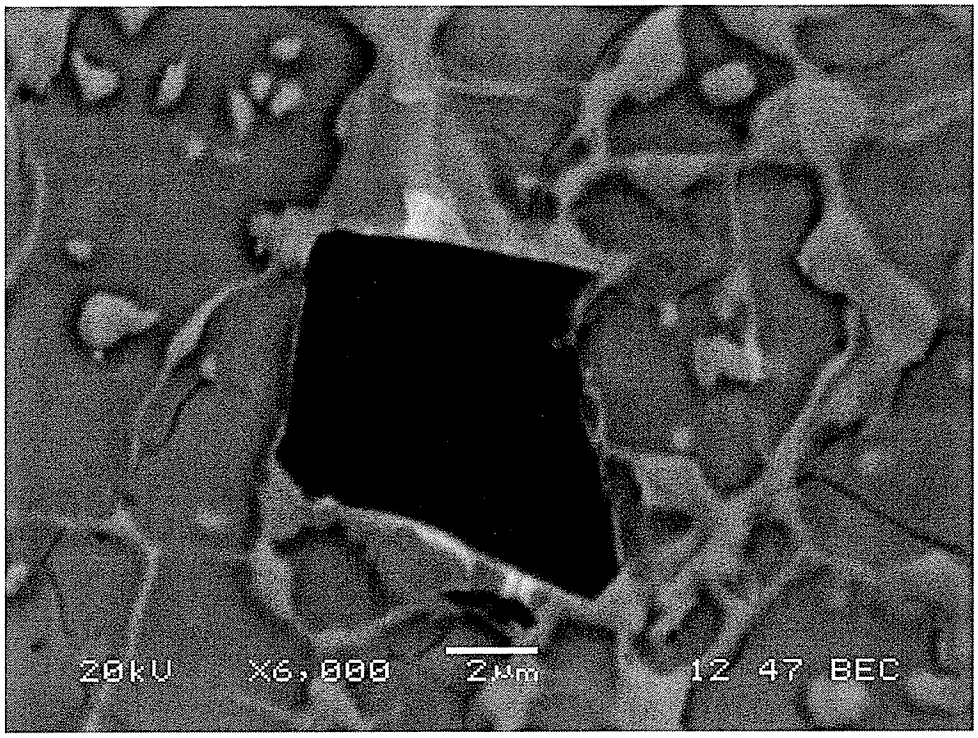

Figure 4.61: Constitutionally liquating Ti rich carbonitride particles surrounded by partially melted δ phase

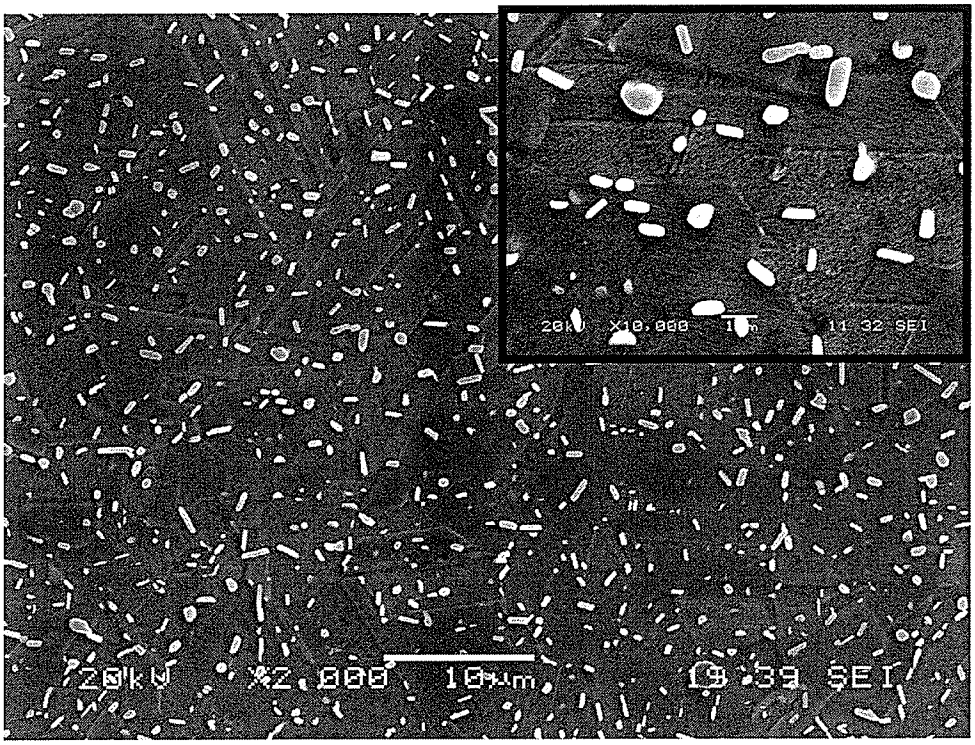

Figure 4.62: Pre-weld microstructure of Inconel 718 (6mm diameter) after 950°C/1hr solution heat treatment

4.4 Secondary Ion Mass Spectroscopy (SIMS)

4.4.1 Introduction:

Superalloys frequently encounter manufacturing and repair welding problems and it has been observed that minor alloying elements have an important role in determining their weldability [43]. The presence of elements like boron[46, 49, 50], sulphur [51, 124], carbon and phosphorus[43, 53] are known to adversely affect weldability of superalloys. The chemical composition of 718 Plus alloy is considerably different than that of the baseline superalloy Inconel 718, and unlike other superalloys, boron and phosphorus were intentionally added to improve creep properties. While, B is known to have beneficial effects on creep properties, presence of P was generally considered to be deleterious to mechanical properties of high temperature alloys. However, recent studies by Cao et al. [125-128], on the effect of boron and phosphorus on creep properties in conventional Inconel 718, suggested that there exists a synergistic effect of boron and phosphorus in improving the grain boundary cohesion. A possible interaction of these elements with the dislocations/vacancies, which eventually improved the creep properties, was also suggested. In comparison to the commercial alloy, stress rupture life of the alloy with high P and B levels increased by approximately three times. The proposed optimum levels of P and B were observed to be 0.022 wt% and 0.012 wt%, respectively. In addition, Song et al. [129] studied the individual effect of phosphorus in Inconel 718, and concluded that phosphorus inhibits grain boundary diffusion and has a notable effect on primary creep of the alloy. 718 Plus alloy was thus developed with intentional additions of B and P and it exhibits better creep properties than conventional Inconel 718[1].

Boron and phosphorus which are melting point depressants of nickel austenitic matrix, segregate to grain boundaries and affect the grain boundary free energy. SIMS analysis has revealed the elemental segregation of B [46], and the deleterious effect of B on weldability has been widely reported [43, 45, 49]. On the contrary, limited direct evidence of segregation of P exists in literature [130, 131]. Although P segregation has been investigated, most of the studies were focused on the effect of P on creep properties. Also, inadequate information is available on the co-segregation of B and P partly due to limitations of the experimental techniques to detect them simultaneously. In order to understand the effects of B and P on the weldability of 718 Plus alloy, two alloys with different B and P contents were studied. This section discusses the occurrence of elemental segregation of B and P in these alloys prior to and after welding in two different pre-weld heat treated conditions. Grain boundary segregation was examined by Cameca IMS-7f magnetic sector Secondary Ion Mass Spectrometer.

4.4.2 Segregation of B and P in solution heat treated condition:

The SIMS analysis did not reveal any segregation of B or P in the 950°C solution heat treated condition, although 1050°C heat treated specimen did show some grain boundary segregation of B in both the alloys. It was not possible to quantify the segregation of B using SIMS; however, the intensity of B image did provide a qualitative indication of its concentration. As seen in Figure 4.63a and 4.63b, the higher B + P alloy, HC 49, exhibited a higher intensity of B ion image, and hence a greater segregation of B compared to HC 20 with normal concentrations of B and P. SIMS was also used to

frequently detect carbon, and occasionally, both C and B were found to be present in some particles. This suggested that, in addition to being segregated at grain boundaries in elemental form, B was also present in some particles as boro-carbide. Phosphorus could not be detected in either of the two alloys, even in the 1050°C pre-weld heat treated condition.

It was observed that when the pre-weld solution heat treatment temperature was increased from 950°C to 1050°C the segregation of B on the grain boundaries increased in both the alloys and was revealed by SIMS. Elements can segregate by two segregation mechanisms, namely, equilibrium segregation first proposed by McLean [54] and by non-equilibrium mechanism first proposed by Aust et al.[132]. The former decreases with increase in the heat treatment temperature due to an increase in the diffusion coefficient of solute atoms, which helps reduce the solute concentration gradient that may exist in an alloy. The non-equilibrium segregation occurs during cooling of the material from the heat treatment temperature. It first involves formation of solute-vacancy complexes at the heat treatment temperature provided the free energy of the system is reduced by their formation i.e., an attraction exists between solute and vacancies. During cooling from the solution treatment temperature the equilibrium concentration of vacancies within the grains decreases. This causes a concentration gradient to develop between vacancies and vacancy-solute complexes within the grains and at the grain boundaries. Under this concentration gradient vacancies and vacancy-solute complexes diffuse to the grain boundaries. At the grain boundaries vacancies are absorbed and the solute atoms are deposited. Since, the equilibrium concentration of vacancies increases with temperature,

the concentration of vacancy-solute complex and hence the non-equilibrium segregation of solute at the grain boundaries also increases with an increase in solution treatment temperature. This would explain the observed increase in B concentration in the specimen heat treated at 1050°C as compared to 950°C.

Another factor that may affect the grain boundary segregation of an element is the grain size because as the grain size increases the total grain boundary area available for segregation to occur decreases. Faulkner's model for non-equilibrium segregation also predicted that grain size has an impact on non-equilibrium segregation; larger grain size leads to higher segregation intensity. When the solution treatment temperature was increased the grain size of the material also increased. However, the increase in the higher B and P alloy (HC 49) was much more significant from 42μm to 116μm as compared to that in lower (HC 20) B and P alloy. Therefore, the grain size effect on segregation would be more significant in HC 49 than in HC 20. Therefore, though the segregation of B could not be quantified, the qualitatively observed increase in the segregation of B in higher B and P alloy would be due to:

1. reduced grain boundary area in the higher B + P alloy due to its larger grain size after 1050°C treatment
2. higher initial B concentration

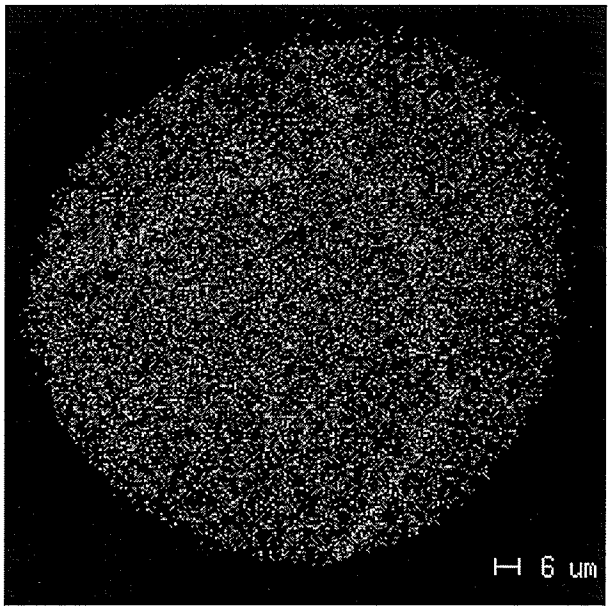

(a)

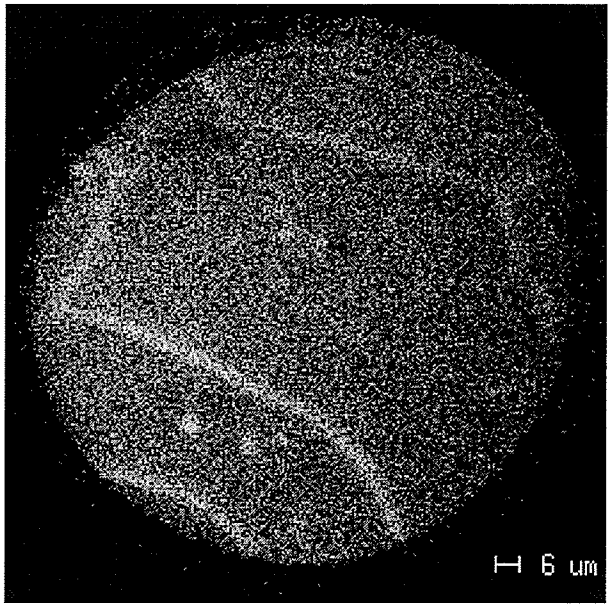

(b)

Figure 4.63: SIMS image of boron after 1050°C/1hr solution heat treatment in (a) HC 20 (low boron + phosphorus alloy) (b) HC 49 (high boron + phosphorus alloy)

4.4.3 Segregation of B and P after welding:

HAZ and fusion zones around the microfissures were examined for any possible segregation of B, P, Nb and C, along with other alloying elements. While analyzing other alloying elements using either O^{2+} or Cs^{+} ion beam, all the images were recorded at the same operational parameters and settings. The microfissures were first examined for B using an O_2^{+} beam and subsequently the same areas were re-analyzed for P using a Cs^{+} ion beam. P mass calibration was first done in a 150 keV P implanted into Si standard (dose: 1×10^{14} atoms/cm^2) and the same operating parameters were used for the subsequent analysis. B and P ion images acquired from microfissures in the HAZ of HC 49 alloy are shown in Figures 4.64 and 4.65. Figures 4.64a and 4.65a show segregation of P on the microfissures marked X and Y respectively. Boron images (Figs.4.64b, 4.65b) show B segregation at the same location as P segregation, suggesting co-segregation of B and P.

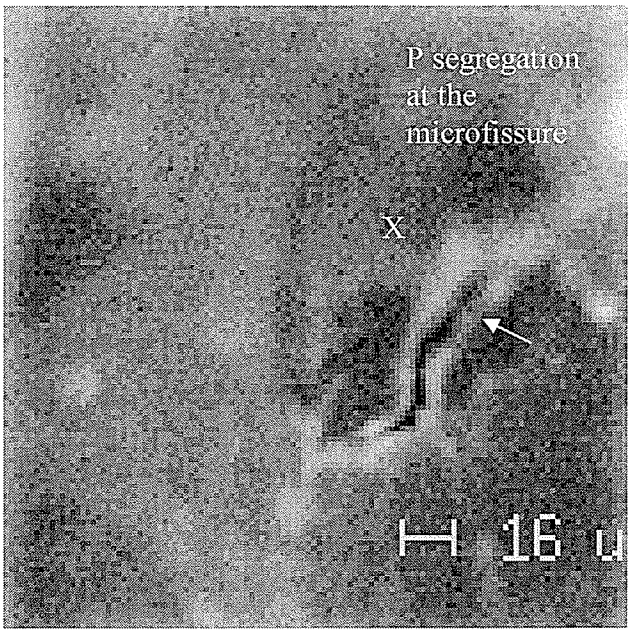

(a)

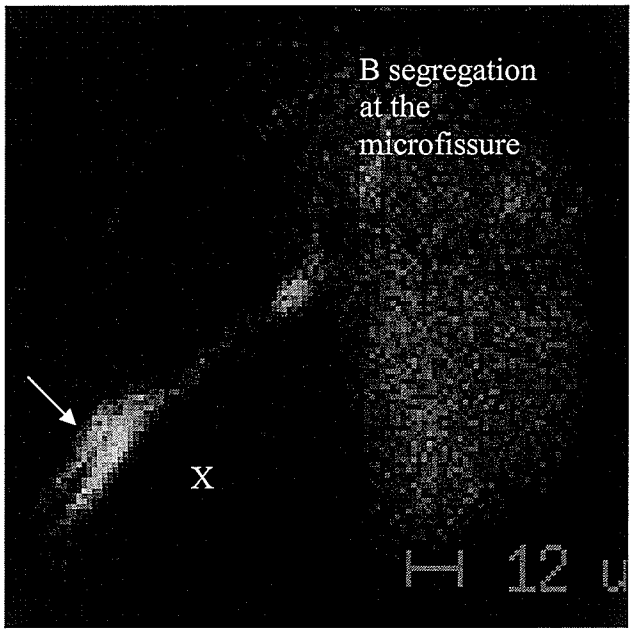

(b)

Fig. 4.64: Secondary ion image of (a) phosphorus and (b) boron at HAZ crack in HC 49

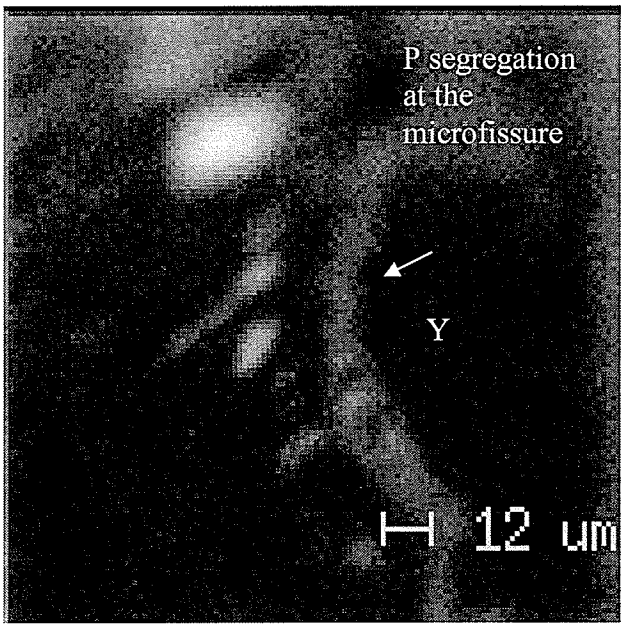

(a)

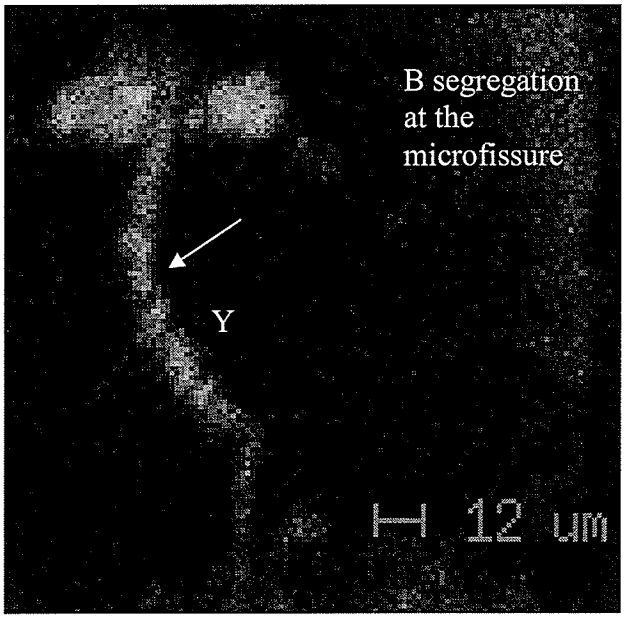

(b)

Fig.4.65: Secondary ion image of (a) phosphorus and (b) boron in HC 49 alloy at HAZ crack

As discussed earlier, the resolidified grain boundaries had Laves + γ eutectic or MC carbides + γ eutectic on them which were principally enriched in Nb, Fe and C. This was corroborated by carbon, boron and niobium ion images obtained from the resolidified grain boundaries, an example of which is shown in Figure 4.66. Figure 4.66 also shows grain boundary particles (arrowed) enriched in B, C and Nb indicating them to be Nb rich boro-carbides. Another example of a backfilled grain boundary near the fusion zone in HC 20 alloy is shown in Figure 4.67. It illustrates Nb, C, Ti and B ion images of the resolidified products which were obtained using the identical SIMS operating parameters and O_2^+ ion beam. Although B was detected, due to concurrent presence of other elements it was not possible to determine if it was present in elemental form or as a boro-carbide in the MC carbide + γ eutectic. The P ion images attempted subsequently at different settings indicated the segregation of P at the same grain boundary.

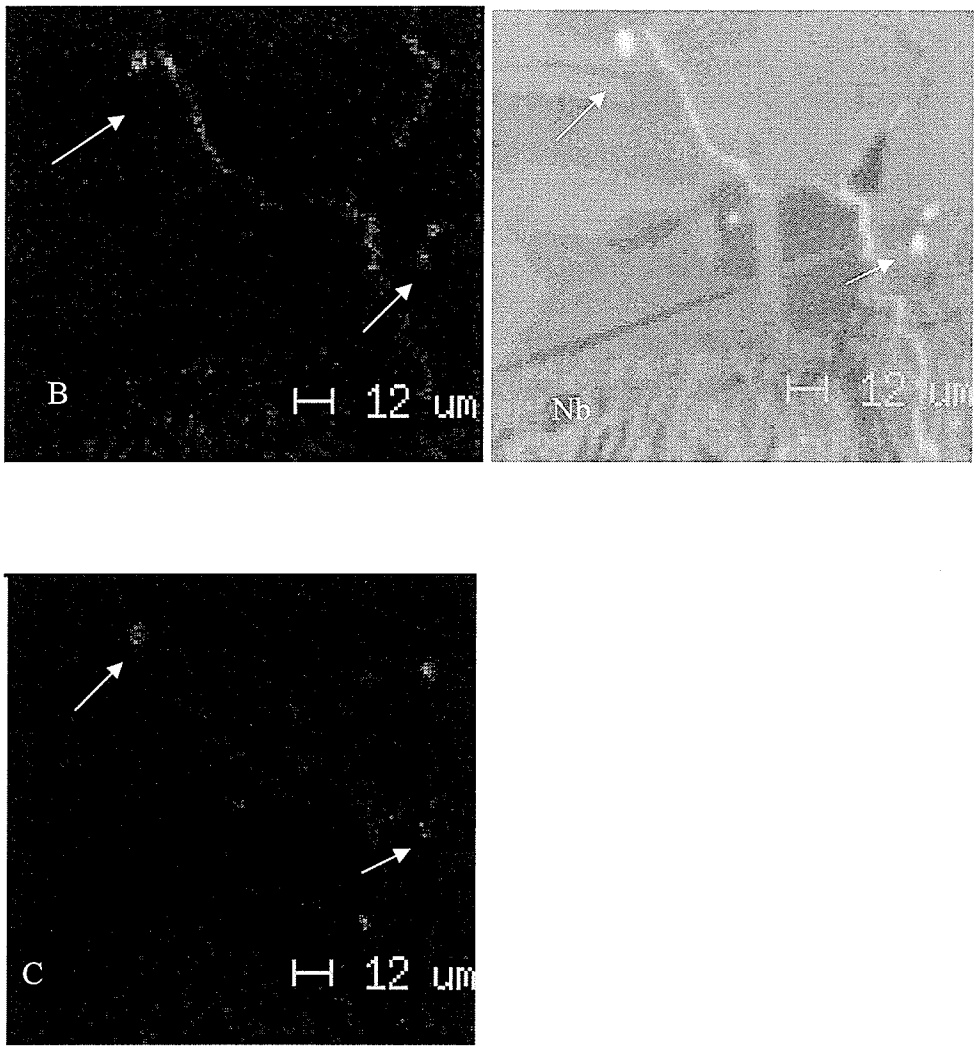

Figure 4.66: SIMS micrographs showing segregation of Boron and Niobium on the resolidified grain boundaries in HAZ of HC 20 alloy

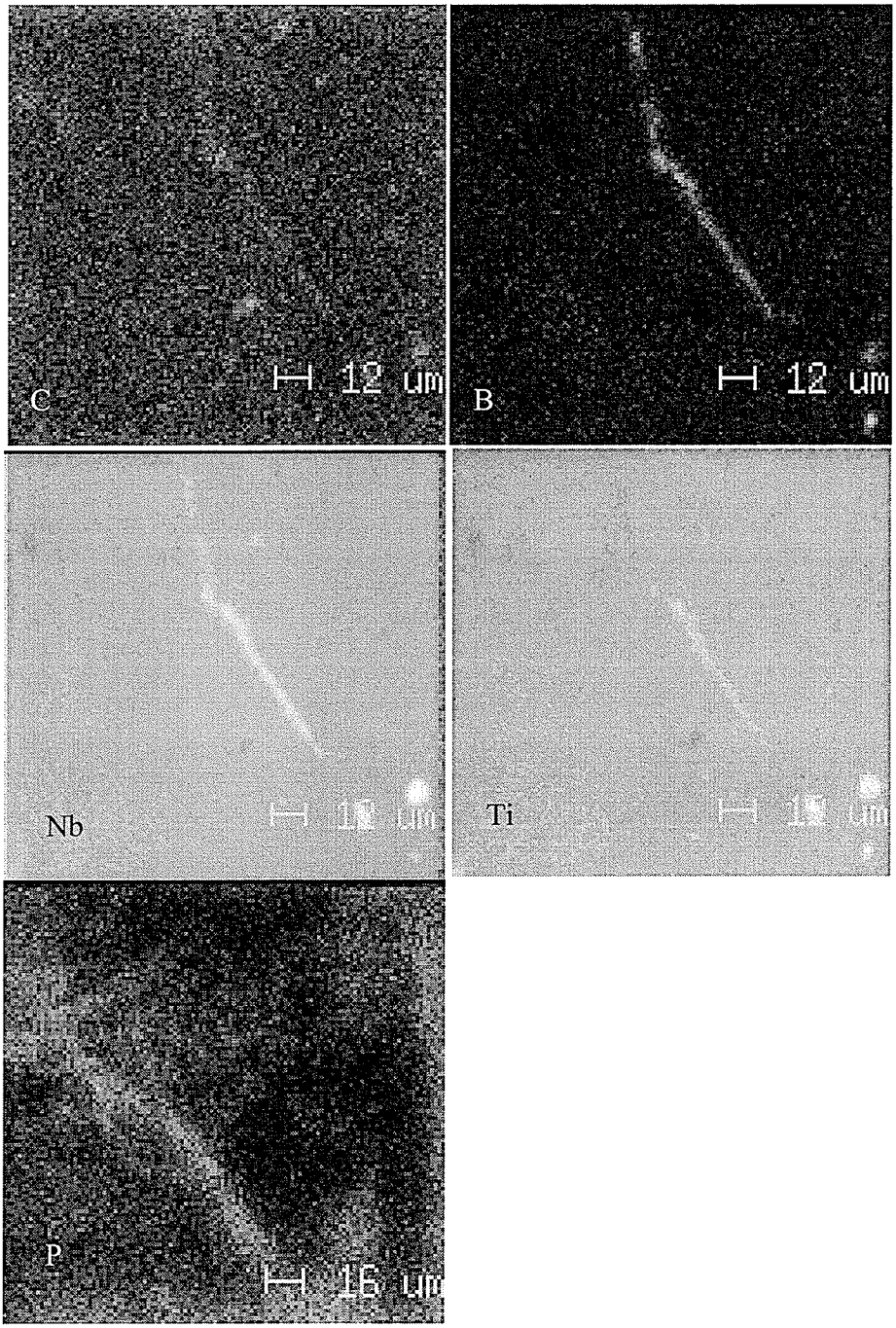

Fig. 4.67: SIMS micrographs showing segregation of Carbon, Boron, Niobium, Titanium and Phosphorus on the resolidified grain boundaries in HAZ of HC 20 alloy

Presence of phosphorus by SIMS analysis has not been reported in the published literature. In the present investigation phosphorus was observed to be present on edges of cracks in both the alloys. Unlike boron, qualitatively no significant difference was observed in the intensity of P ion images of the two alloys inspite of the higher P concentration in HC 49 alloy.

Segregation of P was not observed in the pre-weld heat treated specimen and most of segregation studies of P on grain boundaries have been done by auger electron spectrometer (AES)[125]. This requires an in-situ fracturing of the specimen in the AES which makes this technique more suitable for BCC materials as they undergo ductile-brittle transition at lower temperatures[133, 134]. However, as FCC materials do not undergo this transition, it is very difficult to observe P segregation at grain boundaries of FCC materials by AES, although Thompson et al. have observed P segregation in Inconel 718[124]. Horton et al. [131] are the other group that observed P segregation in Inconel 718 by Atom Probe spectroscopy. Non-equilibrium segregation of P was observed in industrial low alloy steel by Li et al. [133] and in medium carbon Cr steel by Zhang et al. [134], using AES in their study of temper embrittlement. However, none of these studies were focused on the effect of phosphorus segregation on weldability. The weldability studies have evaluated P and S together and reported the effects indirectly by measuring the increase in crack lengths byVarestraint test [48]. Sulphur in 718 Plus alloys, like many other superalloys, is kept to minimum considering its deleterious effects, and hence, the combination of other alloying elements with P needs to be studied more carefully. In the present study P was observed to be segregated on edges of the cracks

that formed on welding. It is likely that P segregation on grain boundary was too small to be detected in the pre-weld specimens. However welding caused liquation cracking and during solidification of the liquated boundaries, P, whose partition coefficient is less than unity in nickel, was rejected by the solidifying liquid in the solidifying by-product. This would increase the concentration of P on the edges of the cracks and when it reaches a critical minimum value, P could be detected by SIMS, and was observed to be concentrated on the edges of the cracks filled with resolidified products.

Boron and phosphorus segregation was found in and around same microfissures in the HAZ indicating co-segregation. B and P both adversely influence weldability which was also observed in a study on the effect of minor alloying elements on the weldability of Inconel 718 by Benhadad et al. [53] where the combined presence of B and P was found to be most detrimental.

4.5 Mechanism(s) of cracking in 718 Plus alloys

4.5.1 Introduction

The microstructural analysis of 718 Plus alloys suggests that microfissuring in the alloy occured due to intergranular liquation in the HAZ. The region of the HAZ immediately adjacent to the fusion zone is subjected to temperatures above the bulk solidus of the alloy and liquate during the weld thermal cycle. Besides the super-solidus liquation, liquid was observed in the HAZ below the bulk solidus of the alloy due to –

i. Constitutional liquation of second phase particles like Nb rich MC type carbides and Ti rich carbonitrides
ii. Segregation of B and P on the grain boundaries.

The presence of this non-equilibrium liquid in the HAZ during welding has been recognized as the primary reason for liquation cracking. Liquation cracking occurs due to inability of the intergranular liquid films to sustain the tensile stresses that develop during the cooling cycle of the welding. The principles governing liquation cracking are fairly well understood, and were discussed in section 2.4.4. Based on the results obtained in this study, the following weld cracking mechanism is proposed for 718 Plus alloy.

4.5.2 Mechanism of HAZ liquation cracking in 718 Plus alloy:

Constitutional liquation of NbC particles and liquation of grain boundaries segregated with B and P would occur during the heating cycle of welding as the temperature approaches the solidus temperature of the alloy. The intergranular liquid layer formed by the combination of these two factors would persists to lower temperatures during the cooling cycle. The contraction of the solidifying fusion zone and the restrain imposed by

the unaffected base-metal leads to development of tensile stresses in the HAZ. At these temperatures, the alloy would be still in the brittle temperature range, where ductility and strength are negligible. The simultaneous presence of the tensile stresses and a weak HAZ would cause the liquated grain boundaries to open up causing cracking. Few cracks that may be connected to the fusion zone would be back-filled by the liquid flowing in from the solidifying fusion zone. Solidification of the liquid in the cracks would result in the observed formation of low melting eutectic phases of γ + Laves phase and γ + MC carbide phases.

As reported earlier, the amount and distribution of carbides (and carbonitrides) was not appreciably different in either of the 718 Plus alloys in both the pre-weld heat treatment conditions. Hence the contribution of constitution liquation in the alloys, in the conditions studied, can be assumed to be the same. The segregation however, was observed to be different in both the alloys and also seems to vary considerably with the heat treatment. Also, the qualitatively observed increase in segregation correlated well with the crack measurements and the hot ductility results.

The higher B+P alloy suffered more HAZ microfissuring in both the heat treated conditions. In combination with the effect of grain size increase, due to the increase in the solution heat treatment temperature, higher concentration of B and P in HC 49 resulted in increased segregation and hence more HAZ cracking. Also, B and P segregation significantly reduced the on-cooling hot ductility, as indicated by the DRT values, of both the alloys compared to the on-heating ductility, as indicated by the NDT

values. Higher B+P alloy had a lower DRT value and a larger brittle temperature range (Table 4.11). Intergranular liquid in the HC 49 would therefore remain liquid to lower temperatures and make the alloy more susceptible to cracking. B has been known to affect the on-cooling hot ductility in Inconel 718 [47], and a similar effect was seen in 718 Plus alloys. The presence of B and P on grain boundaries reduced the melting point of the grain boundary material and, thus, increased the solidification range of 718 Plus alloys. Increase in the solidification temperature range would increase the alloy's susceptibility to HAZ cracking, but it is not a sufficient condition for cracking to occur. Another important requirement for cracking is that the intergranular liquid should wet and spread along the grain boundary in the presence of appreciable tensile stresses.

Wetting of the grain boundary by the liquid depends upon the relative surface energies of the liquid and solid. If HAZ cracking occurred when the liquid was still present on the grain boundaries, then the grain boundary could be thought of as a liquid filled crack. According to the Griffith type equation [135, 136], the stress required for propagation of such a crack would be given by the following equation-

$$\sigma = \sqrt{\frac{8\mu\gamma}{\pi(1-\nu)c}};$$

where σ = crack propagation stress, γ = effective fracture surface energy, μ = shear modulus, ν is Poisson's ratio and c is the crack length. The effective fracture surface energy in this case can be given by

$\gamma = 2\gamma_{SL} - \gamma_{GB}$;

where γ_{SL} is solid-liquid interfacial energy and γ_{GB} is the grain boundary energy. Presence of boron and phosphorus increase the γ_{GB} and thus reduce the effective fracture surface energy which would ultimately reduce the total stress required for crack propagation.

Also, presence of phosphorus was observed to reduce the solid-liquid surface energy,γ_{SL}, in austenitic matrix and improve wettability [48]. The energy conditions which must be satisfied, in order for the liquid to wet the grain boundary, the grain boundary energy, i.e., γ_{GB} must be greater than twice the solid-liquid interfacial energy[82]. With smaller ratios of γ_{SL}/γ_{GB}, liquid can easily spread over the grain boundaries forming continuous thin film, increasing the material's susceptibility to microfissuring.

This study shows that addition of B and P should be carefully controlled for better weldability. The standard 718 Plus alloy HC 20, with lower B and P exhibited a better weldability than the higher B and P version of HC 49, although an optimum level of B and P needs to be determined which can improve the desired creep properties with minimum adverse effect on weldability.

CHAPTER 5 - CONCLUSIONS

The following conclusions were made from the observations made during this study.

i. ***Microstructure of Waspaloy, Inconel 718 and HC 49 718 Plus alloys***

1) Solution heat treated (base metal) Waspaloy microstructure had uniformly distributed γ' particles in the matrix as well as on the grain boundaries. Ti-Mo rich MC type carbides were also distributed randomly throughout the microstructure.
2) Fusion zone microstructure consisted of fine cellular dendritic structure with interdendritic regions enriched in Ti. Extensive intergranular fusion zone solidification cracking was observed in the welds.
3) Constitutional liquation of Ti rich MC type carbides occurred in the HAZ and was suggested to be one of the primary reasons for HAZ liquation cracking. Resolidified grain boundaries in the HAZ were found to be enriched in Ti concentration compared to the composition of the matrix.
4) Microstructure of Inconel 718 after 950°C solution heat treatment consisted of randomly distributed Nb rich MC type carbides and Ti rich carbonitrides. Intra and intergranular precipitation of needle like δ phase was also observed in the microstructure. The microstructure did not change greatly after 1050°C heat treatment except for the dissolution of δ phase and the subsequent increase in the grain size. There was no significant difference in the amount and distribution of carbides and carbonitride particles.
5) Fusion zone of Inconel 718 had a fine cellular dendritic structure with no solidification cracking in either of the pre-weld heat treated conditions.

Undissolved coarse primary Nb rich MC type carbides and carbonitrides associated with eutectic type products were also observed in the fusion zone. Interdendritic regions of the fusion zone were enriched in Nb and Mo, and Laves phases were observed in the interdendritic regions.

6) Constitutional liquation of Nb rich MC type carbide particles (often containing some B) was observed near the fusion zone boundary and on the liquated and cracked grain boundaries in the HAZ. This was considered to the primary reason for liquation cracking in this alloy. The resolidified product on the cracked grain boundaries was identified as γ + Laves eutectic. Although, morphologically the cracking was similar in both the pre-weld heat treated alloys, the 1050°C heat treated material had more cracking in it than the 950°C heat treated material.
7) High B and P 718 Plus alloy, HC 49 had essentially similar microstructure as that of low B and P 718 Plus alloy, HC 20. Also, the microstructure of 718 Plus alloys was very similar to that of the baseline superalloy Inconel 718. The 950°C solution heat treated microstructure consisted of randomly distributed NbC particles and Ti (C,N) particles with δ phase on the grain boundaries. Delta phase dissolved after 1050°C heat treatment and a considerable increase in grain size was observed. The distribution of carbides and carbonitride was not significantly changed.
8) Fusion zone microstructure did not show any cracking and was very similar to that of Inconel 718. Liquation of Nb rich MC type carbide particles was observed in the HAZ on the liquated, cracked and resolidified grain boundaries. SEM/EDS

analytical analysis suggested that the resolidified products on the cracked grain boundaries were γ + Laves eutectic.

ii. Microstructure of HC 20 718 Plus alloy

1. The as received and 950°C solution heat treated microstructure exhibited the presence of fine γ′ particles in the alloy. Other phases observed were Nb rich MC type carbides, Ti rich carbonitrides and needle like δ phase. Heat treatment at 1050°C did not significantly change the amount and distribution of carbides and carbonitrides, but dissolved the grain boundary δ phase. This increased the grain size of the material. γ″ phase was not observed in either the as-received or any of the heat treated conditions.
2. The analysis of microsegregation, that occurred during solidification in the fusion zone of 718 Plus alloy welds, indicated that while Fe, W, Co and Cr segregated into the gamma dendrites, Nb, Mo, Ti and Al were rejected into the interdendritic liquid. The partition coefficients '*k*' at the beginning of solidification were determined by EPMA analysis of the elements – Cr, Co, Ni, Fe, Al, Ti, Nb, Mo and W. The elemental microsegregation resulted in the formation of gamma/carbide eutectic and gamma/Laves eutectic products in the interdendritic regions. Niobium, which is a constituent element of the main strengthening phase γ′, was consumed in forming Laves and MC carbides in the fusion zone, and γ′ precipitates were not observed in the microstructure.
3. 718 Plus alloy suffered from heat affected zone liquation cracking around the welds. Partial healing of the cracks by backfilling was also observed.

4. Heat affected zone liquation occurred by a combination of factors, viz., constitutional liquation of Nb rich MC type carbides, grain boundary liquation due to segregation of boron and due to supersolidus liquation of grain boundaries in the PMZ.
5. Depending on their location and composition, liquated grain boundaries in the HAZ, solidified either as gamma or followed the solidification pattern similar to that observed in the fusion zone, viz., the resolidified grain boundaries had gamma/Laves and gamma/carbide eutectic constituents on them.
6. Standard solution heat treatment and two step aging of HC 20 718 Plus alloy showed uniformly distributed fine γ' particles in the microstructure besides carbides/carbonitrides and δ phase. Over-aging at 650°C for upto 40 hours didn't change the hardness of the alloy significantly.

iii. Segregation of B and P

1. Segregation of B could not be detected in the pre-weld heat treated condition of 950°C for 1 hour by SIMS analysis. 1050°C heat treated material exhibited grain boundary segregation of B in both the 718 Plus alloys, with higher intensity of boron ion image in the higher B and P alloy, HC 49. Segregation of phosphorus was not detected in either of the two pre-weld conditions.
2. Detection of boron after the 1050°C heat treatment which was followed by water quenching indicated that non-equilibrium segregation of boron could not be suppressed by water cooling in this particular case.

3. Phosphorus was detected on the cracks in both the alloys in the HAZ region. The reason for the detection of P only after welding on the resolidified HAZ grain boundaries was suggested to be due to – firstly, too small an amount of P on the pre-weld heat treated grain boundaries to be detected successfully, and secondly the redistribution of P on the liquated grain boundaries during solidification due to a partition coefficient significantly smaller than unity.
4. Boron and P were observed on the same crack edges indicating co-segregation of these elements on the cracked boundaries.
5. Increase in the pre-weld heat treatment temperatures increased the segregation. HC 49 with more B and P showed more cracking in both the conditions when compared to the lower B+P alloy HC 20.
6. Presence of B and P on the cracked grain boundaries clearly indicated that microfissuring in 718 Plus was adversely affected by segregation of these elements.

iv. Weldability of 718 Plus alloys compared with Inconel 718 and Waspaloy

1. Total crack length were smallest in Inconel 718 in both the heat treated conditions and highest in the high B and P 718 Plus alloy, HC 49 in both the pre-weld heat treated condition. The TCL values in HC 20 718 Plus were intermediate between the values in Inconel 718 and HC 49 718 Plus in both the pre-weld conditions.
2. The lower TCL values in Inconel 718 were attributed to lower hardness of the base metal in both the heat treated conditions. The increase in cracking with the

increase in solution heat treatment was attributed to the increase in grain size and increase in non-equilibrium grain boundary segregation.

3. The average TCL values in Waspaloy were significantly higher than in any of the alloys in both the heat treated conditions. Fusion zone cracking was observed only in this alloy, and was more severe than that observed in the HAZ. Extensive cracking in Waspaloy compared to the other alloys was mainly attributed to the inter- and intragranular precipitation of fine γ' particles in the pre-weld heat treated microstructure.
4. The cracking susceptibility of the alloys was in the order of Inconel 718 < HC 20 718 Plus < HC 49 718 Plus < Waspaloy.
5. The hot ductility results of the tests with 10 mm diameter samples indicated that the difference in the on-heating ductility values of Inconel 718, HC 20 and HC 49 alloys was minimal.
6. The on-cooling hot ductility values of Inconel 718 and HC 20 were very similar, with a comparable ductility recovery temperature (DRT) and brittle temperature range (BTR). The on-cooling hot ductility values of the higher B and P 718 Plus alloy, HC 49, were worse, with a 45°C lower DRT and a larger BTR, indicating a crack susceptible microstructure.
7. The hot ductility results with 6 mm diameter samples of Inconel 718 and HC 49 718 Plus alloy, were comparable with comparable nil ductility temperatures (NDT).

8. The on-cooling hot ductility values of Inconel 718 were better than those of HC 49 718 Plus alloy, with HC 49 718 Plus having a much larger BTR compared to Inconel 718.
9. The hot ductility results corroborated the crack measurements data obtained from welds made on 6 mm diameter materials.
10. The trend of the hot-ductility values for the 10 mm and 6 mm specimen diameter remained the same, with the BTRs in the order of Inconel 718 < HC 20 718 Plus < HC 49 718 Plus alloy.
11. Both the weldability evaluation techniques, viz., crack measurements and hot ductility measurements, indicated that the weldability of Inconel 718 was marginally better than that of the 718 Plus alloys. Although, hot ductility values of HC 20 718 Plus were very close to that of Inconel 718. The weldability of the high B and P version of 718 Plus alloy, was significantly poorer when evaluated by either of the techniques. Based on both the evaluation techniques, the cracking susceptibility of the alloys increased in the following order –
    Inconel 718 < HC 20 718 Plus < HC 49 718 Plus < Waspaloy

The two main mechanism(s) of HAZ microfissuring in 718 Plus alloys were suggested to be:

1. Constitutional liquation of second phase particles viz. Nb rich MC type carbides and Ti rich carbonitrides
2. Grain boundary segregation of boron and phosphorus

CHAPTER 6 - SUGGESTIONS FOR FUTURE WORK

1. Grain boundary segregation of boron and phosphorus should be further examined, by heat treating the alloys at different solution heat treatment temperatures and by varying the cooling rate. The study of non-equilibrium and equilibrium segregation mechanism(s) would indicate the optimum combination of solution heat treatment temperature and cooling rate that would give the minimum segregation on the grain boundaries.
2. Post weld heat treatment studies of 718 Plus alloys should be studied without fillers and with fillers to give a more comprehensive evaluation of weldability.
3. HAZ simulation studies using Gleeble thermo-mechanical device should be carried out to further understand the stages of grain boundary liquation in this alloy.
4. Full penetration welds made by electron beam welding or other welding techniques should be examined to evaluate the effect of variation of mechanical restraint and the effect of HAZ area on microfissuring.

REFERENCES

1. Cao, W.D., Kennedy, R. L., *Role of chemistry in 718-type alloys - Allvac 718 Plus Alloy Development,* Superalloys 2004 (Eds. Green, K.A., Pollock, T.M., Harada, H., Howson, T.E., Reed, R.C., Schirra, J.J., Walston, S.), 2004: p. 91.
2. Ernst, S.C., Baeslack III, W.A., Lippold, J.C., *Weldability of high-strength, low-expansion superalloys,* Welding Journal, 1989, **68**(10): p. 418s.
3. Thompson, R.G., Radhakrishnan, B., Mayo, D. E., *Intragranular liquid formation distribution and cracking in the HAZ of alloy 718 welds*, Superalloys 718 - Metallurgy and Applications (Ed. Loria, E.A.), 1989: p.437.
4. Thompson, R.G., Dobbs, J. R., Mayo, D.E., *The effect of heat treatment on microfissuring in Alloy 718,* Welding Journal, 1986, **65**(11): p. 299-s.
5. Huang, X., Chaturvedi, M.C., Richards, N.L., *Effect of homogenization heat treatment on the microsturcture and heat-affected zone microfissuring in welded cast alloy 718,* Metallurgical and materials Transactions A, 1996, **27A**(March): p. 785.
6. Duvall, D.S., Owczarski, W.A., *Studies of postweld heat-treatment cracking in nickel - base alloys,* Welding Journal, 1969, **48**(1) : p. 10s.
7. Penkella, H.J., Wosik, J., Crzyrska-Filemonowicz,A., *Quantitative microstructural characterisation of Ni-base superalloys,* Metarial Chemistry and Physics, 2003, **81**: p. 417.
8. Groh, J.R., *Effect of cooling rate from solution heat treatment on Waspaloy microstructure and properties*, Superalloys 1996 (Eds. Kissinger, R.D., Deye, D.J., Anton, D.L., Cetel, A.D.), 1996: p.621.

9. Maurer, G.E., Jackman, L.A., Domingue, J.A., *Role of Cobalt in Waspaloy,* Superalloys 1980 (Eds. Tien,J.K., Wlodek, S.J., Morrow, H., Gell,M., Maurer, G.E.), 1980: p.43.

10. Dreshfield, R.L., *Evaluation of Mechanical Properties of a low cobalt wrought superalloy*, Superalloys 1992 (Eds. Antolovich, S.D., Stusrud,R.W., Mackay, R.A., Anton, D.L., Khan,T., Kissinger,R.D., Klarstrom,D.L.), 1992: p.317.

11. Fayman, Y.C., *Gamma-Gamma prime partitioning behaviour in Waspaloy,* Materials Science and Engineering, 1986, **82**: p. 203.

12. Rehrer, W.P., Walley, R.F., *Effect of solution treating on the structure and mechanical properties of waspaloy fastener stock,* Heat Treating, 1978, **10**(9): p. 78.

13. Tien, J.K., Jarrett, R.N., *Effect of Cobalt in Nickel - base superalloy,* Conference Proceeding of High temperature alloys for gas turbines (Eds. Brunetaud,R., Coutsouradis,D., Gibbons, T.B.,Lindblom, Y., Medowcroft,D.B., Stickler,R.), Liege, Belgium, 1982: p. 423.

14. Busby, J., *Solution heat treatment of forged waspaloy effect of compositional variation,* Metallurgia Metal Forming, 1972, **39**(9): p. 325.

15. Fayman, C., *Quantitative phase characterization of a nickel base superalloy,* Metals, Materials, Manufacturing: Proceedings of 1985 Metals Congress, Australia, 1985: p. D13.

16. Owczarski, W.A., *Process and metallurgical factors in joining superalloys and other high service temperature materials*, Physical Metallurgy of metal joining, Metallurgical Society of AIME, 1980: p.166.

17. Jackman, L.A., Canada, H.B., Sczerzenie, F.E., *Quantitative carbon partitioning diagrams for waspaloy and their application to chemistry modifications and processing*, Superalloys 1980 (Eds. Tien,J.K., Wlodek, S.J., Morrow, H., Gell,M., Maurer, G.E.), 1980: p.365.

18. Qian, M., Lippold, J.C., *The effect of multiple PWHTs cycles on the weldability of Waspaloy,* Welding Journal, 2002, **81**(11): p. 233-s.

19. Nakao, Y., Mitsuhata,K., *Reheating cracking phenomenon in Ni-base superalloy, Waspaloy,* Quaterly Journal of the Japan Welding Society, 1985, **3**(4): p. 808.

20. Li, Z., Gobbi, S.L., Loreau, J.H., *Laser welding of Waspaloy sheets for aero-engines,* Journal of Materials Processing Technology, 1997, **65**(1-3): p. 183.

21. Owczarski, W.A., Duvall, D.S., Sullivan, C.P., *A model of HAZ cracking in Nickel - base superalloys,* Welding Journal, 1966, **45**(4): p. 145-s.

22. Nakao, Y., *Study on reheat cracking of nickel-base superalloy, Waspaloy,* Transactions of Japanese Welding Society, 1988. **19**(1): p. 66.

23. Guo, H., Chaturvedi, M.C., Richards, N.L., McMahon, G.S., *Interdependence of character of grainboundaries, intergranular segregation of boron and grain boundary liquation insimulated weld heat- affected zone in Inconel 718,* Scripta materialia, 1999, **40**(3): p. 383.

24. Qian, W., Lippold, J.C., *The effect of grain boundary character distribution on the repair weldability of Waspaloy*, Proceeding of 6th International conference, Trends in Welding Research (Eds. David, S.A., Smartt, H., Lippold, J., Vitek, J.M.), Phoenix,U.S.A., 2003: p.603.

25. Norton, S.J., Lippold, J.C., *Development of a gleeble-based test for postweld heat treatment cracking susceptibility*, Proceeding of 6th International conference, Trends in Welding Research, Phoenix, U.S.A., 2003: p.609.

26. Radavich, J.F., *The physical metallurgy of cast and wrought Alloy 718*, Superalloy 718 - Metallurgy and Applications (Ed. Loria, E.A.), 1989: p. 229.

27. Paulonis, D.F., Oblak, J.M., Duvall,D.S., *Precipitation in Nickel base Alloy 718*,Transactions of American Society of Metals, 1969, **62**: p. 611.

28. Cozar, R., Pineau, A., *Morphology of gamma prime and gamma double prime precipitates and thermal stability of Inconel 718 type alloy,* Metallurgical Transactions, 1973, **4**(Jan): p. 47.

29. Gao, M., Wei, R.P., *Grain boundary gamma double prime precipitation and niobium segregation in Inconel 718,* Scripta Metallurgica et Materialia, 1995, **32**(7): p. 987 - 990.

30. Xie, X., Liang, Q., Dong, J., Meng, W., Xu, Z., Chen, M., Wang, F., Cai, Y., Zhang, J., Wang, N., Andrieu, E., Pineau, A., *Investigation of high thermal stability and creep resistant modified Inconel 718 with combined precipitation of gamma double prime and gamma prime*, Superalloys 718, 625, 706 and various derivatives (Ed. Loria, E.A.), 1994: p.711.

31. Azadian, S., Wei, L., Warren, R., *Delta phase precipitation in Inconel 718,* Materials Characterisation, 2004, **53**: p. 7.

32. Sundararaman, M., Mukhopadhyay, P., Banerjee, S., *Precipitation of the delta-Ni_3Nb phase in two nickel base superalloys,* Metallurgical Transactions A, 1988, **19A**(March): p. 453.

33. Gao, M., Wei, R.P., *Grain boundary niobium carbides in Inconel 718,* Scripta Materialia, 1997, **37**(12): p. 1843-1849.

34. Schirra, J.J., Caless, R.H., Hatala. R. W., *The effect of laves phase on mechanical properties of wrought and cast + HIP Inconel 718*, Superalloys 718, 625, 706 and various derivatives (Ed. Loria, E.A.), 1991: p.375.

35. Burke, M.K., Miller, M. K., *Precipitationin Alloy 718: A Combined AEM and APFIM Investigation*, Superalloys 718, 625, 706 and various derivatives (Ed. Loria, E.A.), 1991: p.337.

36. Vincent, R., *Precipitation around welds in the nickel-base superalloy, Inconel 718,* Acta Metallurgica, 1985, **33**(7): p. 1205.

37. Srinivasan, D., *Effect of long-time exposure on the evolution of minor phases in alloy 718,* Material Science and Engineering A, 2004, **A 364**: p. 27.

38. Boesch, W.J., Canada,H.B., *Precipitation reactions and stability of Ni_3Nb in alloy 718,* Journal of metals, 1969, **21**(10): p. 34.

39. Duvall, D.S., Owczarski, W.A., *Further HAZ studies in heat-resistant nickel alloys,* Welding Journal, 1967, **46**(9): p. 423-s.

40. Thompson, E.G., *Hot cracking studies of alloy 718 weld heat-affected zones,* Welding Journal, 1969, **48**(2): p. 70-s.

41. Baeslack III, W.A., Nelson, D.E., *Morphology of Weld Heat-Affected Zone Liquation in cast alloy 718,* Metallography, 1986, **19**: p. 371.

42. Qian, M., Lippold, J.C.,*The effect of annealing twin-generated special grain boundaries on HAZ liquation cracking of nickel-base superalloys,* Acta Materialia, 2003, **51**: p. 3351.

43. Richards, N.L., Chaturvedi, M.C., *Effect of minor elements on weldability of nickel base superalloys,* International Materials Review, 2000, **45**(3): p. 109.

44. Pepe, J.J., Savage, W. F., *Effects of constitutional liquation in 18-Ni Maraging Steel Weldments,* Welding Journal, 1967, **46**(9): p. 411-s.

45. Huang, X., Chaturvedi, M.C., *An investigation of microstructure and HAZ microfissuring of cast alloy 718*, Superalloys 718, 625, 706 and various derivatives (Ed. Loria, E.A.), 1994: p.871.

46. Huang, X., Chaturvedi, M.C., Richards, N.L., Jackman, J., *The effect of grain boundary segregation of boron in cast alloy 718 on HAZ microfissuring - A SIMS analysis,* Acta materialia, 1997, **45**(8): p. 3095.

47. Guo, H., Chaturvedi, M.C., Richards, N.L., *Effect of boron concentration and grain size on weld heat affected zone microfissuring in Inconel 718 base superalloys,* Science and Technology of Welding and Joining, 1999, **4**(4): p. 257.

48. Savage, W.F., Nippes, E.F., Goodwin, G.M., *Effect of minor elements on hot cracking tendencies of Inconel 600,* Welding Journal, 1977, **56**(8): p. 245-s.

49. Kelly, T.J., *Elemental effects on cast 718 weldability,* Welding Journal, 1989(February): p. 44-s.

50. Chen, W., Chaturvedi, M.C., Richards, N.L., McMahon, G., *Grain boundary segregation of boron in Inconel 718,* Metallurgical and Materials Transactions A, 1998, **29A**(July): p. 1947.

51. Guo, H., Chaturvedi, M.C., Richards, N.L., *Effect of sulphur on hot ductility and heat affected zone microfissuring in Inconel 718 welds,* Science and Technology of Welding and Joining, 2000, **5**(6): p. 378.

52. Thompson, R.G., Koopman, M.C., King, B.H., *Grain Boundary Chemistry of Alloy 718 - Type Alloys*, Superalloys 718, 625, and various derivatives (Ed. Loria, E.A.), 1991: p. 53.

53. Benhadad, S., Richards, N.L., Chaturvedi, M.C., *The influence of minor elements on the weldability of an Inconel 718 type superalloy,* Metallurgical and Materials Transactions A, 2002, **33A**(July): p. 2005.

54. McLean, D., *Grain boundaries in Metals*. 1957, Oxford: Clarendon Press.

55. Thompson, R.G., *Microfissuring of alloy 718 in the weld heat affected zone.* Journal of Metals, 1998(July): p. 44.

56. Radhakrishnan, B., Thompson, R.G., *A model for the formation and solidification of grain boundary liquid in the Heat-Affected Zone (HAZ) of welds,* Metallurgical Transactions A, 1992, **23 A**(June): p. 1783.

57. Thompson, R.G., Cassimus, J.J., Mayo, D.E., Dobbs, J.R., *The relationship between grain size and microfissuring in Alloy 718,* Welding Journal, 1985, **64**(4): p. 91-s.

58. Radhakrishnan, B., Thompson, R.G., *Solidification of the nickel-base superalloy 781: A phase diagram approach,* Metallurgical Transactions A, 1989. **20A**(December): p. 2866.

59. Huang, X., Richards, N.L., Chaturvedi, M.C., *Effect of grain size on the weldability of cast alloy 718,* Materials and Manufacturing Processes, 2004, **19**(2): p. 285.

60. Miller, W.A., Chadwick, G.A., *On the magnitude of solid/liquid interfacial energy of pure metals and its relation to grain boundary melting,* Acta Matellurgica, 1967, **15**(4): p. 607.

61. Ojo, O.A., Rihcards, N.L., Chaturvedi, M.C., *Liquid film migration of constitutionally liquated gamma prime in weld heat affected zone (HAZ) of Inconel 738LC superalloy,* Scripta Materialia, 2004, **51**: p. 141.

62. Barker, S.W., Purdy, G.R., *On liquid film migration in aluminum-copper alloys.* Acta Materialia,1998, **46**(2): p. 525.

63. Watanabe, T., *An approach to grain boundary design and ductile polycrystals*, Res Mechanica, 1984, **11**:p.47.

64. Palumbo, G., King, P.J., Lichtenberger, P.C., Aust, K.T., Erb, U., *Grain boundary design and control for intergranular stress-corrosion resistance,* Scripta Metallugica et Materialia, 1991, **25**(8): p. 1775.

65. Chaturvedi, M.C., *Grain boundary engineering and weldability of superalloys.* International Conference on advances in Materials Processing, Kharagpur, India, 2002: p. 1247.

66. Qian, M., Lippold, J.C., *Liquation Phenomena in the simulated heat-affected zone of alloy 718 after multiple post weld heat treatment cycles,* Welding Journal, 2003, **82**(6): p. 145-s.

67. Qian, M., Lippold, J.C., *The effect of rejuvenation heat treatments on the repair weldability of wrought alloy 718,* Materials Science and Engineering A, 2003, **A 340**: p. 225.

68. Kennedy, R.L. *,Allvac 718 Plus ,Superalloy for the next forty years*, Superalloy 718, 625, 706 and various derivatives (Ed. Loria, E.A.), 2005: p.1.

69. Xie, X., Wang, G., Dong, J., Cao, W.D., Keneddy, R., *Structure stability study on a newly developed nickel-base superalloy - Allvac 718 Plus*, Superalloy 718, 625, 706 and various derivatives (Ed. Loria, E.A.), 2005, p.179.

70. Radavich, J, Carneiro,T., *A microstructural study of alloy 718 Plus,* Superalloys 718, 625, 706 and Derivatives (Ed. Loria, E.A.), 2005: p. 329.

71. Xie, X., Xu, C., Wang, G., Dong, J.,Cao, W.D., Kennedy, R.L., *TTT diagram of a newly developed nickel-base superalloy - Allvac 718 plus,* Superalloys 718, 625, 706 and various derivatives (Ed. Loria, E.A.), 2005: p. 193.

72. Cao, W.D., *Solidification and solid state phase transformation of Allvac 718 plus alloy,* Superalloys 718, 625, 706 and various derivatives (Ed. Loria, E.A.), 2005: p. 165.

73. Donachie, M.J., *Superalloys A technical guide*. Second Ed. 2002, Materials Park, OH: ASM International. 439.

74. Kou, S., *Welding Metallurgy*. Second Ed. 2003, Hoboken,New Jersey: John Wiley and Sons., 410.

75. *ASM Handbook Volume 6 Welding, Brazing, and Soldering*. 1993, ASM International, 1299.

76. Richards, N.L., Chaturvedi, M.C., Liu, Y.G., Mount, K., *Optimization of electron beam welding parameters for Incoloy 903,* International journal of materials and product technology, 1996, **11**(3-4): p. 284.

77. Richards, N.L., Chaturvedi,M.C., *The influence of electron-beam welding parameters on Heat-Affected-Zone Microfissuring in Incoloy 903,* Metallurgical and Materials Transactions A, 1994, **25A**: p. 1733.

78. Easterling, K., Ed. *Introduction to the physical metallurgy of welding.* 1992, Butterworth-Heinemann, 270.

79. Borland, J.C., Proceedings of the twenty-sixth Autumn Review Course, *Metallurgical Implication of welding processes, Competitive processes in joining,* England, U.K., 1973: p.94.

80. Prager, M.S., Shira, C.S., *Welding of Precipitation-hardening Nickel- base superalloys.* Weld. Res. Counc. Bull., 1968, **128**.

81. Borland, J.C., *Fundamentals of solidification cracking in welds - I,* Welding and metal fabrication, 1979, **47**(1): p.19.

82. Borland, J.C., *Generalized theory of super-solidus cracking in welds (and castings).* British Welding Journal, 1960, **7**: p. 558.

83. Pellini, W.S., *Strain theory of hot tearing,* Foundry, 1952, **80**(11): p. 125.

84. Ojo, O.A., Richards, N.L., Chaturvedi, M.C., *Liquation of various phases in HAZ during welding of cast Inconel 738LC,* Materials Science and Technology, 2004, **20**(8): p. 1027.

85. Lin, W., Lippold, J.C., Baeslack, W.A., *Analysis of weldability testing techniques for HAZ liquation cracking,* Advacements in synthesis and processes, Toronto, Canada, 1992: p. M464.

86. Lundin, C.D., Qiao, C.Y.P., Lee,C. H., *Standardization of gleeble hot ductility testing: Part1: Histroical review,* Weldability of Materials, Detroit, Michigan, USA, 1990: p. 1.

87. Kreischer, C.H., *A critical analysis of the weld heat-affected zone hot ductility test,* Welding Journal, 1963, **42**(2): p. 49-s.

88. Donati, J.R., Zacharie, G., *Evaluation of hot cracking susceptibility in heat affected zones of welded austenitic 18-10 steels - Discussion of cracking criteria.* 1974, **71**(12): p. 905.

89. Lundin, C.D., Qiao, C.Y.P., Lee, C.H., *Standardization of Gleeble hot ductility testing: Part II: Experimental Evaluation,* Weldability of Materials, Detroit, Michigan, USA, 1990: p. 9.

90. Mehl, M.E., Lippold, J.C., *Effect of delta - phase precipitation on the repair weldability of Alloy 718,* Superalloys 718, 625, 706 and various derivatives (Ed. Loria, E.A.), 1997: p. 731.

91. Savage, W.F., Lundin, C.C., *The varestraint test,* Welding Journal, 1965, **44**(10): p. 433-s.

92. Richards, N.L., Huang, X., Chaturvedi, M.C., *Heat affected zone cracking in cast Inconel 718,* Materials Characterization, 1992, **28**: p. 179 - 187.

93. Jawwad, A.K.A., Strangwood, M., Davis, C.L., *The role of the slope out region on fatigue crack initiation in electron beam welded waspaloy,* Metallurgical and Materials Transactions A, 2003, **34A**(August): p. 1637.

94. Sekhar, N.C., Reed, R.C., *Power beam welding of thick section nickel base superalloys.* Science and Technology of Welding and Joining, 2002, **7**(2): p. 77.

95. Ding, R.G., Ojo, O.A., *Heat affected zone microfissuring in laser beam welded directionally solidified Ni_3Al superalloy,* Scripta Materialia, 2006, **56**: p.5.

96. Murata, Y., Moringag, M., Yukawa, N., Ogawa, H., Kato, M., *Solidification and precipitation behaviour of Inconel 718 and Waspaloy,* The first pacific rim International Conference on Advanced Materials and Processing, Hnagzhou, China, 1992(June): p. 269.

97. Janaki Ram, G.D., Reddy, A.V., Rao, K. P., Madhusudhan, G.R., Sunder J.K., *Microstructure and tensile properties of Inconel 718 pulsed Nd-YAG laser welds,* Journal of Materials Processing Technology, 2005, **167**: p. 73.

98. Radhakrishna, C., Rao, K.P., *The formation and control of Laves phase in superalloy 718 welds,* Journal of Materials Science, 1997, **32**: p. 1977.

99. Knorovsky, G.A., Cieslak, M.J., Headley, T.J., Romig, A.D. Jr., Hemmetter, W.F., Inconel 718 : A Solidification Diagram, Metallurgical Transactions A, 1989. 20A (October): p. 2149.

100. Cieslak, M.J., Headley, T.J., Knorovsky, G.A., Romig, A.D. Jr., Kollie, T., A comparison of the solidification behavior of Incoloy 909 and Inconel 718, Metallurgical Transactions A, 1990, 21A: p. 479.

101. Sims, C.T., Stoloff, N.S., Hagel, W.C. Eds. Superalloys II. 1987, John Wiley & Sons Inc.: United States of America, 615.

102. Baeslack, III.W.A., Lata, W.P., West, S.L., *A study of heat-affected zone and weld metal liquation cracking in Alloy 903,* Welding Journal, 1988, **67**(4): p. 77-s.

103. Nakkalil, R., Richards, N.L., Chaturvedi, M.C., *The influence of solidification mode on heat affected zone microfissuring in a nickel-iron base superalloy,* Acta Metallurgica et Materialia, 1993, **41**(12): p. 3381.

104. Radavich, J.F., *Metallography of alloy 718,* Journal of Metals, 1998(July): p. 42-43.

105. Ram, J.G.D., G.D., Reddy, A.V., Rao, K. P., Madhusudhan, G.R., *Microstructure and mechanical properties of Inconel 718 electron beam welds,* Materials Science and Technology, 2005, **21**(10): p. 1132.

106. Bower, T.F., Brody, H.D., Flemings, M.C., *Measurement of solute redistribution in dendritic solidification,* 1966, **236**(5): p. 624.

107. Gobbi, S., Zhang, L., Norris, J., Richter, K.H., Loreau, J.H., *High powder CO2 and Nd-Yag laser welding of wrought Inconel 718,* Journal of Materials Processing Technology, 1996, **56**: p. 333.

108. Mehrabian, R., Kear, B.H., Cohen, M., Eds. *Rapid Solidification Processing: Principles and Technologies - I*, 1978, Claitor's Publication Division: Baton Rouge, LA, 398.

109. Nakkalil, R., Richards, N.L., Chaturvedi, M.C., *Fusion zone microstructure of electron beam welded Incoloy 903,* Scripta Metallurgica et Materialia, 1992, **26**: p. 545.

110. Ojo, O.A., Richards, N.L., Chaturvedi, M.C., *Microstructural study of weld fusion zone of TIG welded IN 738 LC nickel- based superalloy,* Scripta Materialia, 2004, **51**: p. 638.

111. Huang, C., *Liquation cracking in partial penetration aluminum welds: assessing tendencies to liquate, crack and backfill,* Science and technology of welding and joining, 2004, **9**(2): p. 149.

112. Huang, C., Kou.S., *Liquation cracking in partial-penetration aluminum welds: effect of penetration oscillation and backfilling,* Welding Journal, 2003, **82**(7): p. 184-s.

113. Savage, W.F., Dickinson, D.W., *Electron microanalysis of backfilled hot cracks in Inconel 600,* Welding Journal, 1972, **51**(11): p. 555-s.

114. Nakkalil, R., Richards, N.L., Chaturvedi, M.C., *Microstructural Characterisation of Incoloy 903 Weldments,* Metallurgical Transactions A, 1993. **24A**(May): p. 1169.

115. Romig, A.D., Lippold, J.C., Cieslak, M. J., *An analytical electron microscope investigationof the phase transformations in a simulated heat-affected zone in alloy 800,* Metallurgical Transactions A, 1988, **19A**(January): p. 35.

116. Ojo, O.A., Richards, N.L., Chaturvedi, M.C., *On the role of liquated gamma prime precipitates in weld heat affected zone microfissuring of nickel-based superalloy,* Materials Science and Engineering A, 2005, **A 403** (1-2): p. 77.

117. Ojo, O.A., Rihcards, N.L., Chaturvedi, M.C., *Contribution of constitutional liquation of gamma prime precipitate to weld HAZ cracking of cast Inconel 738 supeeralloy,* Scripta materialia, 2004, **50**: p. 641.

118. Sidhu, R.K., Richards, N.L., Chaturvedi, M.C., *Effect of aluminium concentration in filler alloys on HAZ cracking in TIG welded cast Inconel 718LC superalloy,* Materials Science and Technology, 2005, **21**(10): p. 1119.

119. Banerjee, K., Richards, N.L.,Chaturvedi, M.C., *Effect of Filler Alloys on Heat-Affected Zone Cracking in Preweld Heat-Treated IN-738 LC Gas-Tungsten-Arc Welds,* Metallurgical and Materials Transactions A.Vol.36A, 2005: p. no. 7.

120. Thakur, A., Richards, N.L., Chaturvedi, M.C., *On crack-free welding of cast Inconel 738,* The international journal for the joining of materials, 2003, **15**(4): p. 21.

121. Sidhu, R.K., Richards, N.L.; Chaturvedi, M.C., *Post weld heat treatment cracking in autogenous GTA welded and cast Inconel 738LC superalloy.* Materials Science and Technology, 2007. **23**(2): p. 203.

122. Sekhar, N.C., Reed, R.C., *Effects of post-weld heat treatment on power beam welds in waspaloy and Udimet 720 Li.*, Proceedings of 6th International Conference Trends in Welding (Eds. David, S.A., Smartt, H., Lippold, J., Vitek, J.M.), Phoenix, U.S.A., 2003: p.773.

123. Sidhu, R.K., Ojo, O.A., Chaturvedi, M.C., *Microstructural analysis of laser beam welded directionally solidified Inconel 738,* Metallurgical and Materials Transactions A, 2007, **38**(4): p. 12.

124. Thompson, R.G., Koopman, M.C., King, B.H., *Grain Boundary Chemisty of Alloy 718 Type Alloys*, Superalloys 718, 625, 706 and various derivatives (Ed. Loria, E.A.), 1991: p.53.

125. Cao, W.D., Kennedy,R.L., *The effect on mechanical properties of Alloy 718,* Superalloys 718, 625, 706 and various derivatives (Ed. Loria, E.A.), 1994: p. 463.

126. Cao, W.D., Kennedy, R.L., *Effect and mechanism of phosphorus and boron on creep deformation of alloy 718,* Superalloys 718, 625, 706 and various derivatives (Ed. Loria, E.A.), 1997: p. 511.

127. Cao, W.D., Kennedy. R.L., *Phosphorus- Boron interaction in nickel-base superalloys*, Superalloys 1996 (Eds. Kissinger, R.D., Deye, D.J., Anton, D.L., Cetel, A.D.), 1996: p. 589.

128. McKamey, C.G., George, E.P., Carmicheal, C.A., Cao, W.D., Kennedy, R.L., *Effects of phosphorus and boron on the creep behavior of Waspaloy*, International conference on creep and fracture of engineering materials and structure (Ed. Parker, D.J.), 2001: p. 459.

129. Song, H., Guo, S., Hu ,Z., *Beneficial effect of phosphorus on the creep behaivour of Inconel 718,* Scripta Materialia, 1999, **41**(2): p. 215.

130. Miller, M.K., Horton, J.A., Cao, W.D., Kennedy, R.L., *Characterization of the effects of boron and phosphorus additons to the nickel-based superalloy 718,* Journal De Physicque IV, Colloque C5, 1996. **6**(September): p. C5-241.

131. Horton, J.A., McKamey, C.G., Miller, M.K., Cao, W.D., Kennedy, R.L., *Microstructural Characterization of superalloy 718 with boron and phosphorus additions.* Superalloys 718, 625, 706, and various derivatives (Ed. Loria, E.A.), 1997: p. 410.

132. Aust, K.T., Armijo, S.J., Koch, E.F., Westbrook, K.J., *Intergranular corrosion and electron microscopic studies of austenitic stainless steels,* ASM Transactions, 1967. **60**(3): p. 360.

133. Li, Q., Yang, S., Li, L., Lie, Z., Xu, T., *Experimental study on non-equilibrium grain-boundary segregation kinetics of phosphorus in an industrial steel,* Scripta Materialia, 2002. **47**: p. 389.

134. Zhang, Z., Xu,T., Lin, Q., Yu, Z., *A new interpretation of temper embrittlement dyanamics by non-equilibrium segregation of phosphor in steels,* Journal of Materials science, 2001. **36**: p. 2055.

135. Griffiths, A.A., *The phenomenon of rupture and flow in solids,* Phil. Trans. Roy. Soc., 1920, **A 211**.

136. Huang, X., *A microstructural study of heat affected zone microfissuring of electron beam welds in cast alloy 718*, Ph.D. Thesis, Mechanical Engineering, University of Manitoba, 1994: p.295.

Refereed Journal Publications from the present Thesis:

1. Vishwakarma, K.R., Richards, N.L. and Chaturvedi, M.C.; Microstructural analysis of fusion and heat affected zones in electron beam welded ALLVAC® 718 PLUS ™ superalloy, Article in Press, Materials Science and Engineering A.
2. Vishwakarma, K.R. and Chaturvedi, M.C., Effect of boron and phosphorus on HAZ microfissuring of ALLVAC® 718 PLUS ™ superalloy, Article in Press, Materials Science and Technology.

Publication in Conference Proceedings:

1. Vishwakarma, K.R., Richards, N.L. and Chaturvedi, M.C.; HAZ Microfissuring in EB welded ALLVAC 718 PLUS ™ alloy, Superalloys 718, 625, 706 and Derivatives , pp. 637-647. 2006

Conference Presentations:

1. Vishwakarma, K.R., Richards, N.L. and Chaturvedi, M.C.; HAZ Microfissuring of ALLVAC 718 PLUS , 17th Canadian Materials Science Conference, UBC, Vancouver, Canada, June 2005
2. Vishwakarma, K.R., Richards, N.L. and Chaturvedi, M.C.; Mechanism(s) of cracking in EB welded ALLVAC 718 Plus Superalloy, 18th Canadian Materials Science Conference, McGill University, Montreal, Canada, June 2006